UNIVERSIDADE
BEIRA INTERIOR

Droplet Impact onto Heated Wetted Surfaces:
A Fundamental Study

Daniel de Almeida Vasconcelos Rodrigues

Tese para obtenção do Grau de Doutor em
Engenharia Aeronáutica
(3º ciclo de estudos)

Orientador: Prof. Doutor André Resende Rodrigues da Silva

maio de 2025

UNIVERSIDADE
BEIRA INTERIOR

Droplet Impact onto Heated Wetted Surfaces:
A Fundamental Study

Daniel de Almeida Vasconcelos Rodrigues

Tese para obtenção do Grau de Doutor em
Engenharia Aeronáutica
(3º ciclo de estudos)

Orientador: Prof. Doutor André Resende Rodrigues da Silva

Júri:
Prof. Doutor Jorge Manuel Martins Barata
Prof. Doutor Daniel Cardoso Vaz
Prof. Doutor Miguel Rosa Oliveira Panão
Prof. Doutor Miguel Abreu de Almeida Mendes
Prof. Doutor Leandro Barbosa Magalhães
Prof. Doutora Ana Sofia Oliveira Henriques Moita

15 de abril de 2025

We Lost Ourselves. Lost Our Dream. In The Pursuit Of Great, We Failed To Do Good.

— Viktor, *Arcane*

Declaração de Integridade

Eu, Daniel de Almeida Vasconcelos Rodrigues, que abaixo assino, estudante com o número de inscrição $d2576$ do Curso $3°$ Ciclo em Engenharia Aeronáutica da Faculdade de Engenharias, declaro ter desenvolvido o presente trabalho e elaborado o presente texto em total consonância com o **Código de Integridades da Universidade da Beira Interior.**

Mais concretamente afirmo não ter incorrido em qualquer das variedades de Fraude Académica, e que aqui declaro conhecer, que em particular atendi à exigida referenciação de frases, extratos, imagens e outras formas de trabalho intelectual, e assumindo assim na íntegra as responsabilidades da autoria.

Universidade da Beira Interior, Covilhã 31/10/2024

Acknowledgements

First and foremost, I would like to express my deepest gratitude to my supervisor, Professor André Resende Rodrigues da Silva, for the continuous support and guidance throughout the years at the University of Beira Interior. Countless hours of debate and critical thinking established the foundation for preliminary studies, which were deemed essential to the development of the research topic.

I am extremely grateful for the possibility of advancing this field of research under AEROG - Aeronautics and Astronautics Research Center, a research unit of LAETA - Associate Laboratory for Energy, Transports and Aerospace. I sincerely thank Professor Jorge Manuel Martins Barata, director of AEROG, for providing the resources required for this project. His dedication and expertise towards the research group were unparalleled, prioritizing the work developed by both students and researchers.

Within the scope of the experimental and numerical setup, there are several companies and individuals that directly contributed to this investigation. I would like to thank Mr. Rui Manuel Tomé Paulo for his assistance with the laboratory equipment and technical troubleshooting, and Mr. Rui Ribeiro for assisting with the code implementation. Additionally, my gratitude for Professor Abílio Manuel Pereira da Silva who contributed to the investigation of the bonding agents required for the surfaces. I would also like to thank Master students André Mendes and Pedro Pinto for directly contributing to the research topic, and for accepting my guidance and support throughout their journey.

This achievement would not have been possible without the amazing individuals who have been by my side during this incredible journey. To Rodolfo Lopes, for soothing the work struggles and frustrations with an outside perspective. To Daniela Ribeiro, for the scepticism and dedication towards the research project, and for thriving to push forward. To Inês Ferrão, for being the cornerstone of my PhD journey, for the enduring support towards one another, and for the unwavering courage to stand strong and never give up. These memories will be cherished for a lifetime. Thank you.

Lastly, I would like to extend my appreciation to my family for their unwavering emotional and financial support throughout the years. This would be possible if not for their continuous presence, specially my mother and brother.

Funding

The research project was supported by Fundação para a Ciência e Tecnologia (FCT), Portugal, through the projects number UIDB/50022/2020, UIDP/50022/2020, LA/P/0079/2020, and by the Ph.D. scholarship with the reference SFRH BD/143307/2019. It is also supported by ”Protocolo celebrado entre a UBI e a Caixa Geral de Depósitos (CGD)” with the reference BAD UBI-CGD 2023/2024 FE.

Abstract

The industrialisation and globalisation of the modern world severely increased the demand for energy production, primarily met by a dependence on fossil fuels. The projected exponential growth of the aviation sector will result in an increase in greenhouse gas and pollutant emissions. Due to this, researching sustainable and cleaner alternative fuels is crucial to neutralise the negative effects of conventional fuels.

The physical and chemical processes occurring inside a combustion chamber include fluid dynamics, heat and mass transfer, combustion, among others. Specifically, the phenomena regarding the impact of droplets onto solid surfaces and liquid layers are often encountered in internal combustion engines, heat exchangers and spray cooling. Research on these applications focuses on understanding fluid flow and optimising heat and mass transfer mechanisms. Despite this, single droplets impacting onto liquid films are limited to isothermal conditions, as the influence of temperature on liquid films has been overlooked in the literature. Therefore, the primary objective of this work is researching the phenomena of droplet impact onto heated liquid films. An experimental facility was designed and adapted to account for isothermal and non-isothermal conditions. The key aspects of the experimental facility consist of high-speed imaging and heating systems. Prior to the impact phenomena, the liquid film characterisation is required in terms of temperature fields and evaporation rates. Subsequently, various outcomes from droplet impact are evaluated as a function of the liquid film temperature, including central jets, craters, splashing, and bubbling. Qualitative analysis is conducted on outcome development, while quantitative measurements focus on geometric parameters. Theoretical work is performed regarding the propagation of kinematic discontinuities in liquid layers and time scales for crater and central jet evolution, respectively. The experimental data provides a foundation for the implementation and validation of the numerical model. This model solves the incompressible Navier-Stokes equations coupled with the Volume of fluid (VOF) method under a 2D-axisymmetric assumption. The open-source Computational Fluid Dynamics (CFD) software Basilisk is adopted for the numerical simulations.

Overall, the liquid film temperature and correspondent thermophysical properties play a major role in the impact dynamics. Higher values of the dimensionless temperature promote and increase the occurrence and number of secondary droplets, respectively. This is associated with lower values of viscosity and surface tension, contributing to higher Reynolds and Weber numbers. For the onset of boiling, the oscillations induced on the liquid film are not sufficient to affect the impact phenomena. The presence of vapour bubbles in the impact region decreases both the crown diameter and height, with its effect being more pronounced for the latter.

Keywords

Droplet impact, Heated liquid film, Vapour bubbles, Heat and mass transfer, Interfacial dynamics

Resumo

A industrialização e globalização do mundo moderno impulsionaram drasticamente a procura por produção de energia, atualmente sustentada por combustíveis fósseis. A previsão de crescimento exponencial do setor aeronáutico resultará num aumento de emissão de gases com efeito de estufa e poluentes. Devido a isto, a pesquisa de combustíveis alternativos mais limpos e sustentáveis é crucial para neutralizar os efeitos negativos de combustíveis convencionais.

Dinâmica de fluidos, transferência de massa e calor, combustão, entre outros, são fenómenos físicos e químicos presentes numa câmara de combustão. O impacto de gotas em superfícies sólidas e em filmes de líquido é observado em diversas aplicações industriais, nomeadamente em motores alternativos de combustão interna, permutadores de calor e sistemas de refrigeração por pulverização. Nestas aplicações, a compreensão escoamento de fluidos, e otimização de mecanismos de transferência de massa e calor, são essenciais. Apesar disso, o impacto de gotas isoladas em filmes de líquido está limitado a condições isotérmicas, uma vez que a literatura não considera a influência da temperatura em filmes de líquido. Desta forma, o objetivo principal deste trabalho é investigar os fenómenos do impacto de gotas em filmes de líquido aquecidos. Uma instalação experimental foi desenvolvida e adaptada para abranger condições isotérmicas e não-isotérmicas. A instalação experimental consiste maioritariamente num sistema de captura de imagem a alta velocidade e numa superfície de impacto aquecida. Primeiramente, a caracterização do filme de líquido foi efetuada em termos de campos de temperatura e taxas de evaporação. De seguida, os fenómenos do impacto das gotas são avaliados em função da temperatura do filme de líquido, incluindo jatos centrais, crateras, *splashing*, e *bubbling*. A análise qualitativa é realizada em relação ao desenvolvimento dos fenómenos de impacto, enquanto as medições quantitativas estão direcionadas aos parâmetros geométricos dos mesmos. Estudos teóricos são realizados relativamente à propagação de descontinuidades cinemáticas em fluidos e escalas de tempo para a evolução da cratera e jato central, respetivamente. Os dados experimentais constituem uma base fundamental para a implementação e validação do modelo numérico. Este modelo resolve as equações de Navier-Stokes em regime incompressível integradas com o método VOF (*Volume of Fluid*) considerando uma simetria axial 2D. As simulações numéricas são realizadas com o uso do software de CFD (*Computational Fluid Dynamics*) *open-source Basilisk*.

A temperatura e as propriedades termofísicas do filme de líquido desempenham um papel importante na dinâmica de impacto. Temperaturas adimensionais mais elevadas promovem e aumentam, respetivamente, a ocorrência e o número de gotas secundárias. Isto deve-se a menores valores de viscosidade e tensão superficial, o que contribui para um aumento dos números de Reynolds e Weber. Para o início do ponto de ebulição, as oscilações induzidas no filme de líquido não são suficientes para afetar o fenómeno de impacto. A presença de bolhas de vapor na região de impacto reduz o diâmetro e a altura da coroa, sendo esse efeito mais pronunciado para a altura.

Palavras-chave

Impacto de gotas, Filme de líquido quente, Bolhas de vapor, Transferência de calor e massa, Dinâmica interfacial

Resumo alargado

A industrialização e globalização do mundo moderno impulsionaram drasticamente a procura por produção de energia, atualmente sustentada por combustíveis fósseis. A previsão de crescimento exponencial do setor aeronáutico resultará num aumento de emissão de gases com efeito de estufa e poluentes. Devido a isto, a pesquisa de combustíveis alternativos mais limpos e sustentáveis é crucial para neutralizar os efeitos negativos de combustíveis convencionais. Uma alternativa promissora a estes combustíveis são os biocombustíveis, que podem ser implementados diretamente nas aeronaves convencionais atuais sem necessitar de mudanças significativas.

Dinâmica de fluidos, transferência de massa e calor, combustão, entre outros, são fenómenos físicos e químicos presentes numa câmara de combustão. O impacto de gotas em superfícies sólidas e em filmes de líquido é observado em diversas aplicações industriais, nomeadamente em motores alternativos de combustão interna, permutadores de calor e sistemas de refrigeração por pulverização. Nestas aplicações, a compreensão escoamento de fluidos, e otimização de mecanismos de transferência de massa e calor, são essenciais. Desta forma, o objetivo principal deste trabalho é investigar os fenómenos do impacto das gotas em superfícies de filme de líquido aquecidas. A instalação experimental é composta por vários elementos, incluindo um sistema de captura de imagem a alta velocidade, uma superfície de impacto, um bloco de aquecimento, uma fonte de iluminação, e um sistema de injeção. Várias gamas de temperatura são avaliadas ao longo deste estudo, abrangendo desde condições isotérmicas até ao ponto de ebulição do fluido. Água, n-decano e n-heptano são os fluidos utilizados no estudo experimental devido às diferenças relativamente às propriedades termofísicas e temperaturas de saturação. Adicionalmente, os parâmetros de impacto, nomeadamente a velocidade de impacto da gota e a espessura adimensional do filme de líquido, foram variadas de forma a avaliar a sua influência nos fenómenos de impacto. Estes incluem jatos centrais, crateras, *splashing* e *bubbling*. A análise qualitativa e quantitativa referente a estes eventos incorpora a medição de diferentes parâmetros geométricos, tais como alturas dos jets, diâmetros e profundidade da cratera, entre outros. O trabalho experimental é posteriormente complementado com análises teóricas existentes na literatura, tais como a propagação de descontinuidades cinemáticas e escalas de tempo. O modelo numérico consiste em resolver as equações de Navier-Stokes em regime incompressível adotando um método de captura de interface, especificamente o Volume de Fluido (VOF), em que a curvatura e o vetor normal ao interface são calculados segundo funções de altura. O *open-source* software *Basilisk* foi adotado e adaptado para as simulações numéricas. A validação do modelo numérico é efetuada com dados experimentais, seguido da influência das bolhas de vapor na estrutura da coroa.

Relativamente aos jatos centrais, o aumento da temperatura do filme de líquido induz a fragmentação do jato central. Os combustíveis apresentam jatos mais elevados para maiores temperaturas, estando associado às propriedades termofísicas do filme de líquido. Para a

água, devido aos valores mais elevados de tensão superficial, estes jatos são mais espessos e de altura reduzida sem ocorrência de atomização secundária. A medição das alturas dos jatos mostra um aumento progressivo com o aumento da temperatura do filme de líquido para os combustíveis. No entanto, a influência da temperatura difere para a água, que exibe uma redução da altura do jet para baixas temperaturas. Esta redução pode ser explicada através de escalas de tempo, evidenciando os diferentes efeitos e magnitude relativa das forças de tensão superficial, viscosas e gravitacionais. Em relação às crateras, para condições não-isotérmicas, as diferenças de temperatura estimulam a formação de zonas de recirculação potenciadas por um aumento da temperatura adimensional. Estas regiões são uma consequência da mistura entre a gota fria e o filme de líquido quente, induzindo refração local devido às diferenças de massa específica. As crateras são maioritariamente afetadas pelo aumento de temperatura na fase de retração e separação da parede, e no atraso da propagação da onda capilar.

O aumento da temperatura influencia as dinâmicas de *splash* ao promover a formação de proeminências no topo da coroa, e induz a transição entre o *spread* e o *splash* para todos os fluidos. Semelhante aos jatos centrais, existe uma região intermédia em que o *splash* é reduzido ou mesmo suprimido. Uma correlação de *splash* foi proposta para dividir estes dois regimes, sendo baseada nas propriedades termofísicas do filme de líquido e nas propriedades geométricas e inerciais da gota. Uma adaptação semelhante foi executada para a análise na formação do *bubbling*.

Para condições de ebulição, bolhas de vapor formam-se residualmente na região de impacto para a água, e maioritariamente nas fronteiras da superfície de impacto para todos os fluidos. O n-heptano desenvolve bolhas de vapor de menores dimensões a uma taxa de libertaao elevada. No entanto, a água exibe um comportamento oposto. Para o ponto de ebulição, as oscilações impostas no filme de líquido não são suficientes para afetar o fenómeno de impacto. Esta análise foi complementada com resultados numéricos, em que bolhas de vapor foram implementadas artificialmente no filme de líquido para simular a influência das mesmas no desenvolvimento dos fenómenos de impacto. De uma forma geral, as bolhas de vapor reduzem o diâmetro e a altura das coroas, sendo este efeito mais pronunciado para as alturas. Menores espaçamentos e maiores diâmetros das bolhas de vapor têm um maior impacto na formação da coroa.

Em geral, a temperatura do filme de líquido tem um papel crucial nas dinâmicas de impacto, maioritariamente associado com a variação das propriedades termofísicas. No entanto, a redução da altura dos jatos e a supressão do *splash* para baixas temperaturas requer uma análise mais detalhada relativamente a escoamento de fluidos e transferência de calor e massa, de modo a compreender os mecanismos associados com dinâmicas interfaciais e mudanças de fase.

Index

Acknowledgements . . . vii
Abstract . . . ix
Resumo . . . xi
Resumo Alargado . . . xiii
List of Figures . . . xix
List of Tables . . . xxvii
Nomenclature . . . xxix

1 Introduction **1**
1.1 Motivation . . . 1
1.2 Objectives . . . 3
1.3 Contributions . . . 3
1.4 Thesis Overview . . . 6

2 Literature Review **7**
2.1 Introduction . . . 7
2.2 General Concepts . . . 8
2.3 Pioneer Research . . . 12
2.4 Droplet Impact onto Liquid Films . . . 17
2.4.1 Spreading . . . 18
2.4.2 Coalescence . . . 19
2.4.3 Rebound . . . 20
2.4.4 Jetting . . . 20
2.4.5 Crown Formation . . . 22
2.4.5.1 Diameter and Height . . . 24
2.4.5.2 Crater . . . 25
2.4.5.3 Angle and Thickness . . . 27
2.4.6 Splashing . . . 28
2.4.7 Bubble Encapsulation . . . 32
2.5 Heat and Mass Transfer Phenomena . . . 33
2.5.1 Dry Surfaces . . . 33
2.5.1.1 Film Evaporation . . . 34
2.5.1.2 Nucleate Boiling . . . 35
2.5.1.3 Transition Boiling . . . 37
2.5.1.4 Film Boiling . . . 38
2.5.2 Liquid Films . . . 40
2.6 Numerical Methods . . . 46
2.6.1 Interface Tracking Methods . . . 48
2.6.2 Phase Change Models . . . 53
2.6.2.1 Energy jump condition . . . 55

2.6.2.2 Schrage model . . . 56
2.6.2.3 Lee model . . . 57
2.6.3 Numerical Approach on Two-Phase Flows . . . 58

3 Experimental Methodology 63
3.1 Introduction . . . 63
3.2 Experimental Setup . . . 64
3.3 Experimental Methodology . . . 68
3.4 Liquid Film Characterisation . . . 72
3.4.1 Temperature . . . 73
3.4.2 Evaporation Rate . . . 78
3.5 Image Processing . . . 80

4 Experimental Results 85
4.1 Non-Isothermal Conditions . . . 85
4.1.1 Central Jet . . . 85
4.1.1.1 Visualisation . . . 86
4.1.1.2 Height and Breakup Measurements . . . 88
4.1.1.3 Time Scale Analysis . . . 93
4.1.2 Crater . . . 96
4.1.2.1 Visualisation . . . 97
4.1.2.2 Diameter and Depth Measurements . . . 99
4.1.2.3 Theoretical Analysis . . . 102
4.1.3 Splashing . . . 104
4.1.3.1 Visualisation . . . 104
4.1.3.2 Splashing Occurrence . . . 106
4.1.3.3 Non-Splash/Splash Threshold . . . 109
4.1.4 Bubble Encapsulation . . . 112
4.2 Subcooled Boiling Regime . . . 115
4.3 Saturated Boiling Regime . . . 118
4.3.1 Vapour Bubbles . . . 118
4.3.2 Impact Outcomes . . . 120

5 Numerical Setup 123
5.1 Introduction . . . 123
5.2 Governing Equations . . . 124
5.3 Interface Tracking Method . . . 125
5.4 Numerical Model . . . 127
5.4.1 Time Integration Scheme . . . 127
5.4.1.1 Volume of Fluid (VOF) . . . 127
5.4.1.2 Advection Term . . . 127
5.4.1.3 Viscous Forces . . . 129
5.4.1.4 Projection method . . . 130

5.4.2 Spatial Discretisation . . . 131
5.5 Computational Domain . . . 133
5.6 Convergence Studies . . . 135
5.6.1 Domain . . . 135
5.6.2 Time step . . . 136
5.6.3 Grid . . . 137

6 Numerical Results **139**
6.1 Isothermal Conditions . . . 139
6.2 Subcooled Boiling Regimes - Vapour Bubbles . . . 142
6.2.1 Size and Spacing . . . 142
6.2.2 Initial Displacement . . . 145

7 Conclusions and Future Work **149**
7.1 Conclusions . . . 149
7.2 Future Work . . . 151

References **153**

Appendix **175**

A Fluids Thermophysical Properties **175**

B Aluminium Block **177**

C Thermocouples **179**

List of Figures

2.1 Liquid droplet variations, such as spherical, oscillating between oblate and prolate shapes, internal circulation and deformed droplet. 9
2.2 Examples of surrounding environment for the droplet impact phenomena, such as the existence of a crossflow and the formation of a wake flow-field. . . 10
2.3 Classification of impact targets, including orientation, roughness, porosity, and the presence of a liquid film. 10
2.4 Representation of droplet impact onto a liquid film and correspondent thermophysical properties. 11
2.5 Water drop falling onto a water-milk liquid pool: a) Falling height of $Y = 135$ cm; b) Falling height of $Y = 40$ cm. 13
2.6 Imaging of splashes and droplets obtained through modern stroboscopy: a) Thin ligament breakup; b) Crown splashing. 14
2.7 N-heptane droplet impact onto a stainless steel surface at $T_w = 104°C$: a) $t = 5.6$ ms; b) $t = 8.0$ ms. 16
2.8 Spreading outcome of a 75% Jet Fuel (JF)/25% Hydrotreated vegetable oil (HVO) droplet impact onto a liquid film. 18
2.9 Different stages of complete and partial coalescence. 19
2.10 Complete rebound of a butanol droplet on a liquid film $(0.028 < h^* < 0.048$ and $We = 4)$. 20
2.11 Representation of the central jet height and posterior breakup. 20
2.12 Regime maps for central jet formation, with or without breakup, and crown splash as a function of the Weber, Reynolds and Ohnesorge numbers. 22
2.13 Visual representation of the kinematic discontinuity leading to the crown wall formation subsequent to droplet impact. 23
2.14 Representation of the crown height and outer diameter of a developing crown. 24
2.15 Crater development subsequent to droplet impact: a) $\tau = 2.5$; b) $\tau = 7.5$; c) $\tau = 17.5$. 26
2.16 Representation of the crown outer angle and thickness of a developing crown. 28
2.17 Development of the Rayleigh-Plateau capillary instability on liquid jets. 29
2.18 Occurrence of prompt splash at earlier stages of the impact a) $t = 0$ s; b) $t = 1.67$ s; c) $t = 4.81$ s; d) $t = 11.3$ s. 29
2.19 Occurrence of crown splash at later stages of the impact: a) $t = 0$ s; b) $t = 1.67$ s; c) $t = 4.81$ s; d) $t = 11.3$ s. 29
2.20 Bubble encapsulation phenomenon subsequent to the impact of a 75% jet fuel/25% HVO droplet onto a liquid film ($D_d = 3.0$ mm, $U_d = 4.2$ m/s, $h^* = 0.5$): a) $\tau = 14$; b) $\tau = 56$; c) $\tau = 175$. 33
2.21 Heat transfer regimes of a droplet impacting onto a heated dry surface as a function of the wall temperature (T_w). 34

2.22 Stages of droplet impact and subsequent film evaporation: a) Initial impact; b) Constant wetting area and decreasing droplet height; c) Constant contact angle and decreasing wetting area. 35
2.23 Nucleate boiling regime of an n-heptane droplet impinging onto a heated dry graphite surface ($T_{he} = 150°C$) a) $t = 0$ ms; b) $t = 15$ ms; c) $t = 30$ ms; d) $t = 60$ ms. 36
2.24 Formation of pagoda-like bubbles in the nucleate boiling regime. 37
2.25 Transition boiling regime of an n-heptane droplet impinging onto a heated dry graphite surface ($T_{he} = 170°C$) a) $t = 0$ ms; b) $t = 15$ ms; c) $t = 30$ ms; d) $t = 60$ ms. 37
2.26 The Leidenfrost effect of a single droplet impinging onto a heated surface. . . 38
2.27 Film boiling regime of an n-heptane droplet impinging onto a heated dry graphite surface ($T_{he} = 230°C$) a) $t = 0$ ms; b) $t = 4$ ms; c) $t = 12.5$ ms; d) $t = 46.5$ ms. . 39
2.28 Physical phenomena of liquid film evaporation due to the presence of a heat flux: a) Initial liquid film thickness; b) Critical liquid film thickness; c) Initial liquid ligament breakup in the boundaries; d) Formation of liquid droplets and puddles due to continuous ligament breakup. 40
2.29 Vapour explosion of an ethanol droplet impact onto a glycerol liquid film. . . . 42
2.30 Representation of the life cycle of vapour bubbles during liquid film boiling due to the presence of a heat flux. 43
2.31 High-speed visualisation of the pool boiling regime as a function of the surface roughness and applied heat flux. Working fluid is perfluorinated hydrocarbon (FC-77). 45
2.32 Bubble formation, ligament breakup and puddles on a hated surface following droplet impact. 46
2.33 Numerical simulation of a droplet impacting a liquid film using the MAC method. 49
2.34 Interface reconstruction schemes applied to droplet impact onto a liquid film: a) Original interface; b) SLIC Method; c) Adapted SLIC Method; d) PLIC Method. 50
2.35 Visual representation of interface tracking methods for two-phase flows: a) MAC method; b) VOF method; c) LS method; d) Front tracking method. . . . 52
2.36 Simulation of successive droplets impacting onto a heated liquid film and correspondent temperature fields. 58
2.37 The evolution of a vapour bubble growth and detachment from a solid surface. 59
2.38 Volume fraction fields for different flow patterns in a condensed tube of a steam cracker. 60
2.39 Rising bubble and droplet during free-fall at saturation temperature with phase change. 61
2.40 Nucleation, growth and detachment of vapour bubbles under saturated boiling regimes. 62

3.1 Schematic of the experimental setup. 64
3.2 Adapted schematic of the experimental setup for the vapour bubble measurements. 65

3.3 Ne-1000 syringe pump. 65
3.4 Borosilicate glass container. 66
3.5 Heating system: a) Heating controller device; b) Aluminium block with embedded cartridge heaters. 67
3.6 Image acquisition systems: a) Photron FASTCAM mini UX50 with a Macro Lens Tokina AT-X M100 AF PRO D; b) GoPro Hero 6. 68
3.7 Flowchart of the experimental procedure regarding single droplets impacting heated liquid films. 69
3.8 Precision scale. 71
3.9 Thermocouple positioning on the liquid film. P_1 refers to the position of the first thermocouple, P_2 to the position of the second thermocouple, and so forth: a) Thermocouple displacement in the liquid film; b) Visual representation of the immersed thermocouple. 75
3.10 Liquid film temperature measurements of n-heptane as a function of time for a selected temperature on the heating device: a) $T_{he} = 70°\mathrm{C}$; b) $T_{he} = 110°\mathrm{C}$. . 76
3.11 Liquid film temperature measurements of water as a function of time for a selected temperature on the heating device: a) $T_{he} = 50°\mathrm{C}$; b) $T_{he} = 110°\mathrm{C}$. . . 77
3.12 Liquid film temperature measurements of water, n-heptane and n-decane as a function of the heating element temperature. The dashed horizontal lines correspond to the saturation temperature for each of the fluids. 78
3.13 Liquid film thickness variation due to the presence of a heat flux: a) $t = 0\ \mathrm{min}$; b) $t = 10\ \mathrm{min}$; c) $t = 20\ \mathrm{min}$. 79
3.14 Comparison of the precision scale and high-speed digital camera methods for evaporation rate measurements. 79
3.15 Evaporation rate of n-decane, water and n-heptane for different liquid film temperatures. 80
3.16 Binarisation process of a single droplet for diameter measurements: a) Background image; b) Droplet during free-fall; c) Binarised image. 81
3.17 Binarisation process of a single droplet for impact velocity measurements: a) Droplet during free-fall; b) Droplet frame preceding the moment of impact; c) Binarised image. 82
3.18 Post-processing of the vapour bubbles on the surface impact region: a) Original image; b) Cropping and binarisation; c) Circular object detection function. 82
3.19 Binarisation process of the crater formation. 83
3.20 Binarisation process of the central jet formation: a) Cropped image; b) Binarised image. 83

4.1 Visualisation of central jet formation subsequent to the impact of an n-heptane droplet ($h^* = 1.5$, $\tau = 39.0$): a) $\theta = 0$; a) $\theta = 0.2$; c) $\theta = 0.4$; d) $\theta = 0.6$. 86
4.2 Visualisation of central jet formation subsequent to the impact of an n-decane droplet ($h^* = 1.5$, $\tau = 35.0$): a) $\theta = 0$; a) $\theta = 0.2$; c) $\theta = 0.4$; d) $\theta = 0.6$. 87

4.3 Visualisation of the central jet maximum height subsequent to the water droplet impact as a function of temperature ($h^* = 1.5$): a) $\theta = 0$; b) $\theta = 0.2$; c) $\theta = 0.4$; d) $\theta = 0.6$. 88
4.4 Central jet height measurements of an n-heptane droplet impacting a liquid film for a range of dimensionless temperatures ($0 \leq \theta \leq 0.6$): a) $h^* = 1.0$; b) $h^* = 1.5$. 89
4.5 Visualisation of central jet breakup subsequent to the impact of an n-heptane droplet ($\theta = 0$, $h^* = 1.5$): a) $\tau = 28.7$; a) $\tau = 30.1$; c) $\tau = 42.9$; d) $\tau = 43.9$. . . 90
4.6 Occurrence of central jet breakup of an n-heptane droplet impacting a liquid film for a range of dimensionless temperatures ($0 \leq \theta \leq 0.6$), where n_b is the number of central jet breakups: a) $h^* = 1.0$; b) $h^* = 1.5$. 90
4.7 Central jet height measurements of an n-decane droplet impacting a liquid film for a range of dimensionless temperatures ($0 \leq \theta \leq 0.6$): a) $h^* = 1.0$; b) $h^* = 1.5$. 91
4.8 Occurrence of central jet breakup of an n-decane droplet impacting a liquid film for a range of dimensionless temperatures ($0 \leq \theta \leq 0.6$), where n_b is the number of central jet breakups: a) $h^* = 1.0$; b) $h^* = 1.5$. 92
4.9 Central jet height measurements of a water droplet impacting a liquid film for a range of dimensionless temperatures ($0 \leq \theta \leq 0.6$): a) $h^* = 0.5$; b) $h^* = 1.0$; c) $h^* = 1.5$. 93
4.10 Surface tension, inertial and gravitational time scales as a function of θ for the droplet impact phenomenon: a) N-heptane; b) N-decane. 95
4.11 Time scales as a function of θ for the water droplet impact: a) Surface tension, inertial and gravitational time scales; b) Close-up of the surface tension and gravitational time scales. 96
4.12 Representation of the crater depth and diameter subsequent to droplet impact. 97
4.13 Visualisation of the crater formation subsequent to the impact of a water droplet ($h^* = 1.5$, $\tau = 21.1$): a) $\theta = 0$; a) $\theta = 0.2$; c) $\theta = 0.4$; d) $\theta = 0.6$. 98
4.14 Visualisation of the crater formation subsequent to the impact of an n-decane droplet ($h^* = 1.0$, $\tau = 12.4$): a) $\theta = 0$; a) $\theta = 0.2$; c) $\theta = 0.4$; d) $\theta = 0.6$. 98
4.15 Visualisation of the crater formation subsequent to the impact of a water droplet ($h^* = 1.0$, $\tau = 25.1$): a) $\theta = 0$; a) $\theta = 0.2$; c) $\theta = 0.4$; d) $\theta = 0.6$. 99
4.16 Crater measurements of an n-decane droplet impacting a liquid film for a range of dimensionless temperatures ($0 \leq \theta \leq 0.6$) and impact conditions ($h^* = 1.5$): a) Dimensionless crater depth; b) Dimensionless crater diameter. 100
4.17 Crater measurements of an n-heptane droplet impacting a liquid film for a range of dimensionless temperatures ($0 \leq \theta \leq 0.6$) and impact conditions ($h^* = 1.5$): a) Dimensionless crater depth; b) Dimensionless crater diameter. 101
4.18 Crater measurements of a water droplet impacting a liquid film for a range of dimensionless temperatures ($0 \leq \theta \leq 0.6$) and impact conditions ($h^* = 1.0$): a) Dimensionless crater depth; b) Dimensionless crater diameter. 101

4.19 Crater measurements of a water droplet impacting a liquid film for a range of dimensionless temperatures ($0 \leq \theta \leq 0.6$) and impact conditions ($h^* = 1.5$): a) Dimensionless crater depth; b) Dimensionless crater diameter. 102
4.20 Comparison of theoretical and experimental results regarding crater diameter measurements of a water droplet impact for isothermal conditions: a) $h^* = 1.0$; b) $h^* = 1.5$. 103
4.21 Comparison of theoretical and experimental results regarding crater diameter measurements for isothermal conditions and a dimensionless thickness of $h^* = 1.5$: a) N-heptane; b) N-decane. 103
4.22 Visualisation of the impact phenomena of a water droplet onto a liquid film for different temperatures ($U_d = 2.42\ \mathrm{m/s},\ D_d = 2.67\ \mathrm{mm}$): a) $\theta = 0$, $\tau = 2.72$; b) $\theta = 0.23$, $\tau = 2.27$; c) $\theta = 0.44$, $\tau = 2.72$; d) $\theta = 0.60$, $\tau = 2.49$. 105
4.23 Visualisation of the impact phenomena of an n-heptane droplet onto a liquid film for different temperatures ($U_d = 1.52\ \mathrm{m/s},\ D_d = 2.56\ \mathrm{mm}$): a) $\theta = 0$, $\tau = 1.78$; b) $\theta = 0.19$, $\tau = 1.48$; c) $\theta = 0.37$, $\tau = 1.48$; d) $\theta = 0.81$, $\tau = 1.63$. 106
4.24 Visualisation of the impact phenomena of an n-decane droplet onto a liquid film for different temperatures ($U_d = 1.80\ \mathrm{m/s},\ D_d = 2.72\ \mathrm{mm}$): a) $\theta = 0$, $\tau = 6.62$; b) $\theta = 0.10$, $\tau = 7.94$; c) $\theta = 0.19$, $\tau = 5.96$; d) $\theta = 0.37$, $\tau = 6.62$. 106
4.25 Adapted splashing threshold parameter, K, as a function of the dimensionless temperature, θ, for the various fluids. 111
4.26 Splashing evaluation in terms of adapted Ohnesorge and Reynolds numbers for the experimental conditions. 112
4.27 Evaluation of bubble encapsulation in terms of Ohnesorge and Reynolds numbers using the threshold proposed by Ribeiro et al.. 114
4.28 Evaluation of bubble encapsulation in terms of adapted Ohnesorge and Reynolds numbers using the adapted threshold. 114
4.29 Top view of the vapour bubble growth and distribution on the surface impact region for water ($T_{he} = 110°\mathrm{C}$): a) $t = 150\ \mathrm{s}$; b) $t = 765\ \mathrm{s}$; c) $t = 1620\ \mathrm{s}$. 116
4.30 Top view of the vapour bubble growth and distribution on the surface impact region for water ($T_{he} = 150°\mathrm{C}$): a) $t = 15\ \mathrm{s}$; b) $t = 375\ \mathrm{s}$; c) $t = 810\ \mathrm{s}$. 117
4.31 Top view of the vapour bubble growth and distribution on the surface impact region for n-heptane ($T_{he} = 130°\mathrm{C}$): a) $t = 15\ \mathrm{s}$; b) $t = 105\ \mathrm{s}$; c) $t = 300\ \mathrm{s}$. . . . 117
4.32 Water vapour bubble analysis as a function of the liquid temperature for both heating and stabilisation phases: a) Number of bubbles (N_b); b) Bubble diameter (D_b). 118
4.33 Visualisation of the formation, growth and detachment of water vapour bubbles on the surface boundaries: a) $T_{he} = 110°\mathrm{C}$; b) $T_{he} = 130°\mathrm{C}$; c) $T_{he} = 150°\mathrm{C}$. 119
4.34 Visualisation of the formation, growth and detachment of n-heptane vapour bubbles on the surface boundaries: a) $T_{he} = 110°\mathrm{C}$; b) $T_{he} = 130°\mathrm{C}$. 119
4.35 Visualisation of the vapour bubbles life cycle: a) Initial vapour bubble detachment; b) Ligament critical thickness; c) Ligament breakup leading to vapour bubble release. 120

4.36 Visualisation of the crown formation subsequent to the water droplet impact as a function of temperature: a) $\theta = 0.75$, $\tau = 6.7$; b) $\theta = 0.83$, $\tau = 6.1$; c) $\theta = 0.95$, $\tau = 6.4$. 121
4.37 Visualisation of the central jet maximum height subsequent to the water droplet impact as a function of temperature: a) $\theta = 0.75$, $\tau = 86.2$; b) $\theta = 0.83$, $\tau = 84.2$; c) $\theta = 0.95$, $\tau = 81.8$. 121

5.1 Visual representation of the PLIC method, interface normal vector and height functions. 126
5.2 Representation of scalar and vector fields in a staggered grid. 132
5.3 Tree-grid structure on an orthogonal Cartesian mesh: a) Spatial structure of grid cells under different levels of refinement; b) Spatial structure of ghost points defined by the red (downsampling) and blue (upsampling) circles; c) Tree representation corresponding to the various grid cells and ghost points at different levels. 133
5.4 Example of adaptive mesh refinement based on the discretisation errors of velocity and volume fraction. 133
5.5 Numerical setup. 134
5.6 Interface evolution as a function of the axial and radial dimensions of the numerical domain. 136
5.7 Interface evolution as a function of the CFL condition. 137
5.8 Interface evolution as a function of the grid size. 138
5.9 Crown measurements for single droplet impact as a function of grid size: a) Dimensionless crown outer diameter; b) Dimensionless crown height. 138

6.1 Comparison of experimental and numerical results of crown parameter measurements as a function of dimensionless time ($D_d = 3.0\,\mathrm{mm}$, $U_d = 3.0\,\mathrm{m/s}$, $h^* = 0.2$): a) Dimensionless crown outer diameter; b) Dimensionless crown height. 140
6.2 Qualitative comparison of the droplet impact phenomenon regarding the experimental and numerical results ($D_d = 3.0\,\mathrm{mm}$, $U_d = 3.0\,\mathrm{m/s}$, $h^* = 0.2$). . . . 140
6.3 Comparison of experimental and numerical results of crown parameter measurements as a function of dimensionless time ($D_d = 3.0\,\mathrm{mm}$, $U_d = 3.0\,\mathrm{m/s}$, $h^* = 0.5$): a) Dimensionless crown outer diameter; b) Dimensionless crown height. 141
6.4 Comparison of experimental and numerical results of crown parameter measurements as a function of dimensionless time ($D_d = 3.0\,\mathrm{mm}$, $U_d = 3.0\,\mathrm{m/s}$, $h^* = 1.0$): a) Dimensionless crown outer diameter; b) Dimensionless crown height. 141
6.5 Crown measurements for water droplet impact as a function of the vapour bubble size for $x_v^* = 1.0$: a) Dimensionless crown outer diameter; b) Dimensionless crown height. 143

6.6 Visualisation of water droplet impact as a function of the vapour bubble size for $x_v^* = 1.0$ and $\tau = 6.5$: a) $D_v^* = 1/10$; b) $D_v^* = 1/5$; c) $D_v^* = 1/3$; d) $D_v^* = 1/2$. 143
6.7 Crown measurements for n-decane droplet impact as a function of the vapour spacing for $D_v^* = 1/5$: a) Dimensionless crown outer diameter; b) Dimensionless crown height. 144
6.8 N-decane droplet impact at different time frames for $D_v^* = 1/3$ and $x_v^* = 0.5$: a) $\tau = 0$; b) $\tau = 2.5$; c) $\tau = 3$; d) $\tau = 5$. 144
6.9 Dimensionless crown height measurements for droplet impact for $D_v^* = 1/3$: a) Water; b) N-decane. 145
6.10 Crown measurements for water droplet impact for $D_v^* = 1/2$ and $x_v^* = 1.0$: a) Dimensionless crown outer diameter; b) Dimensionless crown height. 146
6.11 Visualisation of water droplet impact as a function of the vapour bubble initial displacement for $D_v^* = 1/2$, $x_v^* = 1.0$ and $\tau = 8$: a) $x_s^* = 0$; b) $x_s^* = 0.5$; c) $x_s^* = 1.0$; d) $x_s^* = 2.0$. 146
6.12 Crown measurements for n-decane droplet impact for $D_v^* = 1/2$ and $x_v^* = 1.0$: a) Dimensionless crown outer diameter; b) Dimensionless crown height. . . . 147
6.13 Crown measurements for water droplet impact for $D_v^* = 1/3$ and $x_v^* = 1.0$: a) Dimensionless crown outer diameter; b) Dimensionless crown height. 148
6.14 Visualisation of water droplet impact as a function of a single vapour bubble initial displacement ($D_v^* = 1/2$ and $\tau = 3.7$): a) $x_s^* = 0$; b) $x_s^* = 0.5$; c) $x_s^* = 1.0$; d) $x_s^* = 2.0$. 148

B.1 Side and top views of the aluminium block, including embedded cartridge heaters, a thermocouple, and respective dimensions [mm]. 177

List of Tables

2.1 Liquid film regimes for droplet impact. 18
2.2 Review of the existing correlations for non-splash/splash thresholds for single droplet impact onto a liquid film. 31

3.1 Thermophysical properties of water, n-heptane and n-decane at room temperature ($T = 20\,^{\circ}\mathrm{C}$) and correspondent saturation temperatures. 73
3.2 Temperature measurements and standard deviation for the aluminium (Al), graphite (Gr) and borosilicate glass (Gl) surfaces. 75

4.1 Impact parameters and dimensionless numbers of the central jet study cases for different fluids. 85
4.2 Impact parameters of the splashing study for different fluids. 104
4.3 Splashing occurrence percentage as a function of the impact velocity and dimensionless temperature for water: ■ - Splashing; ■ - Spreading; ■ - Transition. 107
4.4 Splashing occurrence percentage as a function of the impact velocity and dimensionless temperature for n-heptane: ■ - Splashing; ■ - Spreading; ■ - Transition. 108
4.5 Splashing occurrence percentage as a function of the impact velocity and dimensionless temperature for n-decane: ■ - Splashing; ■ - Spreading; ■ - Transition. 108
4.6 Experimental conditions for the different fluids in terms of adapted Weber, Reynolds and Ohnesorge numbers. 110
4.7 Experimental conditions for the bubbling outcome of n-heptane and n-decane droplet impact. 113

6.1 Thermophysical properties for water and n-decane at atmospheric pressure. . 142

A.1 Thermophysical properties of pure water at atmospheric pressure. 175

B.1 Aluminium 5083 datasheet. 178

C.1 Specification of the mini-sheathing thermocouples acquired from Therma Thermofühler GmbH, Germany. 179

Nomenclature

a	Bubble encapsulation parameter	$[-]$
$\mathbf{a},\ \mathbf{b}$	Vectors	$[-]$
Bo	Bond number	$[-]$
C	Constant	$[-]$
C_p	Heat capacity at constant pressure	$[\mathrm{J\,kg^{-1}\,K^{-1}}]$
Ca	Capillary number	$[-]$
d	Shortest distance from the interface	$[\mathrm{m}]$
$\mathbf{D}$	Deformation tensor	$[-]$
$\mathbf{D}^*$	Predicted deformation tensor	$[-]$
D_d	Droplet impact diameter	$[\mathrm{m}]$
D_{out}	Crown outer diameter	$[\mathrm{m}]$
E	Specific internal energy	$[\mathrm{J\,kg^{-1}}]$
F	Volume flux in x-direction	$[\mathrm{m\,s^{-1}}]$
$\mathbf{F}_\sigma$	Surface tension forces	$[\mathrm{kg\,m\,s^{-2}}]$
Fr	Froude number	$[-]$
G	Volume flux in y-direction	$[\mathrm{m\,s^{-1}}]$
$\mathbf{g}$	Gravitational acceleration constant	$[\mathrm{m\,s^{-2}}]$
G_{cra}	Theoretical crater parameter	$[-]$
H	Heaviside function	$[-]$
h	Liquid film thickness	$[\mathrm{m}]$
h^*	Dimensionless liquid film thickness	$[-]$
h_d	Droplet Falling Height	$[\mathrm{m}]$
h_x, h_y, h'	First derivatives of the height function	$[-]$
H_{cro}	Crown height	$[\mathrm{m}]$
H_{jet}	Central jet height	$[\mathrm{m}]$
h_{lg}	Latent heat of vaporisation	$[\mathrm{J\,kg^{-1}}]$
$h_{xx}, h_{yy}, h_{xy}, h''$	Second derivatives of the height function	$[-]$
I	Dyadic idemfactor	$[-]$
K	Non-splash/splash boundary	$[-]$
k	Thermal conductivity	$[\mathrm{J\,s^{-1}\,m^{-1}\,K^{-1}}]$
$\mathcal{L}$	Linear operator	$[-]$
L_a	Length scale of wall roughness	$[\mathrm{m}]$
L_{nd}	Non-dimensional length scale of wall roughness	$[-]$

La	Laplace number	$[-]$
M	Molecular weight	$[\mathrm{kg\,mol^{-1}}]$
$\dot{m}$	Mass transfer rate	$[\mathrm{kg\,m^{-2}\,s^{-1}}]$
$\mathbf{n}$	Unit normal vector	$[-]$
N_b	Number of vapour bubbles	$[-]$
n_b	Number of central jet breakups	$[-]$
Oh	Ohnesorge number	$[-]$
p	Static pressure	$[\mathrm{kg\,m^{-1}\,s^{-2}}]$
Pe	Peclet number	$[-]$
Q	Energy source term for the energy equation	$[\mathrm{kg\,m^{-1}\,s^{-3}}]$
q''	Heat flux	$[\mathrm{J\,m^{-2}\,s^{-1}}]$
q_i''	Heat flux across the interface	$[\mathrm{J\,m^{-2}\,s^{-1}}]$
R	Universal gas constant	$[\mathrm{J\,K^{-1}\,mol^{-1}}]$
R_a	Wall roughness	$[\mathrm{m}]$
r_i	Mass transfer intensity factor	$[\mathrm{s^{-1}}]$
R_{cra}	Crater diameter	$[-]$
R_{nd}	Non-dimensional wall roughness parameter	$[-]$
R_{sv}	Specific surface area	$[-]$
Re	Reynolds number	$[-]$
$\mathbf{res}$	Residual	$[-]$
S	Mass source term	$[\mathrm{kg\,m^{-3}\,s^{-1}}]$
T	Temperature	$[\mathrm{K}]$
t	Time	$[\mathrm{s}]$
t_c	Crown thickness	$[\mathrm{m}]$
T_w	Wall temperature	$[\mathrm{K}]$
t_{cra}	Theoretical crater time	$[-]$
$\mathbf{U}$	Velocity vector	$[\mathrm{m\,s^{-1}}]$
$\mathbf{U}^*$	Predicted velocity	$[\mathrm{m\,s^{-1}}]$
$u,\ u_x$	Horizontal velocity	$[\mathrm{m\,s^{-1}}]$
U_d	Droplet impact velocity	$[\mathrm{m\,s^{-1}}]$
$v,\ u_y$	Vertical velocity	$[\mathrm{m\,s^{-1}}]$
We	Weber number	$[-]$
We_c	Critical Weber number	$[-]$
Y	Fall height	$[\mathrm{m}]$
y_{cra}	Crater depth	$[\mathrm{m}]$

Greek Symbols

α	Volume fraction	$[-]$
α_c	Crown angle	$[^\circ]$
α_T	Thermal diffusivity	$[\mathrm{m^2\,s^{-1}}]$
α_{ch}	Characteristic volume fraction	$[-]$
β	Spreading rate	$[-]$
β_{cra}	Theoretical crater parameter	$[-]$
Δt	Time step	$[\mathrm{s}]$
Δt_{max}	Maximum time step	$[\mathrm{s}]$
δ_s	Dirac delta function	$[-]$
Δ_x	Horizontal grid size	$[\mathrm{m}]$
Δ_y	Vertical grid size	$[\mathrm{m}]$
Δ_{min}	Minimum grid size	$[\mathrm{m}]$
ε	Characteristic interface thickness	$[-]$
γ	Accommodation coefficient	$[-]$
κ	Curvature	$[-]$
μ	Dynamic viscosity	$[\mathrm{kg\,m^{-1}\,s^{-1}}]$
μ^*	Dynamic viscosity ratio	$[-]$
ν	Kinematic viscosity	$[\mathrm{m^2\,s^{-1}}]$
ϕ	Level set	$[-]$
ρ	Density	$[\mathrm{kg\,m^{-3}}]$
ρ^*	Density ratio	$[-]$
ρ_m	Averaged density	$[\mathrm{kg\,m^{-3}}]$
σ	Surface tension	$[\mathrm{kg\,m^2\,s^{-2}}]$
σ_{st}	Standard deviation	$[-]$
τ	Dimensionless time	$[-]$
τ_s	Shear stress	$[\mathrm{kg\,m^{-1}\,s^{-2}}]$
τ_{cra}	Theoretical crater parameter	$[-]$
θ	Dimensionless temperature	$[-]$
θ_w	Wall contact angle	$[^\circ]$

Subscripts

0	Moment of impact
air	Surrounding environment
Al	Aluminium
b	Vapour bubbles

c	Condensation
cra	Crater
cro	Crown
d	Droplet
e	Evaporation
f	Liquid film
g	Gas phase
Gl	Borosilicate glass
Gr	Graphite
he	Heating element
L	Static Leidenfrost
l	Liquid phase
L, d	Dynamic Leidenfrost
max	Maximum
min	Minimum
sat	Saturation point
v	Vapour phase
x	X-direction
y	Y-direction

Acronyms and Abbreviations

AEROG	Aeronautics and Astronautics Research Center
AMR	Adaptive mesh refinement
BGM	Bounded gradient maximization
CCD	Charged-coupled devices
CFD	Computational Fluid Dynamics
CFL	Courant–Friedrichs–Lewy
CHF	Critical heat flux
CICSAM	Compressive interface capturing scheme for arbitrary meshes
CLSVOF	Coupled level set and volume of fluid
CMOS	Complementary metal-oxide semiconductor
cpd	Cells per diameter
CPU	Central processing unit
CSF	Continuum surface force
FCT	Fundação para a Ciência e Tecnologia
FPS	Frames per second

GFM	Ghost fluid method
HVO	Hydrotreated vegetable oil
JF	Jet fuel
LAETA	Associate Laboratory for Energy, Transports and Aerospace
LED	Light-emitting diode
LFP	Leidenfrost point
LS	Level set
MAC	Marker and cell
MATLAB	MATrix LABoratory
MPI	Message passing interface
NExBTL	Neste Renewable Diesel
OpenFOAM	Open field operation and manipulation
PIV	Particle image velocimetry
PLIC	Piecewise linear interface calculation
RGB	Red green blue
SLIC	Simple line interface calculation
UBI	Universidade da Beira Interior
VOF	Volume of fluid

Chapter 1

Introduction

The current thesis focuses on the fundamental study of single droplets impacting heated liquid films. For this purpose, the following chapter outlines a preliminary assessment of the research topic. The first section includes the motivation of the current work, including the implementation of sustainable alternatives in the aviation sector, physical and chemical processes occurring inside a combustion chamber, and the validation of numerical models. These elements are integrated into the main objectives, which are comprehensively described in the second section. The development of this study is essential to narrow the gap between single droplet studies and industrial applications in experimental, numerical and theoretical frameworks. These contributions are detailed in the following section. The final section describes the structure of the document.

1.1 Motivation

The industrialisation and globalisation of the modern world severely increased the demand for energy production. This was primarily met by a growing dependency on fossil fuels, which became the primary source due to their availability and cost-effectiveness. The transportation sector significantly relies on fossil fuels, requiring 2808 million tons of fuel equivalent by 2017, representing a total of 28.9% of the global energy consumption [1]. In particular, the global aviation industry operates on a fossil fuel derived product, accounting for 2% to 3% of the global anthropogenic effects [2]. Additionally, this sector is expected to exponentially increase in order to meet global demands in terms of human and cargo transportation. This leads not only to a rapid depletion of fossil fuels but also to an increase in greenhouse gas and pollutant emissions. Therefore, researching sustainable and cleaner alternative fuels is crucial to neutralise the negative effects of conventional fuels. A promising alternative to fossil fuels in the aviation sector is biofuels, which can be directly introduced into the existing aircraft infrastructures without requiring significant modification. These alternative fuels provide solutions to several challenges that the modern world currently faces, including energy security, economic development, and global warming associated with greenhouse gas emissions. Additionally, the current civil aviation legislation allows up to 50% by volume of biofuel in blendings with conventional fuels [3].

The physical and chemical processes occurring inside a combustion chamber involve different mechanisms. In terms of fluid dynamics, the mixing process between the air and fuel determines the combustion efficiency. Additionally, injection systems consisting of fuel sprays are associated with ligament breakup and secondary atomisation, which improve engine per-

formance. In high-temperature environments, heat and mass transfer mechanisms are predominant. Fuel evaporation occurs, and deposited droplets onto the engine walls may not vaporise, leading to unburned hydrocarbons [4]. If proper conditions are met, auto-ignition occurs, leading to combustion. In this context, the droplet impact phenomenon onto liquid films is predominant in a variety of modern industrial applications, including internal combustion engines, heat exchangers, spray cooling and coating, among others. This topic has been extensively researched for a multitude of impact conditions, ranging from surface morphology (dry, wetted, rough, porous) and two-phase flow dynamics (surface tension, evaporation, condensation) to combustion. Despite the growth in research, studies regarding impinging droplets onto liquid films do not account for temperature-related phenomena. New studies regarding single droplet impact onto heated wetted surfaces are required to improve our comprehension of fluid mechanics and heat transfer [5]. This includes phase change processes, such as evaporation/condensation and boiling, coupled with the underlying dynamics of droplet impact, which are essential for modern applications.

The implementation of sustainable alternatives in the aviation sector includes jet fuel and biofuel mixtures aimed at mitigating climate change and achieving lower greenhouse gas emissions. However, several constraints emerged related to their multicomponent nature. Each component has different saturation points and evaporation rates and, when subjected to a constant heat flux, the thermophysical properties of the liquid film are not only dependent on temperature, but also on the mass fraction of each of the components, increasing the difficulty in quantifying the thermophysical properties of the fluids. Due to these reasons, water, n-decane and n-heptane are the fluids adopted for the experiments. Water is a control fluid extensively researched in the literature [6], whereas the n-decane and n-heptane are surrogate fuels for kerosene/jet fuel [7, 8] and diesel [9, 10], respectively. Furthermore, these fluids provide a wide range of thermophysical properties and saturation temperatures.

The experimental data provides a foundation for the implementation and validation of the numerical model. There are several reasons to prioritise numerical advancements in the research industry. Firstly, several practical experiments are quite costly and time consuming, such as particle image velocimetry (PIV) systems, wind tunnels, nuclear reactors, among others. Numerical simulations provide options in terms of availability due to limited resources. The possibility of studying simplified systems or the influence of specific parameters on the physical model that are a restraint in experimental conditions increases the significance of numerical modelling. The numerical analysis associated with these studies is essential to optimize the efficiency of technical systems.

The relation between theoretical work and empirical methods provides a better understanding of the research field, predicting outcomes and improving existing theories. In the context of fluid mechanics and heat transfer, specifically droplet impact phenomena, this includes kinematic discontinuities, splashing mechanisms, crown and crater evolution, and phase change. Theoretical work complements the acquired experimental results, leading to a more refined analysis.

1.2 Objectives

A fundamental study of the phenomena of impacting droplets onto non-heated and heated liquid films is of considerable interest to the scientific community. The main objective of the current work is researching the phenomena of droplet impact onto heated wetted surfaces with the purpose of implementing biofuels in the aviation sector. Achieving such a goal requires the following stages:

- Design and adaptation of an experimental facility to account for non-isothermal conditions focused on heated liquid films;
- Characterisation of the liquid film in terms of temperature fields and evaporation rates. The evaporating and boiling regimes are to be assessed regarding liquid film thickness variation, liquid-gas interface instabilities, and the formation of vapour bubbles;
- Evaluation of the droplet impact outcomes as a function of the liquid film temperature, including central jet, crater, splashing and bubbling. This includes visualisation, geometrical parameter measurements, and development of correlations;
- Theoretical analysis regarding the propagation of a kinematic instability in a liquid layer and time scales for crater and central jet evolution, respectively;
- Implementation and evaluation of a numerical model regarding droplet impact phenomena. Defining the interface tracking method and implementing the energy equation is required to simulate the impact of liquid droplets onto heated liquid films.

1.3 Contributions

The droplet impact phenomena have been extensively researched, both experimental and numerically, which are driven by many practical applications including internal combustion engines, heat exchangers, and cooling devices. Despite this, single droplets impacting onto liquid films are limited to isothermal conditions, as the influence of temperature on droplet outcome and correspondent heat and mass transfer mechanisms has been overlooked in the literature. Introducing the impact of temperature on interfacial dynamics and breakup mechanisms is essential to narrow the gap between single droplet studies and industrial applications.

In order to evaluate the influence of temperature on liquid films and, consequently, the impact phenomena, an experimental facility was designed to account for non-isothermal conditions. The key aspects of the experimental facility, located at the University of Beira Interior, consist of a high-speed imaging system and the presence of a heat source, continuously heating the liquid film by conduction. The liquid film characterisation is required in terms of temperature fields and evaporation rates. This analysis contributes to a deeper understand-

ing of heat and mass transfer regimes applied to wetted surfaces. Subsequently, the droplet impact phenomena are evaluated both qualitatively and quantitatively. The visualisation of the impact phenomena allows identifying liquid-gas interactions for different fluids, impact conditions, and liquid film temperatures. This leads to the measurements of geometrical parameters, which are associated with liquid structures, kinematic discontinuities, breakup mechanisms, among others. The comparison between isothermal and non-isothermal conditions establishes a primary basis for temperature-related phenomena, including differences in thermophysical properties, formation of vapour bubbles, and liquid film instabilities.

The experimental data acquired through quantitative analysis contributes to the validation of theoretical models. The development and refinement of new and existing theories enhance the understanding of multiphase flows and heat transfer applied to the impact phenomena, such as theoretical work regarding wave propagation and time scales. Similarly, the developed empirical analysis serves as a foundation for numerical simulations. The coupling of governing equations with interface tracking methods allows to accurately capture the liquid-gas interface for two-phase flows, providing further insights into interfacial phenomena such as evaporation, condensation and boiling.

During the course of the research project, several articles were published in scientific articles, and the findings were presented in international conferences. These are presented in the following sections.

Journal Articles

1. I. Ferrão, D. Vasconcelos, D. Ribeiro, A. Silva, J. Barata, ”A study of droplet deformation: The effect of crossflow velocity on jet fuel and biofuel droplets impinging onto a dry smooth surface”, *Fuel*, vol. 279, p. 118321, 2020
   https://doi.org/10.1016/j.fuel.2020.118321

2. D. Vasconcelos, A. Silva, J. Barata, ”The impact of temperature on heated liquid films: Crater and jetting impact dynamics”, *Experimental Thermal and Fluid Science*, vol. 147, p. 110944, 2023
   https://doi.org/10.1016/j.expthermflusci.2023.110944

3. D. Vasconcelos, A. Silva, J. Barata, ”Influence of bubble growth and liquid film instabilities on droplet impact phenomena under saturated boiling regimes”, *Atomization and sprays*, vol. 34(4), 2023
   https://doi.org/10.1615/AtomizSpr.2024051142

4. D. Vasconcelos, A. Silva, J. Barata, ”Splashing correlation for single droplets impacting liquid films under non-isothermal conditions”, *Experiments in Fluids*, vol. 66(3), 2025
   https://doi.org/10.1007/s00348-024-03942-6

Scientific conferences

1. D. Vasconcelos, D. Ribeiro, A. Silva, J. Barata, "3D Simulations of Droplets Impacting Liquid Films: Crown Parameters Measurements", 2020 AIAA Science and Technology Forum and Exposition (p. 1578) - Orlando, Florida, 6-10 january 2020
   https://doi.org/10.2514/6.2020-1578

2. J. Cardoso, C. Moura, D. Ribeiro, D. Vasconcelos, J. Barata, A. Silva, "Design and Fabrication of a Low Cost, Push Mode Piezoelectric Stream Droplet Generator with Interchangeable Nozzle", ICLASS 2021, 15^{th} Triennial International Conference on Liquid Atomization and Spray Systems - Edimburgh, United Kingdom, 30 August - 2 September 2021
   https://doi.org/10.2218/iclass.2021.5983

3. P. Pinto, D. Vasconcelos, D. Ribeiro, J. Barata, A. Silva, "Collision Dynamics of a Single Droplet onto a Heated Dry Surface: Jet Fuel and HVO Mixtures", ICLASS 2021, 15^{th} Triennial International Conference on Liquid Atomization and Spray Systems - Edimburgh, United Kingdom, 30 August - 2 September 2021
   https://doi.org/10.2218/iclass.2021.5982

4. D. Vasconcelos, A. Silva, J. Barata, "Comparison of Commercial and Open-Source CFD Solvers on Surface Tension Dominated Flows", ICLASS 2021, 15^{th} Triennial International Conference on Liquid Atomization and Spray Systems - Edimburgh, United Kingdom, 30 August - 2 September 2021
   https://doi.org/10.2218/iclass.2021.5981

5. D. Vasconcelos, A. Silva, J. Barata, "Droplet impact dynamics on subcooled boiling regimes: Effect of dimensionless temperature and impact parameters", EJIL 2022, 5^{th} Meeting of the Young Researchers of LAETA - Lisboa, Portugal, 5-6 May 2022

6. D. Vasconcelos, A. Silva, J. Barata, "Influence of Dimensionless Temperature on Droplet Impact onto Heated Liquid Films for Subcooled Boiling Regimes", ILASS–Europe 2022, 31^{th} Conference on Liquid Atomization and Spray Systems - Virtual, 6-8 September 2022
   http://hdl.handle.net/10400.6/12555

7. D. Vasconcelos, A. Silva, J. Barata, "Influence of Vapour Bubbles Size and Spacing on Droplet Impact Outcomes under Subcooled Boiling Regimes", ILASS–Europe 2022, 31^{th} Conference on Liquid Atomization and Spray Systems - Virtual, 6-8 September 2022
   http://hdl.handle.net/10400.6/12554

8. A. Mendes, D. Vasconcelos, D. Ribeiro, M. Panão, A. Silva, "Does liquid film tem-

perature affects single drop impact dynamics?", TFEC2023, 8^{th} Thermal and Fluids Engineering Conference - Hybrid, MD, USA, 26-29 March 2023
10.1615/TFEC2023.app.046327

9. D. Vasconcelos, A. Silva, J. Barata, "Effect of Vapour Bubble Initial Displacement on Droplet Impact onto Liquid Films", YIC 2023, VII ECCOMAS Young Investigators Conference - Porto, Portugal, 19-21 June 202)
http://hdl.handle.net/10400.6/13404

10. D. Vasconcelos, A. Silva, J. Barata, "Influence of bubble growth and liquid film instabilities on droplet impact phenomena under saturated boiling regimes", ILASS Europe 2023, 32^{nd} Conference on Liquid Atomization and Spray Systems - Napoli, Italy, 4-7 Sept 2023
http://hdl.handle.net/10400.6/14176

11. D. Vasconcelos, A. Silva, J. Barata, "Splashing morphology and crown dynamics of single droplets impinging heated liquid films", LXLASER2024, 21^{st} International Symposium on Application of Laser and Imaging Techniques to Fluid Mechanics - Lisbon, Portugal, 8-11 July, 2024
https://doi.org/10.55037/lxlaser.21st.159

1.4 Thesis Overview

The following document is structured into seven chapters, with the current chapter addressing the motivation and objectives of this work, as well as its contributions to the scientific community. The second chapter focuses on the research field of droplet impact phenomena, ranging from pioneer work to modern applications. The third chapter describes the experimental methodology of the current work, involving the experimental setup and correspondent components, procedure, post-processing analysis and liquid film characterisation. The following chapter presents the experimental results regarding impacting droplets onto heated liquid films. Different impact outcomes are evaluated as a function of the liquid film temperature in terms of overall development and geometrical parameter measurements, which is complemented by a theoretical analysis. Subcooled and saturated boiling regimes are examined concerning vapour bubbles and their subsequent influence on the impact phenomena. The fifth chapter provides a detailed explanation of the numerical model, including the incompressible Navier-Stokes equations and the coupled interface tracking method. The discretisation of the various terms in the governing equations is presented and applied to the computational domain. The numerical results are exhibited in the upcoming chapter, which are initially validated with existing experimental data. The vapour bubbles are investigated in terms of bubble detachment, as well as merging and bursting dynamics. The final chapter refers to the conclusions and possible implementations in future works.

Chapter 2

Literature Review

The current chapter unveils the phenomena of droplet impact. In order to understand the importance of this topic, the first section will introduce multiphase flows, interaction between phases, nature and industrial applications, and its correlation with droplet impact. The second section presents an initial background of the droplet impact phenomena. This includes the properties inherent to the phenomena, such as the droplet, impact surface and surrounding environment, as well as the dimensionless numbers that define the system. Several concepts are mentioned in this section, including droplet deformation, crossflow, temperature and impact targets. The third section details the course of droplet impact research, from the early 20^{th}- century pioneer work to modern applications. The fourth section focuses particularly on the single droplet impact onto liquid films. A characterisation of the liquid film regimes will be presented, followed by the different impact outcomes. These will be thoroughly detailed in terms of crown formation, secondary atomisation, and low and high-velocity impacts. Subsequent to understanding the underlying hydrodynamics of droplet impact, the following section introduces temperature as a significant factor in both heat and mass transfer mechanisms. Due to the scarcity of research regarding droplet impact onto heated liquid films, an initial focus on dry heated walls is required. Heat transfer regimes, ranging from film evaporation below the saturation temperature of the fluid to the film boiling regime over the Leidenfrost point, are thoroughly evaluated and coupled with mass transfer phenomena, such as evaporation, condensation and boiling. Once these concepts are characterised, the final section provides numerical models applied to two-phase flows. These include interface tracking methods for accurately capturing the liquid-gas interface and phase change models for non-isothermal conditions. An overview of numerical models is also provided for insight into different industrial applications.

2.1 Introduction

Nature comprises most of the intrinsic multiphase phenomena, from the micro to the macro scale. Waterfalls, heavy rain, fogs, sediment transport in rivers, blood flowing through veins, among many others, are examples of different multiphase flows. By definition, these are flows that contain mixtures of different phases of matter, which can be solid, liquid, and gas. Considering the multiphase approach, two general topologies of multiphase flows can be defined, which are dispersed phase or separated flows [11]. The dispersed phase flows consist of discrete, non-continuous finite particles (discrete phase) scattered onto a continuous volume field (continuous phase). Examples of dispersed flows include the transport of bubbles within a liquid, as well as droplets within the gas phase. In separated flows, the phases are

separated by interfaces, such as annular flow in a pipe, in which the walls are covered by a liquid film, with the gas flowing in the gas core.

Multiphase flows can be divided into several categories depending on the possible coexisting phases of matter, such as gas-liquid, gas-solid, liquid-solid, liquid-liquid, and three-phase flows [12]. In terms of gas-liquid flows, the most common occurrences are bubble columns within a fluid, or liquid droplets in a gas flow. These are present in a multitude of applications, including microreactors [13], vertical pipes [14] and petrochemical processes [15]. When solid particles are carried by a gas, these are denominated as particle-laden flows. If, however, the continuous phase is a liquid, the flow transitions into a slurry flow. Applications for these flows include fluidised beds [16], pulverised coal combustion [17], and transport of coals and ores through mud. The three-phase flows are a combination of the previously defined categories, such as the presence of bubbles on a slurry flow.

Amidst the entirety of concepts regarding multiphase flows, this thesis will focus on two-phase flows, namely gas-liquid interactions. The physical system involves both droplets and bubbles, as the former relates to the droplet impact onto liquid films and subsequent outcomes and the latter to the nucleation and growth of vapour bubbles on the impact surface under boiling regimes induced by a heat flux. Therefore, the following sections will comprehensively detail these subjects, focusing on the droplet impact phenomena. The topic of vapour bubbles has been overlooked in the literature due to the majority of experimental work being focused on isothermal liquid films or heated dry surfaces. This is also due to the narrow range of the bubble formation on liquid films, which occurs for higher temperature regimes below or near the saturation temperature of the fluid.

2.2 General Concepts

Prior to performing an in-depth analysis regarding the advances in droplet impact research, a general assessment of the phenomena must be provided. As previously specified, multiphase flows can be divided into several categories. In terms of gas-liquid environments, droplets within a continuous air flow impinging onto different surfaces are extremely common in both nature and industrial applications. There are three variables that are inherent to these phenomena: the droplet, the impact surface, and the surrounding air. Understanding the interactions related to the multiphase phenomena is the first step in quantifying the physical aspects of droplet impact.

By definition, a liquid droplet is a finite volume of fluid, partially or entirely bounded by free surfaces. Due to the existence of free boundaries, as well as cohesion forces present at the liquid-gas interface, external forces influence its natural state, leading to different branches on its development. Figure 2.1 displays different forms of the droplet during free fall, prior to impact. These may occur due to external factors, such as a crossflow and temperature gradients, which will be mentioned posteriorly. A droplet may be spherical or deformed,

it may oscillate due to, for example, the detachment from a hypodermic needle or a liquid atomiser, or be under the influence of internal circulation. These variations may be caused by the surrounding environment along the falling trajectory of the droplet. The existence of a crossflow causes deformation of the droplet, and the descent of the droplet leads to the formation of a wake flow-field, as represented by figure 2.2. Once the droplet impinges a surface, its outcome depends on the impact target. Figure 2.3 shows the classification of different impact surfaces. The orientation of the surface, which can be analogous to the droplet impact angle, affects the behaviour of the droplet during the spreading phase. This leads to a symmetric or asymmetric outcome when considering a perpendicular or an oblique impact, respectively. The roughness of a dry surface versus the existence of a liquid film produces completely distinct results, as the underlying mechanisms associated with these surfaces are fundamentally different [18]. The porosity of the material becomes increasingly important if the surface contains void space through which the liquid may leak, such as textiles [19].

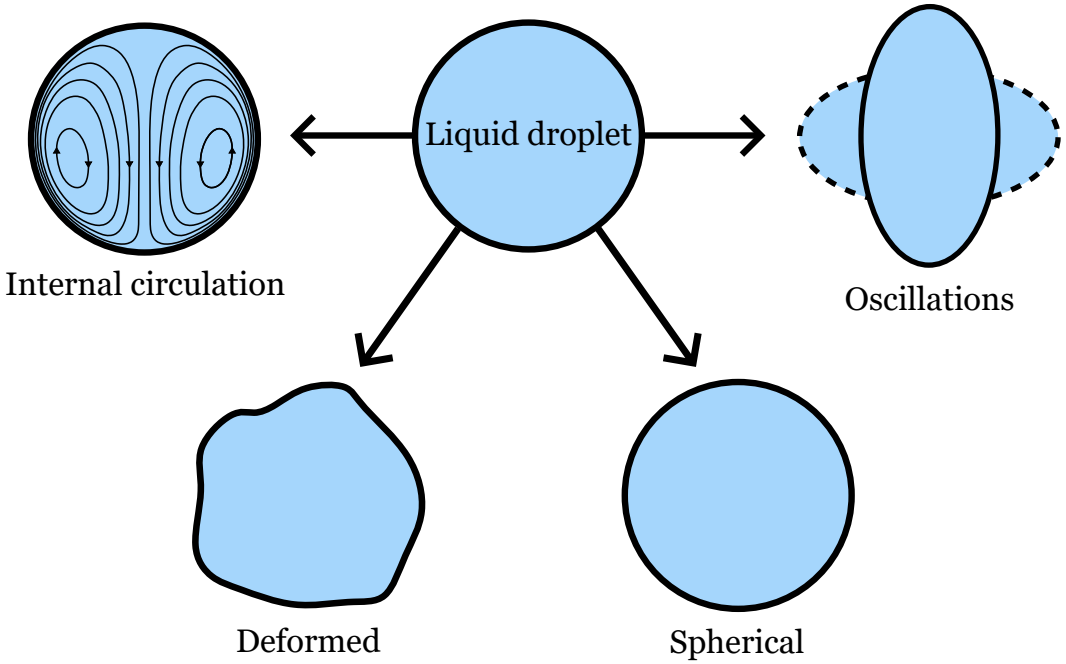

Figure 2.1: Liquid droplet variations, such as spherical, oscillating between oblate and prolate shapes, internal circulation and deformed droplet.

The main subject of this work considers the scenario of a droplet impacting onto a liquid film. As represented by figure 2.4, a single droplet, of impact velocity U_d and diameter D_d, impinges onto a liquid film of thickness h. These have identical thermophysical properties, such as density, viscosity, surface tension, among others, and are surrounded by air. In order to distinguish between the phases, the subscripts l and g refer to the liquid and gas phases, respectively. If the thermophysical properties of the droplet and the liquid film differ (due to pressure or temperature differences), the subscripts d and f are adopted, respectively. In order to comprehend the significance of the thermophysical properties on the dynamics of droplet impact, a set of dimensionless numbers is employed [20]. These allow to reduce the number of variables that describe a system, as well as provide an order-of-magnitude on how such systems behave. The dimensionless numbers are associated with fluid mechanics,

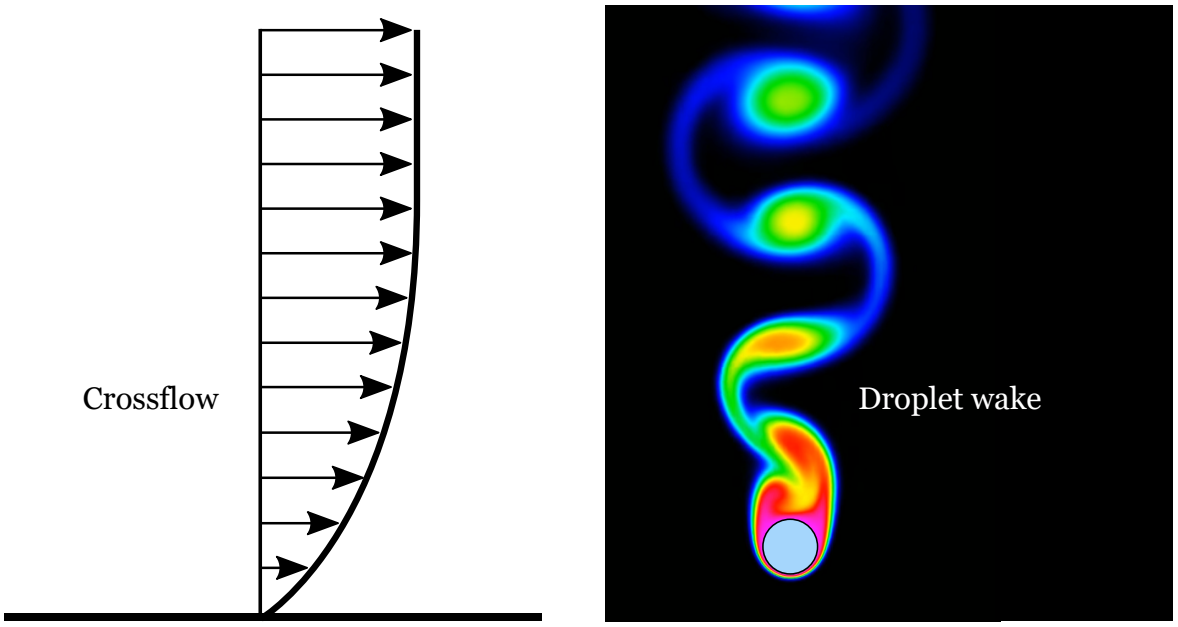

Figure 2.2: Examples of surrounding environment for the droplet impact phenomena, such as the existence of a crossflow and the formation of a wake flow-field.

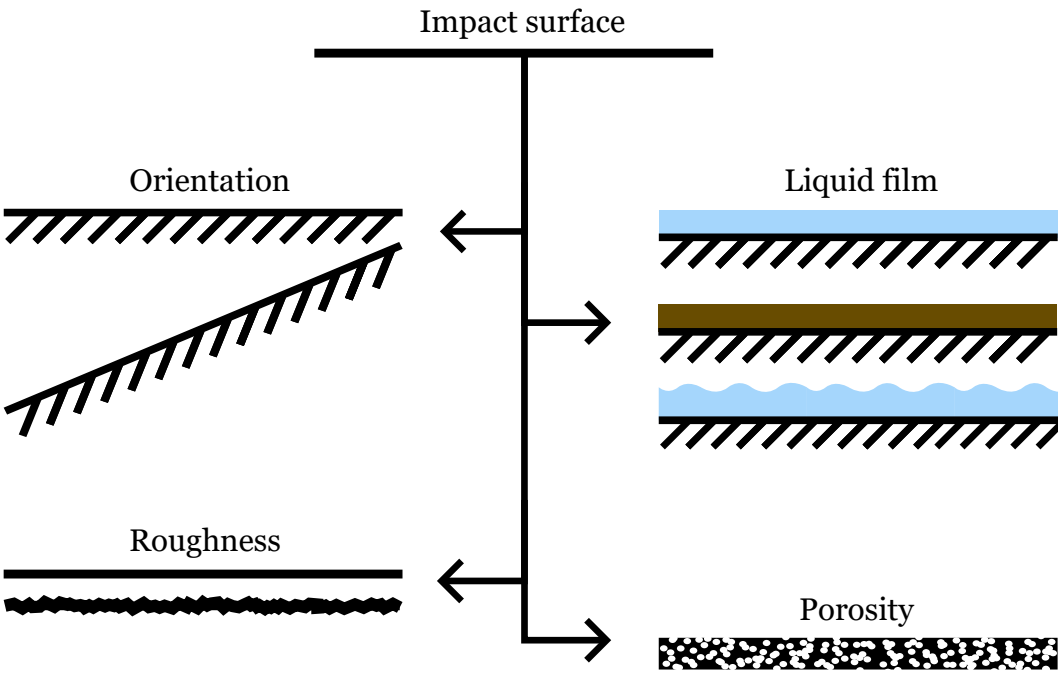

Figure 2.3: Classification of impact targets, including orientation, roughness, porosity, and the presence of a liquid film.

which include thermophysical properties of the fluids, characteristic length scales and inertial parameters. Several examples of dimensionless numbers that define multiphase flows involving droplets are the Reynolds, Weber and Ohnesorge numbers, among others. The Reynolds and Weber numbers are represented by equations (2.1) and (2.2), respectively:

$$Re = \frac{\rho U_d D_d}{\mu} \tag{2.1}$$

$$We = \frac{\rho U_d^2 D_d}{\sigma} \tag{2.2}$$

where ρ is density, μ is viscosity, and σ is the surface tension. The former equation relates the inertial to the viscous forces, whereas the latter represents the ratio of disruptive hydrodynamic to the stabilising surface tension forces. The Ohnesorge number is defined as the ratio between the viscous forces and the inertial and surface tension forces. Due to this relation, it can also be obtained through the Weber and Reynolds numbers, as displayed by equation (2.3).

$$Oh = \frac{\mu}{\sqrt{\rho \sigma D_d}} = \frac{\sqrt{We}}{Re} \tag{2.3}$$

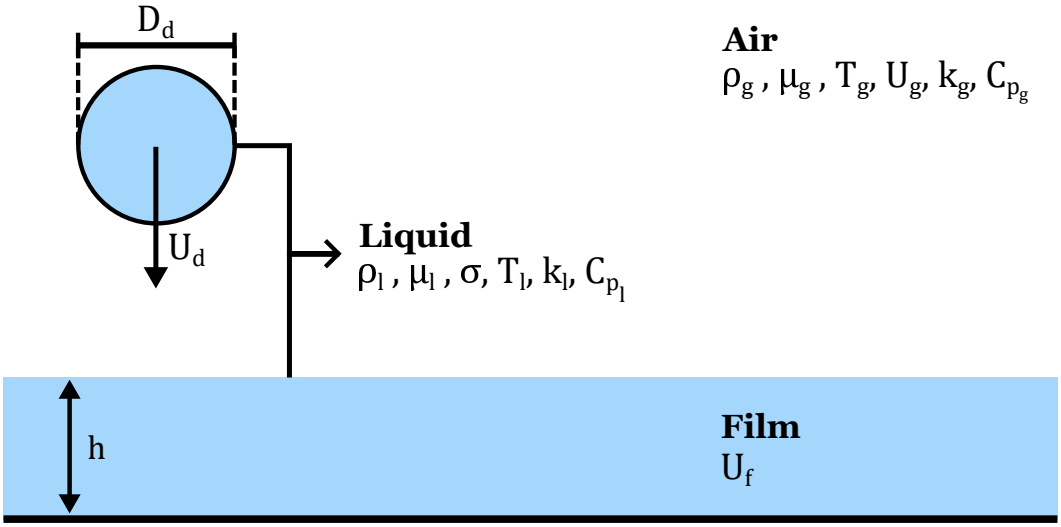

Figure 2.4: Representation of droplet impact onto a liquid film and correspondent thermophysical properties.

For low-velocity impacts, the gravitational forces become significantly more predominant, which can be associated with the Froude number, as shown by equation (2.4):

$$Fr = \frac{U_d}{\sqrt{g D_d}} \tag{2.4}$$

where g is the gravitational acceleration constant. The ratio between the film thickness and the droplet impact diameter defines the dimensionless film thickness, as represented by equation (2.5). The different thickness regimes will be thoroughly explained in the following sections.

$$h^* = \frac{h}{D_d} \tag{2.5}$$

In addition, the Bond number relates the surface tension and gravitational forces, the Capil-

lary number has a similar interpretation to the Ohnesorge number, and the Laplace number represents the ratio between surface tension forces and momentum dissipation. These are displayed by equations (2.6), (2.7) and (2.8), respectively.

$$Bo = \frac{\rho g D_d^2}{\sigma} = \frac{We}{Fr} \tag{2.6}$$

$$Ca = \frac{\mu U_d}{\sigma} = \frac{We}{Re} \tag{2.7}$$

$$La = \frac{\sigma \rho D_d}{\mu^2} = \frac{Re^2}{We} \tag{2.8}$$

However, when considering temperature as a defining quantity, the hydrodynamics associated with the phenomena alter significantly. Additionally, the temperature of the surrounding field may induce the droplet to evaporate or, if the conditions are met, to auto-ignite, leading to droplet combustion. For dry surfaces, the wall temperature, T_w, and the Weber number are the main factors in impact dynamics and thermal-related phenomena [21].

2.3 Pioneer Research

The early 20$^{\text{th}}$ century marked the beginning of the droplet impact study. The pioneering work developed by Worthington is considered a benchmark in droplet impact dynamics. Worthington [22] drew interest in this topic by means of a colleague, leading him to investigate the different patterns of falling mercury and milk droplets onto a glass plate. In order to visualise the structures of the droplets impacting the surface, the principle behind the experimental apparatus is based on an electrical circuit break upon the impact of the droplet onto the glass surface, creating a spark and allowing for the visualisation of the phenomenon at that instant. This spark was delayed and adjusted accordingly to capture the dynamics associated with the impacting droplet at distinct time frames. Worthington [23] follows the previous paper, focused on studying earlier stages of droplet impingement. This complements the data related to the later stages of the phenomena, correlating how the transitions from the initial impact to the final outcome develop. The author introduces the concepts of wall adhesion, wettability, and ambient pressure. A few years later, Worthington [24] initiated the study of solid and liquid spheres onto liquid surfaces. The previous apparatus [22] was improved and adjusted to these experiments. The initial design was based on an electric spark produced by an induction coil, specifically timed to illuminate the moment of impact, or carefully delayed to capture later moments of the impingement phenomena. The improved apparatus uses a second sphere (timing-sphere), falling simultaneously with the main droplet, that collides onto a plate of adjustable height, triggering the electric spark. Initial glances of bubbling formation, cavity growth followed by an emerging jet with possible

breakup, as well as the underlying dynamics related to splashing, are presented. The work developed by Worthington had been, to this extent, based on drawings of the phenomena. The spark produced by the induction coil would allow the author to visualise and draw a specific time frame. However, these would require a minimum number of attempts to assure accuracy. This would lead to uncertainty of the mechanics involved in the fluid interactions, considering that each case is, in itself, unique. In order to improve this mechanism, Worthington and Cole [25] adopted a Leyden-jar spark, in contrast to the induction coil-induced spark, to photograph the droplet impact onto a liquid surface. This way, the drawing limitations imposed by the human eye are overcome by high speed photography, allowing to capture an event with improved precision and detail. The Leyden-jar spark was employed by Lord Rayleigh [26] to study capillary instabilities on free liquid jets. The extensive work of the author over the years is summarised in Worthington [27], such as the formation of liquid crowns and jets, which are displayed in figure 2.5. This jet structure, which is formed subsequent to the droplet impact, would be posteriorly recognised as the Worthington jet by the scientific community.

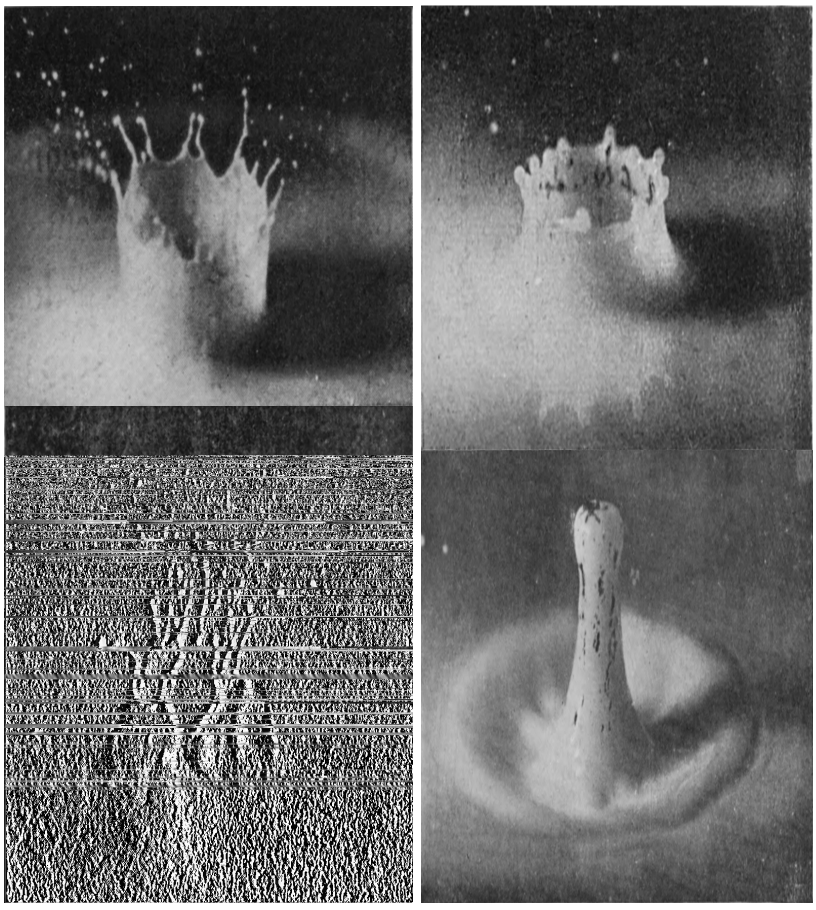

(a) (b)

Figure 2.5: Water drop falling onto a water-milk liquid pool [27]: a) Falling height of $Y = 135\ \mathrm{cm}$; b) Falling height of $Y = 40\ \mathrm{cm}$.

Edgerton [28], by using a technique called stroboscopic imaging, was able to capture droplets and splashing with finer detail. A stroboscope consists of a power supply which discharges electricity onto a capacitor, storing its electrical energy. This energy is then released into a

tube filled with a rare gas, causing its molecules to vibrate rapidly enough to produce a flash of light. Since this process is repeatable as soon as the capacitor recharges, it is possible to create slow-motion pictures. This procedure can be applied from natural events, such as insect flight, rain and human motion, up to technological advancements in the modern world, including turbines and ballistics. Figure 2.6a displays the formation of a droplet which will detach from its source when gravitational exceeds surface tension forces. The liquid ligament will stretch, becoming thinner and thinner until reaching a ruptured state, producing oscillations under a free-fall motion. This droplet will eventually stabilise, followed by the impact onto a liquid film, as displayed by figure 2.6b.

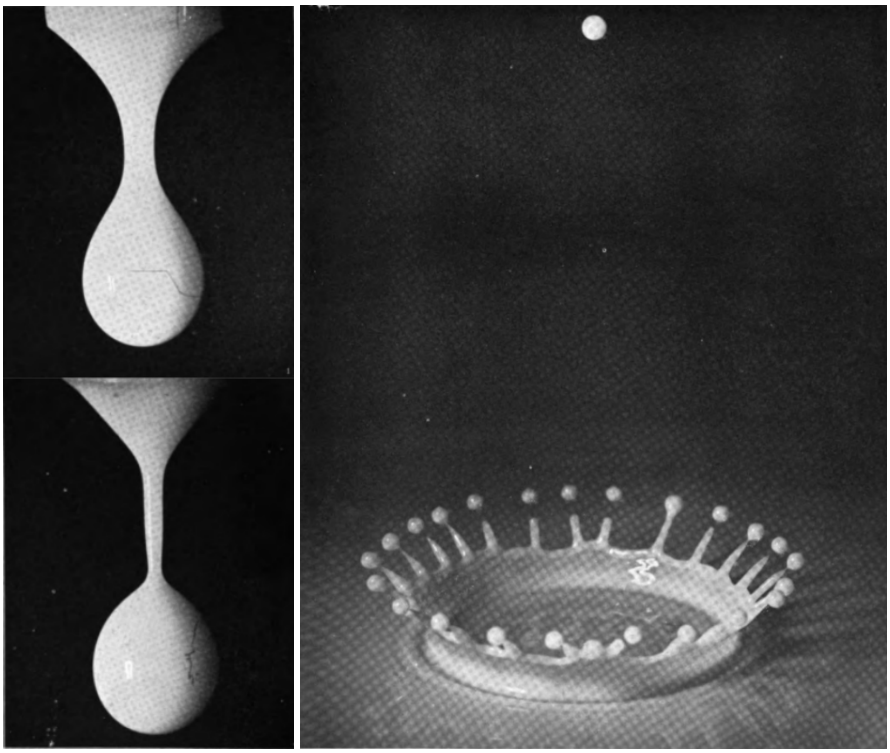

(a) (b)

Figure 2.6: Imaging of splashes and droplets obtained through modern stroboscopy [28]: a) Thin ligament breakup; b) Crown splashing.

Thus far, the efforts performed in the current research were focused on the appearance of the phenomena, mostly related to fluid dynamics. However, there are several other topics that can be explored, such as collisions, compressibility, sound, temperature, among others. Franz [29] investigated the production of sound originating from splashing due to the entry of an object, mainly droplets, onto liquids. The underwater splashing sounds were acquired through a hydrophone placed close to the liquid interface. A complex system consisting of an oscillograph and integrated circuits allowed to obtain sound traces and to perform a spectrum analysis of the sound energy radiated from the splashes, respectively. The underwater noises originate from three different sources. The moment of impact and resonant vibrations of the body are associated with high-impact velocities, whereas bubble entrapment is predominant with low-impact velocities. Related to this topic, Prosperetti and Oguz [30] reviewed both droplet impact onto liquid surfaces and the propagation of underwater noise due to rain. Ac-

cording to the authors, these studies were propelled for military applications, such as sound detection and signal processing, and acoustical techniques to probe phenomena of geophysical nature, such as sea-floor mapping. Lesser & Field [31] studied the effect of compressibility on liquids, focusing on damaging mechanisms onto solid surfaces such as erosion. The early stages are the main focus of this work due to the formation of shock waves associated with the droplet impact. High-pressure edges and cavitation are a direct result of the liquid-solid contact, leading to the jetting phenomenon, as stated by several authors [32, 33]. The different outcomes subsequent to droplet impact, such as jetting, will be specified in the following section. Wachters and Westerling [34] examined the hydrodynamics and heat transfer of a water droplet impinging onto a heated polished gold surface. A stroboscopic lighting technique was applied for the experiments to identify the behaviour of the droplet on the surface, whereas the heat transfer was measured by means of a sensitive flow meter. The experimental results contradict theoretical work in terms of evaporation time. Theory predicts higher evaporation rates for increasing surface temperatures, whereas experimental data shows an opposite behaviour. This tendency is also verified for mist droplets, as analysed by Wachters et al. [35]. However, if sessile droplets are considered, the theoretical analysis is in good agreement [36]. In terms of fluid dynamics, the gradual increase of the wall temperature leads to rebound ($T_w \approx 170°\mathrm{C}$) and formation of vapour bubbles ($T_w \approx 280°\mathrm{C}$). For higher temperatures, a thin vapour layer is formed between the droplet and the impact surface, heavily reducing the local heat transfer and consequently increasing evaporation times. This phenomenon is denominated Leidenfrost [37], as it is a critical point in defining heat transfer regimes.

Chandra and Adevisian [38] studied the collision dynamics of an n-heptane single droplet impacting a heated metallic surface, ranging from ambient temperature up to the Leidenfrost point. The authors focused on the evolution of the wetted area upon impact, including the spreading rate, β, and contact angle, θ_w, as well as phenomena visualisation. These are fundamental in understanding the wettability of a given surface, which is a concept initially defined and developed by Young [39]. Examples of temperature and wetting-related phenomena, such as the formation of vapour bubbles or ligament breakup, are displayed in figure 2.7. The experimental results display a dependency of both parameters on the wall temperature. Higher wall temperatures lead to increasing contact angles and decreasing maximum spreading rates, reaching their maximum and minimum values, respectively, on the Leidenfrost temperature. Above this point, these are assumed to be constant due to the non-contact behaviour between the droplet and the impact surface. Pasandided-Fard et al. [40] also investigated the spreading of a water droplet onto a solid surface. The contact angle was varied by adding surfactant to the fluid, thus reducing its surface tension. The presence of surfactant is not significant in the droplet spreading, although it alters its shape during the receding phase. In terms of liquid-solid interactions, the authors considered both the static and advancing contact angles. The former is considered when the droplet remains at rest on the surface, whereas the latter is measured during the phenomena occurrence, usually associated with spreading. The addition of surfactant leads to a decrease in the static, however exhibits no influence in the advancing contact angles.

Engel [32] attempted a different approach at the phenomena, studying the flow characteristics for different impact surfaces, ranging from smooth to rough. These would include dry clean glass, natural and synthetic rubber, iron surfaces, among others. Visible differences were spotted, generally including spreading for smooth surfaces, transitioning to splashing for rough surfaces. Following this work, Stow and Hadfield [41] used an aluminium alloy, which allowed for different degrees of roughness, and a stainless steel surface as a reference. The results show that the hydrodynamics associated with the impact phenomena, namely splashing, strongly depend on the surface roughness.

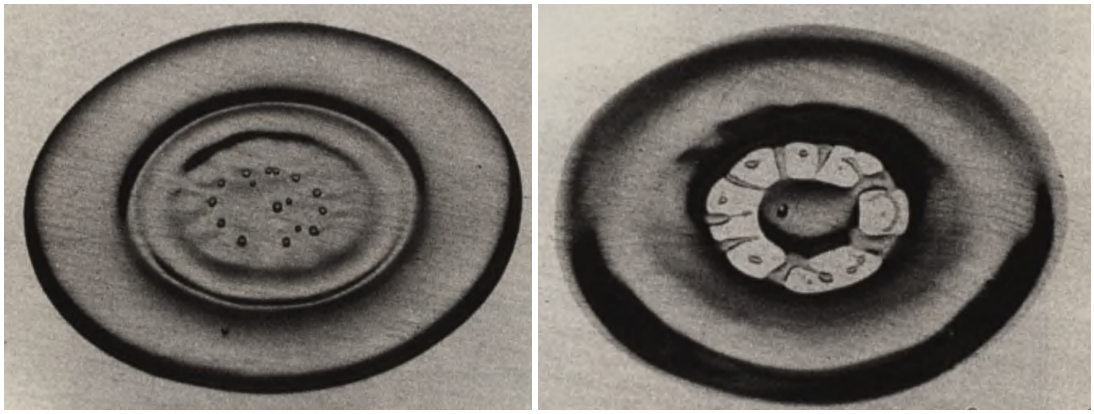

(a) (b)

Figure 2.7: N-heptane droplet impact onto a stainless steel surface at $T_w = 104°\mathrm{C}$ [38]: a) $t = 5.6\ \mathrm{ms}$; b) $t = 8.0\ \mathrm{ms}$.

Peregrine [42] focused on several topics regarding fluid dynamics, namely splashing mechanisms and breaking waves, as well as mathematical and numerical models regarding these topics. Generally, due to the complexity of the physical aspects of multiphase flows, simplifications are required to either achieve exact solutions, such as Couette and Hagen-Poiseuille flows [43], or to increase the efficiency of numerical simulations due to limited computing power. Due to these reasons, mathematical interpretations of the phenomena consisted mostly of one-dimensional models, relating the impact angle, velocity and thicknesses of different liquid layers on crown propagation by applying the Bernoulli theorem. However, due to the flow unsteadiness, this model would become obsolete, as it could not be applied to small-scale splashing events [44]. A model widely accepted by the scientific community is the quasi-one-dimensional model developed by Yarin and Weiss [45]. This model explains the physical nature of splashing in terms of a kinematic discontinuity in the velocity and liquid film thickness distributions. This wave propagates through the liquid layer on the wall, similar in characteristics to a shock wave. In the case of an incompressible fluid, the existence of a mass sink will lead to the emergence of a liquid sheet, propagating up and outwards, creating a crown structure. This will eventually lead to the formation of cusps at the free rim, rupturing from the developing crown and creating secondary droplets.

With the recent development of high-speed imaging, rudimentary methods such as stroboscopy imaging [28], rotating-mirror [46] and beam-splitter cameras have slowly been replaced by newer and improved image capturing methods. Among these, there are two meth-

ods that have received remarkable attention, consisting of the Complementary Metal-Oxide Semiconductor (CMOS) cameras and the Charged-Coupled Devices (CCD) [47]. Both are based on metal-oxide semiconductors and operate under the photo-electric effect, capturing and transforming photons onto electrical charge. This charge would then be registered and transmitted for post-processing, which is distinct for both devices. These are reviewed thoroughly by Thoroddsen et al. [48], which focus on the advancements of high-speed cameras and correspondent applications regarding droplet and bubble dynamics. In summary, these devices revolutionised how the world perceives natural phenomena, which, from a multiphase perspective, includes droplets, bubbles, and free-surface flows.

2.4 Droplet Impact onto Liquid Films

Two-phase flows are, as mentioned in the previous section, extremely intricate due to the extensive number of variables that can affect the phenomena. A fundamental approach to any physical or numerical problem is to reduce the system complexity by limiting the number of variables considered for a given system. Therefore, succeeding the introduction of droplet dynamics and preliminary research, the primary focus will shift onto isothermal liquid films. Internal combustion engines with direct fuel injection [49], spray cooling [50], heat exchangers [51] and ink-jet printing [52] are a few examples in which liquid films play a major role. Depending on the ratio of the film thickness to the droplet diameter, these are characterised differently, as the regimes are dependent on wall properties, such as length scale and roughness. Table 2.1 exhibits diverse ranges of liquid films and pools according to several authors. The regimes presented by Tropea and Marengo [53] are adopted for the present work. For $h^* < 1.5$, liquid films are dependent on wall properties, namely the arithmetical mean value of wall roughness, R_a, and the length scale of the wall roughness, L_a. These parameters can be non-dimensionalised by the droplet diameter, $R_{nd} = R_a/D_d$ and $L_{nd} = L_a/D_d$, respectively. For higher thicknesses, shallow pools are independent of wall features, however dependent on the liquid film thickness. In the case of deep pools, neither wall nor liquid film parameters are a factor in determining the impact outcomes. Considering the liquid film interpretation of Tropea and Marengo [53] and the pre-existing conditions in internal combustion engines [54], the studies developed in this thesis focus on liquid film thicknesses of $h^* < 1.5$.

The following subsections describe the different outcomes subsequent to the single droplet impact onto a liquid film. These are dependent on several parameters, such as the droplet inertia, the thickness of the liquid film, and the physical properties of the fluid, as previously mentioned. Due to this, the outcomes will be introduced based on their impact energy, ranging from low-impact (such as spreading and coalescence) to high-impact velocities (prompt and crown splashing).

Table 2.1: Liquid film regimes for droplet impact.

Author(s)	**Regime**	**Range**
Tropea and Marengo [53]	Thin liquid film	$L_{nd} < h^* < 3R_{nd}^{0.16}$
	Liquid film	$3R_{nd}^{0.16} < h^* < 1.5$
	Shallow pool	$1.5 < h^* < 4$
	Deep pool	$h^* \gg 4$
Cossali et al. [55]	Thin liquid film	$h^* < 1$
	Deep splash	$h^* \gg 1$
Vander Wal et al. [56]	Thin liquid film	$h^* \approx 0.1$
	Thick liquid film	$0.1 < h^* < 10$
	Deep liquid pool	$h^* \gg 10$
Wang and Chen [57]	Thin liquid film	$h^* < 0.1$
	Thick liquid film	$h^* > 0.1$
Motzkus et ak. [58]	Thin liquid film	$h^* < 1$
	Deep splash	$h^* \gg 1$

2.4.1 Spreading

The definition of spreading consists of the droplet impacting onto a surface and, as displayed by figure 2.8, spreading and remaining attached to the surface. During the entire impact process, no formation of secondary droplets is visualised. This phenomenon has received more attention on dry surfaces [59, 60], namely due to wetting and cooling dynamics for specific applications, such as electronic cooling devices. Therefore, for existing liquid films, the droplet impact leads to the spreading and posterior merging of the droplet and liquid film, creating a mechanical wave that expands radially and outwards from the impact region. Spreading can also be denominated as deposition, although the latter fails to produce capillary waves on the liquid film upon impact [61].

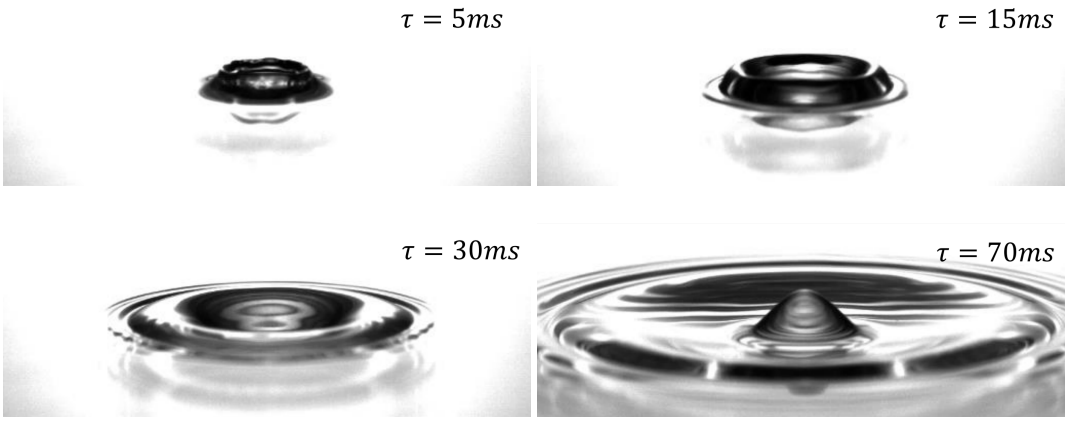

Figure 2.8: Spreading outcome of a 75% Jet Fuel (JF)/25% Hydrotreated vegetable oil (HVO) droplet impact onto a liquid film. Adapted from Ribeiro [62].

2.4.2 Coalescence

The phenomenon of coalescence, similar to spreading, occurs when a droplet interacts with a liquid film at low-impact velocities, although it is more predominant in liquid pools [63, 64]. Figure 2.9 displays the development of the phenomenon and possible branches at later stages. Initially, the droplet approaches the liquid film under a free-fall motion. Prior to impact, the gas layer is pushed outwards until the droplet contacts the liquid surface. At this moment, the liquid-gas interface ruptures, leading to the merge of these structures and allowing the fluid to flow from the droplet onto the liquid film. From this point onward, there are two possible outcomes. If the droplet fully merges with the liquid film, full/complete coalescence occurs. However, if a secondary droplet is formed as a consequence of the initial merging, then this phenomenon is defined as partial coalescence. These regimes can be quantified as a function of the Ohnesorge number. According to Aryafar and Kavehpour [65], for $Oh > 1$, complete coalescence occurs, as no secondary droplets are formed during this process, whereas for $Oh < 1$, partial coalescence is predominant. For the latter regime, the authors studied the ratio of the secondary to the primary droplet radius as a function of the Ohnesorge number. For $Oh \ll 1$, the droplet ratio is rather independent of the Ohnesorge number. However, when approaching the transition boundary, $Oh \to 1^-$, the droplet ratio reduces significantly.

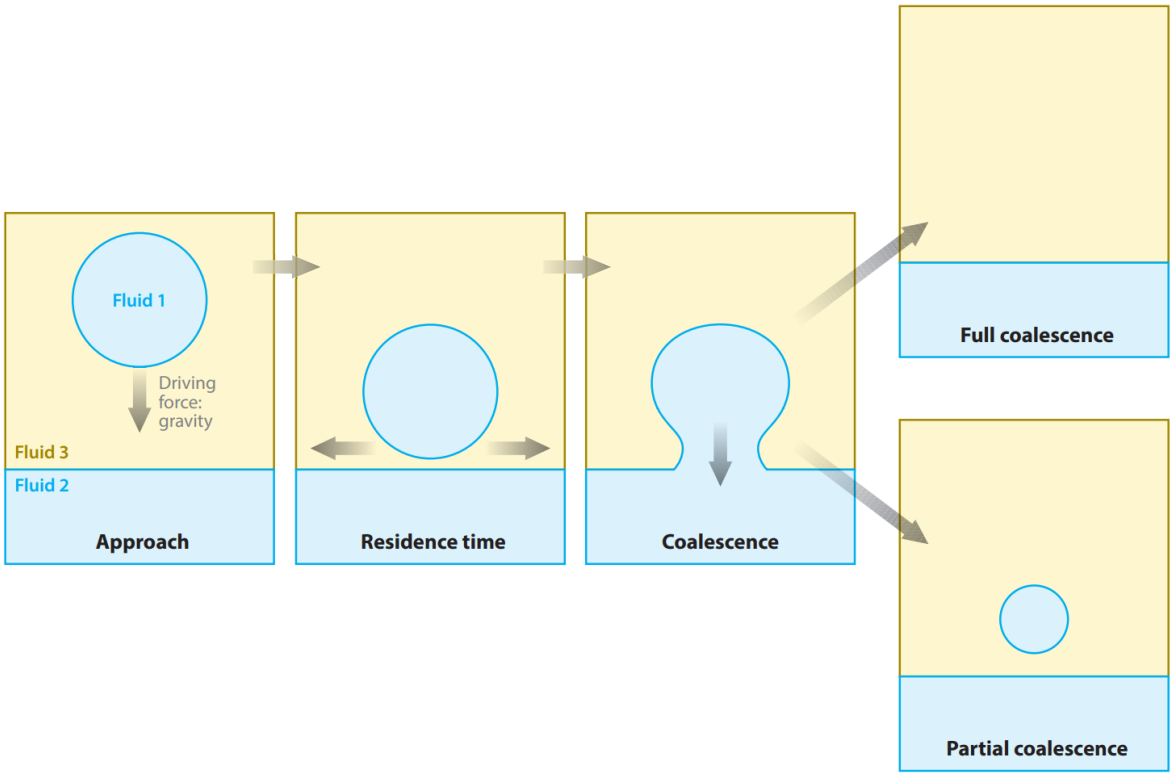

Figure 2.9: Different stages of complete and partial coalescence. Adapted from Kavehpour [66].

Different interactions have also been considered as a factor in the coalescence process, including the marangoni effect, which is described by surface tension gradients due to different fluids [64]. This would include water droplets impinging onto oil surfaces, a phenomena typically researched in fire suppression [67]. External electric fields are also a factor that may

induce disturbances in coalescence, as deeply reviewed by Eon et al. [68].

2.4.3 Rebound

In the presence of extremely thin liquid films, the impacting droplet may avoid coalescence in its entirety [69]. In these cases, the droplet experiences a phenomenon denominated as rebound, which consists of the droplet bouncing on the surface until its kinetic energy dissipates, leading to spreading and, posteriorly, merging with the liquid film. This phenomenon is commonly encountered on dry surfaces, especially superhydrophobic [70]. According to Rioboo et al. [71], this phenomenon can be divided into partial and complete rebound. The former indicates that part of the droplet remains at the surface, whereas for the latter, the droplet fully detaches from it, as displayed by figure 2.10. Despite its predominance on dry surfaces, these outcomes can be reproduced onto thin liquid films, including spreading and coalescence [72].

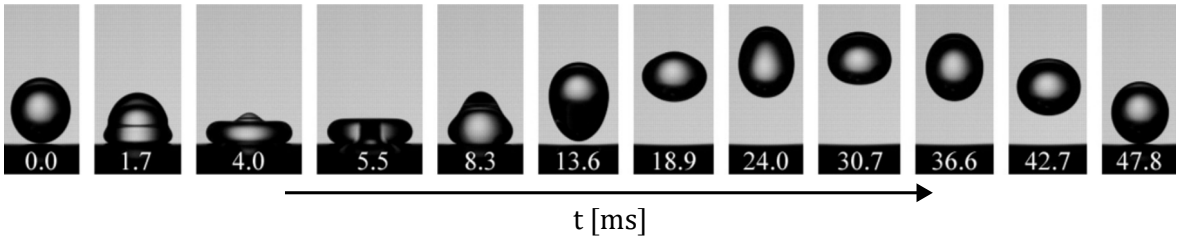

Figure 2.10: Complete rebound of a butanol droplet on a liquid film ($0.028 < h^* < 0.048$ and $We = 4$). Adapted from Liang et al. [69].

2.4.4 Jetting

Subsequent to the crater maximum expansion and the development of the impact phenomena, a retraction period occurs. This retraction will lead to the collapse of the crater, creating an upward jet. Figure 2.11 displays the rising of a central jet at later stages which, due to the thinning of the liquid ligaments, may lead to the formation of secondary droplets. These central jets, also denominated as Rayleigh jets, are dependent on the balance between inertial, viscous and surface tension forces. Specific dynamics of the central jet include pinch-off [73], which can be followed by secondary atomisation. The location of the pinch-off is affected by different sphere accelerations, in which the position tends to shift from lower to higher for increasing acceleration values [74].

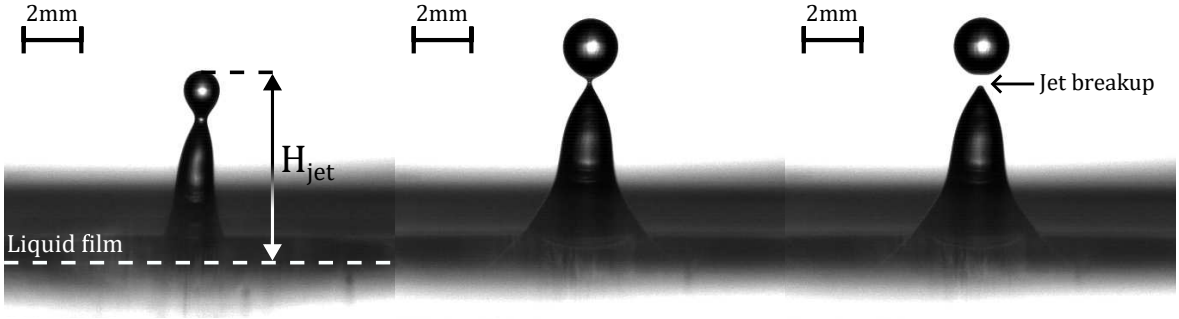

Figure 2.11: Representation of the central jet height and posterior breakup.

Castillo et al. [75] developed regime maps for three different regimes, consisting of the formation of central jets, with or without possible breakup, and crown splash subsequent to the droplet impact onto deep pools. Despite the disparity between thin liquid films and deep pools, the work performed by Castillo et al. [75] clarifies the influence of the liquid properties on the instabilities leading to jet breakup and secondary atomisation. According to figure 2.12, the transition boundaries separate the different regimes, which are defined by both experimental and numerical data. The Weber and Reynolds regime maps display the importance of the inertia on the impact outcome, as these are both dependent on the impact velocity. An increase in this parameter leads to an evolution to the upper-right region of the map, which is consistent with the transition from no breakup to central jet breakup and, posteriorly, crown splash. The regime map for the Ohnesorge number, however, displays a distinct behaviour. For $Oh < 0.091$, an increase in the Ohnesorge number requires a higher critical Weber number, We_c, for breakup to occur, in which secondary droplets ranging from $0.5D_d$ to $2D_d$ may form. As stated in the literature, high viscosity on liquid jets reduces the kinetic energy [76]. In other words, the growth rate of the Rayleigh-Plateau instabilities is dampened for increasing values of viscosity. This effect can be identified in figure 2.12, as the Rayleigh jet breakup region shortens until reaching $Oh = 0.091$. From that point forward, the jet breakup is suppressed regardless of the Weber number, meaning that the droplet impact phenomena develop from no breakup directly to crown splashing. Manzello and Yang [77] studied the impact of water droplets onto liquid surfaces, namely water and HFE7100. The experimental conditions range from $We = 5.5$ to $We = 206$, and from $h^* = 0.6$ to $h^* = 8.1$. Higher impact velocities lead to an increase in the central jet height. In terms of the experimental observations, no jet breakup was verified for the lower liquid film thicknesses, $h^* = 0.6$ and $h^* = 1.3$. However, for deep pools and above the critical Weber number, the outcome transitions from no jet formation/breakup to jet breakup, meaning that higher liquid film thicknesses promote the occurrence of jet breakup. The central jet height was measured as a function of the liquid film thickness for $We = 123$ and $We = 203$. For $h^* < 2.3$, an increase in the liquid film thicknesses generates higher central jet heights. However, increasing the liquid film thickness beyond this value leads to a reduction in the maximum jet height, which is more significant for $We = 206$. Ma et al. [78] considered both experimental and numerical analysis for correlating the Weber number with geometrical parameters of the impact phenomena, such as crater, central jet and secondary atomisation. The central jet formation is delayed for higher Weber numbers, which is associated with longer crater expansion times. The maximum central jet heights prior and subsequent to the pinch-off increase linearly with the Weber number, despite displaying lower determination coefficients for higher Weber numbers. The correspondent times for these heights are strongly correlated with the dimensionless parameter.

The fluid viscosity also exhibits a role in the jet evolution. Michon et al. [79] investigated the jet formation due to cavity retraction. For $Fr < 60$, no jet emerges from the impact region. An increase in the droplet velocity ($Fr > 60$) prompts the formation of the central jet. For $Fr \in [90, 210]$, the jet ejection velocity increases significantly, achieving velocities 3.5 to 4 times higher than the droplet impact velocity. This regime is also characterised by sec-

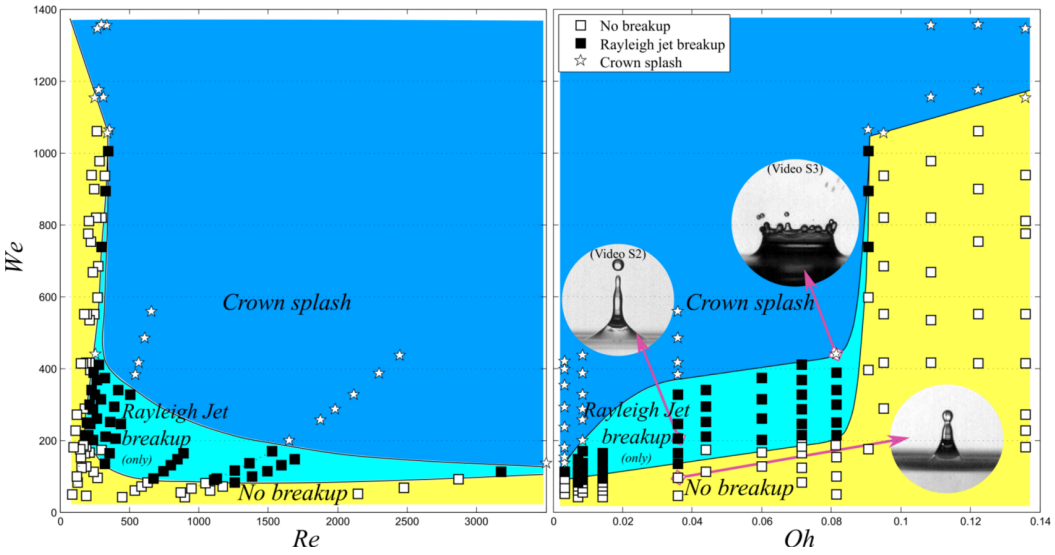

Figure 2.12: Regime maps for central jet formation, with or without breakup, and crown splash as a function of the Weber, Reynolds and Ohnesorge numbers [75].

ondary droplets considerably small, reaching values as low as one tenth of the initial droplet diameter. For higher Froude numbers, $Fr \in [210, 1000]$, the jet ejection velocity decreases drastically, whereas the secondary droplets increase in size. The central jet grows faster with the increase of the liquid viscosity up to $\mu_l = 6\,\mathrm{mPa\,s}$, which is contrary to the popular belief that an increase in viscosity leads to dissipation and underdevelopment of the velocity fields. This is due to the dampening of small capillary waves present in the liquid-gas interface, which smooths the cavity collapse and leads to faster and thinner jets that emerge from the impact region. These results were also verified by Ghabache et al. [80]. For $\mu_l > 6\,\mathrm{mPa\,s}$, the jet velocity decreases up to $\mu_l = 15\,\mathrm{mPa\,s}$. At this high viscosity region, bubble entrapment and high-speed jets are suppressed and, for $Fr > 300$, the jet emerging velocity is independent of the liquid viscosity.

2.4.5 Crown Formation

One of the most common occurrences in droplets impacting onto liquid films is the development of a crown-like structure, such as the well known Edgerton crown [28]. The formation of a liquid crown can be explained by Yarin and Weiss [45]. According to the authors, due to the liquid layer covering the surface, a kinematic discontinuity in the velocity and liquid film distributions emerges subsequent to the droplet impact, displaying characteristics of a shock wave that propagates in an incompressible fluid. Therefore, the liquid droplet impinges a static liquid film, which must be redirected from a downwards to a radial to an upwards direction, promoting the formation of the crown. The emergence of the liquid sheet corresponds to the mass sink of the discontinuity. This governing mechanism has been approved by the scientific community for the development of a crown and is represented by figure 2.13.

The anatomy of the crown/splash was evaluated by several authors. Geppert et al. [82] con-

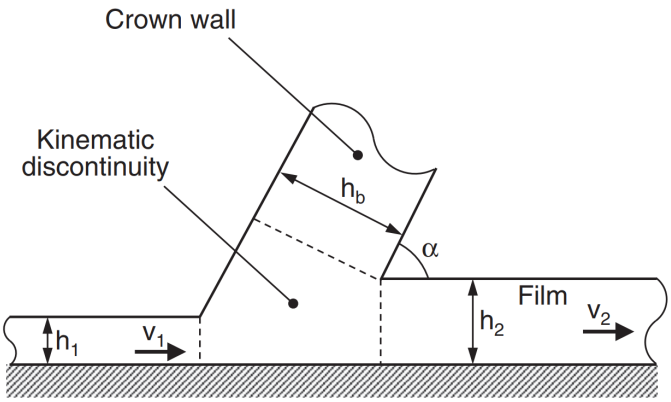

Figure 2.13: Visual representation of the kinematic discontinuity leading to the crown wall formation subsequent to droplet impact [5, 81].

sidered both similar and dissimilar fluids for crown classification and splashing boundaries. The impact map regime for similar fluids follows a standard approach, in which a well-defined transition region separates deposition from splashing. The crowns are relatively similar for the studied range, displaying bubble and jet formation for increasing values of Weber and liquid film thickness. However, the developing crowns for dissimilar fluids are fundamentally different. For the no-splashing regime, the crown exhibits a v-shape for lower liquid film thicknesses and a cylindrical shape for thicker liquid films. New phenomena arise for splashing crowns, consisting in crown bottom breakdown and hole formation. These are exclusively visualised for very thin liquid films ($h^* < 0.1$), as the crown walls are extremely thin, leading to the breakup of the liquid ligaments that constitute the crown. Gao and Li [83] studied the influence of flowing films on the crown sheet. For static liquid films, the crown expands similarly across all directions, displaying fingers that eventually lead to secondary atomisation. For flowing liquid films, however, the crown is asymmetric. The crown expanding in the film flow direction is relatively smooth, exhibiting a stable crown rim with no finger formation. On the opposite side, the crown displays irregularities such as fingers and secondary atomisation, as well as the variation of the crown height as a consequence of these instabilities. Liang et al. [84] numerically studied the influence of the density and viscosity ratios, $\rho^* = \rho_l/\rho_g$ and $\mu^* = \mu_l/\mu_g$, on the crown formation, respectively. Decreasing the density ratio causes the crown to bend from an out to an inward position, therefore clearly altering its shape. Despite this, the splashing phenomenon is not affected by the differences in curvature. In terms of viscosity, lower ratios delay the crown from expanding, eventually inhibiting its formation. In this case, the splashing phenomenon can be suppressed. Similarly to Geppert et al. [82], Lu et al. [85] used laser-induced fluorescence methods to visualise the crown breakup processes for ethanol droplets and glycerol aqueous solution liquid films. Three different regimes were identified, which include splash breaking, hole breaking, and mixed breaking. These occur for increasing Weber numbers, meaning that, over the critical Weber number, splashed breaking occurs, followed by hole breaking and, lastly, mixed breaking. Higher viscosities delay the occurrence of these phenomena.

The overall crown formation can be defined by several geometrical parameters, such as the

crown height, radius, thickness, angle, and crater beneath the crown. The following sections will thoroughly detail these properties, as well as influencing parameters.

2.4.5.1 Diameter and Height

Figure 2.14 displays how the height, H_{cr}, and outer diameter, D_{out} of a crown are measured. The crown height is defined as the vertical distance from the liquid film surface (represented by the dashed line) to the base of the crown rim. The crown outer diameter is described as the horizontal distance between two opposite sides of the crown rim.

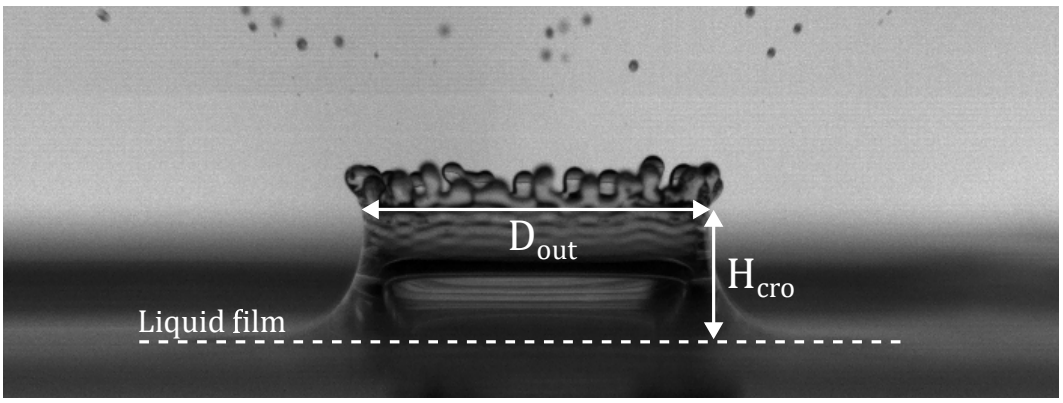

Figure 2.14: Representation of the crown height and outer diameter of a developing crown.

The crown diameter has been investigated by several authors, both theoretically and experimentally. Yarin and Weiss [45] theoretically predicted the dependency of the crown diameter with the square root of time, as displayed by the following equation, $D^*_{cr} = C\left(\tau - \tau_0\right)^n, n = 1/2$, where C is a constant, $\tau = tU_d/D_d$ is the dimensionless time, and τ_0 is the dimensionless time at the moment of impact. This correlation was applied and adapted by Cossali et al. [86] to account for the experimental data obtained. Results show that the exponent n is independent of both the impact velocity and dimensionless thickness, whereas the constant C increases with the Weber number. Liang et al. [87] showed that the crown diameter increases with lower dimensionless thicknesses, whereas the Weber number does not exhibit a clear influence on the parameter. Mukherjee and Abraham [88] numerically studied the droplet impact phenomenon in an axisymmetric assumption, focusing on the influence of liquid film thickness, density and viscosity ratios in the crown evolution. For $0.1 < h^* < 0.25$, the crown diameter shows a weak positive growth with the liquid film thickness. This tendency shifts for $h^* > 0.25$, meaning that the crown diameter decreases for thicker liquid films. Recent research on crown diameter involves different experimental conditions, such as flowing liquid films [89]. Higher values of impact velocity lead to an increase in both the up and downstream crown radius. However, increasing the liquid film flow rate, which leads to an increase in the liquid film velocity, produces opposite reactions on the crown expansion, which are higher and lower crown radius for downstream and upstream, respectively.

In terms of crown height, similar studies have been performed in comparison to the diameter, as these parameters are generally coupled in the crown formation and evolution. The theoretical work performed by Roisman and Tropea [81] shows a substantial increase in the

crown height for thicker liquid films. However, the experimental data provided by Cossali et al. [86] exhibits a weak dependence of the crown height on the liquid film thickness and a strong dependence on the Weber number. The results are in agreement with Roisman and Tropea [81] for thin liquid films, $h^* = 0.29$, although the theoretical model overestimates the crown height for higher values of h^*. Mukherjee and Abraham [88] performed axisymmetric computations on developing crowns, as previously mentioned. A decrease in the density and viscosity ratios delays the growth of the crown, reaching the maximum height at later stages and eventually leading to lower crown heights. The influence of the liquid film follows an identical approach to the crown diameter, in which, for increasing values of h^*, the crown height increases for $h^* < 0.25$ and decreases for $h^* > 0.25$. Xu et al. [89] studied the water droplet impact onto a burning fuel liquid pool. The maximum crown height is nearly independent of the Weber number, displaying a slight decrease for higher Weber numbers. This is due to the transition from a crown to a bubble formation, altering the impact phenomenon.

2.4.5.2 Crater

The formation of a crater can be observed in figure 2.15. Studies regarding crater formation and evolution have been reviewed by Prosperetti and Oguz [30]. Overall, the crater depth and width are the two geometrical parameters that define the crater evolution and are the focus of most of the experimental work. Berberović et al. [90] analysed the influence of the liquid film thickness, impact velocity and fluids physical properties on the crater shape, as well as the formation and propagation of capillary waves following the droplet impact. The Froude number was not considered due to the negligible effect of the gravitational forces on the initial stage of the crater. For lower liquid film thicknesses, $h^* = 1.0$ and $h^* = 2.0$, the depth of the cavity is constrained by the impact surface. For the crater diameter, an increase in the Weber number and a decrease in the film thickness leads to higher crater diameters. The maximum crater diameters occur for later stages of the phenomena for the Weber number and film thickness variation. The crater depth is also influenced by these parameters, as the maximum depth is achieved faster for lower film thicknesses, and the sudden change of the crater depth occurs at earlier stages for lower Weber numbers. Bisighini et al. [91] studied the impact of a single droplet onto semi-infinite liquid targets, focusing on crater formation. The maximum crater depth and corresponding time increase with the Weber number. The measurement curves for crater width and depth display smoother lines for higher Weber numbers. This is associated with the progression from surface tension dominated flows, which are influenced by the propagation of waves, to higher energy impacts, in which the amplitude of the capillary waves is reduced. The crater width maintains its growth even if it reaches its maximum depth due to liquid film constraints. The authors also mentioned that preceding experimental data displayed scattering results, either due to unclear tendency of the results or to data unreliability, such as experimental errors associated with refraction, liquid interface for determining the impact point, etc. In terms of viscosity, higher Ohnesorge numbers lead to shallower craters (reduction in crater depth) due to the viscous forces overcoming surface tension effects [75].

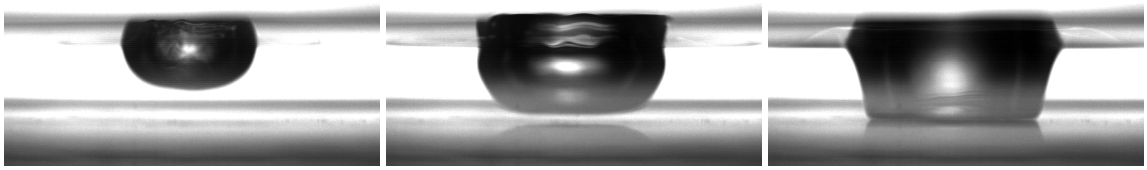

(a) (b) (c)

Figure 2.15: Crater development subsequent to droplet impact: a) $\tau = 2.5$; b) $\tau = 7.5$; c) $\tau = 17.5$.

Theoretical work on crater expansion diversified into different aspects, such as energy conversion [92], analytical solutions for penetration depth [90] and predictions for maximum cavity radius [93]. Overall, developed theoretical models on penetration depth are limited to deep pools, as the constraint of a solid wall on thin liquid films restrains the cavity expansion. These models include partial-sphere geometrical model of the cavity [92] and potential velocity fields [94], which can only be applied if the penetration depth is much smaller than the initial liquid film thickness [94]. In terms of crater diameter, Roisman et al. [95] studied the expansion of the crater based on the propagation of a kinematic discontinuity [45]. The velocity of the propagation is calculated based on a modified quasistationary Bernoulli equation [81] to account for surface tension and average pressure drop. The derivation of the Bernoulli equation neglects pressure drop due to viscous dissipation, as it solely influences the thickness of the boundary layer. The derived equation is an ordinary differential equation for the propagation of the crater radius. An asymptotic solution can be described for $We \ggg 1$ and $Fr \ggg 1$, in which the previous gravitational and surface tension terms are relevant exclusively for later stages of the crown propagation. Therefore, the crater radius, R_{cra}, and correspondent crater time, t_{cra}, can be defined by equations (2.9) and (2.10), respectively:

$$R_{cra} = \sqrt{\beta_{cra} t_{cra} - \left(\frac{2h^*}{R_{cra\ max} We} + \frac{4}{We} + \frac{h^{*2}}{Fr} \right) \frac{t_{cra}^2}{h^*}} \tag{2.9}$$

$$t_{cra} = t - \tau_{cra} \tag{2.10}$$

where β_{cra} and τ_{cra} are constants. The maximum crater radius, $R_{cra\ max}$, corresponds to the instant at which the radius reaches its maximum propagation radius and is represented by equation (2.11):

$$R_{cra\ max} = \frac{\beta_{cra}\sqrt{h^*}}{2\sqrt{G_{cra}}} - \frac{h^*}{G_{cra} We} \tag{2.11}$$

where G is a theoretical crater parameter expressed by equation (2.12). The theoretical parameters τ_{cra} and β_{cra} were fitted to the obtained experimental data as a function of the dimensionless liquid film thickness. These parameters are characterised by equations (2.13)

and (2.14), respectively.

$$G_{cra} = \frac{4}{We} + \frac{h^{*^2}}{Fr} \tag{2.12}$$

$$\tau_{cra} = 0.8h^{*^{1.7}} \text{ for } 0.5 < h^* < 2 \tag{2.13}$$

$$\beta_{cra} = 0.62h^{*^{-0.33}} \text{ for } 0.5 < h^* < 2 \tag{2.14}$$

2.4.5.3 Angle and Thickness

The crown angle and thickness are not as extensively researched as the previous parameters, as research until this point is mostly focused on splashing mechanisms, crown formation and outcome development. For the case of crown thickness, several difficulties arise regarding experimental conditions, such as obtaining optical access for thickness measurements.

The crown angle, α_c, is defined between the liquid film surface and the outer crown wall, as represented by figure 2.16. Fedorchenko and Wang [96] provided experimental observations for impacting droplets onto liquid layers. Evidence shows that the crown angle is independent of the liquid film thickness for $h^* > 0.25$, exhibiting crown walls normal to the liquid film, $\alpha_c = 90°$. For $h^* < 0.25$, in comparison to the previous regime, the crown displays lower angles, $\alpha_c < 90°$, as it expands radially and upwards. The angle monotonically decreases for lower values of liquid film thickness, as displayed by the following equation, $\cos\alpha = 1 - 4h^*$. This was also verified by other authors [97, 98], as thin films display shallow crowns that develop outwards (acute angles), smoothly increasing with h^*. Ribeiro et al. [99] researched the influence of the liquid film thickness on the bubble encapsulation phenomenon, which will be introduced in section 2.4.7. The crown sheet angle is normal to the liquid film for $h^* = 0.4 - 1.0$. For $h^* < 0.4$, the crown presents difficulties in closing to form a bubble due to lower inertia in the rising sheet and lower crown angles.

The crown thickness, t_c, varies as the crown expands, typically displaying thicker areas adjacent to the base of the crown and gradually decreasing until reaching the crown rim. A representation of the local crown thickness is displayed in figure 2.16. Cossali et al. [86] defined a nominal thickness consisting of the differences between the outer and the inner diameters of the crown. No correlation was provided between the liquid film and crown thickness, as the fluctuation measurements could have originated from the nominal thickness assumption. However, it is possible to identify that the crown thickness increases significantly over time. Che and Matar [100] concluded that the crown thickness is dependent on the liquid film thickness, where thicker liquid films lead to an increase in the crown thickness. This can be explained by the differences in fluid volume in the impact region, as the crown fluid origi-

nates from both the droplet and the liquid film. This was also verified by Ribeiro et al. [101]. Viscosity also plays a role in the crown thickness and stability, in which irregular crowns with finger formation and secondary atomisation are associated with low viscosity, whereas high viscosity regimes display smooth crown walls [56]. Burzynski and Bansmer [102] experimentally investigated the influence of flowing liquid films on the crown thickness. Increasing the film velocity produces additional capillary waves, which propagate to the expanding crown.

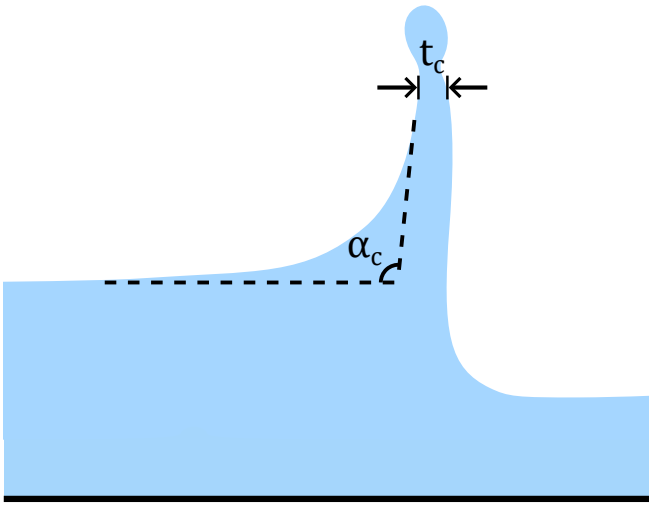

Figure 2.16: Representation of the crown outer angle and thickness of a developing crown.

2.4.6 Splashing

Low energy impacts involving single and multiple droplets usually develop into spreading, rebound and coalescence, as previously mentioned. These outcomes are characterised by simple topological structures, as the main droplet retains its initial shape until merging with the solid substrate or liquid film, smoothly advancing and consequently reaching stabilisation. An increase in the system entropy through means of increasing kinetic and thermal effects leads to more complex topology changes, such as splashing. This phenomenon is defined by the detachment of secondary atomisation, which is considerably smaller than the impacting droplet from the crown rim. The main mechanism for the production of secondary droplets is the Rayleigh-Plateau capillary instability [103,104]. This instability is also related to the Rayleigh-Taylor instability, which consists of the interaction between fluids of different densities, where the lighter fluid pushes the heavier fluid [105, 106]. As displayed by figure 2.17, initially, a liquid jet with a constant radius is falling through gravity. For increasing lengths, the jet is susceptible to small perturbations, causing the liquid jet to enter an oscillating state. In unstable systems, these external disturbances will exponentially increase, leading to higher curvatures of the liquid-gas interface. Consequently, the jet reaches a critical state and breaks into small secondary droplets [107].

The mechanisms of liquid jet breakup from the crown rim are predominantly Rayleigh-Plateau instabilities. However, if the formation of the crown does not involve secondary atomisation, such as during the early stages of the crown formation or fluids with high surface tension, the Rayleigh-Taylor capillary instabilities occur [108]. In order to comprehend splash-

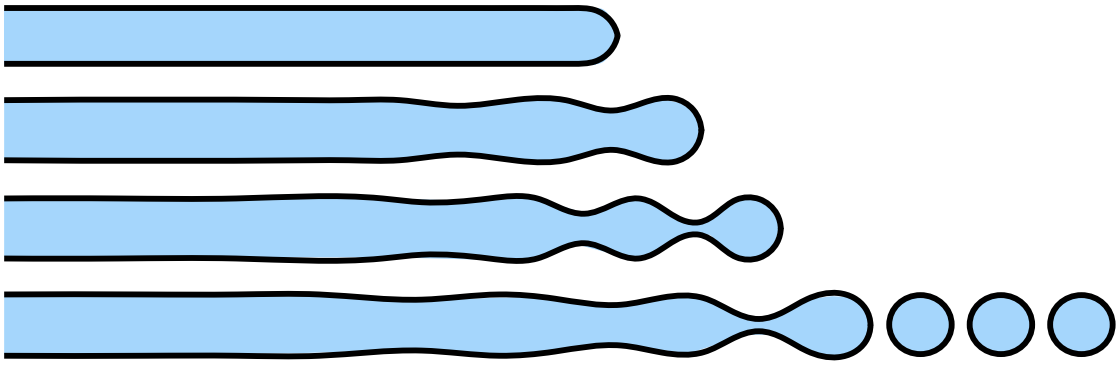

Figure 2.17: Development of the Rayleigh-Plateau capillary instability on liquid jets.

ing in two-phase flows and, more specifically, in droplet impact phenomena, one must distinguish the different sources of secondary atomisation. Cossali et al. [55] identified two splashing mechanisms based on the Ohnesorge number: prompt and delayed/crown splash. The prompt splashing is associated with low viscosity values and refers to the release of secondary droplets at the early stages of the outcome, $t << D_d/U_d$. At this stage, the crown is under development, and the secondary droplets originate from the breaking ejecta sheet. At later stages, when the crown fully develops and reaches its maximum height, the secondary droplets are released from the crown rim. This event is denominated as crown splashing. In comparison, secondary droplets from this stage are considerably larger than the secondary droplets that originated from prompt splashing. The formation of secondary atomisation due to prompt and crown splashing can be visualised in figures 2.18 and 2.19, respectively.

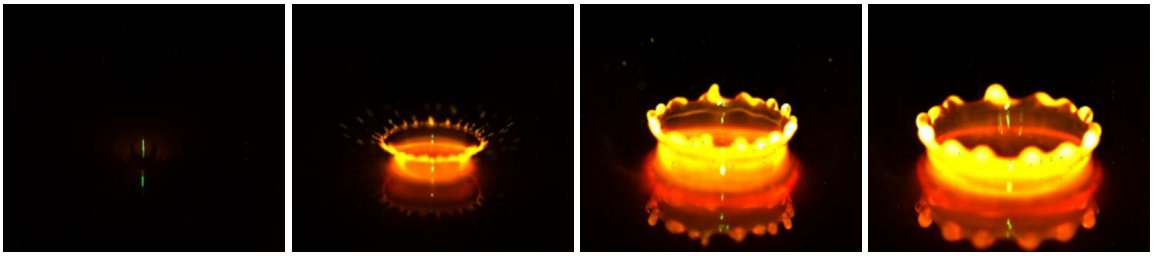

(a) (b) (c) (d)

Figure 2.18: Occurrence of prompt splash at earlier stages of the impact [109]: a) $t = 0$ s; b) $t = 1.67$ s; c) $t = 4.81$ s; d) $t = 11.3$ s.

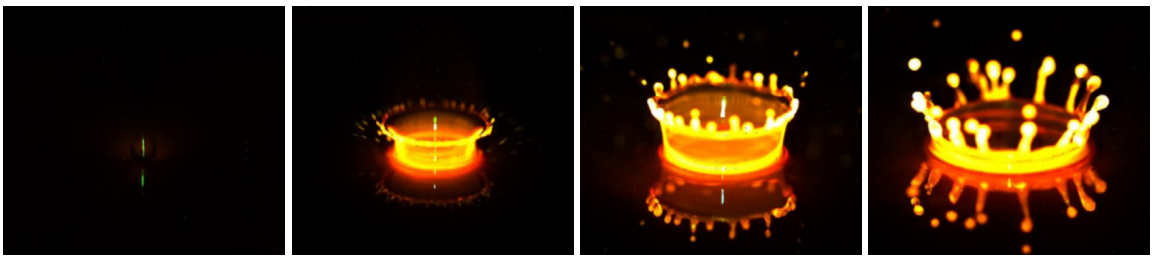

(a) (b) (c) (d)

Figure 2.19: Occurrence of crown splash at later stages of the impact [109]: a) $t = 0$ s; b) $t = 1.67$ s; c) $t = 4.81$ s; d) $t = 11.3$ s.

Extensive research has been performed regarding influencing parameters on the splashing phenomena. Vander et al. [56] studied impacting droplets onto liquid films of variable

thickness considering different fluids such as water, n-heptane and methanol. Splashing is strongly dependent on the liquid film thickness, displaying occurrences for the lower thicknesses, $h^* = 0.1$. Increasing the impact velocity would exhibit splashing for the higher liquid film thicknesses. Viscosity has an opposite effect for dry and liquid film surfaces, promoting splashing on the dry surface and inhibiting it on wetted surfaces. For liquid films, an increase in viscosity delays the splashing effects, as well as decreasing the number of splashing droplets and increasing their mean size. Surface tension also indicates a similar behaviour in terms of the number and size of secondary droplets. Higher values of surface tension suppress the splashing phenomenon, regardless of the impacting surface. Vander et al. [110] also researched the influence of roughness on dry and thin film surfaces, which is a significant parameter, as previously stated [53]. Rougher surfaces lower the splashing threshold and affect the splashing dynamics. The differences between thermophysical properties of the different fluids are insignificant in comparison with the surface roughness on the outcome. Wang and Chen [57] studied droplet impact onto extremely thin liquid films ($h^* < 0.1$) of aqueous solutions of glycerol. Results show that the critical Weber number for the onset of splashing is independent of the liquid film thickness. Higher viscosity fluids increase the value of the critical Weber number. The splashing characteristics of the thin and thick liquid films are distinct. For $h^* < 0.1$, the developing crown shatters at early stages of the impact due to the very thin crown walls. This breakup is distinct from thick crowns, as it initiates on the crown base as opposed to the regular crown rim. Motzkus et al. [111] studied the number and size of secondary droplets as a function of the impact velocity and liquid film thickness. Higher Weber numbers increase the number of emitted secondary droplets. Splashing was not verified for $We = 159$, meaning that the experimental conditions are below the critical Weber number. The liquid film thickness variation has no visible influence on the phenomenon for $We = 281$ and $We = 549$. However, when considering a higher Weber number, $We = 808$, the number of emitted droplets increases for lower liquid film thicknesses.

In order to comprehend the role of each of these properties on the mechanisms of splashing, several authors investigated the conditions required for splashing to occur. A splashing threshold parameter, K, was defined to account for the different variables that characterise the phenomena. Table 2.2 displays the splashing correlations proposed by several authors for isothermal single droplet impact onto liquid films. Yarin and Weiss [45] quantitatively studied the splashing phenomenon, taking into account the thermophysical properties of the fluid (density, viscosity and surface tension), the droplet diameter and impact velocity, frequency, surface roughness, temperature and sound velocity. The authors characterised the threshold in terms of the Capillary number in the form of $Ca = C\lambda^{-3/4}$, where $\lambda = (\nu/f)^{1/2}\,\sigma/\left(\rho\nu^2\right)$ is the viscosity length, ν is the kinematic viscosity, and f is the frequency of the droplet train. This is equivalent to the correlation in table 2.2, which is based on the Weber and Ohnesorge numbers (for direct comparison with the remaining authors). Cossali et al. [55] developed an empirical correlation as a function of the liquid film thickness and surface roughness. Distinct from Yarin and Weiss [45], the splashing threshold parameter varies with the liquid film thickness, requiring more impact energy for splashing to occur on thicker liquid films. The different combination of dimensionless numbers has been considered for a wide range

Table 2.2: Review of the existing correlations for non-splash/splash thresholds for single droplet impact onto a liquid film.

Author(s)	**Fluids**	**Experimental Conditions**	**Correlation(s)**
Yarin and Weiss [45]	Ethanol, ethanol-glycerol-water mixtures	$U_d < 30$ m/s $D_d = 70 - 340$ µm	$K = WeOh^{-0.4} = 2400$
Mundo et al. [112]	Water-ethanol-sucrose	$We = 94 - 2204$ $Re = 195 - 2694$	$K = OhRe^{1.25} = 57.7$
Cossali et al. [55]	Water, water-glycerol mixtures	$We = 200 - 1600$ $Oh = 2.2 \times 10^{-3} - 1.41 \times 10^{-1}$ $h^* = 0.08 - 1.2$	$K = WeOh^{-0.4} = 2100 + 5880h^{*1.44}$
Han et al. [54]	Water, water-glycerol mixtures	$We = 200 - 1600$ $Oh = 2.2 \times 10^{-3} - 1.41 \times 10^{-1}$ $h^* = 0.08 - 1.2$	$K = \left(1500 + \frac{650}{R_a^{0.42}}\right)\left[1 + 0.1Re_n^{0.5}\ \min(\delta, 0.5)\right]$
Rioboo et al. [113]	Glycerol-water, Hexadecane, $PDMS_5$, $PDMS_{10}$	$We = 41 - 890$ $Oh = 1.14 \times 10^{-2} - 5.48 \times 10^{-2}$ $h^* = 7 \times 10^{-3} - 0.19$	$K = WeOh^{-0.4} = 2100$
Okawa et al. [114]	Water	$We = 2.5 - 980$ $Oh = 1.5 \times 10^{-3} - 8.4 \times 10^{-3}$ $h^* = 0.43 - 68$	$K = WeOh^{-0.4} = 2100$
Vander Wal et al. [115]	Water, 30% glycerol/water, heptane, decane, hexadecane, methanol, butanol, n-propanol	$We = 127 - 1200$ $Re = 988 - 1.39 \times 10^4$ $Oh = 2.49 \times 10^{-3} - 6.51 \times 10^{-2}$ $h^* = 0.1 - 10$	$K = OhRe^{1.17} = 63$
Huang and Zhang [116]	Water, oil	$log(We) = 0.3 - 3.4$ $log(Re) = 1.5 - 3.9$ $h^* = 0.3 - 1.3$	$K = (WeRe)^{0.25} = 25 + 78^{1.44}$
Gao and Li [83]	Water, water-glycerin mixtures	$D_d = 2.6 - 4.6$ mm $U_d = 0.63 - 4.2$ m/s $h^*U_f^* = 0.05 - 0.18$	$K = WeRe^{0.5}\left(1 + \bar{h}_f\bar{U}_f^2\right)\left(1 + \bar{h}_f\bar{U}_f\right)^{1/2} = 3378$
Okawa et al. [117]	Water, water-glycerol and water-ethanol mixtures	$We = 185 - 2040$ $Oh = 1.92 \times 10^{-3} - 3.75 \times 10^{-2}$ $h^* = 0.2 - 3.3$	$K_{early} = WeOh^{-0.581} = 8123$ $K_{late,thin} = WeOh^{-0.359} = 5195h^{*0.5}$ $K_{late,thick} = We = 1138$
Zhu et al. [118]	Distilled water	$D_d = 1.95$ mm $U_d = 2.3 - 4.5$ m/s $h^* = 0.08 - 0.18$	$K = WeOh^{-0.4} = 1880 + 156122h^{*2.017}$

of experimental conditions. The splashing threshold is mostly presented as a product of the Weber and Ohnesorge numbers, $K = WeOh^{-0.4}$ [113, 114]. Mundo et al. [112] and Vander Wal et al. [115] display the correlation in a different form, which is based on the Reynolds and Ohnesorge numbers. Han et al. [54] improved the correlation of Cossali et al. [55], proposing an alternative to reduce the effect of liquid film thickness.

Most recently, the splashing thresholds have been adapted to account for distinct dynamics of the impact phenomena. Gao and Li [83] investigated this topic for flowing films, in which the splashing threshold is also dependent on the liquid film average thickness and velocity. An increase in these parameters leads to a lower threshold, thereby inducing splashing at lower values of the Weber and Reynolds numbers. Okawa et al. [117] categorised the prompt and crown splashing mechanisms into two separate thresholds, distinguishing the early and late splashing stages accordingly. In terms of prompt splashing, the threshold is displayed as a function of the Weber and Ohnesorge numbers and is independent of the liquid film thickness. For the crown splash and thick liquid films, the threshold is independent of both the Ohnesorge number and liquid film thickness, meaning that it can be solely defined by the Weber number. Thinner liquid films follow a similar tendency to Cossali et al. [55]. Zhu et al. [118] follow an analogous approach, presenting a boundary between prompt and crown splashing. In comparison with the work presented by previous authors, which was focused on non-splash/splash boundaries, this particular threshold displays higher boundary values, which is expected due to both lower and upper regimes being characterised by splashing phenomena.

2.4.7 Bubble Encapsulation

This phenomenon was initially captured by Worthington [27]. It occurs when, following the droplet impact, the expanding crown tends inwards and eventually forms a closed structure similar to a bubble dome, trapping the gas phase, as displayed by figure 2.20. The impact conditions required to prompt bubble encapsulation usually involve high velocity impacts, ranging from $U_d = 10\ \mathrm{m/s}$ to $U_d = 20\ \mathrm{m/s}$ according to several authors [119–121]. Most recently, Ribeiro et al. [99, 122] investigated the mechanisms of bubble encapsulation, defining a criterion for the onset of this phenomenon. The correlation proposed by Vander Wal et al. [115] provided the best agreement for the experimental data. The authors adapted this criterion to account for the influence of the Ohnesorge number and liquid film thickness. Opposite to the standard non-splash/splash boundaries, in which values below a certain threshold lead to deposition, and above to splashing, the occurrence of bubbling is confined between two limiting boundaries. Therefore, considering the Ohnesorge number in the transition boundary of Vander Wal et al. [115], $K = Re_d Oh_d^{0.8547} = 34.5$, the criterion for the onset of bubble encapsulation is $K_{be} = ln(34.5/Re_d)/ln(Oh_f), K_{be} = 1.022 - 1.142$. This domain is valid for liquid film thicknesses of $h^* = 0.4 - 1$.

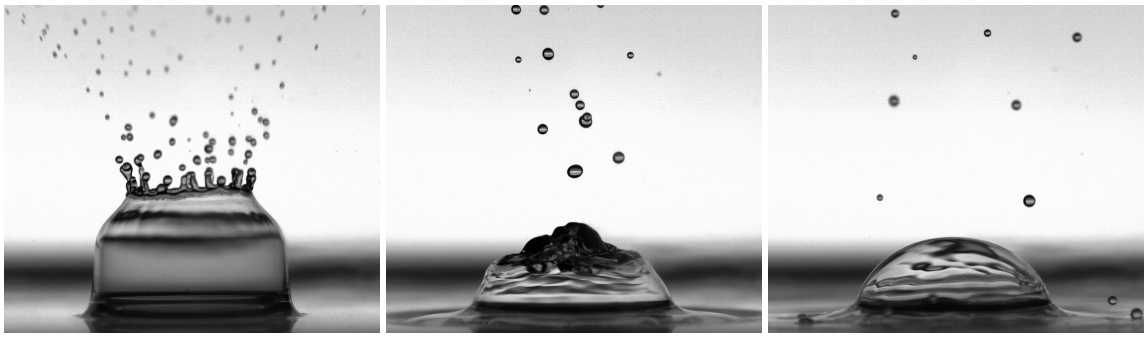

(a) (b) (c)

Figure 2.20: Bubble encapsulation phenomenon subsequent to the impact of a 75% jet fuel/25% HVO droplet onto a liquid film ($D_d = 3.0$ mm, $U_d = 4.2$ m/s, $h^* = 0.5$) [99]: a) $\tau = 14$; b) $\tau = 56$; c) $\tau = 175$.

2.5 Heat and Mass Transfer Phenomena

Most modern industrial applications involve thermal effects in terms of heat flux and phase change, which include heat exchangers, heat pipes, electronic cooling devices and internal combustion engines. Coupling these phenomena with the underlying dynamics of multi-phase flows exponentiates the number of variables present in the system, leading to extremely complex phenomena. These range from evaporation and boiling at lower temperatures to Leidenfrost effects for higher temperature regimes. If the experimental conditions reach a critical temperature, the droplets may enter an auto-ignition state, leading to the combustion of the droplet. Due to this, in order to comprehend the role of temperature on both heat and mass transfer mechanisms, the following subsections will thoroughly detail the impact onto dry heated surfaces and posteriorly correlate with the pre-existence of a liquid film.

2.5.1 Dry Surfaces

Similarly to liquid films, dry surfaces have been comprehensively studied from the droplet impact perspective. The most common phenomena captured on isothermal dry surfaces are bouncing, spreading and splashing [123], which are analogous to the outcome development on liquid films. As previously mentioned, Bernardin et al. [21] stated that both the wall temperature and the Weber number are the main parameters in defining the droplet impact phenomena. In this context, the outcomes can be classified from a heat transfer or a hydrodynamic perspective. In terms of the former, four different regimes can be identified as a function of the wall temperature and droplet evaporation time, which consist of film evaporation ($T < T_{sat}$), nucleate boiling ($T_{sat} < T < T_{\text{CHF}}$), transition boiling ($T_{\text{CHF}} < T < T_L$), and film boiling ($T > T_L$), where T_{sat} is the saturation temperature of the fluid, T_{CHF} is the critical heat flux temperature, and T_L is the Leidenfrost temperature. These regimes were established by several authors, such as Ko and Chung [124], and are displayed in figure 2.21. In order to fully understand the transitions between the different regimes, each temperature range will be evaluated separately and analysed in thermal and hydrodynamic effects.

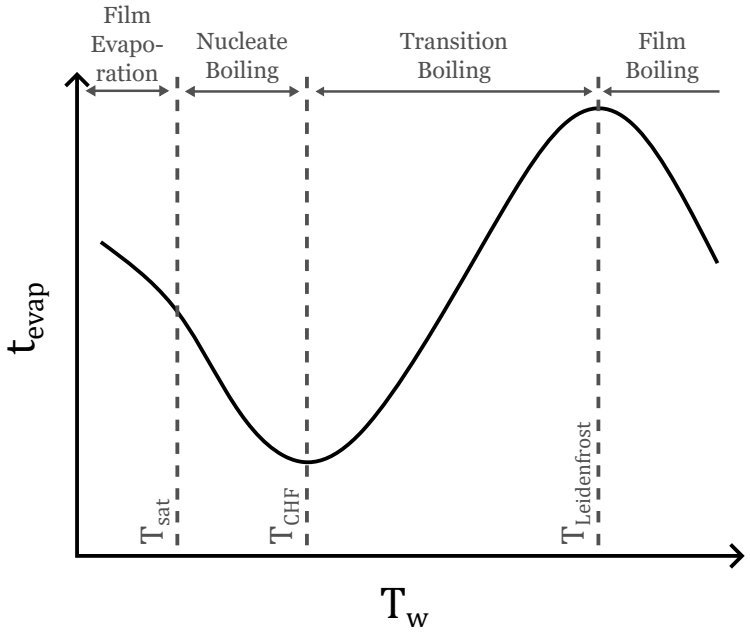

Figure 2.21: Heat transfer regimes of a droplet impacting onto a heated dry surface as a function of the wall temperature (T_w).

2.5.1.1 Film Evaporation

The film evaporation regime is associated with relatively low temperatures, ranging from ambient conditions up to the onset of nucleate boiling, which is near the saturation temperature of the fluid ($T < T_{sat}$). This regime can also occur for $T > T_{sat}$ if the conditions are not suitable for vapour bubble nucleation to develop. As the name suggests, this regime is characterised by a single-phase change mechanism, as the thermal conditions are not sufficient for boiling phenomena to occur. In order to explain the following regimes, clear distinctions between evaporation and boiling must be established, as these are fundamentally distinct. Evaporation is defined as a slow process that does not produce vapour bubbles and occurs at the liquid-gas interface. It is also not restricted to a specific temperature, meaning that, regardless of the local temperature, whether it is closer or further from the boiling point, evaporation occurs. Higher temperatures also promote a higher evaporation flux on the liquid-gas interface. For boiling, this phenomenon only arises when reaching temperatures near the saturation temperature of the fluid. It is a rather violent and quick process due to the nucleation of vapour bubbles. This is also due to the boiling process occurring within the boundaries of the liquid (each control volume with suitable conditions for boiling to emerge), opposite to the liquid-gas interface for evaporation.

Cazabat and Guéna [125] reviewed sessile droplets in atmospheric pressure and inert surfaces. The authors explained in detail the phases of film evaporation, which is mainly divided in three different stages. Initially, the droplet spreads and remains attached to the surface. There are three parameters crucial in defining the development of film evaporation: contact angle, droplet radius and droplet height. Figure 2.22 displays the evolution of the sessile droplet on a solid surface. For the first stage, the contact angle of the droplet will slowly decrease, whereas the droplet radius is pinned, as represented by figure 2.22b. This leads to

a decrease in the droplet height due to the fluid evaporation and a constant droplet radius. When the contact angle reaches a critical value, the sessile droplet is forced to decrease its wetting area, therefore decreasing the droplet radius while maintaining a relatively constant contact angle. This is visualised by figure 2.22c. For the third stage, both the droplet radius and contact angle decrease continuously until reaching the end of the lifetime, which is a combination of the previous stages.

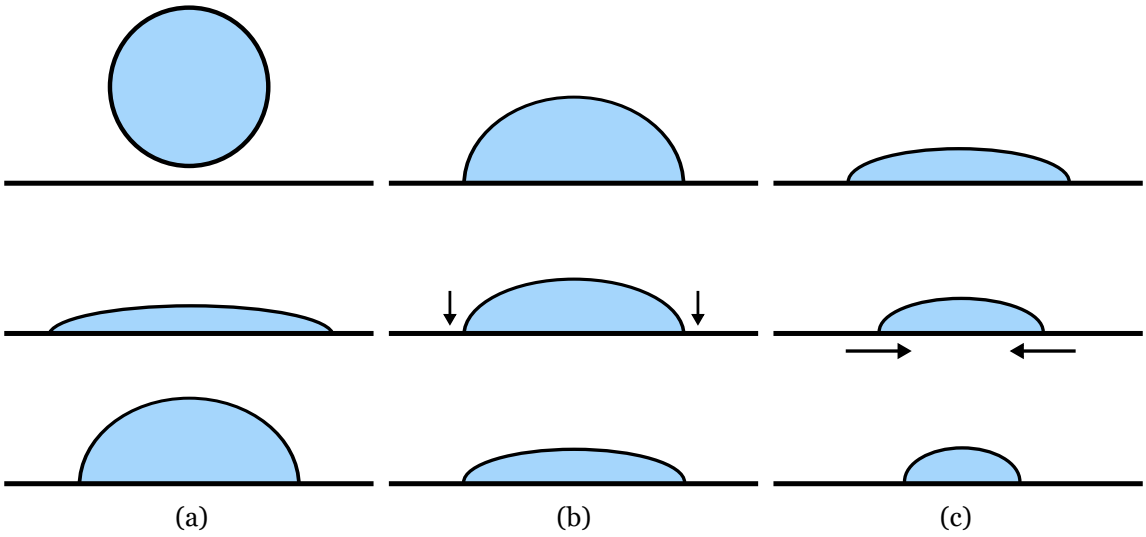

Figure 2.22: Stages of droplet impact and subsequent film evaporation: a) Initial impact; b) Constant wetting area and decreasing droplet height; c) Constant contact angle and decreasing wetting area.

Experimental work performed on this regime focuses on several aspects, such as heat transfer, contact angle and temperature variation, among others. Gleason et al. [126] evaluated the evaporation rate and flux as a function of the substrate temperature and respective contact angles. The analysis consists of both phenomena visualisation and infrared imaging. Results show that an increase in the contact angle leads to higher evaporation rates. However, the evaporation flux exhibits an opposite reaction due to the increase of thermal resistance. The critical contact angle is also dependent on the surface roughness, as most studies with water droplets estimate these angles to be approximately $2° - 4°$ for glass [127], and $5° - 10°$ for stainless steel [127, 128]. It is also worth mentioning that the evaporation stages previously displayed are specific for water droplets, meaning that different fluids, such as fuels (low surface tension fluids), require further research [127, 129]. In terms of evaporation time, the stage of constant wetting area and decreasing droplet height, which is represented by figure 2.22b, accounts for more than half of the total evaporation time [130, 131].

2.5.1.2 Nucleate Boiling

This regime is achieved when the wall temperature reaches a temperature slightly higher than the saturation temperature of the fluid, $T_w > T_{sat}$. When the droplet impinges onto a wall, a small bubble is trapped between the droplet and the substrate, similar to the impact occurrence on liquid films [132]. The difference in temperatures induces a heat flux from the heated wall to the droplet, continuously increasing its temperature. This leads to the phase change of the liquid in form of vapour bubbles, as the fluid approaches its saturation tem-

perature [133]. The phenomenon can be visualised in figure 2.23. The transition from film evaporation to the nucleate boiling regime, as the name suggests, is characterised by the onset of boiling in the contact region between the droplet and the heated wall. From this point onward, increasing the wall temperature leads to higher heat fluxes and reduced evaporation times, which is represented in figure 2.21. This also leads to a more violent phenomenon due to the instability of vapour bubbles, affecting their size and release frequency. This regime is valid until reaching a condition where the evaporation time is minimised, which is associated with the heat flux being maximised. This is defined as the critical heat flux (CHF) temperature.

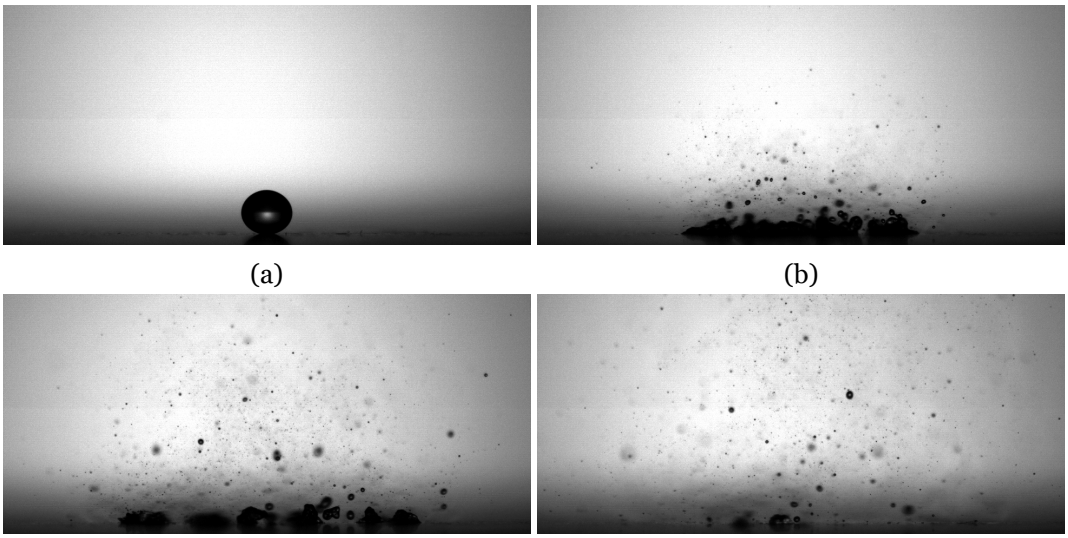

Figure 2.23: Nucleate boiling regime of an n-heptane droplet impinging onto a heated dry graphite surface ($T_{he} = 150^{\circ}\mathrm{C}$) a) $t = 0$ ms; b) $t = 15$ ms; c) $t = 30$ ms; d) $t = 60$ ms.

In terms of secondary atomisation, Cossali et al. [134] researched the effect of surface roughness and viscosity for moderate Weber numbers. For the impact morphology, this regime is characterised by the large production of secondary droplets with reduced size, which are released in a direction normal to the heated wall. This is opposed to conditions above the critical heat flux temperature, which will be detailed in the following sections. The surface roughness and viscosity display a weak dependence on the nucleate boiling regime, slightly altering its morphology and mean drop diameters. This effect is more noticeable for temperature regimes above the CHF point. Moita and Moreira [135] investigated the morphology disintegration of water and fuel droplets on heated surfaces with variable wettability and topography, as well as a wide range of Weber, Reynolds and Ohnesorge numbers. At isothermal conditions, the surface topography and wettability are a main factor in the impact dynamics. For the nucleate boiling regime, rough surfaces enhance boiling and bubble explosion, as these occur in earlier stages in comparison to smooth substrates. Consequently, this also leads to larger secondary droplets originating from secondary atomisation. Fluids with high surface tension (low Weber numbers) display a lower heat transfer area due to the cohesion forces, therefore generating fewer secondary droplets. Two mechanisms for secondary droplet formation have been visualised by several authors, consisting of the breakup of thin

jets [136] and jet ejection from pagoda-like bubbles [135]. The latter can be visualised in figure 2.24.

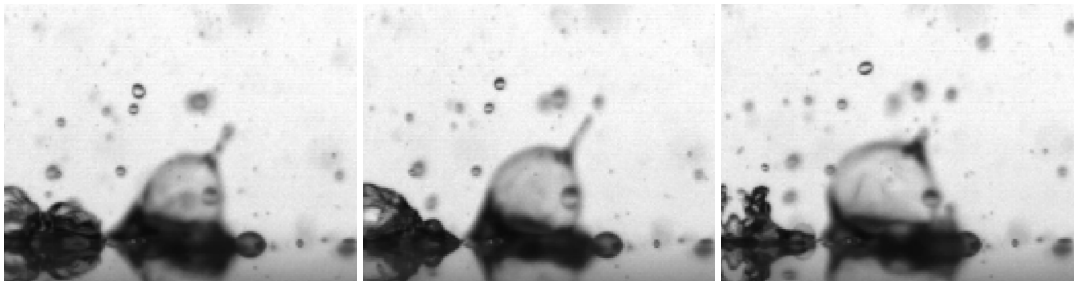

Figure 2.24: Formation of pagoda-like bubbles in the nucleate boiling regime.

2.5.1.3 Transition Boiling

The critical heat flux temperature defines the boundary for the lowest droplet evaporation time. This also occurs due to the increased wetting area of the spreading droplet. However, for higher wall temperatures, a small vapour layer between the droplet and the wall will form, lowering the heat transfer and increasing the evaporation time. This particular phenomenon is denominated as the Leidenfrost phenomenon, which will be thoroughly detailed in the following regime. Assessing both the lower and upper boundaries (CHF and Leidenfrost temperature, respectively) is difficult due to the nature of this regime. According to Xu et al. [137], the major difference between nucleate and transition boiling is the droplet maintaining contact with the surface. For the latter, the existence of a vapour layer diminishes the contact between the droplet and the wall, whereas for the nucleate boiling regime, the droplet fully contacts the surface. Figure 2.25 shows the transition boiling regime for an impacting n-heptane droplet.

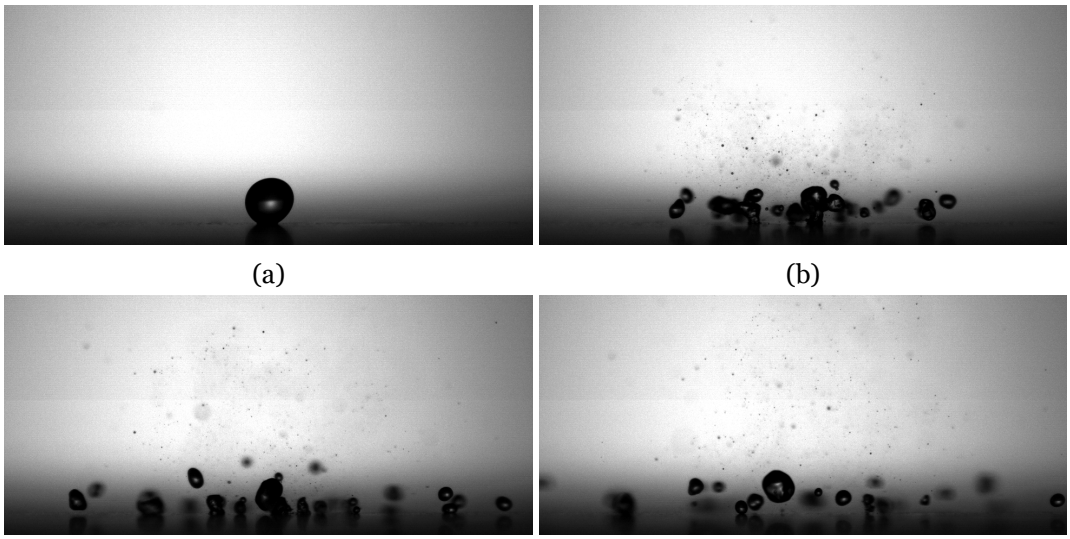

Figure 2.25: Transition boiling regime of an n-heptane droplet impinging onto a heated dry graphite surface ($T_{he} = 170°\mathrm{C}$) a) $t = 0$ ms; b) $t = 15$ ms; c) $t = 30$ ms; d) $t = 60$ ms.

2.5.1.4 Film Boiling

As mentioned in the previous regime, above the CHF temperature, a small vapour layer is formed between the droplet and the heated wall. Significantly increasing the wall temperature will lead to longer evaporation times due to the reduced heat flux until reaching a local maximum, as displayed by figure 2.21. This condition is defined as the Leidenfrost point (LFP), in which the droplet does not impinge onto the surface, but rather levitates in a vapour layer [138], which is represented by figures 2.26 and 2.27. This is opposite to the previous regimes, where the droplet would either maintain full contact with the surface (film evaporation and nucleate boiling) or oscillate between contacting the surface and levitating on a vapour layer (transition boiling).

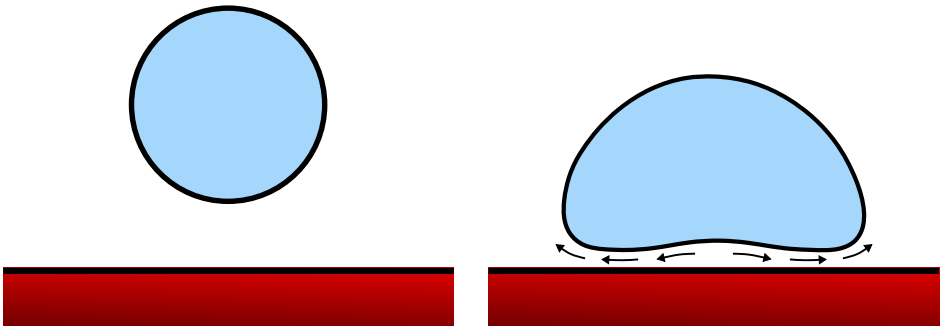

Figure 2.26: The Leidenfrost effect of a single droplet impinging onto a heated surface.

The film boiling regime is initiated at the LFP temperature. This regime is not limited to higher temperatures, meaning that an increase in the heat flux will lead to lower evaporation times without shifting the droplet impact outcome. Research on this subject has focused more on sessile than impinging droplets [139, 140]. Due to this, several authors define the static LFP temperature, T_L, for sessile droplets and the dynamic LFP temperature, $T_{L,d}$, for impacting droplets. The LFP temperature can be determined by a thermodynamic or a hydrodynamic perspective [141], where the former associates T_L as the condition for the lowest evaporation time, and the latter on a specific temperature required to prompt the formation of a vapour layer.

There are several factors that influence the static LFP temperature. Talari et al. [142] reviewed the effect of micro and nanostructured surfaces, focusing on increasing the LFP temperature due to the thermal insulation provided by the vapour layer. Microstructure surfaces increase the contact between the droplet and the substrate, whereas nanostructures increase the wetting characteristics of the fluid. However, several drawbacks arise with these surfaces, such as excessive vapour generation and vapour entrapment within the structures. Therefore, a combination of multiscale surfaces is required to enhance the LFP temperature. Misyura [143] investigated the LFP temperature as a function of the wall roughness. For $We = 0$ (sessile droplet), an increase in wall roughness leads to a higher LFP temperature. In the case of an impinging droplet, $We > 1$, the LFP temperature decreases due to the pressure drop subsequent to impact. Bernardin and Mudawar [139] also verified that polished surfaces display a lower LFP temperature in comparison to rough surfaces. In terms

of thermophysical properties, Qiao and Chandra [144] added surfactants to boiling water droplets. Results show that lower values of surface tension reduce the LFP temperature, however show no influence in terms of evaporation times. Gravity was evaluated by Maquet et al. [145], ranging between 1 to 20 times the Earth gravity. Evaporation times of the droplet are reduced for increased gravity effects, as well as a slight increase in the LFP temperature. The presence of an electrical field was tested by Celestini and Kirstetter [146] between the droplet and the heated substrate. The vapour layer thickness can be reduced by applying a certain voltage, and the Leidenfrost point can be suppressed when the applied voltage reaches/surpasses a critical value. Gottfried et al. [147] studied the film boiling regime for water, n-octane and ethanol droplets, among others. For organic fluids, the LFP temperature ranges from $100°\mathrm{C}$ to $105°\mathrm{C}$ above the saturation temperature of the fluid. Water exhibits a distinct behaviour, where the LFP temperature is dependent on the surface and deposition method and varies between $150°\mathrm{C}$ and $210°\mathrm{C}$ above the saturation temperature.

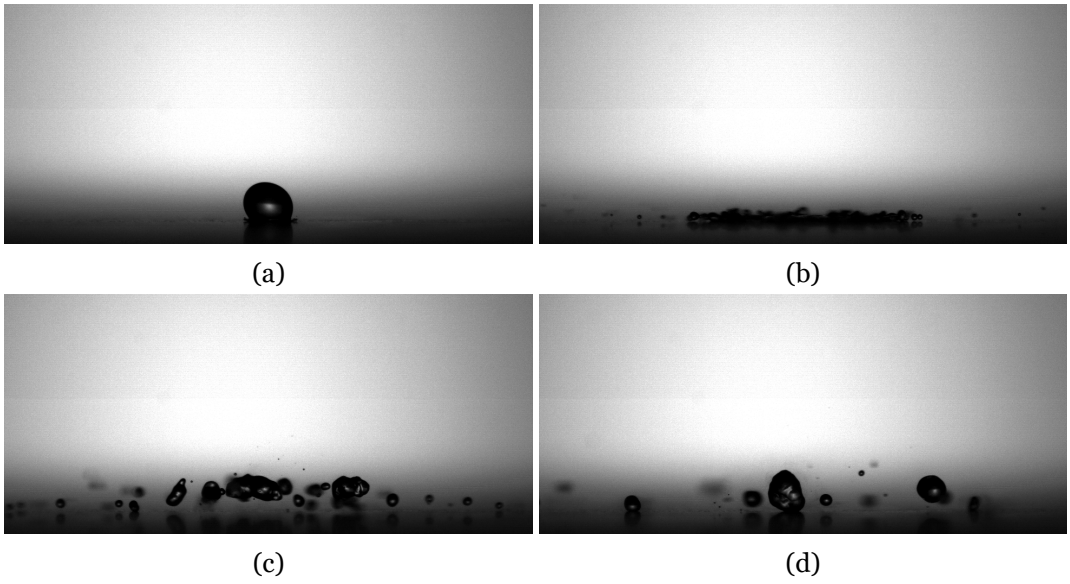

Figure 2.27: Film boiling regime of an n-heptane droplet impinging onto a heated dry graphite surface ($T_{he} = 230°\mathrm{C}$) a) $t = 0$ ms; b) $t = 4$ ms; c) $t = 12.5$ ms; d) $t = 46.5$ ms.

For momentum-driven phenomena, where the impact velocity is a factor, the dynamic LFP temperature is considered, reaching higher values than the static LFP temperature [148]. Similarly to the static point, different experimental conditions may alter the dynamic Leidenfrost threshold. In terms of impact velocity, there is no consensus in the scientific community regarding its effect on the Leidenfrost temperature. These range from authors stating that the effect of the impact velocity is negligible [149,150], to increase [151,152] or decrease [153,154] the dynamic Leidenfrost temperature with the increase of impact velocity. A similar tendency is also verified for surface roughness, as the experimental data gathered for a wide range of conditions exhibit divergent results [21, 143, 155].

Possible outcomes for the film boiling regime differ significantly from isothermal conditions. According to Wachters and Westerling [34], the droplet disintegration develops from no disintegration ($We < 30$), to disintegration after the receding phase ($30 < We < 80$), to disin-

tegration subsequent to impact ($We > 80$). For low Weber numbers, the droplets will spread laterally, followed by the receding lamella bouncing off the surface [156]. Similarly, Akhtar et al. [157] defined several impact outcomes, ranging from pure rebound and rebound with breakup to splashing with the increase of the Weber number.

2.5.2 Liquid Films

In the presence of a liquid film, the impact phenomena differ considerably in comparison to dry heated surfaces. Figure 2.28 illustrates the influence of a constant heat flux on a thin liquid film. For liquid film temperatures below the saturation temperature of the fluid, there is no formation of vapour bubbles on the impact surface, meaning that no boiling occurs. Therefore, the liquid film is solely affected by a continuous evaporation flux which, due to the non-infinite boundaries of the impact surface, will lead to a gradual decrease of the liquid film thickness. Similarly to isothermal conditions, guaranteeing a constant liquid film thickness throughout experiments is crucial, as this parameter is a defining factor in the droplet impact outcome [58, 97]. If the liquid film reaches a critical thickness, a ligament breakup will occur, which is usually initiated at the boundaries of the surface. This will prompt continuous ligament breakup of the liquid film which, due to the evaporation, will lead to the formation of liquid droplets and puddles. From this point onward, each of these liquid structures will develop similarly to a sessile droplet in a heated surface, as represented by figure 2.28.

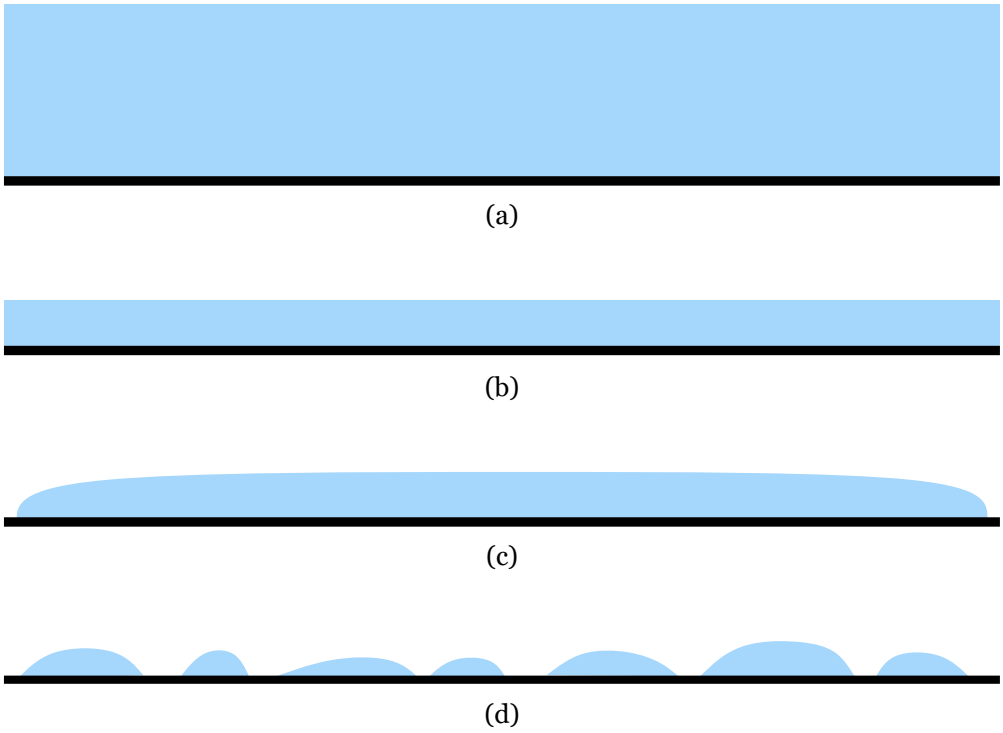

Figure 2.28: Physical phenomena of liquid film evaporation due to the presence of a heat flux: a) Initial liquid film thickness; b) Critical liquid film thickness; c) Initial liquid ligament breakup in the boundaries; d) Formation of liquid droplets and puddles due to continuous ligament breakup.

Research on this topic has been overlooked in the literature, as the experimental and numerical work focuses on isothermal liquid films and dry heated surfaces. However, several

authors approached this field, focusing on specific applications, such as fire suppression, characterised by water-oil interactions and immiscible properties of the droplet and the liquid film. Soriano et al. [158] focused on the heat transfer and hydrodynamics of single and multiple droplets. The heating device consisted of a thin layer of Indium Tin Oxide on a Zinc Selenide substrate in order to provide both infrared and optical access to the impact phenomena. For single droplet impingement, the residual film thickness beneath the crater is not affected by the droplet parameters. Xu et al. [89] evaluated the impact of water droplets on burning alcohol deep pools. Due to the existence of flames and differences in thermophysical properties and saturation temperature of the fluids, the outcomes differ from the classical droplet-liquid film interactions mentioned in section 2.4. Three different regimes were visualised for increasing Weber numbers. The splashing-injecting regime consists of the formation of a crown with secondary atomisation, followed by a central jet and subsequent breakup. In the later stages of the regime, a water wave train develops on the surface of the fuel liquid film, which is restrictive to interactions between different fluids. The splashing-injecting-secondarily injecting regime is analogous to the previous regime, with the main distinction being the growth and breakup of a secondary jet following the collapse of the first jet. For higher Weber numbers, the developing crown may bend inwards, closing at the top, forming a bubble which will eventually break due to variations in internal pressure. The impact velocity is affected by the burning flame, as the resistance effect induced by the fire plume on the falling droplet increases for higher Weber numbers.

Succeeding this work, Xu et al. [159] investigated water droplet impact onto a deep pool of ethanol, focusing on heated liquid films as opposed to the burning flame in the previous study. The crown/jetting and bubble outcomes were also visualised, including a different regime denominated as penetration regime. This event is characterised by a water wave train on the ethanol surface, as well as the dissolution of the water droplet in the ethanol pool. For the latter, the droplet impinges the ethanol interface, maintaining its spherical form, and slowly descends within the liquid pool. This will lead to the droplet gradually dissolving into the liquid film. For the liquid film temperature, the authors defined a dimensionless parameter, $\theta = (T_f - T_{air}) / (T_{sat} - T_{air})$, which correlates the temperatures of the surrounding air, liquid film, and fluid saturation point. Results show that an increase in the liquid film temperature leads to a decrease in the critical Weber number, meaning that, for a constant Weber number, an increase in the liquid pool temperature will lead to a transition in the impact regimes. For $We < 100$, the regimes will transition from crater-jet to penetration with the increase in temperature. For $We > 200$, a similar behaviour is spotted, with transitions between crater-jet and surface bubble. An identical approach to these results are the impact regimes requiring a lower Weber number to prompt for a heated liquid pool. This is due to the decrease in the thermophysical properties of the liquid pool (namely density, viscosity and surface tension), meaning that temperature is a major factor in defining impact outcomes. For crown measurements, the crown height is influenced by the impact velocity, however it is weakly dependent on the liquid pool temperature. Wu et al. [160] performed a similar study for ethanol droplets impacting heated glycerol pools. The penetration and dissolving regimes were verified for lower liquid film temperatures. However, for higher temperatures,

new phenomena arise due to the violent interactions between droplet and liquid film. Figure 2.29 exhibits the vapour explosion of an ethanol droplet impacting onto a heated glycerol pool with a temperature of $T_f = 185°\mathrm{C}$. This phenomenon is defined by a rapid increase in temperature of the liquid droplet which will enter an evaporation state, causing an abrupt release of energy. The initial stages of the impact show the crown formation and secondary atomisation, followed by the rise of a central jet. At $t = 130$ ms, the vapour explosion begins to occur. A cavity rapidly expands at $t = 133$ ms and $t = 135$ ms, causing the detachment of several secondary droplets. This can also lead to the ejection of a secondary central jet from the impact region. The vapour explosion will also develop fluctuations in the air-liquid interface, such as mechanical waves, and these disturbances must dissipate in order for the liquid film to stabilise.

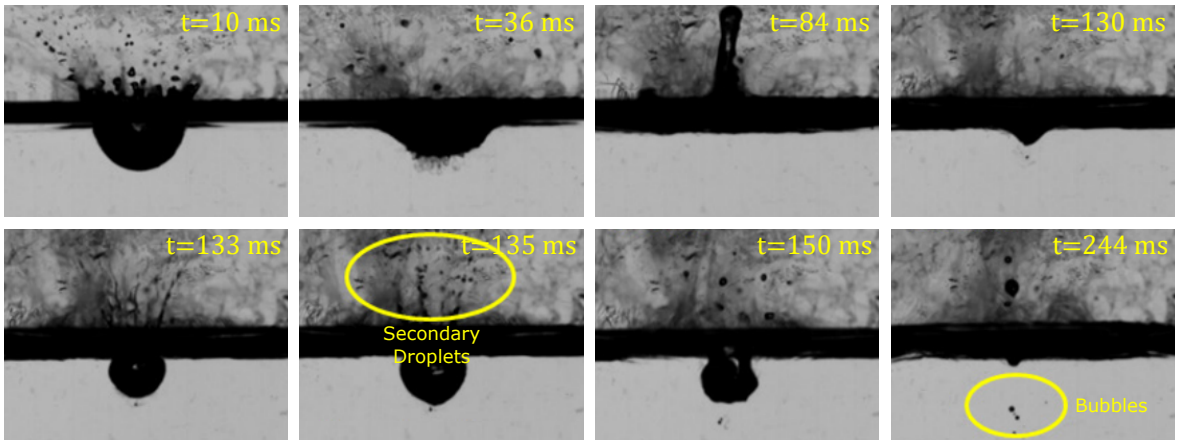

Figure 2.29: Vapour explosion of an ethanol droplet impact onto a glycerol liquid film. Adapted from Wu et al. [160].

By increasing the liquid pool temperature to $T_f = 220°\mathrm{C}$, the droplet may instantly evaporate and, similarly to the dry heated surface, enter the nucleate boiling regime. Contrary to the vapour explosion, this condition emerges at earlier stages of impact due to the abrupt phase change of the droplet. With respect to the impact regimes, the temperature required to prompt both penetration and vapour explosion decreases with higher Weber numbers, which is in accordance with previous authors [159, 161]. Kumar et al. [67] studied a wider range of temperatures for a methanol droplet impinging onto a heated mustard oil surface, reaching the LFP temperature. For this condition, an increase in the Weber number shifts the outcome from spreading, bubble bursting to a cavity crater formation and explosion. More recently, Wu et al. [162] researched the hydrodynamic properties of ethanol on heated glycerol liquid film. Sputtering was visualised in several outcomes, and consists of the release of secondary droplets at high temperatures and Weber numbers at the contact region between the droplet and the liquid film. This is similar to the definition of nucleate boiling on liquid films described previously [160]. Apart from the regime mapping, a quantitative analysis of the crown geometrical parameters, such as diameter and height, was performed as a function of the Weber number and liquid film temperature. An increase in the Weber number leads to an increase in both the diameter and height of the crown. However, the variation in crown diameter is less susceptible to higher Weber numbers in comparison to the height.

The maximum height can be mathematically expressed as a function of the Weber number, $H^*_{max} = 0.0026We$. For the liquid film temperature, the crown diameter is independent of this parameter, however the maximum diameter increases. The crown height increases significantly with the liquid film temperature. These can be explained due to the variation of the thermophysical properties, namely viscosity and surface tension, which decrease with temperature.

The previous studies were all performed for liquid film temperatures below the boiling point, meaning that the liquid films are only subjected to evaporation. However, temperatures close to the saturation temperature of the fluid will prompt boiling in the form of vapour bubbles on the impact surface. This will affect the overall impact phenomenon as the liquid film transitions from a static to a dynamic condition, in which the vapour bubbles will grow and detach from the impact surface, slowly ascending until reaching the surface, collapsing and generating fluctuations in the liquid-gas interface. This leads to local changes in the liquid film thickness, impact angle due to the mechanical waves on the liquid film, among others. Therefore, vapour bubbles require characterisation in terms of life cycles, influence on the liquid film, etc.

Figure 2.30 displays the life cycle of vapour bubbles on a heated surface covered by a liquid film. The conventional life cycle of a vapour bubble is as follows: nucleation, growth and rupture/detachment. Every surface at a microscopic level exhibits roughness irregularities. The most used parameter to describe the average absolute deviation of these irregularities is the arithmetic average height, R_a. The existence of these irregularities in the surface, which are denominated as nucleation sites, allows the formation of vapour bubbles on the impact surface. These will continuously grow due to the presence of a heat flux and liquid film temperatures near the boiling point, increasing its radius. When the vapour bubbles reach a critical size, in which the buoyancy overcomes the surface tension forces, the air ligament breaks, detaching the vapour bubble from the surface. These will rise through the liquid film until reaching the liquid-gas interface and, in most cases, bursting, creating instabilities at the liquid surface.

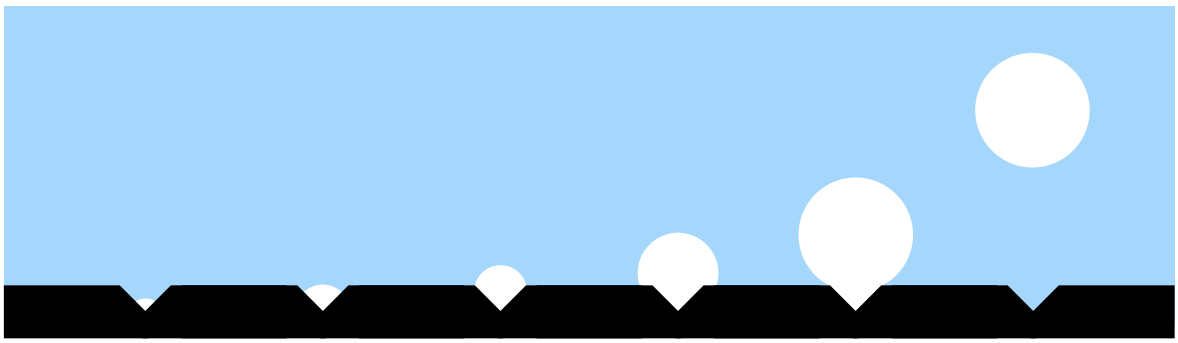

Figure 2.30: Representation of the life cycle of vapour bubbles during liquid film boiling due to the presence of a heat flux.

Existing studies regarding vapour bubbles are not intertwined with droplet impact, meaning that these are mainly investigated separately. Qiu et al. [163] studied the growth and

detachment dynamics of a single bubble on degassed distilled water under subcooled and saturation conditions. This was achieved by designing a cylindrical cavity as the nucleation site, which was etched through deep reactive ion etching. The diameter growth for the bubble and bubble base differ significantly under normal conditions. For the former, it steadily increases until stabilising at later stages prior to detaching from the surface. For the latter, the bubble base expands, reaching a maximum value followed by its decrease. The vapour bubbles detach from the surface at the moment this value reaches approximately zero (ligament breakup). Under low-gravity conditions, bubbles achieve longer growth periods and larger diameters in comparison with standard gravity. Subcooling conditions also induce reduced bubble growth rates and increased bubble diameters. McHale and Garimella [164] researched the influence of surface roughness and heat flux on a high-density region of nucleation sites. Qualitative results can be visualised in figure 2.31. The roughened surface ($R_a = 5.89$ µm) displays a significantly higher number of nucleation sites in comparison to the polished surface ($R_a = 0.03$ µm), which can be explained due to a higher number of surface irregularities. Nucleation sites on the polished surface are, to a limited extent, isolated from neighbouring sites, which can be verified by the growth and detachment of single bubbles from the surface. The rough surface displays a more chaotic behaviour, from a cluster of nucleation sites to bubble coalescence during its growth and detachment. In terms of heat flux, an increase in this parameter leads to a higher bubble release rate and an increased number of nucleation sites. For low heat fluxes, the vapour bubbles mostly display singular dynamics, whereas for high heat fluxes, interactions between vapour bubbles are predominant. The bubble diameter subsequent to ligament breakup also increases for increasing values of the wall superheat.

Gong et al. [165] experimentally studied boiling mechanisms in liquid films, focusing on the critical heat flux, wall temperature and bubble and dry spot dynamics. For the last, the authors employed a high-speed camera to record the experiments from a top view. Results show that the CHF temperature is independent of the liquid film thickness, similar to the pool boiling regime. The dry spots may be reversible or irreversible, depending on the regime. The CHF temperature defines the threshold between reversible (below the CHF point) and irreversible (above the CHF point). From the threshold point onward, the surface cannot be rewetted, leading to the dry out of the heated surface. Additionally, increasing heat fluxes lead to a higher bubble density per unit area. Li et al. [166] focused on single bubble generation on superhydrophobic surfaces. This surface consists of a silicon wafer with etched nanowires that supports a thin layer of polytetrafluoroethylene. Studies were performed for a heat flux range of 0.3 W/cm^2 to 20.1 W/cm^2. The bubble detachment frequency increases for higher wall superheat values until reaching a critical value. From that point onwards, the detachment frequency remains practically constant, which is based on the low efficiency of heat transfer effects due to the presence of a vapour layer. The contact area of the vapour bubbles reduces in a shorter time frame for higher wall superheat conditions in comparison to lower temperatures. Regardless of the temperature, the slope of the contact area as a function of time steadily decreases. Gatapova and Gatapova [167] examined the formation of microbubbles in both heated surfaces and thin liquid films. Figure 2.32 displays the differ-

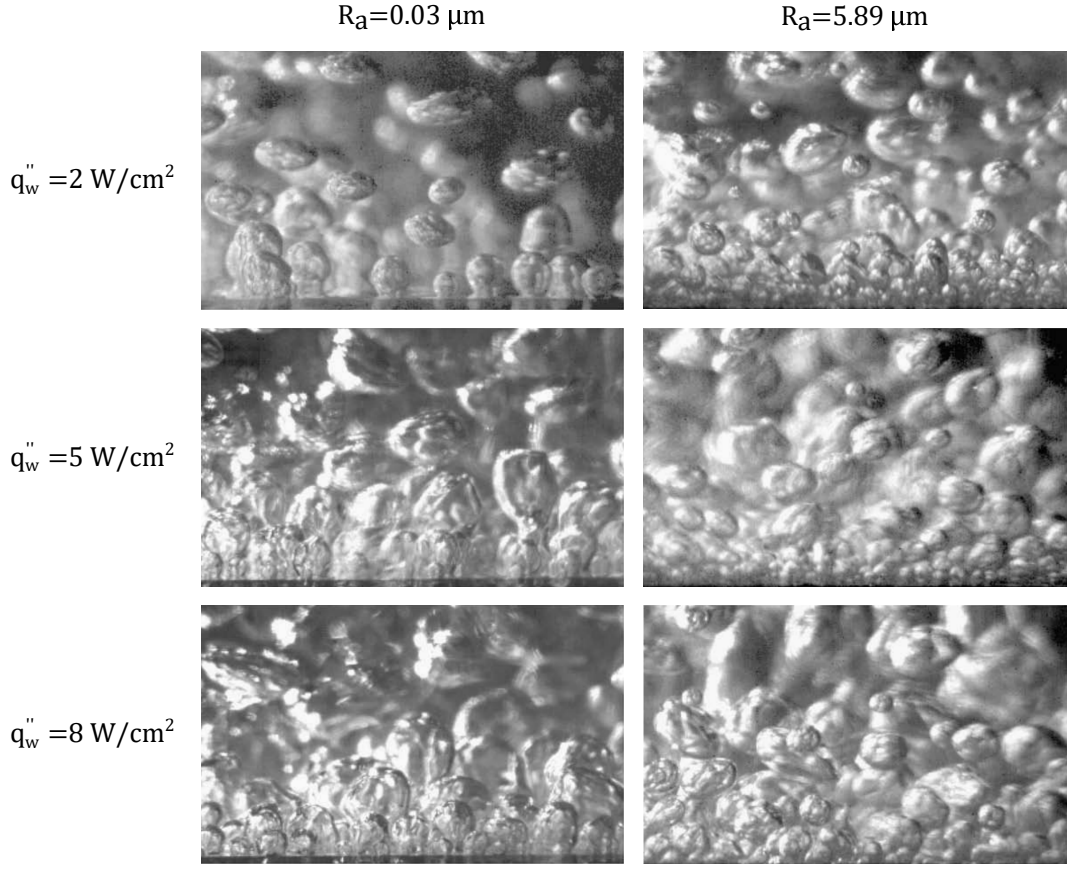

Figure 2.31: High-speed visualisation of the pool boiling regime as a function of the surface roughness and applied heat flux. Working fluid is perfluorinated hydrocarbon (FC-77). Adapted from McHale and Garimella [164].

ent stages of the vapour bubbles life cycle on a dry heated surface. Subsequent to the droplet impact, vapour bubbles start to form and grow on the surface ($t = 1.33$ ms and $t = 3.45$ ms). These are arranged in a single layer continuously affected by a heat flux. The number and size of bubbles are dependent on both temperature and time of exposure. During the spreading stage, bubbles coalesce and burst, followed by the rewetting of the surface. However, for increased values of heat flux, this process is no longer reversible, meaning that for later stages, the film breaks irreversibly due to bubble burst and dry patch formation. Therefore, thin liquid film breakup occurs due to irreversible bursting bubbles, which are induced by either bubble coalescence or the propagation of mechanical waves.

Despite the different applications previously mentioned, a fundamental analysis of the droplet impact onto heated liquid films is required. This includes droplet-liquid film interactions, temperature-related phenomena (Bénard–Marangoni convection, sensible heating, evaporation and condensation), differences in thermophysical properties, impact outcomes, among others. Research on these topics would improve the understanding of droplet impact onto heated liquid films and associated interfacial phenomena.

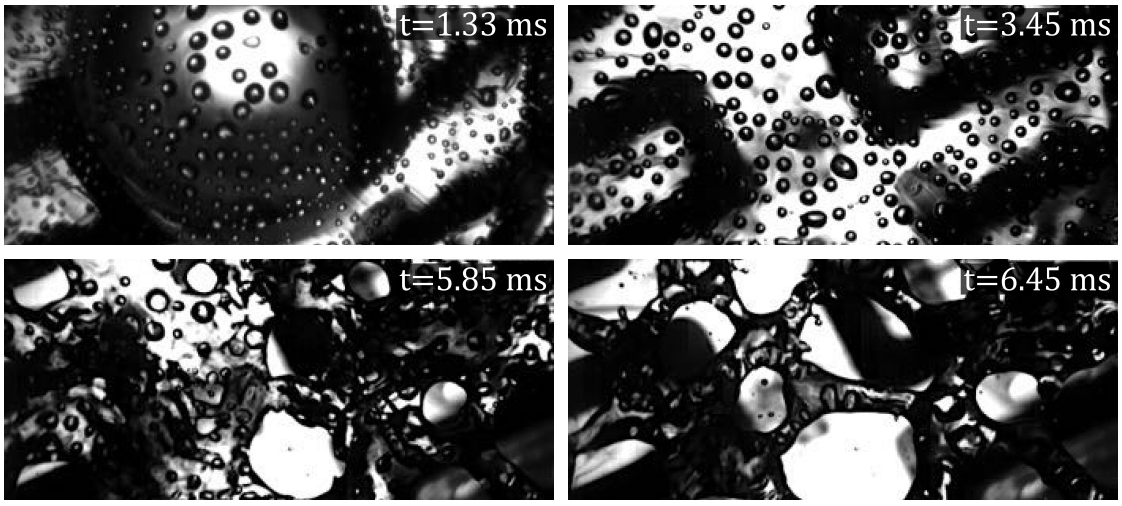

Figure 2.32: Bubble formation, ligament breakup and puddles on a heated surface following droplet impact. Adapted from Gatapova and Gatapova [167].

2.6 Numerical Methods

Prior to the development of modern computing, several numerical solutions based on iterative methods were considered unattainable, as the system of non-linear equations associated with these models consists of solving innumerous algebraic equations. For simplified cases, such as one-dimensional solutions or Euler equations, solutions are achievable. However, for complex systems, such as the Navier-Stokes equations, which involve fluid flow, turbulence, among other concepts, these algebraic equations are impossible to solve. The evolution of central processing units (CPU) revolutionised numerical computing, as the capacity of executing billions of actions per second allowed for iterative solving in an efficient manner.

There are several reasons to prioritise numerical advancements in the research industry. Firstly, several practical experiments are quite costly and time-consuming. This is applied for particle image velocimetry (PIV) systems, nuclear reactors, particle accelerators, among many other applications. Numerical simulations provide options in terms of availability due to limited resources. It is also possible to study simplified systems or the influence of certain parameters on the physical model that are a restraint in experimental conditions. The possibility of neglecting viscosity for the Navier-Stokes equations or varying surface tension in two-phase flows allows the understanding of fluid dynamics and interfacial phenomena. The numerical analysis associated with these studies is essential to optimise the efficiency of technical systems, which may include reduction of energy consumption, reduction of pollutant emissions, among others.

From a numerical perspective, multiphase systems differ from single-phase due to the presence of one or more interfaces between phases. These require additional treatment due to the increased complexity of the interface. A standard approach to handling multiphase flows is to adopt the local instance formulation for each independent phase, followed by appropriate jump conditions to account for the interface. This class of methods, which require

tracking the interface, are defined as interface tracking methods. Therefore, the governing equations account for each phase separately, followed by the interfacial balance through the mass, momentum and energy equations [168].

Prior to presenting the evolution of interface tracking methods for multiphase flows, the formulation for the motion in the continuum must defined. Firstly, the definition of the continuum revolves around the concept that fluid flow is regarded as continuous matter, meaning that properties such as density and velocity do not display discontinuities between two points in space. This formulation allows for a better assessment of the Navier-Stokes equations, specifically in terms of local derivatives. Following this definition, there are several ways to describe fluid flow. The two most common techniques are the Eulerian and the Lagrangian approach. For the former, the variations of the fluid flow, such as velocity, temperature and pressure, are specified at a fixed point and at a given time with respect to a stationary/moving frame. For the latter, fluid particles are marked and tracked individually throughout the flow, and their variation is described along each specific trajectory. The Eulerian framework is the most analogous with the experimental analysis, and therefore it is widely used in fluid mechanics [168]. According to Popinet [169], Eulerian fields are particularly suited for fluid mechanics due to the necessity of dealing with large deformations. These can either be coupled with a Lagrangian (Euler-Lagrange) or Eulerian (Euler-Euler) representation of the interface. In the Lagrangian formulation, transport is rather simple, however it presents difficulties in large deformations such as ligament breakup and coalescence. On the contrary, the Eulerian formulation can handle topology changes accurately, however, leading to more complex transport schemes [169]. Due to these reasons, the former is more suited for flows with an increased number of particles, such as sprays and thermal plasma, whereas the latter is more fitted for single droplets and bubbles. Therefore, from a macroscopic assessment of the fluids, where the continuum formulation is applied, two-phase flows are governed by the incompressible Newtonian Navier-Stokes equations, consisting of the general conservation laws of mass, momentum and energy, as displayed by equations (2.15), (2.16) and (2.17), respectively:

$$\frac{\partial}{\partial t}(\rho) + \nabla \cdot (\rho \mathbf{U}) = 0 \tag{2.15}$$

$$\frac{\partial}{\partial t}(\rho \mathbf{U}) + \nabla \cdot (\rho \mathbf{U}\mathbf{U}) = -\nabla p + \nabla \cdot \left[\mu \left(\nabla \mathbf{U} + (\nabla \mathbf{U})^{\mathrm{T}}\right)\right] + \rho \mathbf{g} + \mathbf{F}_{\sigma} \tag{2.16}$$

$$\frac{\partial}{\partial t}(\rho E) + \nabla \cdot [\mathbf{U}(\rho E + p)] = \nabla \cdot (k \nabla T) + Q \tag{2.17}$$

where t is time, $\mathbf{U}$ is the velocity vector, p is the static pressure, $\mathbf{F}_{\sigma}$ are the surface tension forces, E is the specific internal energy, k is the thermal conductivity, and Q is the energy source term for the energy equation. These equations must be coupled with an interface

tracking method to account for the liquid-gas separation layer. The following subsections will thoroughly describe the development of numerical methods applied to multiphase flows, focusing on the Euler-Euler approach and related interface tracking methods. This will account for interfacial dynamics, such as surface tension, as well as heat and mass transfer phenomena, which include evaporation and condensation.

2.6.1 Interface Tracking Methods

In an Euler-Euler field, the interface tracking methods are associated with the one-fluid formulation, which consists of applying the same conservation equations over the entire domain, with the thermophysical properties such as density and viscosity varying sharply across the interface. However, the interface between phases requires special treatment due to interfacial dynamics such as singular forces (surface tension) or jump conditions (phase change) [170].

Over the years, several methods were developed in order to accurately track/capture the interface. Harlow and Welch [171] developed the marker and cell (MAC) method, which consists of placing marker particles in the fluid, as displayed by figure 2.33. These are only implemented as visual tracers in order to track the fluid shape and do not influence the system of equations to be solved. If a cell does not contain marker particles, there is no fluid within the cell. If the cell contains marker particles and is in the vicinity of an empty cell, it is a surface cell. The remaining cells, which contain marker particles and are not in the vicinity of empty cells, are filled with fluid. These particles move according to the velocity components in the neighbouring cells. However, this method does not provide an accurate representation of the interface, as physical properties associated with free surfaces, such as surface tension and contact angle, are not correctly accounted for. Additionally, the unit normal vector and curvature are also difficult to compute. Examples of this method include the complete and partial breaking of a dam to study wave formation and breakup. This technique was adopted by Harlow and Shannon [172] to simulate droplet impact onto flat plate, shallow and deep pool. The splashing phenomenon and the associated dynamics are investigated for different droplet diameters, impact velocities and dimensionless thickness. Due to the complexity of the simulation and the lack of computational resources in the 20^{th} century, viscosity and surface tension were not considered for the numerical simulations. For the shallow pool, the pressure-to-density ratio shows an initial peak value, corresponding to the initial impact, followed by a gradual decrease, relating to the fluid movement outwards of the impact region. This ratio tends to have higher values on the impact region at earlier stages of the impact, and, for later stages, these values transition from the impact to the outer region.

The pioneer method developed by Harlow and Welch [171] served as a foundation for improving numerical methods applied to multiphase flows. Hirt and Nichols [173] developed the Volume of Fluid (VOF) method which is a free-surface technique capable of modeling several immiscible fluids by solving a single set of momentum equations and tracking the volume fraction, α, of each phase on the computational domain. In each control volume,

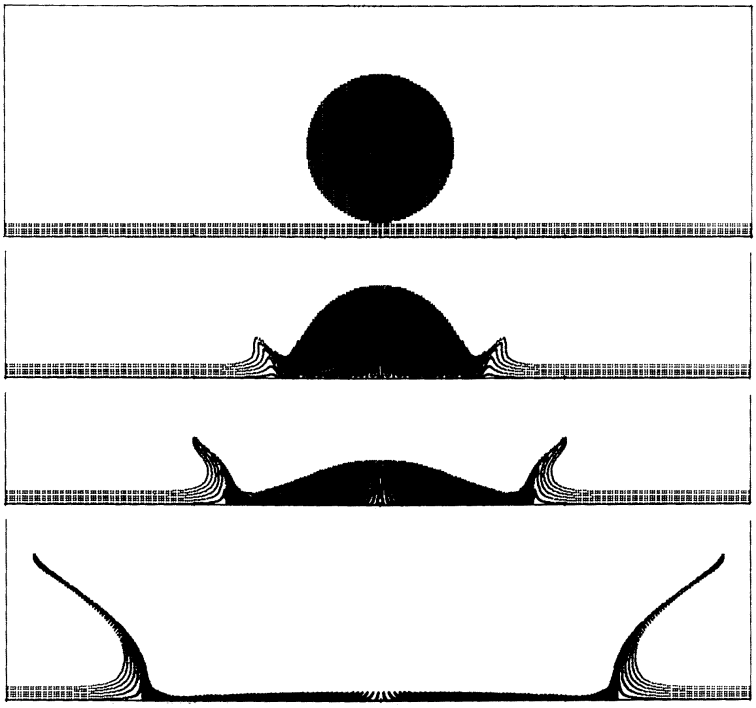

Figure 2.33: Numerical simulation of a droplet impacting a liquid film using the MAC method. Adapted from Harlow and Shannon [172].

this parameter ranges from $\alpha = 0$ for the gas phase, to $\alpha = 1$ to the liquid phase. Values between these consist on the interface between phases, as exhibited by equation (2.18). The volume fraction equation is represented by equation (2.19). Due to the interface being tracked by a color function, and due to the absence of a diffusion term in the volume fraction equation, this method is inherently conservative. However, there are disadvantages to the method, generally associated with the poor capability of calculating the interface unit normal vector, $\mathbf{n}$, and curvature, κ, resulting in an interface with low quality. These parameters can be calculated based on the volume fraction field, as displayed by equations (2.20) and (2.21), respectively.

$$\alpha = \begin{cases} 0 & \text{for the gas phase} \\ 0 < \alpha < 1 & \text{for the interface} \\ 1 & \text{for the liquid phase} \end{cases} \tag{2.18}$$

$$\frac{\partial \alpha}{\partial t} + \nabla \cdot (\mathbf{U}\alpha) = 0 \tag{2.19}$$

$$\mathbf{n} = \frac{\nabla \alpha}{|\nabla \alpha|} \tag{2.20}$$

$$\kappa = \nabla \cdot \mathbf{n} \tag{2.21}$$

In terms of the liquid-gas interface, the VOF method may be associated with interface reconstruction schemes. The most adopted reconstruction schemes consist in piecewise constant and linear schemes, as depicted in figure 2.34. The simple line interface calculation (SLIC) [174] allows to geometrically approximate the fluid interface based on its orientation. Due to the simplicity of the method, these approximations are only either parallel or perpendicular to the axis orientation. This leads to a straightforward approach in both time advancement and contact discontinuities. The piecewise linear interface calculation (PLIC) [175], as the name suggests, is defined by a straight line whose orientation is dependent on the unit normal vector to the interface. This is an improvement to single orientation techniques, as it provides a more accurate description of the liquid-gas interface. A disadvantage to this scheme is the interface discontinuity between adjacent cells due to the disalignment of the surfaces orientation. There are also VOF formulations that do not require interface reconstruction, such as the compressive interface capturing scheme for arbitrary meshes (CICSAM) [176] and the bounded gradient maximisation (BGM) scheme [177]. These schemes do not perform a geometric reconstruction of the interface. Instead, the schemes focus on solving the advection equation by algebraic methods, such as upwind and/or downwind schemes. This approach will lead to several inconsistencies, namely interface diffusion with a finite thickness.

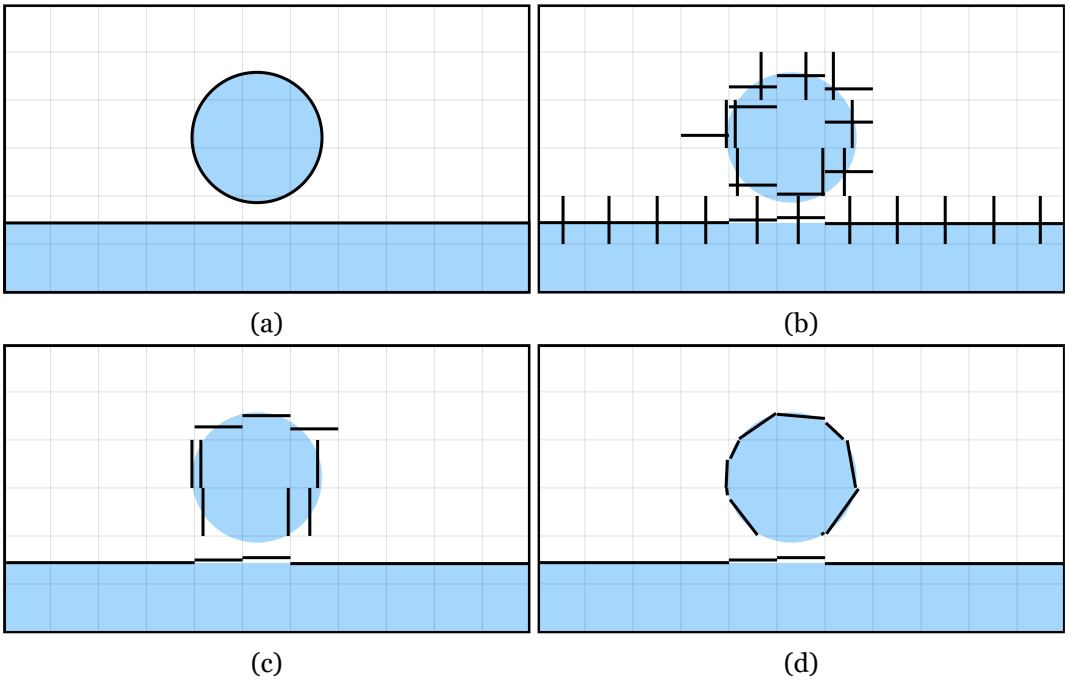

Figure 2.34: Interface reconstruction schemes applied to droplet impact onto a liquid film: a) Original interface; b) SLIC Method [174]; c) Adapted SLIC Method by Hirt and Nichols [173]; d) PLIC Method [175].

Another popular method for interface tracking is the level set (LS) method, developed by Osher and Sethian [178]. The level set function is used to represent the interface as a signed distance. Correspondingly, this function assumes the interface as a zero level set and can be expressed, in a two-phase flow, as:

$$\phi = \begin{cases} +|d| & \text{for the gas phase} \\ 0 & \text{for the interface} \\ -|d| & \text{for the liquid phase} \end{cases} \tag{2.22}$$

where d is the shortest distance from the interface. This scalar is advected similarly to the volume fraction presented in equation (2.19). The algorithm does not track the interface explicitly, meaning that its location is given by interpolating its values on the mesh. This method is particularly suited in capturing complex surface topologies, however lacks mass conservation after several time steps due to not maintaining the continuous properties of a signed function. Therefore, it requires re-initialisation in order to satisfy this condition. The unit normal vector and curvature are evaluated as a function of the level set property analogous to the volume fraction. The representation of the previous methods on a numerical grid can be visualised in figures 2.35b and 2.35c. In order to overcome these disadvantages, Sussman and Puckett [179] developed a mixed method denominated as coupled level set and volume of fluid (CLSVOF) method. This method is superior in discretising the advection equation and in computing the interface curvature in surface tension dominated flows in comparison to the LS and VOF methods, respectively. Alternatively, several authors follow a different approach to interface tracking. Tryggvason et al. [180] developed a front-tracking technique for direct numerical simulations of multiphase flows, which consists of explicitly tracking the interface by using connected marker points. Despite this technique being more complex than a marker function, the increased accuracy and robustness reduce errors associated with the advection of this term. Figure 2.35d displays how these marker points are represented in a two-phase flow. Due to the Lagrangian nature of these markers, the front requires restructuring as a function of the fixed grid, as the inherent properties of two-phase flows involve deformation and stretching. Interfacial dynamics, such as surface tension or phase change, are computed based on the marker points and transferred to the static grid.

Most recently, the unit normal vector and curvature have been evaluated using height functions [181]. The procedure to compute these parameters is divided into several steps. Initially, the direction of the maximum unit normal vector must be defined for the orientation of the height function. Then, posterior to evaluating the local volume fractions, the curvature is computed by differentiating the height functions, as represented by equation (2.23).

$$\kappa = \frac{h''}{\left(1 + h'^2\right)^{3/2}} \tag{2.23}$$

These geometric functions compute the curvature from volume fractions/level set function directly on the interface, where the VOF/LS methods estimate the curvature on the cell centres, leading to a better approximation. Additionally, the method is not affected by the exact distribution of volume fraction in a column, as it avoids erroneous curvature estimations due to spatial averaging [169].

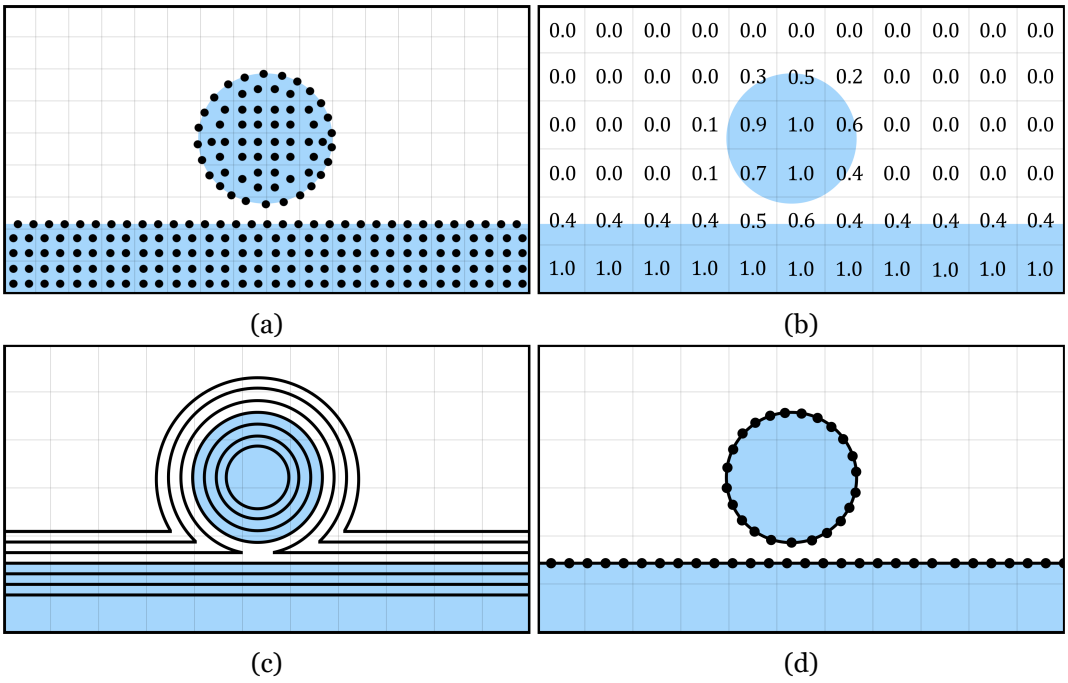

Figure 2.35: Visual representation of interface tracking methods for two-phase flows: a) MAC method; b) VOF method; c) LS method; d) Front tracking method.

The existence of an interface between phases in a one-fluid formulation requires special treatment in order to achieve interfacial balance in the governing equations. For two-phase flows, the interpretation of surface tension is a crucial step in adapting the acting forces in the interface into a numerical perspective. Overall, two different formulations of surface tension are considered in two-phase flows, consisting of the integral and volumetric approaches [169]. For the former, surface tension is defined as a force per unit length tangential to the curve. This can be applied to two-dimensional curves affected by interfacial tension. Due to the nature of the approach, momentum conservation for surface tension is ensured, both locally and globally. This formulation was mostly used in Lagrangian representations of the interface [182] and front-tracking methods [180]. The latter formulation relies on the numerical approximation of the surface Dirac function. In a two-phase flow perspective, this function ensures that the delta property, defined as δ_s, is equal to 0 in all of the domain, with the exception of the interface between phases. This approximation leads to a direct evaluation of the volumetric term associated with surface tension, which is represented by equation (2.24):

$$F_\sigma = \sigma\kappa\delta_s\mathbf{n} = \sigma\kappa\nabla H \tag{2.24}$$

where ∇H is the Heaviside function. The computation of this volumetric term differs in terms of the numerical approximation of the Heaviside function. Brackbill et al. [183] developed the continuum surface force (CSF) model, which accounts for two and three-dimensional effects of surface tension on a continuum assumption. For this approach, the Heaviside function is based on a color function, c, which is analogous to the volume fraction, as presented by equation (2.25).

$$H_\alpha = \begin{cases} 0 & \text{if } \alpha < 0.5 \\ 1 & \text{if otherwise} \end{cases} \tag{2.25}$$

For the case of the level set, the approximation of the smooth function is based in the signed distance to the interface, as exhibited by equation (2.26):

$$H_\phi = \begin{cases} 0 & \text{if } \phi < -\varepsilon \\ 1 & \text{if } \phi > \varepsilon \\ \frac{1}{2}\left[1 + \phi/\varepsilon + \sin\left(\pi\phi/\varepsilon\right)/\pi\right] & \text{otherwise} \end{cases} \tag{2.26}$$

where ε is the characteristic interface thickness. This approach, in comparison to the VOF approximation, displays a smoother transition of both the Dirac delta and the Heaviside function due to the nature of the function. Several other authors adopt a similar smoothing, such as Peskin (elastic membranes) and Unverdi and Tryggvason (front tracking) [184, 185]. Another particular method that adopts the level set function is the ghost fluid method (GFM) [186], which treats the liquid-gas interface as a moving boundary and enforces the interfacial jump conditions in the pressure gradient term. Despite being associated with the level set, this is also applicable for VOF through the CSF method, as represented by equation (2.27). Additionally, the physical properties of the liquid and gas phases must be defined on the numerical field. Both arithmetic and harmonic means are employed to account for the different phases in the calculation of these properties. These are dependent on the interface tracking method and consequent surface tension model. The VOF method utilises the volume fraction, the LS method the level set function and correspondent Heaviside function, and front tracking methods an indicator function which, similar to the Heaviside function, is used to smooth the properties at the interface.

$$H = \begin{cases} 1 & \text{if } \phi > 0 \text{ (LS) or } c > 0.5 \text{ (VOF)} \\ 0 & \text{otherwise} \end{cases} \tag{2.27}$$

2.6.2 Phase Change Models

The complexity of two-phase flows is substantially reduced for isothermal conditions. The Navier-Stokes equations are simplified into mass and momentum general conservation laws, neglecting the energy equation, and the previous interface tracking methods account for surface tension and interfacial dynamics rather accurately. However, modern industrial applications involve temperature-related phenomena, such as cooling, combustion, evaporation and condensation, among others. These are associated with significant changes in temperature, leading to the emergence of heat fluxes and phase change processes. Due to this, the energy equation must be considered in numerically solving two-phase flows with

phase change. Depending on the specific application, special terms can be neglected or taken into account. These, usually considered as source terms, may include surface tension, phase change, chemical reactions, among other intrinsic interfacial phenomena that may arise in two-phase flows.

In order to understand how to incorporate interfacial mass transfer in two-phase flows, the energy equation must first be adapted for the physical nature of two-phase flows. Despite the different forms of the energy equation, such as total energy, enthalpy, kinetic energy, temperature, internal energy, among others, for two-phase flows with phase change under the one-fluid formulation, one of the most suitable forms of the energy equation utilises temperature as the defining property. This equation can be derived from equation (2.17) by substituting the specific internal energy for temperature and neglecting pressure due to the incompressible condition, resulting in equation (2.28):

$$\frac{\partial}{\partial t}\left(\rho T\right) + \nabla \cdot \left(\rho \mathbf{U} T\right) = \nabla \cdot \left(k \nabla T\right] + Q \tag{2.28}$$

Similarly, the mass conservation equation, which is represented by equation (2.15), must be coupled with the VOF method. The combination of these results in a more complex equation that accounts for both mass transfer and conservation of the different phases, as displayed by equation (2.29):

$$\frac{\partial}{\partial t}\left(\alpha_k \rho_k\right) + \nabla \cdot \left(\alpha_k \rho_k \mathbf{U}_k\right) = S_k \tag{2.29}$$

where the subscript k refers to one of the phases (liquid or gas), and S_k is the volumetric mass source term. Analogously, mass transfer phenomena must also be considered along the liquid-gas interface, which requires accurate implementation of the mass, momentum and energy terms. Equations (2.30), (2.31) and (2.32) display the jump conditions for the velocity, momentum transfer rate and energy transfer rate, respectively:

$$\left(\mathbf{U}_g - \mathbf{U}_l\right) \cdot \mathbf{n} = \dot{m}\left(\frac{1}{\rho_g} - \frac{1}{\rho_l}\right) \tag{2.30}$$

$$\dot{m}\left(\mathbf{U}_g - \mathbf{U}_l\right) \cdot \mathbf{n} = \left(\tau_{s,g} - \tau_{s,l}\right) \cdot \mathbf{n} - \left(p_g - p_l\right)\mathbf{I} \cdot \mathbf{n} + \sigma\kappa\mathbf{n} \tag{2.31}$$

$$q_i'' = \dot{m} h_{lg} \tag{2.32}$$

where $\dot{m}$ is the mass transfer rate, τ_s is the shear stress, $\mathbf{I}$ is the dyadic idemfactor, q_i'' is the heat flux across the interface and h_{lg} is the latent heat of vaporisation. The mass transfer

parameter is computed normal to the interface based on both the density and velocity of each of the phases, as depicted in equation (2.33). According to the equation, a positive net force corresponds to evaporation, whereas a negative value relates to condensation.

$$\dot{m} = \rho_g \left(\mathbf{U}_g - \mathbf{U}_i\right) \cdot \mathbf{n} = \rho_l \left(\mathbf{U}_l - \mathbf{U}_i\right) \cdot \mathbf{n} \tag{2.33}$$

Bearing in mind the intricate dynamics of two-phase flows, the incorporation of heat and mass transfer requires phase change models that are adequate for the numerical background thoroughly detailed in the previous sections, namely the Navier-Stokes equations coupled with an interface tracking method under a one-fluid formulation. Therefore, the following subsections will provide an in-depth analysis of phase change models. These include the Rankine-Hugoniot jump condition, the Schrage model and the Lee model, which are specifically suited for two-phase flows in combination with the VOF method.

2.6.2.1 Energy jump condition

The Rankine-Hugoniot jump condition [187] is based on a physical model that assumes the interfacial temperature to be equal to the saturation temperature and includes heat transfer as conduction between phases, as represented by equation (2.34).

$$q_i'' = \mathbf{n} \cdot \left(k_l \nabla T_l - k_g \nabla T_g\right) = \dot{m} h_{lg} \tag{2.34}$$

This relation can also be obtained by the product between the mass flux and the latent heat of vaporisation. The correspondent volumetric mass source term can be achieved in the following form:

$$S_g = -S_l = \dot{m} |\nabla \alpha_g| \tag{2.35}$$

where the volume fraction term, $|\nabla \alpha_g|$, is equal to the ratio of the cell interfacial area to its volume. Several authors simplified this term for a more accessible implementation in both commercial and in-house codes, as well as a straightforward approach in terms of computation. For instance, the volumetric mass source term can be determined as a function of both temperature and volume fraction gradients [188, 189], as displayed by equation (2.36). Sun et al. [190] assumed a thermal conductivity and heat capacity of the saturated phase equal to zero. The temperature of the saturated phase is equal in any region containing this phase, leading to negligible heat conduction.

$$S_g = -S_l = \frac{k \left(\nabla T \cdot \nabla \alpha_l\right)}{h_{lg}} \tag{2.36}$$

Overall, the energy jump condition does not account for the contribution of kinetic energy, and it is not dependent on empirical coefficients due to its physical basis. The assumptions mentioned previously impose several limitations on the model, such as requiring validation for a specific application. The source terms should be studied over a wide range of conditions and compared with experimental data in order to quantify these terms and their applicabilities [191].

2.6.2.2 Schrage model

The Schrage model [192] was developed to account for evaporation/condensation rates of pure substances. It is based on the kinetic theory of gases under the Hertz-Knudsen equation [193,194]. This theory states that the velocity of particles, such as molecules, follows the Maxwell-Boltzmann velocity distribution. For non-equilibrium conditions, a special treatment is required to account for interphase mass transfer. The net mass flux, $\dot{m}$, consists of the absolute sum of vaporisation and condensation across the interface, as represented by equation (2.37):

$$\dot{m} = \dot{m}_e - \dot{m}_c = \gamma \sqrt{\frac{R}{2\pi M}} \left(\rho_{sat}\left(T_l\right) \sqrt{T_l} - \Gamma\left(U_r\right) \rho_v \sqrt{T_v} \right) \tag{2.37}$$

where γ is the mass accommodation coefficient, R is the universal gas constant, M is the molecular weight, $\rho_{sat}\left(T_l\right)$ is the saturated gas density at a temperature T_l, and the subscripts e, c and v refer to evaporation, condensation, and the vapour phase, respectively. The function $\Gamma\left(U_r\right)$ incorporates the effects of macroscopic vapour motion, where U_r is the ratio of the macroscopic speed of vapour to the most probable thermal speed of vapour molecules. The equation can be reduced by considering the ideal gas law and assuming $U_r = 0$, meaning that $\Gamma\left(U_r\right) \approx 1$. This leads to equation (2.38):

$$\dot{m}_g = -\dot{m}_l = \frac{2}{2-\gamma_c} \sqrt{\frac{M}{2\pi R}} \left[\gamma_c \frac{p_g}{\sqrt{T_{g,sat}}} - \gamma_e \frac{p_l}{\sqrt{T_{l,sat}}} \right] \tag{2.38}$$

If the evaporation and condensation occur at similar rates, the mass accommodation coefficient is equal for both phase change processes, $\gamma_c = \gamma_e = \gamma$, simplifying equation (2.38) into the following:

$$\dot{m}_g = -\dot{m}_l = \frac{2\gamma}{2-\gamma} \sqrt{\frac{M}{2\pi R}} \left[\frac{p_g}{\sqrt{T_{g,sat}}} - \frac{p_l}{\sqrt{T_{l,sat}}} \right] \tag{2.39}$$

Due to the previous assumptions, equation (2.37) is described as exact Schrage relation, whereas equations (2.38) and (2.39) are referred as approximate Schrage relations. In order to apply this model, the mass accommodation coefficient, γ, must be determined, typically

by comparison between experimental results and analytical solutions. According to the literature, several authors predicted this value based on different applications and conditions. Liang et al. [195] defined a range of $\gamma = 0.8$ to $\gamma = 1.0$ for argon in a planar nanochannel. Vaartstra et al. [196] quantified the accuracy of the Schrage equations for high flux operating conditions similar to industrial applications, and water yields better results for $\gamma < 0.5$. Wang et al. [197] assumed an accommodation coefficient of $\gamma = 1$ for octane, a non-polar fluid. Kassemi and Kartuzova [198] focused on cryogenic tank pressurisation, namely interfacial dynamics and vapour phase turbulence. Hydrogen simulations are performed for $\gamma = 1$ in the sharp interface model, whereas the VOF method requires coefficient values in the order of $\gamma < 0.1$. Voigtländer et al. [199] established $\gamma = 1$ for water cloud modelling and a lower limit of $\gamma = 0.3$ due to experimental uncertainty.

2.6.2.3 Lee model

The Lee model [200] is widely popular for simulating phase change processes due to its simplified saturation model. As a derivative of the Schrage model, the kinetic contribution is not considered, and phase change is proportional to the difference between the interfacial temperature and the saturation temperature of the fluid. This model assumes mass transfer at a constant pressure and a quasi thermo-equilibrium state, which can be calculated from the following equations:

$$S_g = -S_l = r_{i,c}\alpha_g\rho_g\frac{(T - T_{sat})}{T_{sat}} \quad \text{for condensation } (T > T_{sat}) \tag{2.40}$$

$$S_g = -S_l = r_{i,e}\alpha_l\rho_l\frac{(T - T_{sat})}{T_{sat}} \quad \text{for evaporation } (T > T_{sat}) \tag{2.41}$$

where r_i is an empirical coefficient denominated as mass transfer intensity factor, which units are s^{-1}. This parameter is a key factor in the Lee model and is defined by equations (2.42) and (2.43) for condensation and evaporation, respectively:

$$r_{i,c} = R_{sv}\frac{2\gamma}{2-\gamma}h_{lg}\sqrt{\frac{1}{2\pi RT_{sat}}}\frac{\rho_l}{\rho_l - \rho_g} \tag{2.42}$$

$$r_{i,e} = R_{sv}\frac{2\gamma}{2-\gamma}h_{lg}\sqrt{\frac{1}{2\pi RT_{sat}}}\frac{\rho_g}{\rho_l - \rho_g} \tag{2.43}$$

where R_{sv} is the specific surface area. The mass transfer intensity factor has been systematically determined by researchers as highly empirical, similar to the accommodation coefficient. It is extremely volatile, displaying a wide range of values for different conditions [201–203]. It is also affected by several elements, such as flow geometry and conditions, grid size, time step, mass transfer phenomena, among others.

2.6.3 Numerical Approach on Two-Phase Flows

Research on this topic has been focused on several aspects, including interface tracking techniques and heat and mass transfer phenomena, as previously mentioned. These are inherent to both nature and industrial applications and have been a primary focus in understanding interfacial dynamics. Several authors have studied this subject in a variety of applications and conditions, focusing on the numerical approach to the phenomena. Rieber and Frohn [204] studied a single droplet impact on a liquid film by coupling the incompressible Navier-Stokes equations on a three-dimensional assumption with the VOF method. The formation of secondary atomisation, cusps and fingers due to free rim instabilities is the main focus of the authors. A random disturbance based on a Gaussian distribution is initially imposed in the velocity fields of the droplet and liquid film to approximate the numerical simulations to the physical phenomenon of splashing, ligament formation and breakup. Results suggest that, at the free rim, the cusp formation leading to fingers and splashing is driven by the Rayleigh instability [205]. Liang et al. [206] studied single and multiple droplet impingement onto a liquid film covering a solid wall heated by conduction, as can be seen by figure 2.36. The CLSVOF method is employed to capture the liquid-gas interface, whereas no phase change processes are considered (no source term in the energy equation). The heat transfer coefficient on the impact region exceeds the undisturbed liquid film due to the temperature differences in the residual liquid film. Additionally, several blind spots were visualised due to flow stagnation occurring beneath the liquid sheet. Following this work, Liang et al. [207] incorporated the Lee model to simulate phase change and evaluate droplet and bubble dynamics. The vapour bubbles that contact the liquid sheet lead to the wall rupture and eventually the disintegration of the crown. The heat transfer coefficient is reduced for increasing numbers of vapour bubbles. The bubble detachment can be inhibited by decreasing the contact angle.

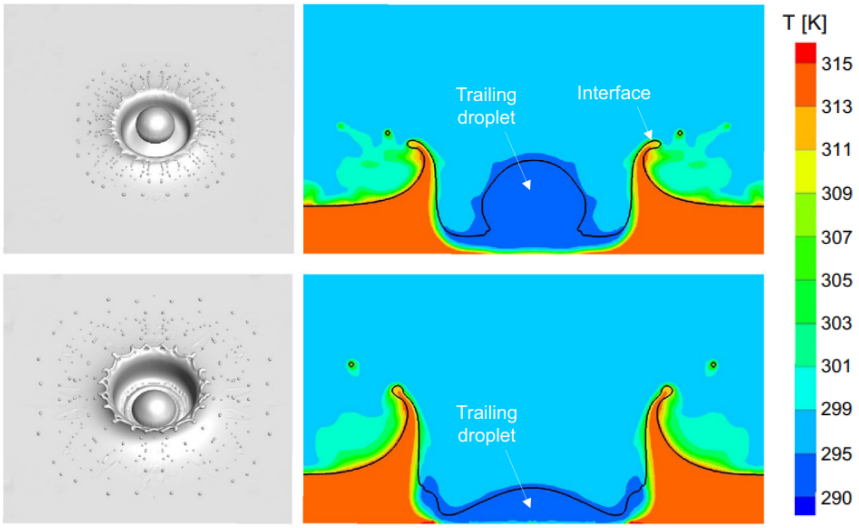

Figure 2.36: Simulation of successive droplets impacting onto a heated liquid film and correspondent temperature fields [206].

Wang et al. [208] analysed heat transfer characteristics and impact dynamics of a double droplet onto a moving liquid film. A higher local wall heat flux is obtained for higher im-

pact velocities, smaller droplet spacing, and thinner liquid films. Hardt and Wondra [209] developed an evaporation model coupled with an interface tracking method under a continuum formulation. This model is introduced as an evaporation mass flux as a function of the interface and saturation temperatures. In order to validate this model, a two-dimensional film boiling problem is simulated, as can be seen in figure 2.37. The grayscale region represents temperature fields, and the black lines the liquid-gas interface. A manual trigger of the Rayleigh-Taylor instability is required to amplify the liquid film oscillations, prompting the growth and release of vapour bubbles. It is possible to notice that the influence of temperature on the vapour bubble is limited by the proximity to the heated wall, as the bubble temperature rapidly decreases subsequent to the rupture of the liquid ligament.

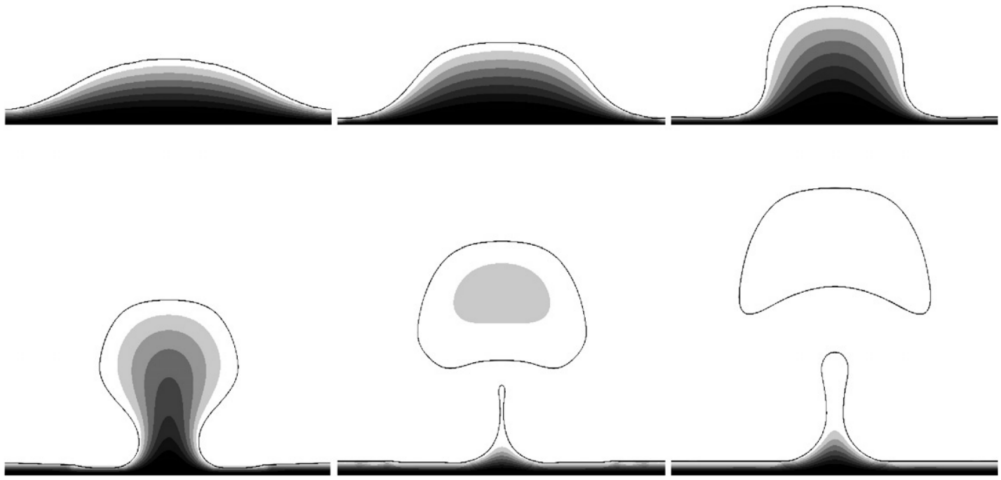

Figure 2.37: The evolution of a vapour bubble growth and detachment from a solid surface [209].

Ranjan et al. [210] applied the Schrage model to simulate evaporation in capillary wick structures. These are commonly used in cooling devices to maximise the heat transfer rate and minimise thermal resistance. Due to the non-isothermal nature of the phenomena, a surface tension gradient will develop on the interface, leading to Marangoni convection. Overall, the induced flow due to temperature differences increases the heat transfer rates. However, if the wall superheat is extremely low, convection has a negligible effect on the evaporation mass flux. Higher contact angles lead to a lower evaporation heat transfer due to the decrease of the wetting area. Qiu et al. [211] performed experimental and numerical condensation studies on circular tubes under microgravity conditions. Both the Lee and the Schrage model (based on the Hertz-Knudsen equation) are implemented in the 2D-axisymmetric simulation coupled with the VOF method. Overall, both models display similar trends regarding both local heat transfer coefficients and wall temperatures. In terms of fluid temperature, the Schrage model is not capable of correctly simulating the mass transfer rate, as the model underpredicts the temperature due to γ not being adjusted for the test case. In the case of the Lee model, saturation temperature is achieved for phase change conditions, therefore validating the numerical model for the current application. De Schepper et al. [212] simulated different flow regimes during film boiling in a convection tube of a steam cracker under an Euler-Euler formulation. These can be visualised on figure 2.38. Due to the continuous mass evaporation, the amount of vapour increases, which has a higher velocity than the liq-

uid phase. This leads to the transition between different regimes (bubble and slug flows for initial stages, wavy and stratified flows for later stages).

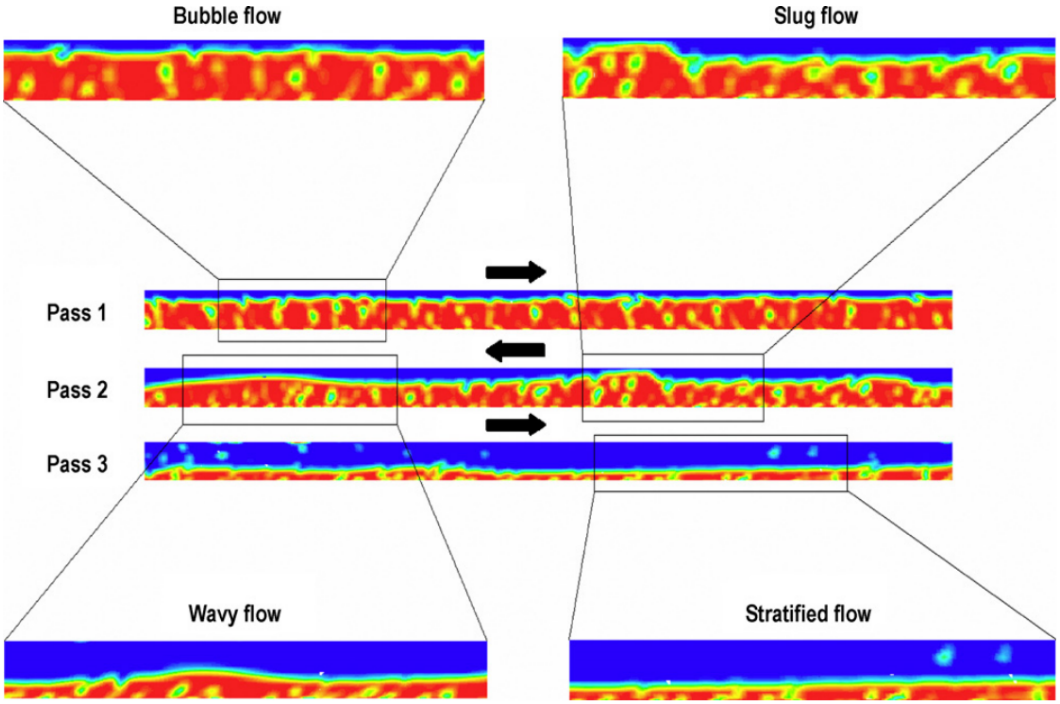

Figure 2.38: Volume fraction fields for different flow patterns in a condensed tube of a steam cracker [212].

Son and Dhir [213] also investigated the flow regime evolution during film boiling using the LS method for interface tracking coupled with the energy jump condition for phase change. The accuracy of the continuous surface force (CSF) model decreases with phase change processes. The evolution of the liquid-gas interface was analysed for different wall superheats. For low temperatures, the bubbles are released alternatively between bubble nucleation sites or, as the authors mentioned, nodes and antinodes. An increase in the wall superheat leads to the formation of vapour bubbles on both nodes, which is in agreement with experimental results present in the literature. Chen et al. [214] studied FC-72 condensation in microchannels, focusing on heat and fluid flow. Fluid patterns are similar to previous studies [212], as the flow develops and transitions between regimes based on both distance from the inlet and wall temperature. Yap et al. [215] presented a three-phase flow model with phase change, followed by a comparison to standard verification examples. These include one and two-dimensional vaporisation problems, rising bubble and falling droplet, and solidification, as can be seen by figure 2.39. This model utilises two level-set functions, as opposed to one level-set function by Osher and Sethian [178], providing a different approach to interface tracking. Sielaff et al. [216] focused on the coalescence of two single bubbles with varying distances of nucleation sites. The numerical work utilises the VOF method with the energy jump condition to account for coalescence and phase change effects, respectively. Pressure variations affect the coalescence frequency, and different spacings between nucleation sites affect the optimal pressure.

Pournaderi and Pishevar [217] proposed a new approach to simulate droplets impacting onto

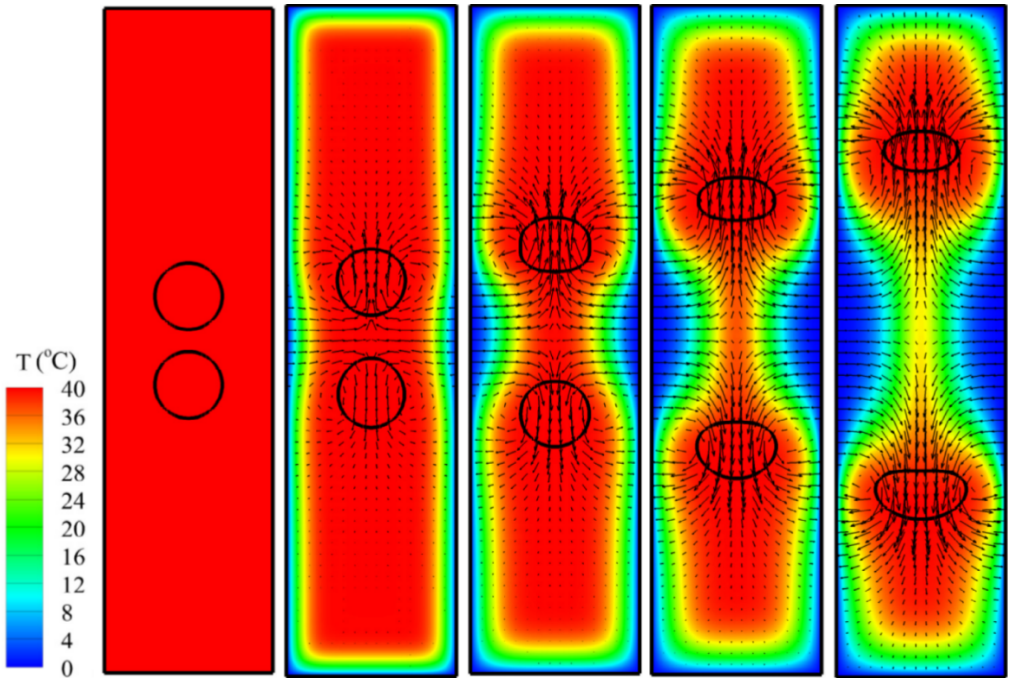

Figure 2.39: Rising bubble and droplet during free-fall at saturation temperature with phase change [215].

heated surfaces. The procedure involves solving the mass, momentum and energy equations coupled with the level set method for interface tracking and the ghost fluid method for interfacial jump conditions. Heat transfer is evaluated as a function of several parameters, such as impact velocity and surface tension. An increase in the impact velocity leads to an increase in both the heat transfer rate and heat dissipation, and a decrease in surface tension leads to similar effects. Polymeric additives show no significant influence on heat transfer characteristics. Alizadehdakhel et al. [218] analysed two-phase flow dynamics with evaporation and condensation on a thermosyphon, focusing on the input heat flow and fill ratio. Temperature measurements along the thermosyphon display a good agreement with experimental data with the exception of the adiabatic regime, which is due to energy losses not being considered in the numerical model. The thickness of the liquid film increases downwards, which may cause a decrease in thermal resistance at the upper regions of the thermosyphon. For the measured regimes, a fill ratio of 0.5 is optimal in terms of performance, as higher values induce the formation of liquid film or large bubbles in the lower parts of the evaporator, decreasing the heat transfer rate and, consequently, the efficiency of the thermosyphon.

Sato and ňiceno [219] proposed a mass conservative phase change model that calculates the mass transfer rate directly at the interface. It is based on the energy jump condition applied to the incompressible Navier-Stokes equations, including the enthalpy conservation equation. Verification of the numerical model involves several study cases, such as the growing of a spherical vapour bubble in a superheated liquid where gravity is neglected, and rising of a vapour bubble under similar conditions with gravity enabled. Additionally, nucleate pool

boiling simulations are conducted and compared with experimental data for a better assessment of the numerical model. The life cycle of a vapour bubble can be visualised on figure 2.40. The colors represent temperature fields, where blue corresponds to $T - T_{sat} = 0.5\,\mathrm{K}$ and pink to $T - T_{sat} = 9.0\,\mathrm{K}$. It is possible to identify the different stages of vapour bubbles life cycle. Initially, the vapour bubble increases in size until reaching a critical condition in which the air-liquid ligament breaks, detaching from the surface. From that point onwards, the vapour bubble will rise due to buoyancy forces until eventually reaching the liquid-gas interface. On the impact surface, a new vapour bubble is formed on that same nucleation site, beginning a new cycle. Subsequent to detachment, the temperature of the vapour bubble rapidly stabilises, as the wall temperature has a more significant local than global effect on the vapour bubbles.

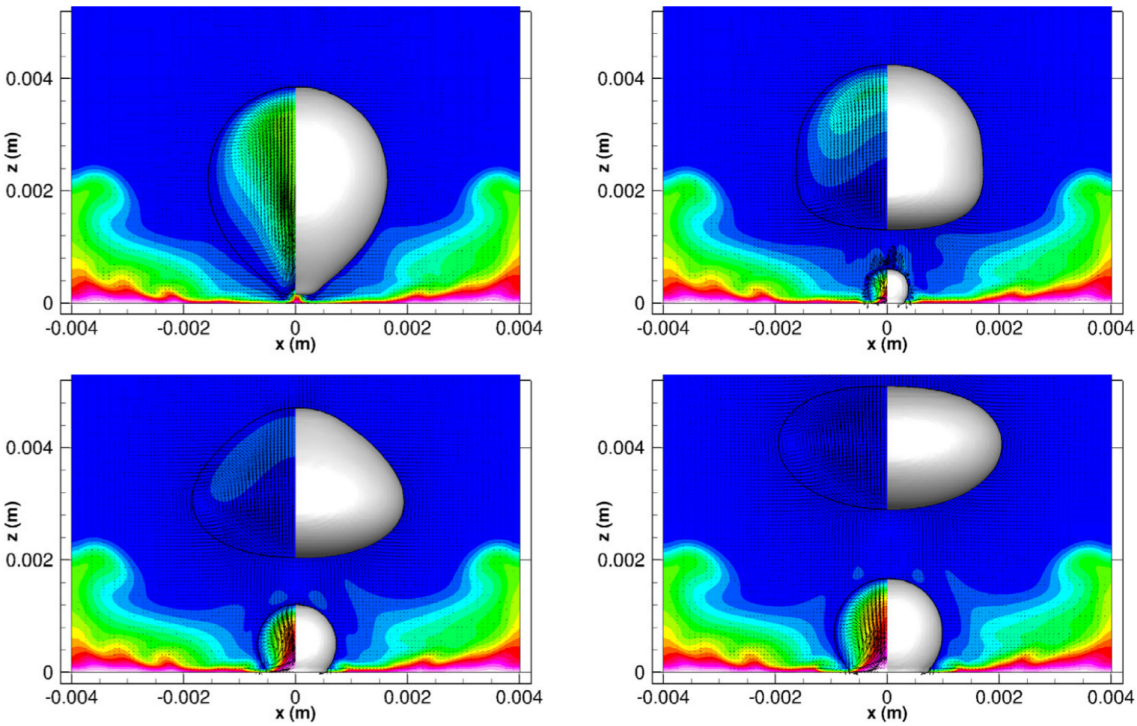

Figure 2.40: Nucleation, growth and detachment of vapour bubbles under saturated boiling regimes [219].

Chapter 3

Experimental Methodology

Following the literature review, the present chapter focuses on the experimental methodology of the phenomena of droplet impact onto heated liquid films. This involves the experimental setup and correspondent components, methodology, post processing procedure for diameter and impact velocity measurements, among others. Due to the presence of a heat flux, the liquid film characterisation will also be provided in terms of temperature and evaporation rate.

3.1 Introduction

Designing and building an experimental setup focused on single droplet impact onto heated liquid films requires a thorough understanding of fluid mechanics, heat transfer and dissipation, among others. In order to properly design this facility, there were several concepts taken into consideration during this process. Initially, due to the presence of a heated liquid film (which implies a heat flux from a heat source), the materials must be capable of withstanding high temperatures, as well as a wide range of temperatures, ranging from ambient temperature up to the saturation temperature of the fluid. The surface requires optical access (transparent to both visible and infrared lighting) in order to capture the impact phenomena, such as borosilicate glass or quartz. Materials with high thermal conductivity are recommended to avoid heat dissipation and maintain a constant temperature at any region containing liquid film. However, materials with these specific properties are extremely scarce and/or not affordable, such as diamond or sapphire. Therefore, there must be a compromise between thermal and optical properties for an optimal setup. The impact surface should have a radial configuration to account for wave propagation due to the existence of a liquid film. This surface must prevent fluid leakage and guarantee a certain liquid film thickness throughout the experiments. Curvature near the base and radial wall (similar to a petri dish) is not optimal, as it distorts the image visualisation due to the local curvature and increases the difficulty in calculating the liquid film thickness (an integral of the surface diameter as a function of its volume would be required to specify a certain liquid film thickness). In terms of heat source, the standard approach in the literature is to heat the surface by cartridge heaters embedded in the element (conduction), allowing to control both the heat flux and wall temperature with the aid of embedded and external thermocouples.

Considering the specifications mentioned previously, an experimental facility was adapted and optimised to account for droplet impact dynamics and heat transfer. This includes droplet and liquid film inertial and geometrical parameters, such as droplet diameter, impact ve-

locity, and liquid film thickness, temperature variations from ambient conditions up to the saturation temperature of the fluid, as well as different fluids.

3.2 Experimental Setup

The experimental setup is illustrated in figures 3.1 and 3.2, where the former relates to the general setup, and the latter to an adaptation for the vapour bubble measurements on the impact surface. The individual components of the setup include the droplet dispensing system, the imaging acquisition, the heating system, the impact surface, the illumination set and the precision scale.

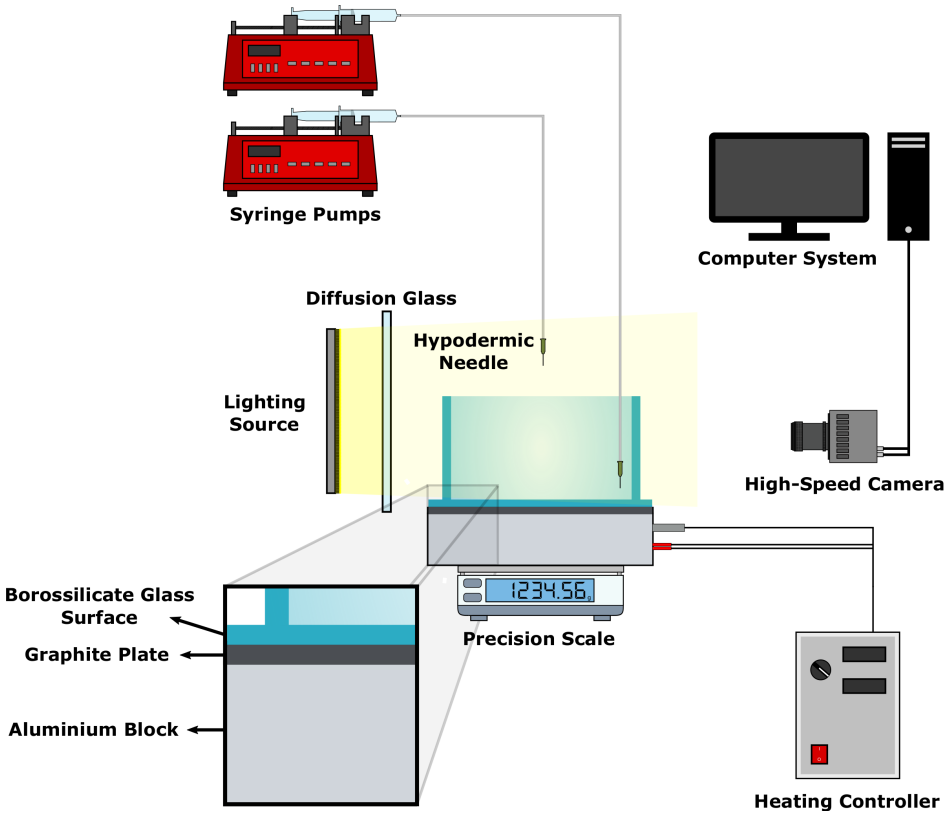

Figure 3.1: Schematic of the experimental setup.

The droplet dispensing system consists of two NE-1000 syringe pumps (New Era Pump Systems Inc., Farmingdale, NY, USA) connected through tubes to a hypodermic needle. The syringe pump with the hypodermic needle aligned at the periphery of the impact surface is related to the evaporation rate, whereas the syringe pump at the centre of the surface corresponds to the droplet impact. By imposing a specific flow rate on the syringe pump (as a function of the volume and diameter of the syringe), these will push the fluid through the plastic tubes until reaching the hypodermic needle. The syringe pump can be visualised in figure 3.3. The droplet will slowly form at the tip of the needle and, by adjusting the flow rate, detach when the gravity forces exceed the surface tension forces. At this point, the droplet enters a free-fall motion, oscillating at the initial stages due to ligament breakup between the droplet and the tip of the needle. These slowly dissipate until the droplet stabilises during its

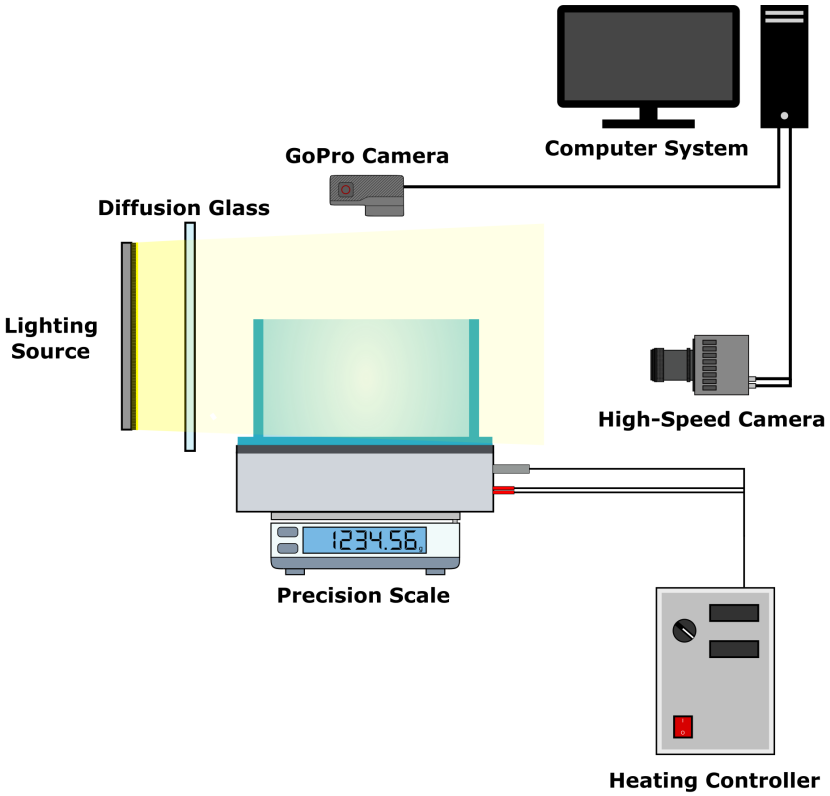

Figure 3.2: Adapted schematic of the experimental setup for the vapour bubble measurements.

Figure 3.3: Ne-1000 syringe pump.

descent, increasing in velocity due to the influence of gravity.

Subsequently, the droplet impinges onto a stationary liquid film supported by a borosilicate glass container. This container was specifically designed to account for numerous experimental conditions. Borosilicate glass is an affordable material in comparison to high-end materials, such as quartz glass or sapphire, and easier to manufacture. It has a low coefficient of thermal expansion, making it highly resistant to thermal shock (approximately $\Delta T = 170°\mathrm{C}$) and a high resistance to chemical stress. The latter provides the surface with an inert behaviour, meaning that it will not chemically interact with the liquid film. The translucent nature of the borosilicate glass provides optical access to the impact phenomena

by means of high-speed imaging. As previously mentioned, typical transparent materials are associated with low values of thermal conductivity, which is the case for borosilicate glass. This leads to a lower heat flux between the source and the surface (which acts as an insulator material). In accordance with the previous properties, borosilicate glass was the most optimal choice in terms of optical and thermal properties for the current setup. Figure 3.4 exhibits the borosilicate glass two-part container. The initial hypothesis for this container was a single surface which could support the liquid film without fluid leakage. This would guarantee a specific liquid film thickness throughout the experiments, which is a significant parameter for droplet impact onto wetted surfaces. However, one-part containers with these specifications were unavailable due to different reasons which were mainly related to mass production issues and manufacturer limitations. Petri dishes were initially considered for temperature measurements and impact studies, however difficulties arose regarding manufacturing precision and local base curvatures, which would affect both impact visualisation and temperature fields. Following this chain of reasoning, a glass plate of dimensions $150\ \mathrm{mm} \times 150\ \mathrm{mm} \times 2\ \mathrm{mm}$ and a hollow cylinder with an internal diameter of $D = 120\ \mathrm{mm}$ and a thickness of $e = 5\ \mathrm{mm}$ were acquired (Normax, Portugal). As represented in figure 3.4, the glass plate is the base of the container and the hollow cylinder is the radial wall surrounding the liquid film. These have to be attached in order to prevent fluid leakage in the contact area between the plate and the cylinder. An acetoxy silicone, LOCTITE® SI 5366, is a bonding agent specifically designed for sealing up to operating temperatures of $T = 250°\mathrm{C}$. It requires 5 minutes of surface curing exposed to atmospheric moisture to dry, followed by a full cure process of 7 days for optimal physical, thermal and electrical properties. This sealing agent does not chemically react with the fluids, such as water and fuels, meaning that no contamination occurs within the liquid film.

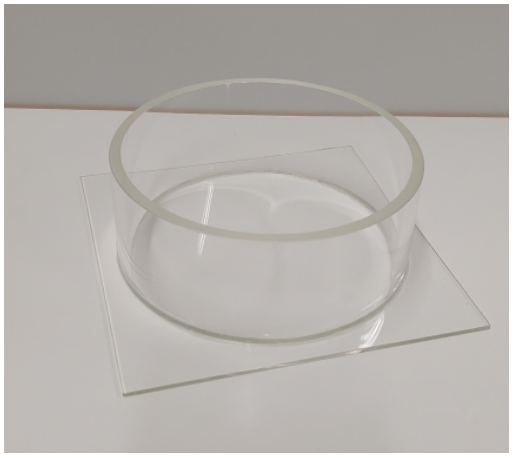

Figure 3.4: Borosilicate glass container.

The two-part borosilicate glass surface is positioned over an aluminium block that acts as a heat source in order to heat the liquid film by conduction. The heating system is the main element of the experimental setup, as presented by figure 3.5. It is composed of a heating device connected to an aluminium block of dimensions $150\ \mathrm{mm} \times 150\ \mathrm{mm} \times 30\ \mathrm{mm}$ (Mecafil, Portugal). Fixated laterally into the aluminium block are four embedded cartridge heaters of $250\ \mathrm{W}$ each, providing a heat source and, consequently, a heat flux through conduction. Each

cartridge heater has a length of $125\ \mathrm{mm}$ and is positioned $12\ \mathrm{mm}$ beneath the aluminium surface. The design and datasheet of the aluminium block are exhibited in Appendix B. In order to control the temperature imposed on the impact surface, a type-k thermocouple is embedded in the aluminium block $7.5\ \mathrm{mm}$ below the aluminium surface. The desired temperature is imposed on the heating device, triggering the heating coils within the cartridge heaters. When the temperature measured by the thermocouple coincides with the temperature imposed on the heating device, the heating coils shut down. If the thermocouple measurement deviates from the heating device temperature, the heating system is designed to correct these variations, either by heating the aluminium block or decreasing its temperature due to heat loss to the surroundings (by switching off the cartridge heaters). The imposed heat flux is oriented upwards, heating the borosilicate glass surface and the static liquid film, providing uniform temperature fields. A graphite plate of dimensions $150\ \mathrm{mm} \times 150\ \mathrm{mm} \times 4\ \mathrm{mm}$ is positioned amidst the aluminium block and the borosilicate glass surface. The main reason for an additional plate is to block the lighting reflections of the aluminium on the liquid film, which influences both high-speed and thermal imaging. The thermal conductivity of graphite is extremely high, acting as a heat conductor and providing a more uniform temperature field.

(a) (b)

Figure 3.5: Heating system: a) Heating controller device; b) Aluminium block with embedded cartridge heaters.

In terms of image acquisition, the droplet impact phenomena are captured by a high-speed digital camera, namely a Photron FASTCAM mini UX50 (Photron, Tokyo, Japan). The 1.3 megapixel CMOS sensor provides an image resolution of 1280×1024 pixels at a frame rate of 2000 fps for full frame performance, reaching a maximum frame rate of 160000 fps for reduced resolutions (1280×8 pixels). This camera is equipped with a high-speed Gigabit Ethernet interface, providing a stable connection to a local computer and allowing for secure file transfer. A manual trigger input is adopted to initiate the recording of the impacting phenomena. A Macro Lens Tokina AT-X M100 AF PRO D (Kenko Tokina Co., Ltd., Tokyo, Japan) is coupled to the high-speed camera to allow for a higher spatial resolution at a focusing distance of $0.3\ \mathrm{m}$, as well as variable aperture and focal plane. In terms of vapour bubbles on the impact surface, a different recording device was required due to the need of

fully capturing the borosilicate glass surface. Therefore, a GoPro Hero 6 with lapse settings was adopted for a top-view analysis of the liquid film. This camera and settings enable image acquisition during extended periods of time and on a wider physical frame in comparison to the high-speed digital camera, meaning the spatial accuracy is reduced. There cameras are displayed in figure 3.6. Opposed to the high-speed camera, as displayed in figure 3.1, a 20 W light-emitting diode (LED) lamp supplies a powerful light-focused source, which requires light diffusion through a specific glass to provide uniform lighting of the impact phenomena.

(a) (b)

Figure 3.6: Image acquisition systems: a) Photron FASTCAM mini UX50 with a Macro Lens Tokina AT-X M100 AF PRO D; b) GoPro Hero 6.

The precision scale is employed to verify the liquid film weight and, consequently, its thickness. This will be thoroughly detailed in the next section, as it is a defining step in the experimental methodology.

3.3 Experimental Methodology

Figure 3.7 depicts a flowchart of the experimental procedure for single droplets impinging onto heated liquid films. Prior to studying the droplet impact phenomena, we must verify the conditions regarding the surrounding air and the droplet/liquid film. Air temperature and humidity were kept at $20 \pm 2°\mathrm{C}$ and $50 \pm 3\%$, respectively. The initial step is determining the droplet impact parameters, namely the diameter and impact velocity. Defining these parameters prior to the impact phenomena is essential, as the dimensionless numbers, such as Reynolds, Weber and Ohnesorge, are dependent on fluids thermophysical properties and geometrical parameters. In order to analyse these properties, a droplet is released from the hypodermic needle, entering a free-fall motion, until impinging onto the liquid film, and both the diameter and impact velocity are measured subsequent to release and prior to impact. The droplet trajectory is recorded with the aid of a high-speed camera at a frame rate of 2000 fps and a shutter speed between $1/16000$ s and $1/25000$ s for the diameter and impact velocity measurements, respectively. A higher shutter was required for the impact velocity due to the proximity of the droplet to the impact surface and liquid film. The droplet diameter is calculated by averaging the horizontal and vertical diameters during free-fall. In contrast, the impact velocity is defined by the vertical difference of centroids of the last

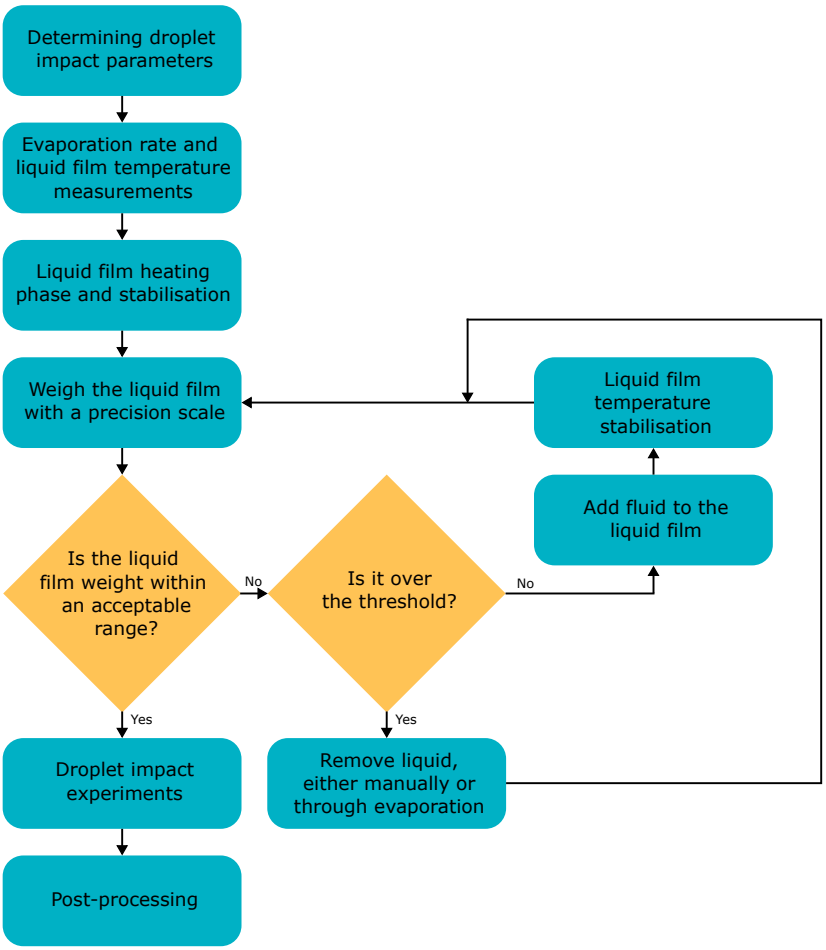

Figure 3.7: Flowchart of the experimental procedure regarding single droplets impacting heated liquid films.

frame before impact and successive prior frames. The horizontal differential is negligible due to the dominated vertical motion of the droplet. A considerable number of frames are analysed to guarantee proper diameter and impact velocity measurements. The MATLAB software is employed for the measurements of these parameters, which is based on binarisation and detection of contiguous regions. These will be thoroughly detailed in following sections. Following the droplet geometrical properties, the liquid film must also be assessed. In isothermal conditions, the fluid evaporation rate is negligible, and the liquid film thickness is solely determined by the ratio between the volume and the area of the surface, as performed by several authors [97, 113, 220]. However, due to the presence of a heat source positioned below the impact surface, the liquid film temperature slowly increases through conduction. This leads to an increase in evaporation rate and, consequently, to a decrease in liquid film thickness. This parameter requires constant monitoring, as it is extremely relevant due to its influence on the impact outcome. A precision scale is adopted to verify the liquid film thickness by weight and the evaporation rate measurements. This process is repeated for each impacting droplet to ensure a constant liquid film thickness. The evaporation rate measurements obtained from the precision scale are associated with a liquid film temperature. The measured temperature on the aluminium block (which is imposed on the heating device) will differ from the liquid film temperature due to heat dissipation to the environment, thermal

contact resistance between the different surfaces, among others. Therefore, liquid film temperature measurements are crucial to determine the fluid thermophysical properties and to characterise both the heating system and the impact phenomena. Several type-k immersion thermocouples are coupled to a height gauge with micrometre precision and connected to a data logger for the liquid film temperature measurements. The details of these thermocouples are presented in Appendix C. The experimental results for temperature and evaporation rate measurements of the liquid film will be presented in the following section.

Once the droplet and liquid film geometrical parameters are fully characterised, the heating phase is initiated. During this phase, a temperature is selected in the heating device, leading to a temperature increase in the aluminium block and, consequently, in the liquid film. The heating phase occurs for earlier stages and, during this process, the liquid film temperature steadily rises, as it is verified by the immersion thermocouple temperature measurements. For the current setup, this phase extends for approximately $t = 10\ \mathrm{min}$. At the end of the heating phase, the liquid film temperature reaches a maximum value, which the heating device is capable of maintaining over extended periods of time. This phase is defined as the stabilisation phase, and the droplet impact experiments are conducted and analysed during this phase. However, due to evaporation, the liquid film thickness initially established prior to the heating and stabilisation phases changes over time, as the liquid film temperature increases from ambient conditions up to the stabilisation regime. Due to this, the liquid film must be re-evaluated prior to the droplet impact to guarantee a specific liquid film thickness throughout the experiments. This can be achieved by weighing the liquid film using a precision scale, as displayed by figure 3.8. This electronic analytical scale has a maximum weighing capacity of $5000\ \mathrm{g}$ and a precision measurement of $0.01\ \mathrm{g}$, which is within the scope of the current work. The weighing procedure is initiated by verifying the liquid film weight during the stabilisation phase, which is dependent on several parameters, such as the surface area, the fluid density at liquid film temperature (thermophysical property temperature dependent), and the liquid film thickness. These measurements are performed during the liquid film stabilisation phase due to the constant liquid film temperature. The borosilicate glass surface with the liquid film is then positioned on the precision scale, and the liquid film weight is assessed. An acceptable range for the liquid film weight presents a relative standard deviation of 2.5% with a confidence interval of 95%. For values outside this acceptable range, two different procedures are taken into account. If the film weight exceeds the recommended threshold, meaning that there is an excess of fluid and, consequently, a higher liquid film thickness, then fluid should be removed, either manually through a syringe or through evaporation over a period of time. This process advances until the liquid film weight is within the acceptable range. If, due to excess evaporation, the liquid film weight drops below the lower threshold boundary, fluid should be added to the liquid film in order to increase its thickness. This requires an additional heating phase until reaching a stabilisation temperature due to the fact that the external fluid added to the liquid film is at ambient conditions, therefore requiring an additional step. In order to optimise this phase, a bath fluid set at liquid film temperature would prevent the need for additional heating phases. The liquid film is then weighted and evaluated for the acceptable threshold values. This iterative process is

concluded when the liquid film weight is within a confidence interval of 95%. These extra steps require exceptional accuracy in handling the fluid addition/removal, weighting, and threshold evaluation in order to achieve the desired liquid film thickness.

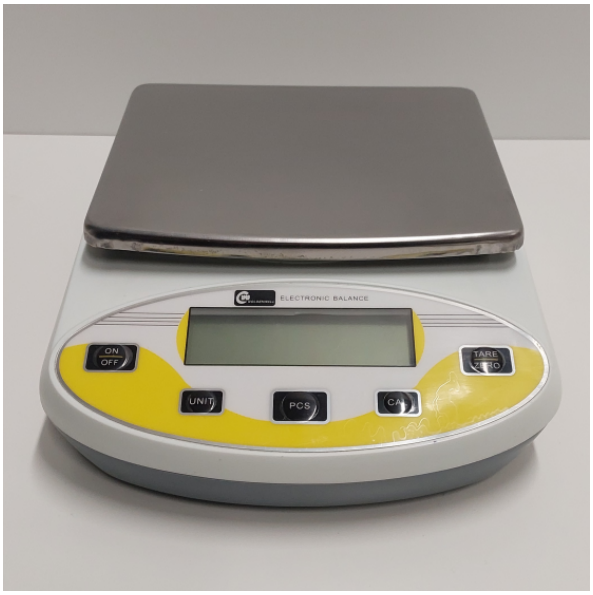

Figure 3.8: Precision scale.

Once all these conditions are met regarding the liquid film and droplet properties, the impact phenomena begin. The droplet is released from the hypodermic needle, impacting the heated liquid film and the event is recorded by means of a high-speed digital camera, as previously stated. The number of impacting droplets per experimental condition usually ranges between 3 and 5 for isothermal conditions, as stated by several authors [75, 221, 222]. Due to the influence of temperature on the liquid film and the impact phenomena, and following previous works [99, 223], a minimum number of 10 droplets are considered for each experimental condition. This ensures both consistency and repeatability of the impact outcomes and experimental results. Water, n-heptane and n-decane are the fluids adopted for the experiments, as these cover a wide range of thermophysical properties and saturation temperature. Further details regarding these fluids are presented in the following section prior to the liquid film temperature and evaporation rate analysis. The gathered experimental data from the image acquisition devices are subjected to a post-processing analysis. The primary assessment of the results consists of image visualisation, focused on identifying different impact outcomes, the influence of both thermophysical properties and saturation temperatures on isothermal and non-isothermal conditions, intrinsic dynamics related to two-phase flows (such as ligament breakup, crown formation and life cycle of vapour bubbles), among others. Different geometrical parameters can be measured from the experimental results, including height and outer diameter of the crown, central jet height and consequent breakup and bubble release frequency. These are achieved by applying a binarisation procedure through a MATLAB algorithm. The specific methods related to subtraction, binarisation and detection techniques are thoroughly detailed in section 3.5.

3.4 Liquid Film Characterisation

In non-isothermal conditions, the phenomena of droplet impact can be governed by the droplet geometrical parameters, such as diameter and impact velocity, the thermophysical properties of the fluids and, in pre-wetted surfaces, the thickness of the liquid film. The different combinations of these parameters define several non-dimensionless numbers, such as the Weber, Reynolds and Ohnesorge numbers, as previously mentioned. However, these do not account for temperature gradients or differences in thermophysical properties within the physical system. Due to the scarcity of droplet impact research regarding heated liquid films, dimensionless numbers related to heat and/or mass transfer have not been implemented to describe temperature-related phenomena, such as the Prandtl (ratio of momentum to thermal diffusivity), Peclet (ratio of convective to diffusive mass transfer) and Grashof (ratio of buoyancy to viscous forces) numbers. The different dimensionless numbers should be adapted to account for both non-isothermal and isothermal conditions.

For the current setup, the thermophysical properties of the droplet and liquid film differ due to the presence of a heat flux positioned underneath the surface. This is identical to the experimental work developed by Xu et al. [159], who investigated the impact behaviour of water droplets onto ethanol surfaces. To distinguish the transition regimes, the authors defined a non-dimensional pool temperature based on the liquid film temperature, the boiling point of the ethanol, and the environmental conditions. Despite the droplet impacting onto a liquid film of a dissimilar fluid, this is analogous to a droplet impacting onto a heated liquid film due to the differences in thermophysical properties, implying a similar approach in terms of dimensionless analysis. Therefore, the dimensionless temperature was adapted to the current work, as exhibited by equation (3.1):

$$\theta = (T_f - T_{air}) \,/\, (T_{sat} - T_{air}) \tag{3.1}$$

This parameter correlates the saturation temperature of the fluid, T_{sat}, the temperature of the liquid film, T_f, and the temperature of the surrounding air, T_{air}. The temperature of the impinging droplet is equal to the ambient temperature. The dimensionless temperature is limited to a working range between $\theta = 0$ and $\theta = 1$, where the former corresponds to ambient conditions ($T_f = T_{air}$) and the latter to saturation conditions ($T_f = T_{sat}$). Maintaining an existing liquid film beyond this range is not possible for the existing experimental setup, which would include cold surfaces (and possible solid-liquid phase change) and stable liquid films for boiling conditions.

As mentioned in the previous section, liquid film characterisation is required in terms of temperature fields and evaporation rates. Water, n-heptane and n-decane are the fluids adopted for the experiments. These fluids were selected based on a number of specifications regarding different aspects. Primarily, a wide range of thermophysical properties and saturation temperatures allow for different studies to be considered, such as the comparison between

low and high viscosity/surface tension fluids, as displayed by table 3.1. Water is a control fluid extensively researched in the literature [6], whereas the n-decane and n-heptane are surrogate fuels for kerosene/jet fuel [7, 8] and diesel [9, 10], respectively. Different fluids were considered for the experiments, such as jet fuel/HVO and mixtures, due to their importance to the modern world, such as the need to mitigate climate change and to achieve lower greenhouse gas emissions. However, several constraints emerged related to the fluids and the borosilicate glass surface. Due to the multi-component nature of jet fuel and biofuel, each component has different saturation points and evaporation rates. When subjected to a constant heat flux, the thermophysical properties of the liquid film are not only dependent on temperature, but also on the mass fraction of each of the components, increasing the difficulty in quantifying the thermophysical properties of the fluids. In terms of the impact surface, the acetoxy silicone used to glue the two parts of the container has a maximum operating temperature of $T = 250°\mathrm{C}$, which is a limiting value in comparison to the boiling point of these fuels, which have an upper boundary up to approximately $T = 300°\mathrm{C}$. This would lead to a lack of structural integrity, causing fluid leakage and possibly damaging the impact surface and aluminium block.

Table 3.1: Thermophysical properties of water, n-heptane and n-decane at room temperature ($T = 20\ °\mathrm{C}$) and correspondent saturation temperatures.

Fluid	$\rho\,[\mathrm{kg/m^3}]$	$\mu\,[\mathrm{mPa\,s}]$	$\sigma\,[\mathrm{mN/m}]$	$T_{sat}\,[°\mathrm{C}]$
Water	998.2	1.002	72.73	99.8
N-heptane	685.8	0.412	20.29	98.4
N-decane	732.1	0.929	23.89	174.1

3.4.1 Temperature

Prior to performing liquid film temperature measurements, the temperature fields of the different surfaces, namely aluminium, graphite and borosilicate, were verified. These were performed to provide insight in terms of heat conduction, dissipation, and temperature layers. Six type-k immersion thermocouples were placed on the different surfaces, and concealed with aluminium tape to ensure both proper adhesion on the surface, and isolation from the surrounding environment, ensuring a higher accuracy in terms of temperature measurements. The thermocouples placement on solid surfaces is analogous to the liquid film and is illustrated in figure 3.9a. The thermocouple probe positioned in the impact region is displayed by the blue cross, represented by P_1. The red crosses, which refer to the remaining thermocouples, are oriented both straight (P_4, P_5, P_6) and radially (P_2, P_3, P_4). This orientation allows for tangential and radial temperature profiles. The average temperature measurements and correspondent standard deviation on the different solid surfaces are presented in table 3.2, and the surface layering is displayed in figure 3.1. The temperatures and standard deviations correspond to the averaging of the six thermocouple measurements during the stabilisation phase, meaning that it accounts for both the radial and straight-oriented thermocouples. In terms of temperature variation, the measurements on the aluminium are identical to the heating element temperature. A slight decrease is verified for higher tem-

peratures ($T_{he} = 170°\mathrm{C}$ and $T_{he} = 190°\mathrm{C}$), which is expected due to the temperature differences between the aluminium block and the surrounding air. For the standard deviation, lower temperatures display a lower value ($\sigma_{st_{Al}} \approx 0.2°\mathrm{C}$), increasing for higher temperatures ($\sigma_{st_{Al}} \approx 0.5°\mathrm{C}$). The addition of a second layer (graphite) causes a material dissimilarity in the contact region, inducing a thermal contact resistance. As graphite possesses a high thermal conductivity, temperature differences are solely due to the thermal resistance and possible heat losses to the environment. For lower temperatures, $T_{he} < 70°\mathrm{C}$, the temperature differences are not noticeable. However, higher heating element temperatures show a slight decrease in the temperature measurements, as these display discrepancies ranging between $T = 2°\mathrm{C}$ and $T = 3°\mathrm{C}$. The third layer, which relates to the borosilicate glass impact surface, creates a thermal contact resistance between the graphite and the borosilicate layers. Opposite to the previous layer, the thermal conductivity of borosilicate glass is relatively low, meaning that the temperature fields are expected to be influenced. Lower temperatures ($T_{he} < 70°\mathrm{C}$) exhibit a temperature drop ranging between $T = 1°\mathrm{C}$ and $T = 2°\mathrm{C}$, whereas for higher temperatures, a selected heating element temperature of $T_{he} = 190°\mathrm{C}$ leads to a surface temperature of $T_{Gl} = 181.6°\mathrm{C}$. The standard deviation is relatively similar for all surfaces.

This preliminary study enables the distinction between temperature profiles, as well as predicting the heated liquid film regime. Transitioning from solid to wetted surfaces is the following step, as the liquid film is formed above the borosilicate glass surface. The liquid film temperature measurements are performed by positioning the six type-k thermocouples within the liquid film. However, the approach of concealing the thermocouples with aluminium tape is only applicable to solid surfaces. In the case of liquid films, the thermocouples should be positioned in a configuration similar to figure 3.9b. These are placed within the liquid film with a $90°$ curvature to maximise the contact area between the thermocouple and the liquid (and minimise the influence of the surrounding air), as well as maintaining a minimum distance from the solid wall. The distribution of the thermocouples in the liquid film is represented by figure 3.9a. Considering the thin liquid films used in the experimental conditions, guaranteeing a proper positioning of the thermocouples in terms of spatial distribution and liquid depth is crucial for temperature measurements. In order to properly position the thermocouples in the liquid film, these were coupled to a height gauge with micrometre precision. This instrument provides height measurements from a reference surface by applying a vertical motion. Due to the Vernier scale present in these devices, an accuracy in the order of micrometres can be achieved. The measurements were performed at a vertical distance of $0.1 \pm 0.05\ \mathrm{mm}$ from the borosilicate glass surface. In terms of spatial distribution, a component consisting of metal hollow tubes connected to a plate was attached to the height gauge, where each tube corresponds to the placement of a thermocouple.

The liquid film temperature measurements were performed for water, n-heptane and n-decane, ranging from ambient temperature up to the saturation temperature of the fluid. The methodology was stated in the previous section, in which the thermocouples are positioned in the liquid film, and the heating device is set for a specific temperature. From

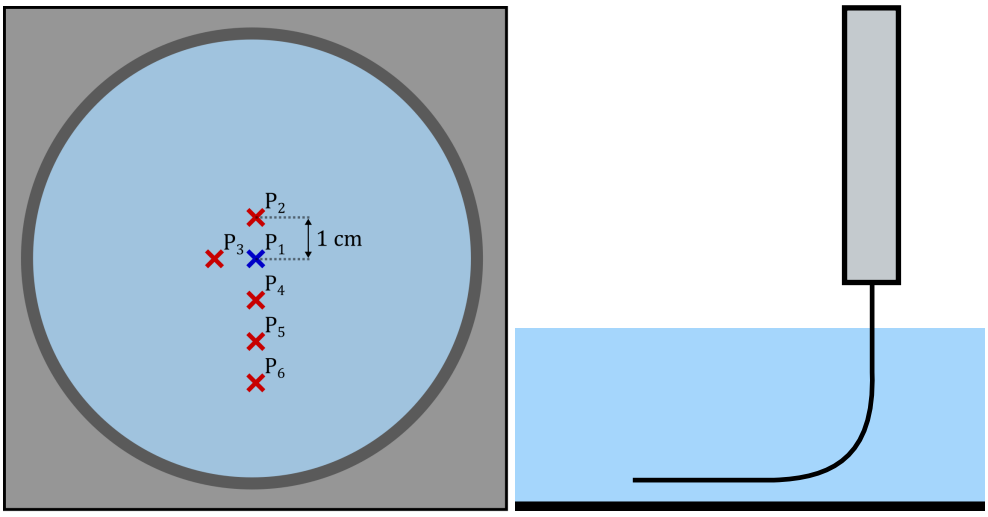

Figure 3.9: Thermocouple positioning on the liquid film. P_1 refers to the position of the first thermocouple, P_2 to the position of the second thermocouple, and so forth: a) Thermocouple displacement in the liquid film; b) Visual representation of the immersed thermocouple.

Table 3.2: Temperature measurements and standard deviation for the aluminium (Al), graphite (Gr) and borosilicate glass (Gl) surfaces.

T_{he}[°C]	T_{Al} [°C]	$\sigma_{st_{Al}}$ [°C]	T_{Gr} [°C]	$\sigma_{st_{Gr}}$ [°C]	T_{Gl} [°C]	$\sigma_{st_{Gl}}$ [°C]
30	30.01	0.15	29.96	0.13	30.14	0.22
40	40.02	0.20	40.15	0.22	39.19	0.07
50	50.30	0.35	50.00	0.24	49.29	0.12
60	60.10	0.32	59.85	0.11	58.87	0.09
70	70.33	0.28	70.01	0.32	68.50	0.14
80	80.45	0.22	79.47	0.22	78.01	0.13
90	90.41	0.41	89.18	0.19	87.64	0.24
100	100.43	0.21	99.25	0.24	97.20	0.17
110	110.46	0.39	108.97	0.20	106.65	0.32
130	130.21	0.35	128.61	0.37	125.45	0.40
150	149.76	0.49	147.66	0.27	144.16	0.37
170	169.57	0.55	166.82	0.46	162.8	0.48
190	189.22	0.47	186.16	0.42	181.63	0.45

that point onward, the liquid film temperature is continuously affected by the heat source, increasing in temperature until reaching a stabilisation temperature. Figures 3.10 and 3.11 display the evolution of temperature over an extended period of time for n-heptane and water, respectively. For figures 3.10a and 3.10b, a temperature of $T_{he} = 70°\mathrm{C}$ is selected in the heating device. Prior to the measurements, the liquid film is at ambient temperature or a lower selected temperature from a previous experimental condition. In the initial stages, the liquid film undergoes a sharp increase in its temperature. For $t > 10$ min, temperature reaches a stable condition of approximately $T_f = 66.5°\mathrm{C}$, which is slightly lower than the one established on the heating device. The liquid film averaging temperature and standard deviation are calculated during the stabilisation phase, as the heating phase corresponds to a

transient state which is not suited for quantifying the liquid film properties. The temperature measurements in the former phase are performed for a minimum of $t = 20$ min for a proper assessment of the liquid film properties. In terms of oscillations, it is possible to verify that temperature stabilises relatively smoothly for lower temperatures. However, increasing the heating device temperature to $T_{he} = 110°\mathrm{C}$, as presented by figure 3.10b, leads to a more unstable condition in comparison to lower temperatures, increasing the standard deviation of the temperature measurements. For this condition, the n-heptane liquid film stabilises at a temperature of $T_f = 95.7°\mathrm{C}$, which is close to the saturation temperature of the fluid. At this regime, the liquid film exhibits a state of continuous boiling, in which vapour bubbles nucleate on the impact surface, increasing in size until detaching and bursting onto the liquid film surface, creating wave instabilities. Higher heating element temperatures will display similar liquid film temperatures, as the energy provided by the continuous heat flux contributes to phase change processes.

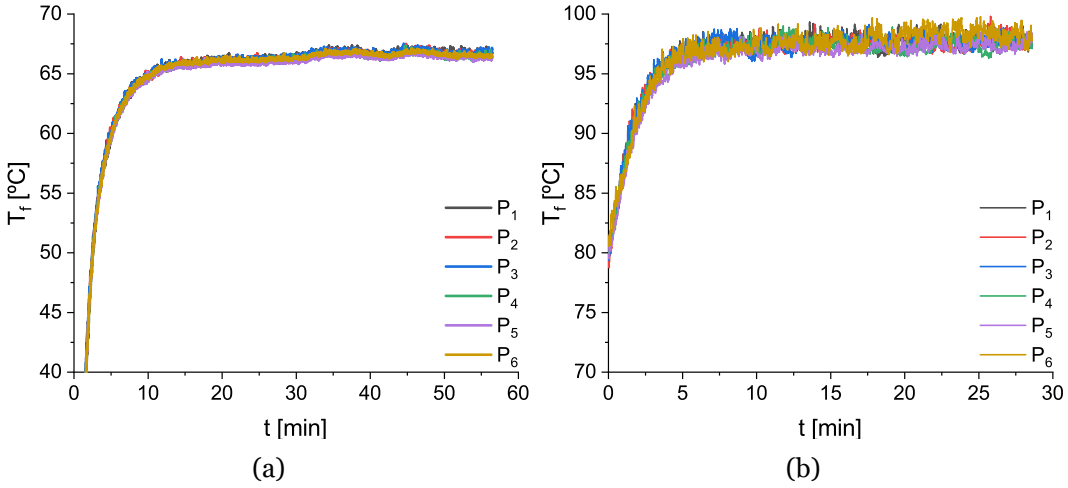

Figure 3.10: Liquid film temperature measurements of n-heptane as a function of time for a selected temperature on the heating device: a) $T_{he} = 70°\mathrm{C}$; b) $T_{he} = 110°\mathrm{C}$.

For water, the stabilisation temperature as a function of the heating device temperature, as seen by figure 3.10, is considerably lower in comparison to n-heptane, as a temperature of $T_{he} = 50°\mathrm{C}$ leads to a liquid film temperature of $T_f = 45.6°\mathrm{C}$. This is an identical absolute temperature loss to the n-heptane at a temperature of $T_{he} = 70°\mathrm{C}$, which is due to the differences in thermophysical properties. Water has a higher specific heat capacity in comparison to n-heptane, meaning that more energy is required to change the temperature of the fluid per unit mass. Additionally, the thermal diffusivity, which is the ratio of the heat conduction to heat storage capabilities, is lower in water than in fuels. For identical heating device temperatures, which translates to similar heat fluxes, fuels reach a higher stabilisation temperature relative to water. The standard deviation for water measurements also increases for the different temperature ranges. However, these oscillations are predominant with water liquid films due to both the high surface tension and the absence of a Marangoni effect. Fuels are characterised by low values of surface tension, meaning that these fluids accumulate on the walls of the borosilicate glass container, as well as on the immersion thermocouples. This creates a protective coating surrounding the thermocouples, minimising heat transfer

processes with the surrounding environment. However, this does not occur for water liquid films, meaning that a portion of the thermocouple is directly exposed to the surrounding air, influencing liquid film temperature measurements. For higher temperatures, these oscillations are amplified due to a larger temperature difference between the liquid film and the surrounding air. For figure 3.11b, a heating device temperature of $T_{he} = 110°\mathrm{C}$ results in an average liquid film temperature of $T_f = 79.6°\mathrm{C}$, which is considerably lower. For this condition, a slight decrease in temperature is verified over extended periods of time for the different thermocouples. Due to how the immersion thermocouples are positioned in the liquid film, as visualised in figure 3.9b, the liquid film thickness slowly decreases, exposing a higher portion of the thermocouples to the surrounding environment. This results in the temperature measurements experiencing a slight decrease for increased time exposures. The placement of the thermocouples within the liquid should be improved to suppress the influence of the surrounding environment.

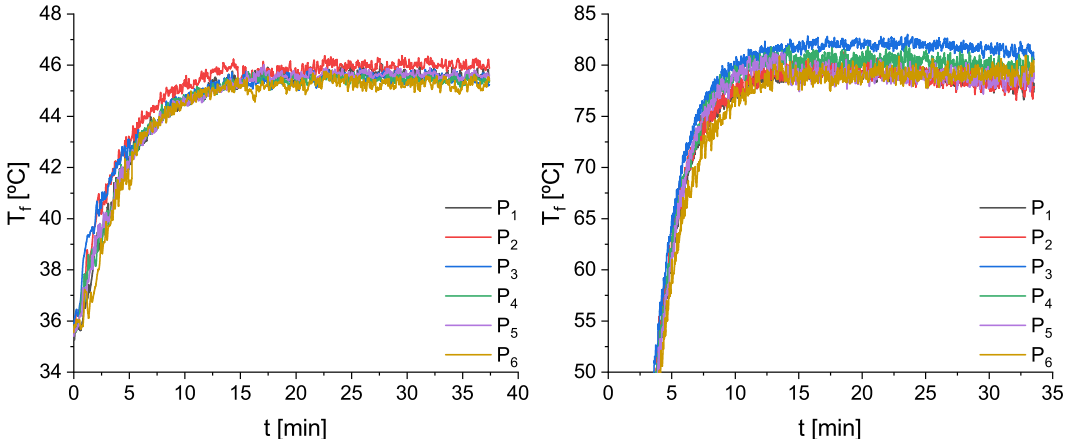

Figure 3.11: Liquid film temperature measurements of water as a function of time for a selected temperature on the heating device: a) $T_{he} = 50°\mathrm{C}$; b) $T_{he} = 110°\mathrm{C}$.

The liquid film measurements were analysed as a function of the selected heating device temperatures, as exhibited by figure 3.12, where the colored dashed horizontal lines correspond to the saturation temperature of the fluids. N-decane features a wider range of temperatures due to a higher saturation temperature ($T_{sat} = 174.1°\mathrm{C}$). For temperatures close to the ambient temperature, fluids display similar values, as heat losses are negligible. For $T_{he} \geq 70°\mathrm{C}$, water does not follow a linear tendency as opposed to n-decane and n-heptane. This is explained due to the differences in thermophysical properties, namely the specific heat capacity, as previously mentioned. In order to reach the water boiling point, a heating device temperature of $T_{he} = 150°\mathrm{C}$ is required. For the fuels, these maintain an identical linear for the studied temperature range. N-heptane reaches the boiling point for $T_{he} = 110°\mathrm{C}$, whereas n-decane requires a selected heating device temperature of $T_{he} = 190°\mathrm{C}$. Temperatures above the saturation temperature of the fluids ($\theta > 1$) are unattainable to the current experimental setup, as the liquid film reaches its maximum temperature (saturation temperature) for a specific heating device temperature and, for values beyond this threshold, the energy added to the system contributes solely to the liquid film phase change, substantially

increasing its evaporation rate. The maximum relative error associated with the temperature measurements is 2.02% for water, 0.45% for n-heptane and 0.52% for n-decane.

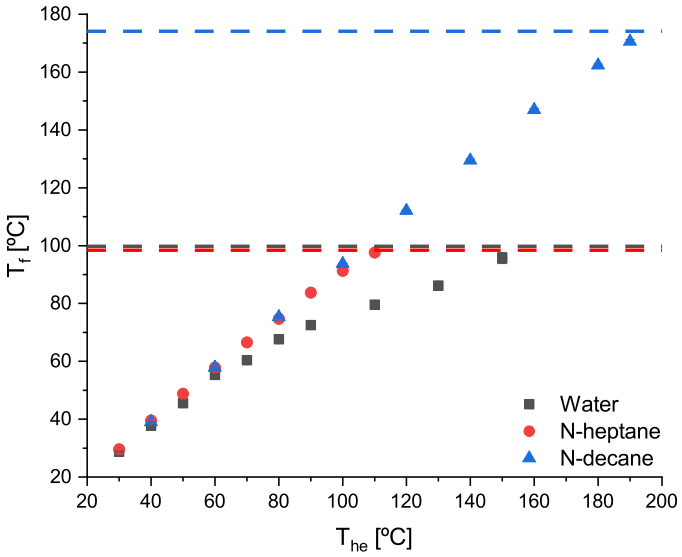

Figure 3.12: Liquid film temperature measurements of water, n-heptane and n-decane as a function of the heating element temperature. The dashed horizontal lines correspond to the saturation temperature for each of the fluids.

3.4.2 Evaporation Rate

In order to guarantee a constant liquid film thickness throughout the experiments, the evaporation rate of the different fluids as a function of temperature must be quantified. The primary method for the evaporation measurements relies on weighting the liquid film with a precision scale. In order to follow a standard procedure for the evaluation of the evaporation rate, the borosilicate glass surface weight is determined prior to these experiments without the presence of the liquid film. Following this step, a known volume of fluid is added onto the impact surface, which translates to a specific weight. This value is registered as the liquid film initial weight. The impact surface is positioned above the aluminium block, which acts as the heat source of the experimental setup. A temperature is selected on the heating device, triggering the cartridge heaters and increasing the temperature of the surrounding elements. As previously mentioned, the liquid film temperature displays an initial heating phase, followed by a stabilisation period where its temperature reaches a steady condition. The evaporation rate measurements are performed for the latter stage, similarly to the averaging film temperatures. The stabilisation phase is characterised by a linear mass change over time, meaning a constant liquid film temperature. During this phase, the borosilicate glass surface containing the liquid film is weighed every $t = 5$ min for a minimum duration of $t = 20$ min in the stabilisation phase, similarly to the liquid film temperature measurements. The container is shifted between the aluminium surface and the precision scale for these measurements, assuring a minimum time allocation for this procedure and reducing heat losses during the weighing phase. The evaporation rate is obtained by analysing the liquid film weight variation for a constant liquid film temperature. Due to the existence of a liquid surface whose thickness varies over time, the liquid film evaporation rate, which is ini-

tially defined as a mass flow rate, is converted into a thickness velocity of units $\mathrm{mm/min}$. The secondary method utilises the high-speed digital camera to capture the liquid-gas interface, tracking its thickness variation over time, as demonstrated by figure 3.13. This is a direct approach in terms of measuring the liquid film thickness variation, providing validation for the weighing method. The liquid-gas interface is detected through binarisation, similar to the identification of the droplet during free-fall. The specifications of this method are presented in the next section.

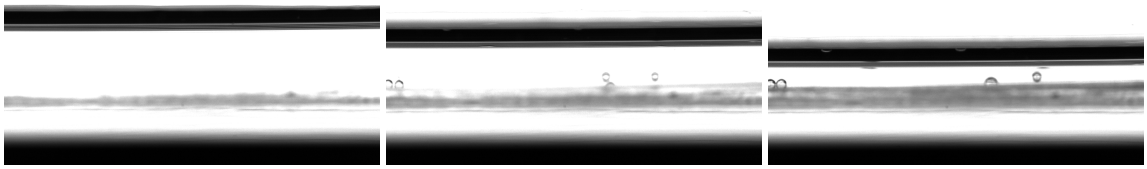

(a) (b) (c)

Figure 3.13: Liquid film thickness variation due to the presence of a heat flux: a) $t = 0$ min; b) $t = 10$ min; c) $t = 20$ min.

Figure 3.14 features the liquid film thickness variation as a function of temperature for the weighing and interface tracking methods. Both methods are capable of accurately measuring the water liquid film variation. As expected, a higher liquid film temperature contributes to an increased evaporate rate. The visualisation method was applied for water in terms of validating the precision scale weighting procedure. For fuels, the second method was not employed due to several constraints, including difficulty tracking the liquid-gas interface in low surface tension fluids (the presence of a Marangoni flow in the radial walls distorts the image visualisation and, consequently, the binarisation process) and limited resources (due to the prolonged duration of the evaporation rate experiments, performing both methods would result in a substantial resource depletion).

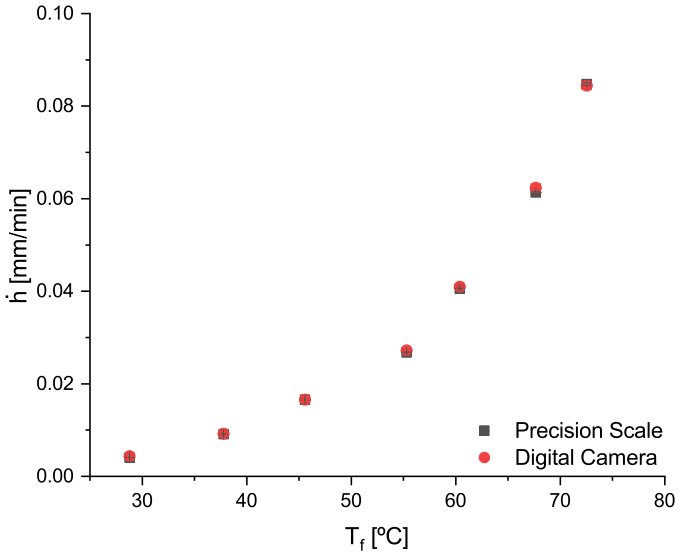

Figure 3.14: Comparison of the precision scale and high-speed digital camera methods for evaporation rate measurements.

Figure 3.15 displays the evaporation rates for water, n-decane and n-heptane as a func-

tion of the liquid film temperature. The liquid film evaporation rate is represented by $\dot{h}$ due to the nature of the phenomena. The water and n-heptane display higher evaporation rates in comparison with n-decane due to lower saturation temperatures. Water reveals an abrupt evaporation rate increase for higher temperatures, which is associated with a more chaotic behaviour of the boiling regime. Both fuels follow an identical trend with no steep change in terms of evaporation rate. N-decane was not analysed for temperatures higher than $T_f > 90°\mathrm{C}$ due to limited fuel supply, as previously mentioned. Following this analysis, a flow rate equal to the evaporation rate of the fluid is imposed on the second syringe pump to compensate for the liquid film thickness variation during the heating and stabilisation phases. This process, coupled with the weighting procedure, guarantees the experimental conditions required for droplet impact in terms of the liquid film.

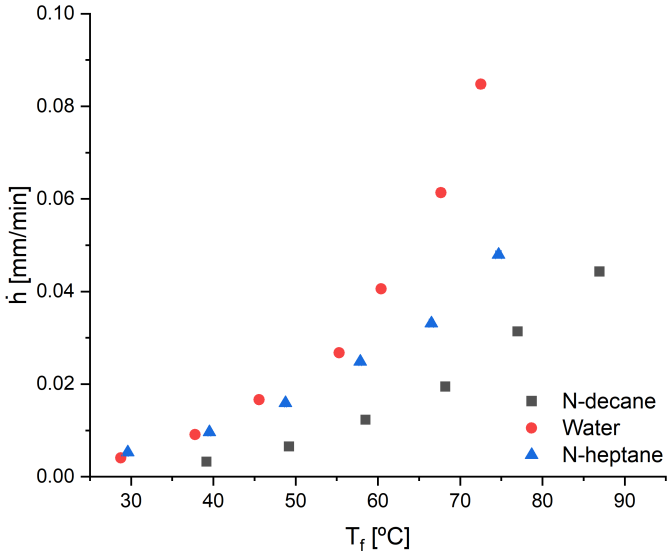

Figure 3.15: Evaporation rate of n-decane, water and n-heptane for different liquid film temperatures.

3.5 Image Processing

For experimental procedures involving high-speed digital cameras, a portion of the post-processing consists in the quantitative analysis of several geometrical parameters, including the droplet impact diameter and velocity, crown height and diameter, jet height, and vapour bubbles number and size. The post-processing was executed by aid of a MATLAB algorithm consisting of binarisation and detection functions of contiguous regions.

The droplet impact parameter measurements, namely diameter and impact velocity, are executed prior to the impact experiments for determining the dimensionless numbers. The former is analysed during the trajectory of the falling droplet following the initial oscillations of the initial ligament breakup, and the latter is considered for the frames preceding the impact onto the liquid film. Figures 3.16 and 3.17 illustrate the frames considered for the diameter and impact velocity measurements, respectively. The experimental imaging is obtained in a greyscale, meaning that no conversion is required for post-processing (as it is required for red green blue (RGB) imaging). Initially, background subtraction is performed between fig-

ures 3.16b and 3.16a to differentiate the droplet from its surroundings. The resulting image is then binarised through the Otsu method [224]. This method creates a binary image by determining a global threshold based on the zeroth and first-order cumulative moments of the grey-level histogram. This leads to an automatic and optimal threshold selection that is not based on the local fluctuations of the field. The processed image subsequent to binarisation is then subjected to several steps in terms of noise reduction. First, a function to perform filling of background pixels is required to accurately delineate the falling droplet. This increases the local pixel number of the considered structure, distinguishing it from surrounding background noise. All connected elements under a certain pixel threshold (background noise) are then removed, obtaining a final processed image as displayed by figure 3.16c. In order to perform the diameter measurements, a function denominated as *regionprops* is applied to the binarised image, creating a structure array for each object (connected component) of the image. The measured properties consist of horizontal and vertical dimensions, centroid, and area. The droplet diameter is calculated by averaging the horizontal and vertical measurements. This process is applied to a significant number of frames to ensure consistency and reliability of the measurements. The centroids are also quantified to ensure a vertical droplet trajectory, meaning that the horizontal displacement is negligible. In terms of impact velocity, the binarisation process is identical to the previous method and is defined by the difference of centroids of the last frame before impact and successive prior frames, overlooking the negligible horizontal displacement for calculation simplicity. The time differences between frames are associated with the frame rate of the high-speed digital camera. A frame rate of 2000 fps translates to a time interval of $\Delta t = 0.5$ ms between consecutive frames. The pixel size is obtained by positioning a hypodermic needle in the droplet-falling plane. A snapshot of the outline of the needle is captured by the imaging system, which is followed by the binarisation process. The image is cropped to isolate the needle from its surroundings, and its outer diameter is measured in terms of pixels. The dimensions of the needle, specifically the outer diameter, are previously defined, meaning that the pixel size can be calculated. The pixel size is then implemented to the remaining measurements performed by the algorithm.

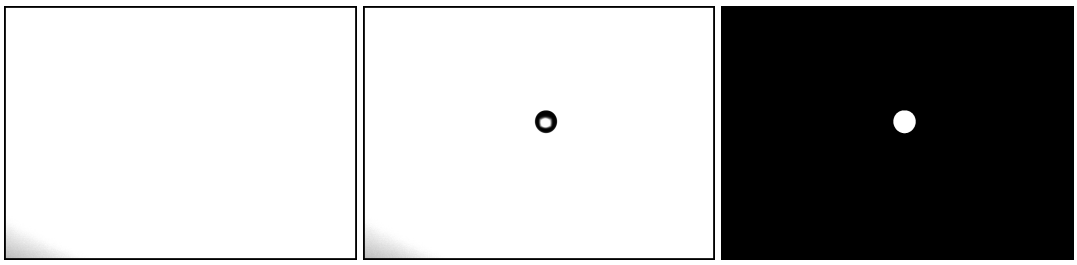

Figure 3.16: Binarisation process of a single droplet for diameter measurements: a) Background image; b) Droplet during free-fall; c) Binarised image.

A similar procedure is applied to the vapour bubbles in terms of subtraction and binarisation. These are analysed from both side and top-view perspectives to account for different nucleation sites of the vapour bubbles. For the side perspective, the algorithm is identical to the procedure of the droplet measurements, whereas for the top view, the numerical code re-

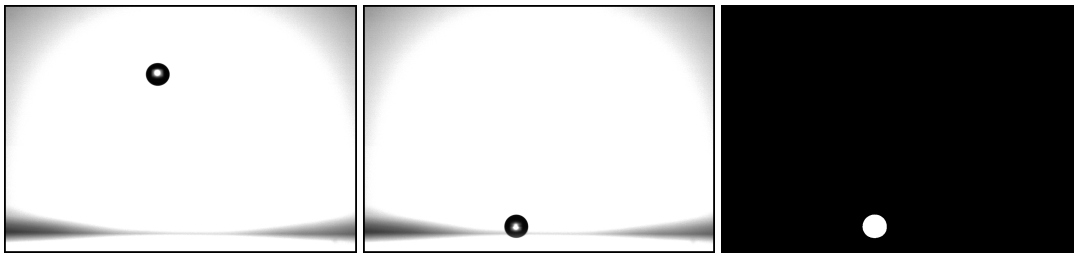

(a) (b) (c)

Figure 3.17: Binarisation process of a single droplet for impact velocity measurements: a) Droplet during free-fall; b) Droplet frame preceding the moment of impact; c) Binarised image.

quires tweaking in several aspects. The vapour bubbles and corresponding post-processing can be visualised in figure 3.18. The first step consists of a circular cropping of the image due to the design of the container. This is required to isolate the vapour bubbles from the boundaries of the container, which may have deposited droplets or lighting spots. These increase the amount of background noise, affecting the threshold global value and reducing the accuracy of the binarisation process. Following the isolation and binarisation of the impact surface, the vapour bubbles are identified and measured in terms of spatial distribution and diameter, respectively. In order to obtain the geometrical properties of the vapour bubbles, an object detection function based on the Circular Hough transform [225] is applied to the binary image, as represented by figure 3.18c. This approach focuses on finding circles based on an estimation of their centres and radius from the computation of an accumulator array. This method is implemented due to its robustness in the presence of noise or variations in lighting. However, the accuracy of this method is limited for circles with a radius smaller than 5 pixels. Due to the limitation of the function in terms of requiring a minimum diameter, vapour bubbles below the specific threshold are evaluated by the *regionprops* function.

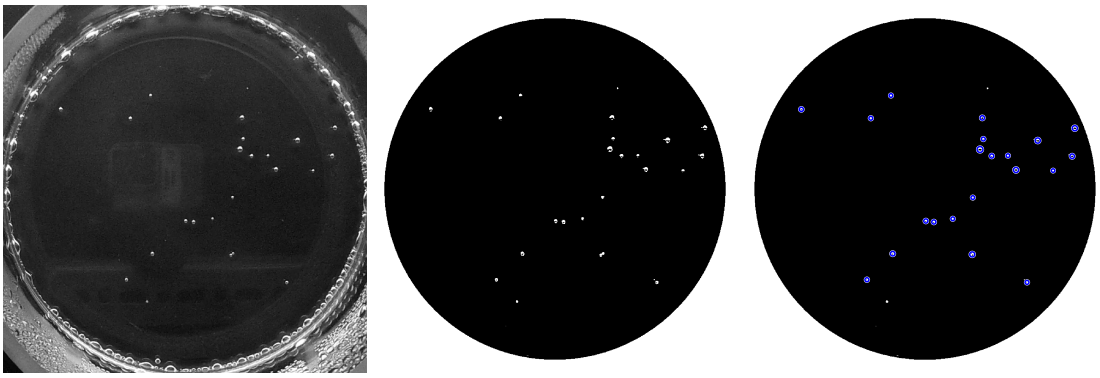

(a) (b) (c)

Figure 3.18: Post-processing of the vapour bubbles on the surface impact region: a) Original image; b) Cropping and binarisation; c) Circular object detection function.

The crater and jet parameter measurements follow a similar approach to the droplet analysis in terms of background subtraction and binarisation. Figure 3.19 displays the binarisation procedure for crater formation subsequent to droplet impact. An initial cropping is required to properly isolate the crater. The resulting cropped image is delimited by an upper and lower boundary corresponding to the liquid film interface and impact surface, respectively. This

step improves the binarisation process, as possible background noise from outer regions is not considered in the processed image. The binarisation and noise removal procedures are similar to the previously described methods of measuring the droplet diameter and impact velocity, utilising the Otsu method [224] and removing all connected elements under a certain pixel threshold. The *regionprops* function is then employed, measuring several geometrical properties of the detected element, such as horizontal and vertical measurements. The crater depth corresponds to the vertical distance between the liquid film interface and the bottom of the crater, which is obtained by the previous function. The crater diameter is determined by the horizontal distance between the outer boundaries of the crater at a liquid film depth of 50% of the initial film thickness. This is due to the available experimental data in the literature [95, 226].

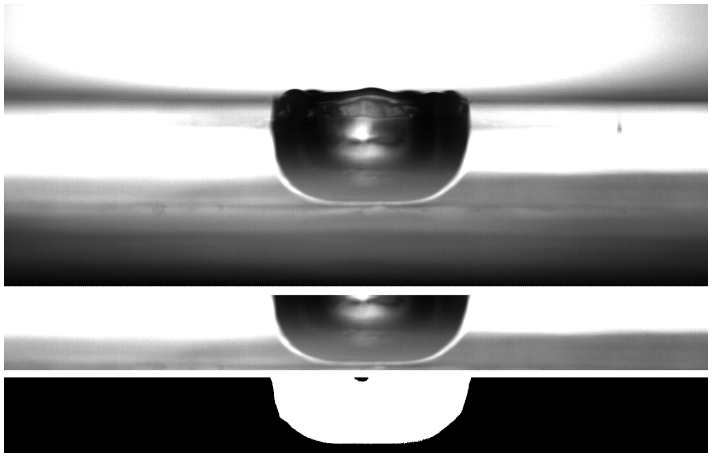

Figure 3.19: Binarisation process of the crater formation.

In terms of central jet post-processing, the procedure is identical to the crater analysis. The central jet is manually located and cropped, as displayed in figure 3.20a, and the bottom boundary corresponds to the liquid film interface, as opposed to the crater boundaries. Binarisation and noise removal are then employed, obtaining figure 3.20b. The central jet height, which is defined as the vertical distance between the liquid film interface and the top of the central jet, is obtained through the *regionprops* function.

(a) (b)

Figure 3.20: Binarisation process of the central jet formation: a) Cropped image; b) Binarised image.

Chapter 4

Experimental Results

The current chapter exhibits the experimental results regarding single impacting droplets onto heated liquid films. Different outcomes are thoroughly evaluated, including central jets, craters, bubbling and splashing, in terms of visualisation, geometrical parameter measurements (such as height, diameter, depth, and so on), and theoretical analysis. Experimental conditions range from ambient temperatures ($\theta = 0$) up to the onset of boiling ($\theta = 0.95$). These are divided into non-isothermal and boiling conditions. The former consists of low temperature regimes focused on the differences of thermophysical properties, and mass transfer processes being limited to evaporation. The latter introduces boiling conditions due to higher heat fluxes or temperature environments, leading to phase change and the nucleation, growth and possible rupture of vapour bubbles. The vapour bubbles are also investigated for subcooled and saturated boiling regimes.

4.1 Non-Isothermal Conditions

4.1.1 Central Jet

Table 4.1 displays the droplet impact parameters, such as the diameter and impact velocity, which are required to calculate the dimensionless numbers for the central jet analysis. In order to obtain similar Weber numbers, due to the water higher surface tension in comparison to the n-decane and n-heptane, the water droplet requires a higher impact velocity. To evaluate the influence of temperature on the impact phenomena, different conditions were considered, which include two dimensionless thicknesses, $h^* = 1.0$ and $h^* = 1.5$, and a range of dimensionless temperatures, $\theta = 0$, $\theta = 0.2$, $\theta = 0.4$ and $\theta = 0.6$. Qualitative and quantitative analyses are performed regarding jet evolution, and central jet height and breakup measurements, respectively. The growth and possible breakup of the central jet is represented in figure 2.11. The height of the jet, H_{jet}, is defined as the vertical distance from the gas-liquid interface to the top of the jet. If there is a detachment of a secondary droplet from the main central jet, breakup occurs, leading to a sudden decrease of its height and to the formation of secondary atomisation. This study has been thoroughly detailed [227].

Table 4.1: Impact parameters and dimensionless numbers of the central jet study cases for different fluids.

Fluid	$\mathbf{D_d}$ [mm]	$\mathbf{U_d}$ [m/s]	**We**	**Re**	**Fr**	$\mathbf{h^*}$	θ
Water	2.67 ± 0.04	2.71 ± 0.01	269	7208	280	$0.5 - 1.5$	$0 - 0.6$
N-heptane	2.56 ± 0.06	1.75 ± 0.01	265	7450	122	$1.0 - 1.5$	$0 - 0.6$
N-decane	2.72 ± 0.07	1.80 ± 0.01	270	3856	121	$1.0 - 1.5$	$0 - 0.6$

4.1.1.1 Visualisation

Prior to the central jet height and breakup measurements, a qualitative analysis is performed regarding central jet evolution and dependence on the liquid film temperature. For visualisation purposes, the results displayed correspond to a liquid film thickness of $h^* = 1.5$, which translates to higher and thicker central jets and possible jet breakup.

Figure 4.1 exhibits the central jet formation for the n-heptane droplet impact as a function of dimensionless liquid film temperature. Subsequent to the crater maximum expansion and the development of the impact phenomena, a retraction period leads to the collapse of the crater, creating an upward jet. For $\theta = 0$, the central jet emerges, reaching a maximum height and gradually decreasing until merging with the liquid film. The structure of the central jet indicates that the maximum height was previously reached, meaning that $\tau = 39.0$ corresponds to the descent stage of the central jet at isothermal conditions. No secondary droplets originating from the central jet are spotted. An increase of the dimensionless temperature to $\theta = 0.2$ does not lead to significant changes in the central jet. The central jet displays similar elements to the previous case in terms of both height and thickness, and no jet breakup occurs.

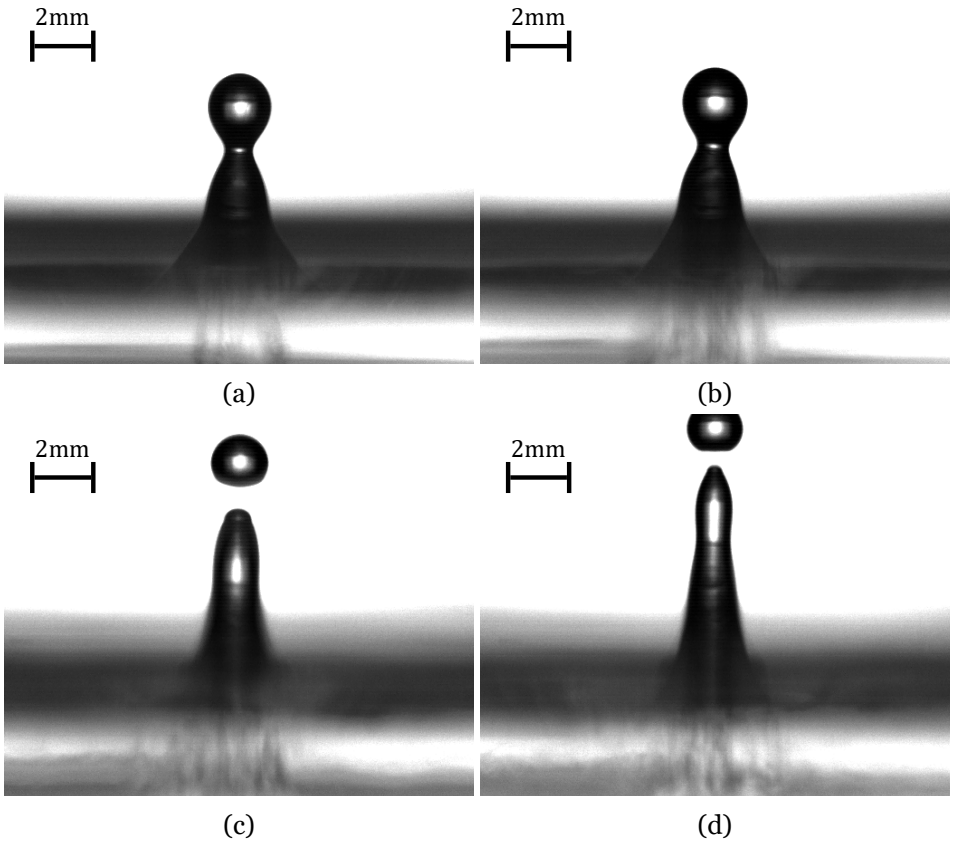

Figure 4.1: Visualisation of central jet formation subsequent to the impact of an n-heptane droplet ($h^* = 1.5$, $\tau = 39.0$): a) $\theta = 0$; a) $\theta = 0.2$; c) $\theta = 0.4$; d) $\theta = 0.6$.

For higher temperatures, $\theta = 0.4$ and $\theta = 0.6$, several differences are noticeable in comparison to the previous conditions. The central jets are significantly higher and exhibit a thinner

jet, which is associated with the thermophysical properties of the liquid film. Additionally, the maximum central jet height occurs for later stages of the impact, meaning that the central jets continue to increase in height for $\tau = 39.0$ until achieving a maximum value. An increase in the liquid film temperature also induces central jet breakup. These are similar to the n-decane impact phenomena represented by figure 4.2. Lower temperatures display similar central jet heights despite slight differences in terms of breakup stages. Increasing the liquid film temperature to $\theta = 0.4$ substantially increases the central jet height and number of breakup occurrences. For $\theta = 0.6$, due to the jet height, the high-speed digital camera required adjustments to the field of view of the impact phenomena in order to capture the full extent of the central jet. The n-decane central jets display thinner and higher jets in comparison to n-heptane due to the differences in viscosity. The density and surface tension values are relatively similar between the fluids.

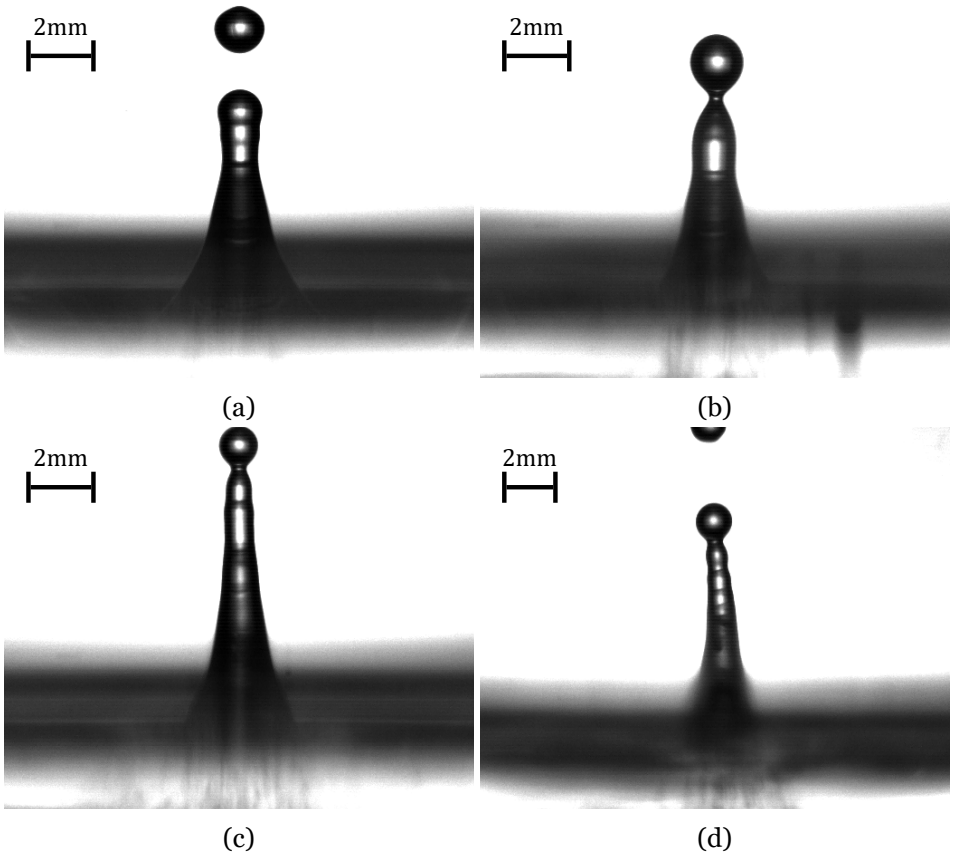

Figure 4.2: Visualisation of central jet formation subsequent to the impact of an n-decane droplet ($h^* = 1.5$, $\tau = 35.0$): a) $\theta = 0$; a) $\theta = 0.2$; c) $\theta = 0.4$; d) $\theta = 0.6$.

For water, due to the higher value of surface tension, the central jets maximum height shown by figure 4.3 are visually distinct in comparison to fuels. The central jets exhibit thicker ligaments and reduced heights, which also correlates with no breakup occurrences. For lower temperatures, $\theta = 0$ and $\theta = 0.2$, the central jets are relatively similar and display identical structures. However, the central jet for $\theta = 0.2$ is thinner in comparison to the isothermal condition. This is more perceptible for increasing liquid film temperatures, as the central jets for $\theta = 0.4$ and $\theta = 0.6$ show an increase in the central jet height and a decrease in its thickness. Despite the temperature increase, it is not sufficient to induce secondary atomi-

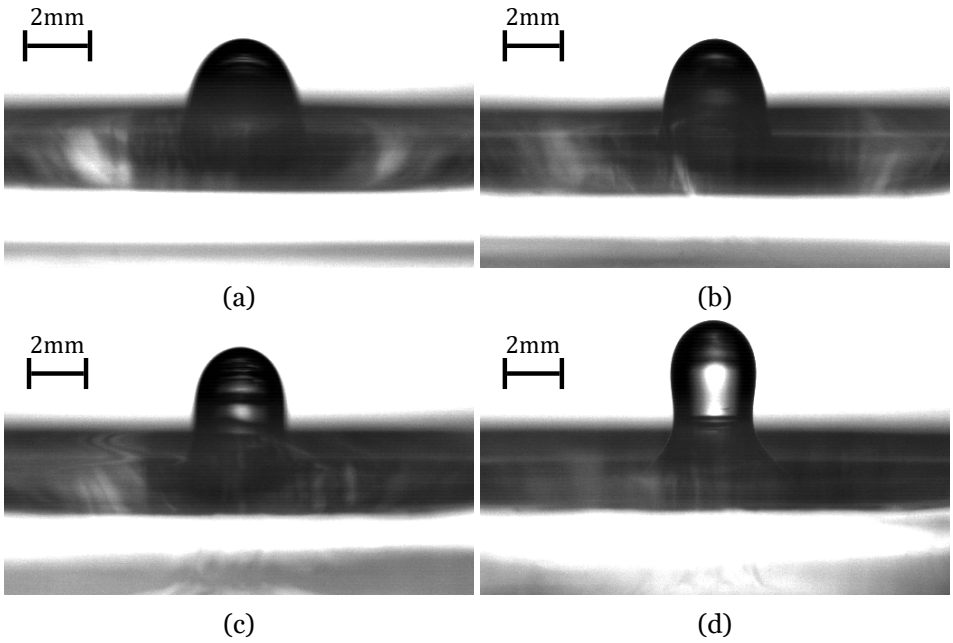

Figure 4.3: Visualisation of the central jet maximum height subsequent to the water droplet impact as a function of temperature ($h^* = 1.5$): a) $\theta = 0$; b) $\theta = 0.2$; c) $\theta = 0.4$; d) $\theta = 0.6$.

sation from the central jet, as opposed to the n-heptane impact. The central jet height and breakup measurements of the different fluids are presented in the following section.

4.1.1.2 Height and Breakup Measurements

Figure 4.4 displays the measurements of the dimensionless central jet height, $H^*_{jet} = H_{jet}/D_d$, as a function of dimensionless time, $\tau = tU_d/D_d$, for the n-heptane droplet impact. Figure 4.4a refers to the lower liquid film thickness, $h^* = 1.0$, and figure 4.4b to the higher thickness, $h^* = 1.5$. For the former thickness, the jet height measurements exhibit similar patterns for lower temperatures, namely $\theta = 0$ and $\theta = 0.2$. The curves follow a continuous path, starting from the emerging central jet, reaching its maximum height, followed by a gradual decrease until merging with the film. The smoothness of the curves is associated with no central jet breakup, as the jet maintains its single structure throughout the impact phenomena. However, for higher temperatures, $\theta = 0.4$ and $\theta = 0.6$, the jet height substantially increases, showing higher measurements for increasing values of θ. Additionally, for $\theta = 0.4$ and $\theta = 0.6$, the curves display several irregularities opposite to the smoothness at lower temperatures. These can be denominated as line irregularities, which are associated with a secondary droplet detaching from the central jet, breaking its ligament and causing a sudden height decrease. For $h^* = 1.5$, the increase of the dimensionless temperature promotes higher central jets. The jet height measurements show a progressive increase across the different dimensionless temperatures, ranging from $\theta = 0$ to $\theta = 0.6$. The duration of the growth and merging of the central jet is also affected by the liquid film temperature, similar to the lower thickness. The maximum jet height occurs at later stages of impact for higher temperatures, which leads to an elongation of the jet development. In terms of breakup, there are considerably more discontinuities on single curves compared to the lower thick-

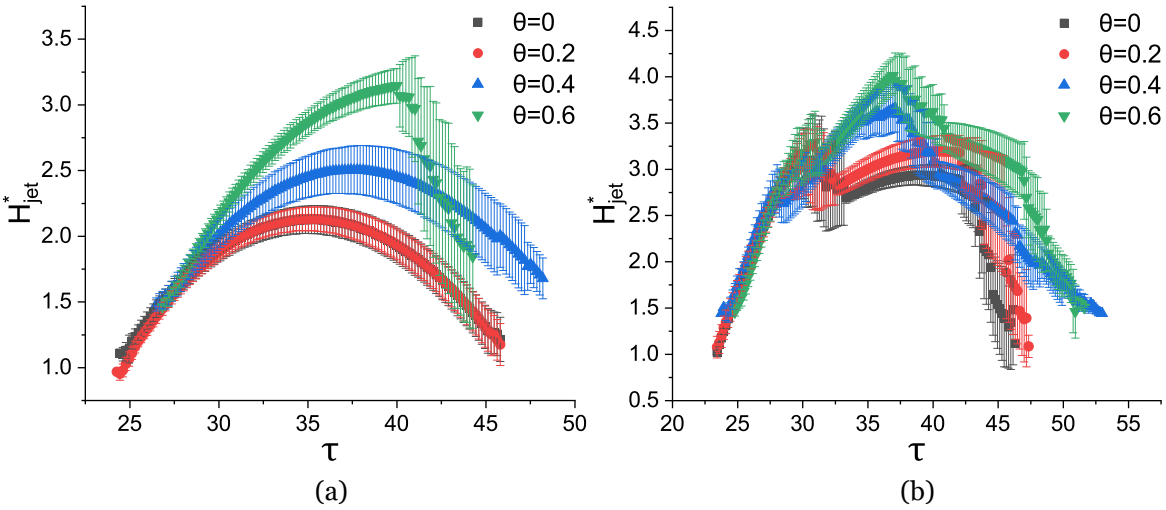

Figure 4.4: Central jet height measurements of an n-heptane droplet impacting a liquid film for a range of dimensionless temperatures ($0 \leq \theta \leq 0.6$): a) $h^* = 1.0$; b) $h^* = 1.5$.

ness, meaning that there is more than one secondary droplet originating from the central jet at different stages of the impact phenomena.

Figure 4.5 displays the formation and breakup of the central jet for the higher liquid film thickness and $\theta = 0$. The higher film thickness study case is displayed for visualisation purposes due to several instances of central jet breakup. The first breakup occurs during the formation of the central jet, at $\tau = 29,4$, prior to reaching the maximum jet height and maintains its growth after the detachment of the secondary droplet. The following breakup occurs at later stages, $\tau = 43,4$, during the descent of the central jet. These are aligned with the line discontinuities represented in figure 4.4b.

In order to quantify how the dimensionless temperature affects the promotion of the jet breakup, as well as the number of central jet breakups, n_b, associated with the jet evolution, these parameters were evaluated as a function of temperature across all fluids. Figure 4.6 illustrates the percentage associated with the number of central jet breakup occurrences as a function of θ. For the lower thickness, figure 4.6a, the lower temperatures ($\theta = 0$ and $\theta = 0.2$) exhibit no central jet breakup, which corresponds to $n_b = 0$ with an occurrence percentage of $p = 100\%$. For $\theta = 0.4$, there are $p = 80\%$ of occurrences where no breakup occurs ($n_b = 0$), and $p = 20\%$ in which the central jet breaks once ($n_b = 1$). Further increasing the liquid film temperature to $\theta = 0.6$ increases the breakup occurrences for $n_b = 1$ to $p = 100\%$, meaning that all jets are affected by breakup and produce one secondary droplet. For $h^* = 1.5$, figure 4.6b, breakup tendencies are visualised for the entire range of dimensionless temperatures. Similar to the lower thickness, a shift occurs in the breakup occurrence percentage from isothermal to non-isothermal conditions. The central jet breaks twice ($n_b = 2$) for $\theta = 0$ and $\theta = 0.2$, with a $p = 100\%$ occurrence for both cases, as represented by figure 4.5. When increasing the temperature up to $\theta = 0.4$, the central jets break $n_b = 2$ to $n_b = 3$ times with a $p = 80\%/p = 20\%$ occurrence, respectively. For the highest temperature, $\theta = 0.6$, nearly all of the jets formed exhibit the detachment of 3 secondary droplets during its development,

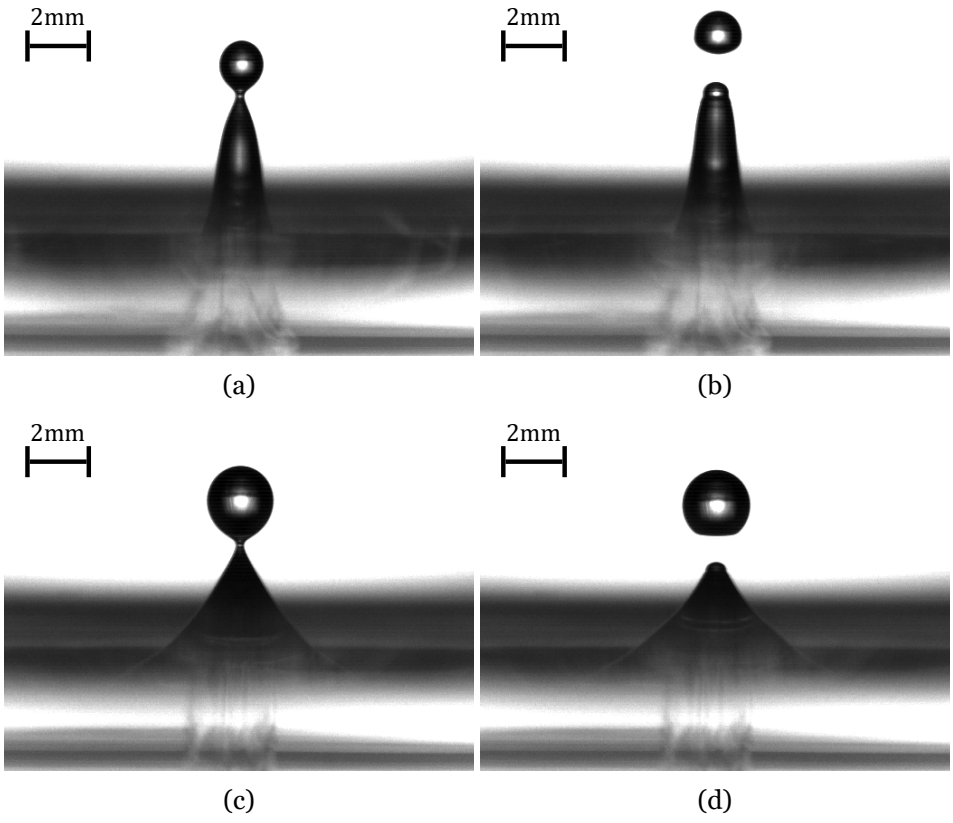

Figure 4.5: Visualisation of central jet breakup subsequent to the impact of an n-heptane droplet ($\theta = 0$, $h^* = 1.5$): a) $\tau = 28.7$; a) $\tau = 30.1$; c) $\tau = 42.9$; d) $\tau = 43.9$.

exhibiting a $p = 10\%/p = 90\%$ occurrence for 2 and 3 jet breakups, respectively. Overall, the experimental results presented for the n-heptane droplet impact for the various conditions show that higher liquid temperatures not only promote central jet breakup but also increase the number of produced secondary droplets.

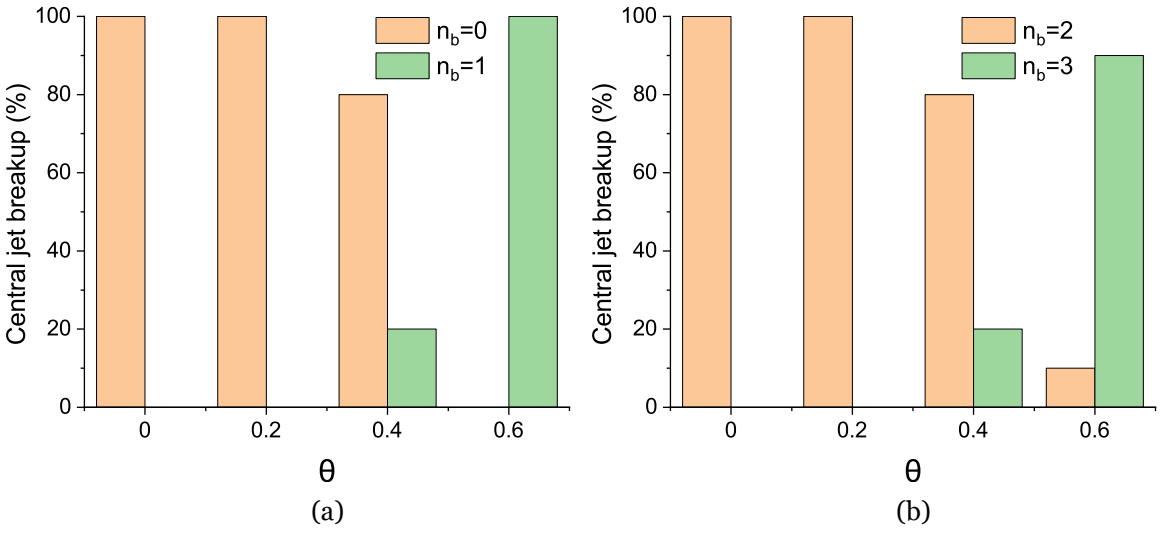

Figure 4.6: Occurrence of central jet breakup of an n-heptane droplet impacting a liquid film for a range of dimensionless temperatures ($0 \leq \theta \leq 0.6$), where n_b is the number of central jet breakups: a) $h^* = 1.0$; b) $h^* = 1.5$.

The n-decane follows an analogous approach in terms of jet formation and breakup. The central jet height measurements and correspondent breakup for the n-decane droplet impact are presented in figures 4.7 and 4.8, respectively. Higher temperatures lead to an increase in jet height, as well as the duration of the phenomena, for both liquid film thicknesses, as shown by figures 4.7a and 4.7b. In terms of breakup, several line discontinuities are identified for the different stages of the jet formation, being more predominant for the higher film thickness. These, similarly to n-heptane, occur due to central jet breakup. For $h^* = 1.0$, the curves associated with lower temperatures are relatively uniform ($\theta = 0$ and $\theta = 0.2$), becoming more erratic for $\theta = 0.4$ and $\theta = 0.6$. For the higher film thickness, the breakup tendencies are noticeable for the entire range of dimensionless temperatures.

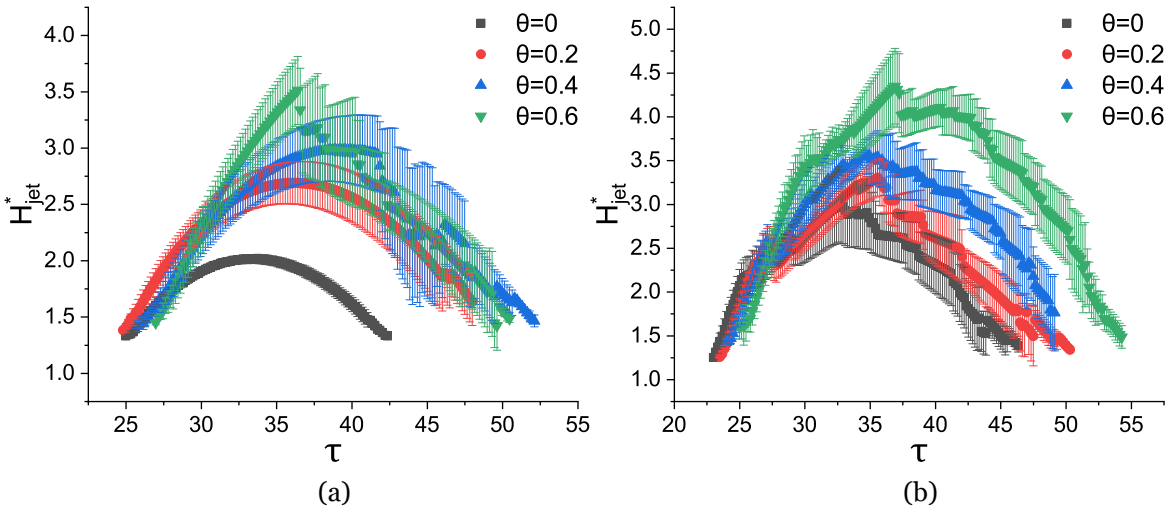

Figure 4.7: Central jet height measurements of an n-decane droplet impacting a liquid film for a range of dimensionless temperatures ($0 \leq \theta \leq 0.6$): a) $h^* = 1.0$; b) $h^* = 1.5$.

The number of central jet breakups is displayed for these thicknesses in figure 4.8a and 4.8b. For the lower thickness, the central jet does not break at isothermal conditions, $\theta = 0$, displaying a $p = 100\%$ occurrence of no secondary atomisation from the central jet ($n_b = 0$). The jet starts to break for $\theta = 0.2$, having a $p = 10\%$ occurrence for $n_b = 1$. For higher temperatures, there is a clear transition in the breakup event, exhibiting a $p = 60\%$ occurrence for one secondary droplet for $\theta = 0.4$ and a full shift to central jet breakup for $\theta = 0.6$. The higher thickness case, opposite to the previous case study, shows various fluctuations in terms of secondary atomisation from the central jet. For $\theta = 0$, the jet breakup ranges from $n_b = 1$ to $n_b = 3$ times. For the following temperature, $\theta = 0.2$, there are no circumstances in which the jet breaks one time ($n_b = 1$). Similarly, for $\theta = 0.4$, the jet breakup percentage correspondent to $n_b = 2$ is equal to $p = 0\%$ and, for the upper temperature range, $\theta = 0.4$ and $\theta = 0.6$, the number of secondary droplets ranges between $n_b = 3$ and $n_b = 5$, which is an increase in comparison to lower temperatures.

Overall, the number of secondary droplets originating from the central jet breakup is promoted by higher values of θ, which is in agreement with the experimental results previously described. Both fuels display identical trends, as higher temperatures promote jet break and increase the number of secondary droplets originating from the central jet. The dependence

of the fluids thermophysical properties with temperature is also a defining factor in the impact phenomena, as higher temperatures lead to lower values of surface tension and viscosity. Additionally, higher Weber and lower Ohnesorge numbers promote jet breakup [75, 79], which can depict a direct correlation with the thermophysical properties of the liquid film.

The water central jet analysis is displayed in figure 4.9. The height measurements were performed for an additional liquid film thickness, $h^* = 0.5$. In general, the jet height measurements are considerably lower in comparison to fuels, mostly due to the differences in surface tension. However, the influence of temperature on the jet evolution for lower temperatures differs from the remaining fluids. The central jet measurements display similar tendencies for the different liquid film thicknesses, in which the maximum height shows a reduction between $\theta = 0$ and $\theta = 0.2$. From that point onward, the maximum height progressively increases with higher liquid film temperatures. With the exception of $\theta = 0.2$, the duration of the impact phenomenon increases with θ, which is also associated with reaching higher maximum jet height values. The maximum height also occurs at later stages when increasing the liquid film temperature. Breakup analysis is not required for water, as the curves follow a continuous path and do not display any discontinuities for the different stages of jet evolution.

Taking into account the experiment results for the distinct fluids, the increase of θ leading to higher central jet heights is associated with the differences in thermophysical properties due to the heated liquid film, such as lower values of surface tension and viscosity. However, the unexpected reduction for $\theta = 0.2$ requires further analysis. This includes different impact conditions, dimensionless temperatures, and bottom and top-view imaging. Numerical and theoretical approaches could also provide different insights regarding heated liquid films and subsequent impact phenomena.

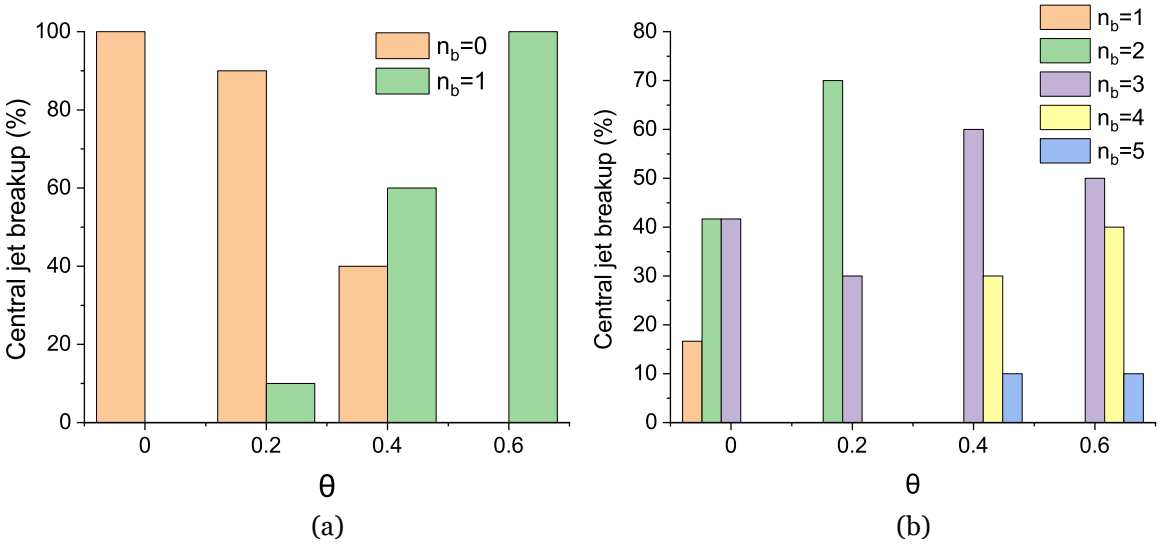

Figure 4.8: Occurrence of central jet breakup of an n-decane droplet impacting a liquid film for a range of dimensionless temperatures ($0 \leq \theta \leq 0.6$), where n_b is the number of central jet breakups: a) $h^* = 1.0$; b) $h^* = 1.5$.

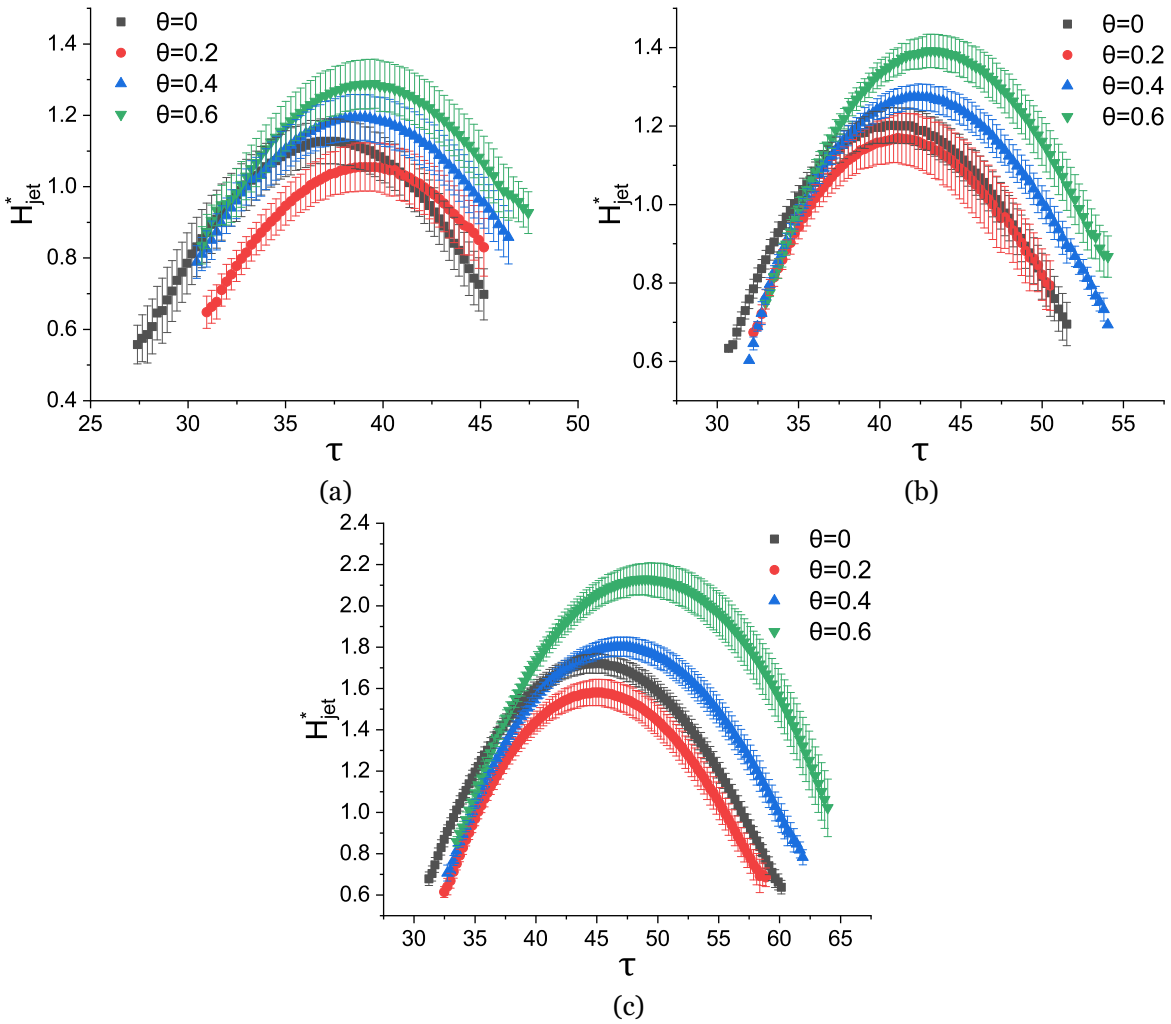

Figure 4.9: Central jet height measurements of a water droplet impacting a liquid film for a range of dimensionless temperatures ($0 \leq \theta \leq 0.6$): a) $h^* = 0.5$; b) $h^* = 1.0$; c) $h^* = 1.5$.

4.1.1.3 Time Scale Analysis

The physical aspects associated with the droplet impact phenomena differ both in fluid mechanics and thermal processes. These are traditionally interconnected, resulting in a great number of different branches related to the impact process, manifesting in a wide range of scales, such as the size of the impinging droplet and the resulting secondary droplets from the crown rim, or the vapour bubbles formed due to cavitation. Similarly, non-isothermal conditions near the Leidenfrost point create a thin vapour layer during impacting droplets, preventing the droplet from contacting the surface. These also include differences in surface roughness, mass and transfer processes.

In order to quantify the magnitude of the different parameters in a specific application, Rein [228] considered time scale characteristics of these effects. For impacting droplets onto liquid films, the parameters include the droplet diameter and impact velocity, the density, viscosity, surface tension and thermal diffusivity of the fluid, and the gravitational acceleration. The time scales characteristic of the droplet impact phenomena for inertia, surface tension, gravity, viscosity and temperature are defined by equations (4.1)–(4.5), respectively:

$$t_{conv} = D_d/U_d \tag{4.1}$$

$$t_\sigma = \left(\rho_f D_d^3/\sigma_f\right)^{1/2} \tag{4.2}$$

$$t_{grav} = \sqrt{D_d/g} \tag{4.3}$$

$$t_{vis} = D_d^2/\nu_f \tag{4.4}$$

$$t_{therm} = D_d^2/\alpha_{T_f} \tag{4.5}$$

where α_T is the thermal diffusivity. The dimensionless numbers can be defined as the ratio of different time scales, such as the Weber number, $We = (t_\sigma/t_{conv})^2$, the Reynolds number, $Re = t_{vis}/t_{conv}$, and the Ohnesorge number, $Oh = t_\sigma/t_{vis}$. Several dimensionless numbers are not considered in the current analysis, such as the Mach number, due to the incompressibility condition associated with low velocity impacts. Due to non-isothermal conditions, the time scales were adapted to account for the thermophysical properties of the heated liquid film. This approach is based on the assumption that the liquid film volume is several orders of magnitude higher than the droplet, meaning that the impact phenomena develop at liquid film temperature. Therefore, the time scales are calculated based on the droplet diameter and impact velocity, as well as the thermophysical properties of the liquid film, which are temperature dependent.

Figure 4.10 displays the surface tension, inertial and gravitational time scales as a function of θ for the fuels. The viscous and thermal time scales are not presented due to being 2 and 6 orders of magnitude higher to the remaining time scales, respectively. The time scales are defined for a temperature interval of $0 < \theta < 1$, consistent with the different heat regimes. Inertia is a main factor in both fluids, as it is the lowest of all the scales, followed by the influence of the gravitational forces. These do not alter with θ due to their non-dependency on the liquid film thermophysical properties and are solely dependent on the droplet inertial properties (diameter and impact velocity) and gravitational acceleration. The surface tension time scale varies with θ due to its dependency on density and surface tension, which are temperature dependent properties, as previously mentioned. The surface tension time scale increases with higher values of θ, mostly due to the decrease of the surface tension (density also decreases but at a lower rate). Overall, the differences between the time scales are noticeable, where the surface tension time scale has a lower influence on the overall phenomena in comparison to the gravitational and inertial terms. The time scales do not intersect at any

point for the considered temperature regime, meaning that the relative magnitude between these parameters is not affected. Therefore, the time scales can be represented by equation 4.6, which is applied for both conditions of n-heptane and n-decane.

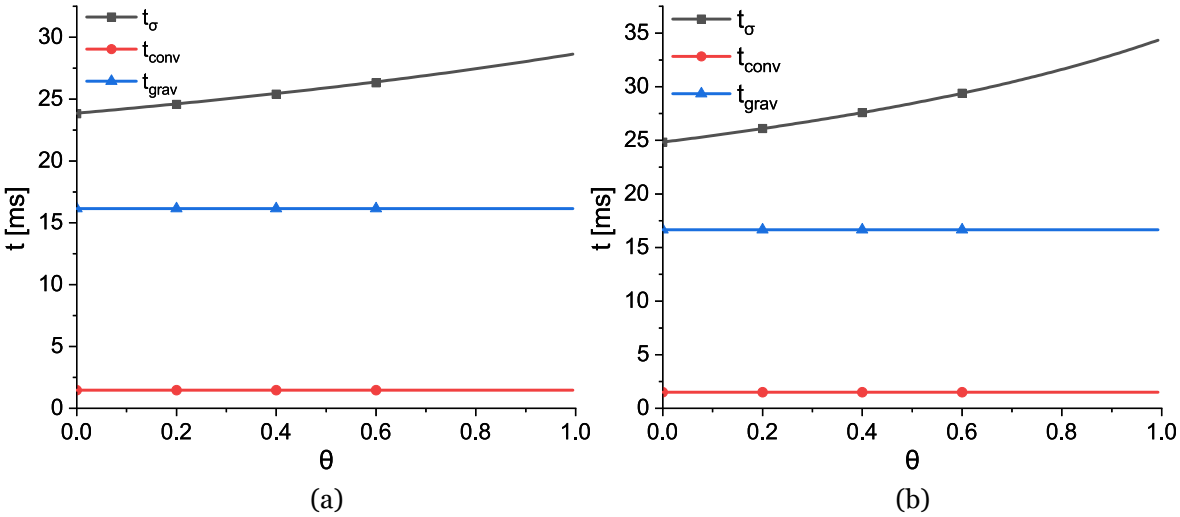

Figure 4.10: Surface tension, inertial and gravitational time scales as a function of θ for the droplet impact phenomenon: a) N-heptane; b) N-decane.

$$t_{conv} < t_{grav} < t_{\sigma} \tag{4.6}$$

For water, the time scale analysis is shown in figure 4.11, where 4.11a displays the surface tension, inertial and gravitational time scales as a function of θ, and 4.11b evidences the surface tension and gravitational scales in close detail. Similarly to fuels, the inertial time scale is lower than the remaining scales for the entirety of the temperature range, meaning that the inertial forces are the predominant scale. In terms of the gravitational and surface tension time scales, these exhibit significant differences in comparison to the previous results. For fuels, the gravitational has more influence than the surface tension time scale, $t_{grav} < t_{\sigma}$, regardless of the temperature value. For water, due to the high surface tension value and associated temperature variation, the curve correspondent to the surface tension time scale diminishes, meaning that surface tension has a more dominant effect in comparison to fuels. Due to this, the gravitational and surface tension time scales intersect at approximately $\theta = 0.27$. For that reason, there is a region where the time scale associated with surface tension is predominant, which corresponds to $\theta < 0.27$, and a region where gravitational forces exceed surface tension, which is $\theta > 0.27$. A bracket relation between the time scales for different domains of θ is displayed by equation (4.7).

Fuels show a clear distinction between the different time scales, whereas water has a shift between surface tension and gravitational time scales. This deviation, which occurs at $\theta = 0.27$, is followed by a gradual increase in the jet height for higher values of θ. Therefore, water displays similar behaviour to fuels for $\theta > 0.27$, as the time scales follow the same relation for that specific temperature range, and a distinct behaviour for $\theta < 0.27$, as previously men-

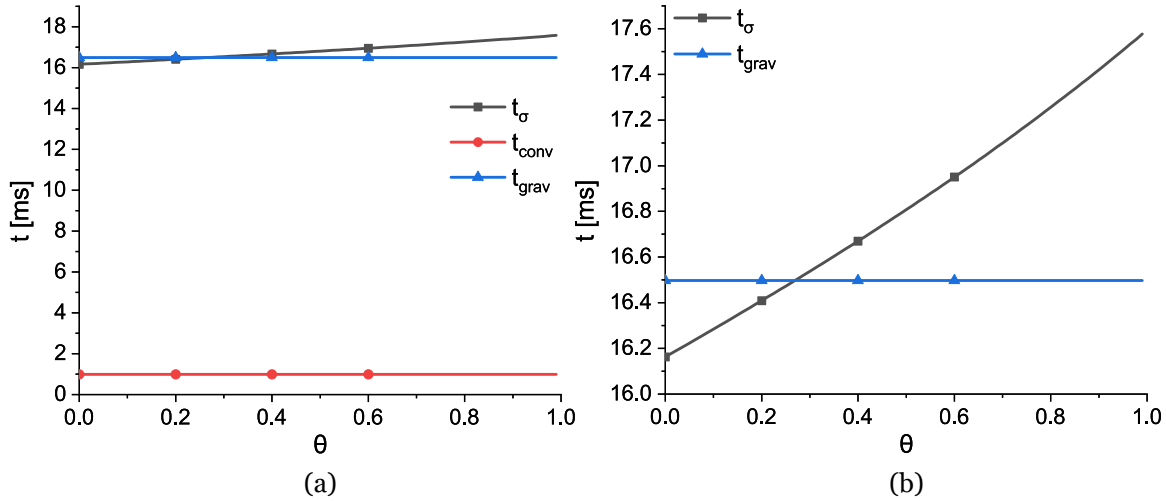

Figure 4.11: Time scales as a function of θ for the water droplet impact: a) Surface tension, inertial and gravitational time scales; b) Close-up of the surface tension and gravitational time scales.

tioned. This shift between prevalent time scales might provide insight into the distinctions regarding jet height reduction at $\theta = 0.2$. In order to refine these results, a different approach to θ could involve calculating the dimensionless numbers as a function of the thermophysical properties of the liquid film. This could give a distinct insight into how temperature affects the liquid film and subsequent impact phenomena, which could be considered for future works.

$$\begin{cases} t_{conv} < t_\sigma < t_{grav}, & \text{for } \theta < 0.27 \\ t_{conv} < t_{grav} < t_\sigma, & \text{for } \theta > 0.27 \end{cases} \tag{4.7}$$

4.1.2 Crater

Similarly to central jets, the crater expansion and posterior collapse were evaluated for different impact conditions, which are represented by table 4.1. Qualitative and quantitative analyses are performed regarding crater expansion, and depth and diameter measurements, respectively. The crater geometrical parameters are measured according to figure 4.12. The crater penetration depth, y_{cra}, is defined as the vertical distance from the liquid-gas interface to the bottom of the crater. The crater diameter, D_{cra}, is represented by the horizontal distance between the crater walls at a vertical displacement of $y = 0.5h$, which corresponds to the horizontal line equidistant between the liquid-gas interface and the impact surface. These are in accordance with both experimental and theoretical work performed in the literature [90, 95].

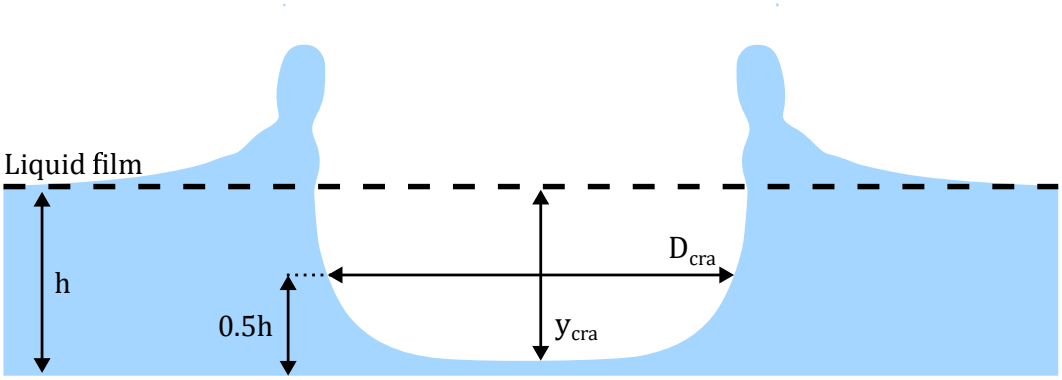

Figure 4.12: Representation of the crater depth and diameter subsequent to droplet impact.

4.1.2.1 Visualisation

In order to properly visualise the dynamics of crater development, different evolution stages are considered, ranging from the initial expansion, to the maximum crater diameter and penetration depth, to its retraction.

Figure 4.13 illustrates the influence of θ on the crater overall development for the water droplet impact at intermediate stages of the crater expansion for the higher liquid film thickness. In terms of crater shape, these display different configurations, as the liquid film temperature affects their growth, altering its local curvature near the impact surface. For $\theta = 0$, the crater is entering its receding phase, which is followed by the crater maximum expansion. For higher temperatures, the receding phase appears to be delayed, as the craters exhibit a more conical shape and a higher angle adjacent to the impact surface. This may also be associated with the capillary wave formed subsequent to impact, which propagates both on the liquid film and crater. Additionally, it is possible to visualise the existence of temperature-related dynamics near the crater and the impact surface. For $\theta = 0$, no visible dynamics are captured in terms of temperature differences due to the droplet and the liquid film being at equal temperatures (isothermal conditions). However, an increase in the liquid film temperature, $\theta > 0$, due to the temperature differences, temperature-related dynamics near the crater boundaries begin to emerge, which are properly captured with the high-speed digital camera. These are denominated as recirculation zones and are promoted by increasing values of θ. These regions are a consequence of the mixing of the cold droplet and heated liquid film, inducing refraction due to density differences. The refraction phenomenon is intensified for higher liquid film temperatures.

The crater expansion is similar to n-decane, as presented by figure 4.14. Opposite to the previous case, these correspond to earlier stages of the impact, during which the crater has not expanded to its maximum diameter. The recirculation zones are visible for $\theta > 0$, similar to water, though they are less perceptible due to limitations in optical access. This includes local evaporation and the Marangoni effect near the container walls, distorting the image visualisation. In terms of crater shape, there is also a slight shift, transitioning from an oblate ($\theta = 0$ and $\theta = 0.2$) to a conical shape ($\theta = 0.4$ and $\theta = 0.6$). This might be due to the maxi-

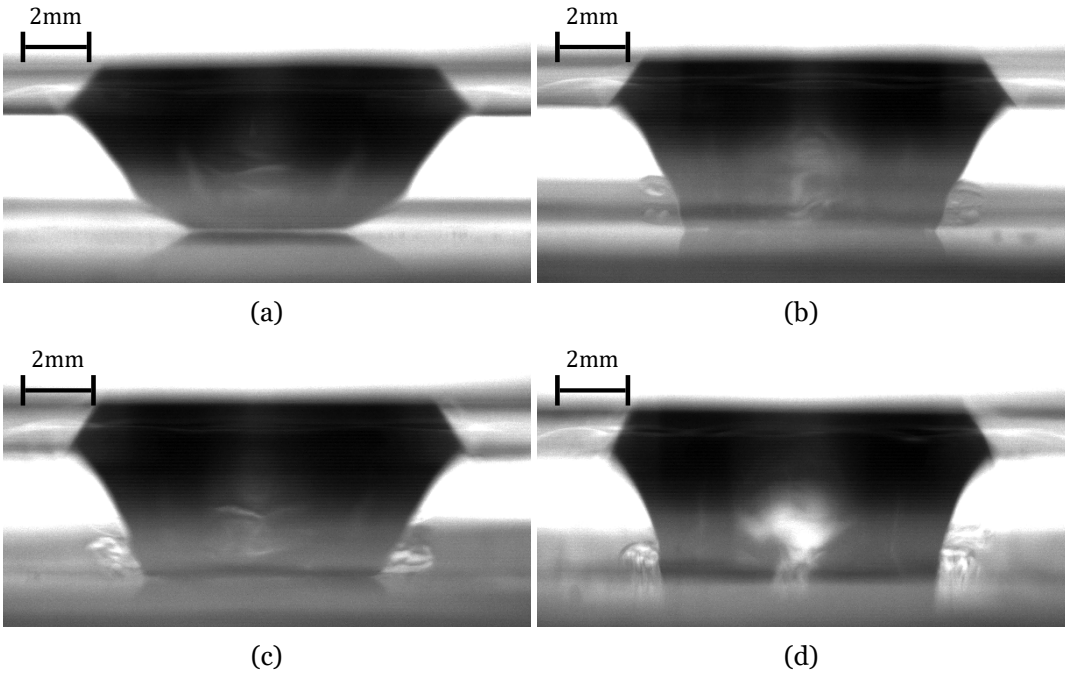

Figure 4.13: Visualisation of the crater formation subsequent to the impact of a water droplet ($h^* = 1.5$, $\tau = 21.1$): a) $\theta = 0$; a) $\theta = 0.2$; c) $\theta = 0.4$; d) $\theta = 0.6$.

mum crater diameter being influenced by the liquid film temperature, leading to differences in its formation. This is also associated to the capillary wave that propagates onto the crater, affecting the crown shape and, posteriorly, its development. The n-heptane exhibits similar tendencies to n-decane in terms of crater formation, expansion and ejection, and will not be displayed in the visualisation analysis. Therefore, this analysis is limited to n-decane, opting to display two liquid film thicknesses for water to provide a more diverse study.

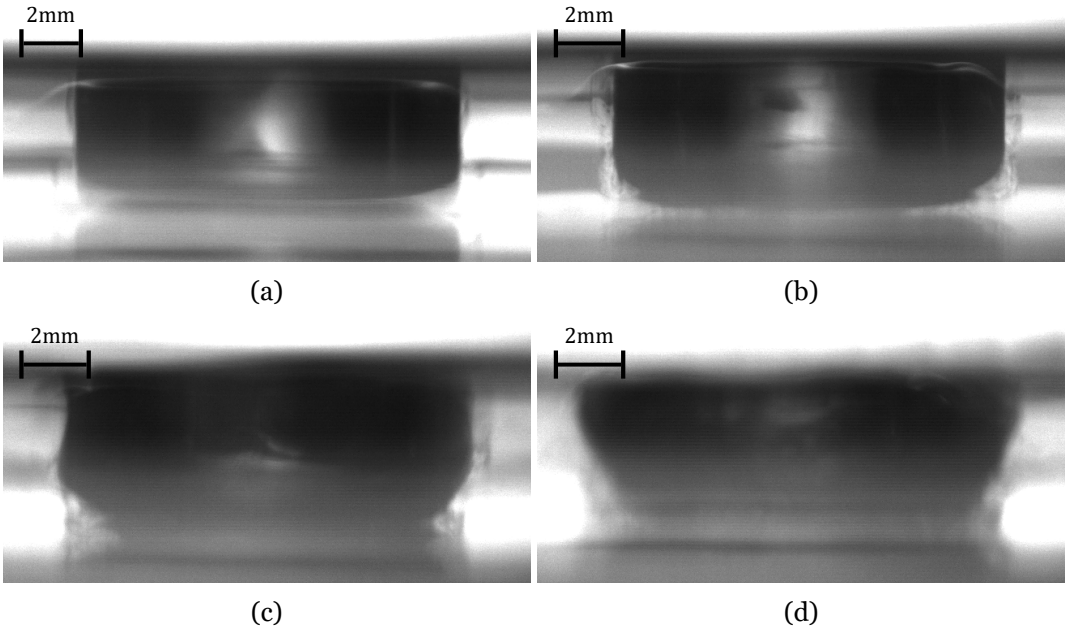

Figure 4.14: Visualisation of the crater formation subsequent to the impact of an n-decane droplet ($h^* = 1.0$, $\tau = 12.4$): a) $\theta = 0$; a) $\theta = 0.2$; c) $\theta = 0.4$; d) $\theta = 0.6$.

In order to examine the different evolution stages, figure 4.15 shows the influence of θ on the later stages of crater development for the water droplet impact and lower liquid film thickness. In general, an increase in the liquid film temperature influences the crater ejection times. For $\theta = 0$, the crater has detached from the impact surface, leading to the formation of a central jet (the crater retraction during later stages coincides with the emergence of the central jet). However, for $\theta = 0.2$, the crater still maintains contact with the impact surface, as a small number of ligaments are approaching breakup. This is similar to the following condition, $\theta = 0.4$, with an increased number of ligaments and, consequently, the crater contact area with the impact surface. For the highest temperature, $\theta = 0.6$, no ligaments are visible in the crater contact region, indicating that the crater is still undergoing its retraction period, lagging in terms of development in comparison to lower temperatures. Therefore, higher temperatures lead to an increase in the duration of the impact phenomena, namely the crater expansion and posterior retraction, leading to a delay in the crater ejection times. Similarly, the delay of the capillary wave also influences the crater detachment.

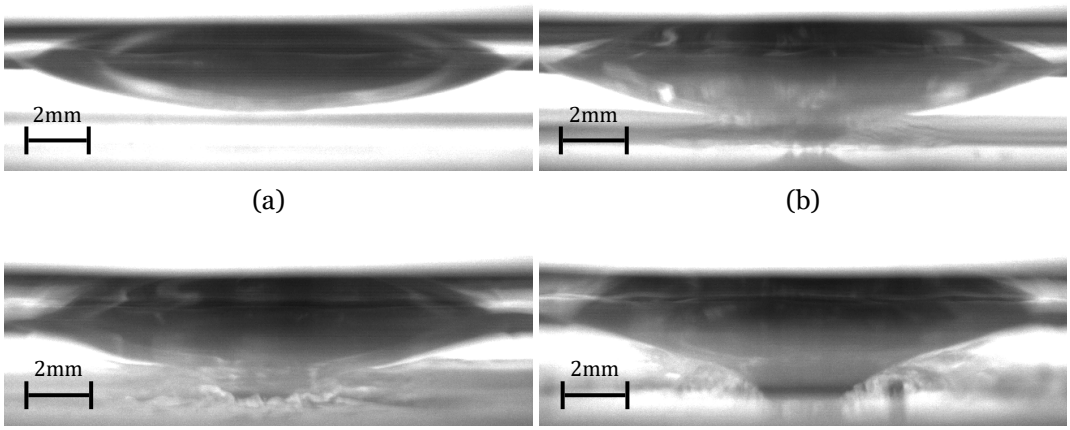

Figure 4.15: Visualisation of the crater formation subsequent to the impact of a water droplet ($h^* = 1.0$, $\tau = 25.1$): a) $\theta = 0$; a) $\theta = 0.2$; c) $\theta = 0.4$; d) $\theta = 0.6$.

4.1.2.2 Diameter and Depth Measurements

Figure 4.16 exhibits the crater penetration depth and diameter measurements for the n-decane droplet impact for $h^* = 1.5$. The crater measurements for fuels were not considered for the lower liquid thickness, $h^* = 1.0$, due to interferences associated with refraction, leading to post-processing difficulties. In terms of crater depth, as displayed by figure 4.16a, the initial expansion is similar across all temperatures. The droplet impacts the liquid film, forming a crater that expands outwards from the impact point until reaching the impact surface, which corresponds to $y^*_{cra} = h^* = 1.5$. From that point onward, the crater maintains the contact with the impact surface during the intermediate stages of the impact phenomena until retracting, leading to the ejection of the crater. As visualised previously, the detachment of the crater differs for different liquid film temperatures. For $\theta = 0$ and $\theta = 0.2$, the crater ejection occurs at approximately $\tau = 19$ and $\tau = 19.7$, respectively. However, for higher temperatures, the crater ejection times increase to $\tau = 20.7$ for $\theta = 0.4$, and $\tau = 21.5$ for $\theta = 0.6$.

This is due to several factors, such as the variation of the thermophysical properties of the liquid film, as well as the delay of the capillary wave associated with the crater retraction, influencing the crater development at later stages. For the crater diameter measurements, as presented by figure 4.16b, as these occur at a vertical displacement of $y = 0.5h$, the curves follow a path similar to a parabolic function. Additionally, this implies that the crater measurements are initiated once the crater reaches a propagation depth of $y^*_{cra} = 0.5$. Overall, the initial diameters are identical regardless of the liquid film temperature. The maximum diameters are achieved for intermediate stages of the crater formation, exhibiting similar values despite a slight increase for $\theta = 0$. However, the duration for which the maximum diameters are maintained is affected by temperature. Increasing values of θ lead to extended time intervals in which the diameter remains at its maximum, meaning that the crater enters the refraction stage at later stages. As previously stated, the propagation depth is associated with the capillary wave, which is delayed for higher temperatures, meaning that the crater preserves its maximum expansion for longer periods of time. Additionally, the crater exhibits higher diameter measurements for increasing liquid film temperatures during the retraction period.

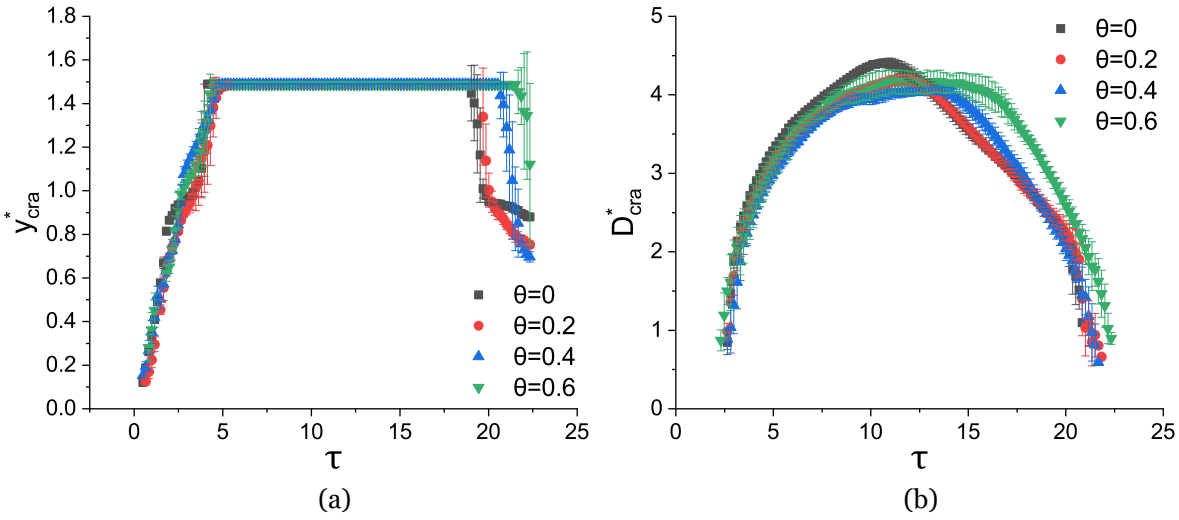

Figure 4.16: Crater measurements of an n-decane droplet impacting a liquid film for a range of dimensionless temperatures $(0 \leq \theta \leq 0.6)$ and impact conditions $(h^* = 1.5)$: a) Dimensionless crater depth; b) Dimensionless crater diameter.

The crater development for the n-heptane droplet impact is similar to the previous case, as visualised in figure 4.17. The initial expansion until reaching the bottom wall follows the same tendency as n-decane. In terms of crater detachment, $\theta = 0$ and $\theta = 0.2$ display the lower ejection times, increasing for higher temperatures. Regarding diameter measurements, the maximum diameter is identical to the various dimensionless temperatures. The correspondent time step to the maximum diameter also occurs for later stages for $\theta > 0$, despite being less noticeable in comparison to the previous case.

Lastly, figures 4.18 and 4.19 show the crater measurements for the water droplet impact for $h^* = 1.0$ and $h^* = 1.5$, respectively. It is important to highlight several details regarding the crater measurements. For the lower thickness, the crater penetration depth behaves similarly

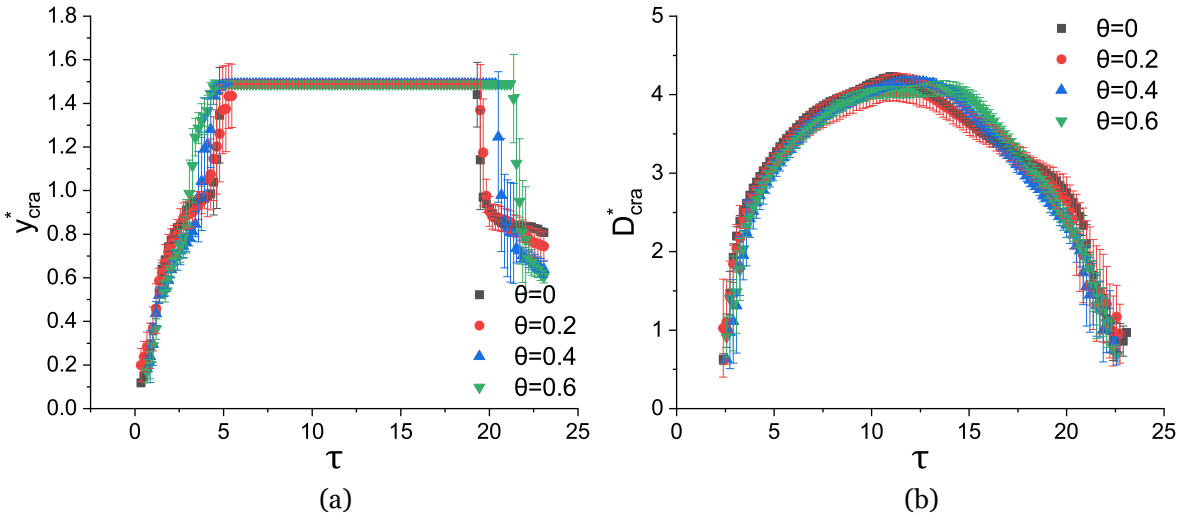

Figure 4.17: Crater measurements of an n-heptane droplet impacting a liquid film for a range of dimensionless temperatures $(0 \leq \theta \leq 0.6)$ and impact conditions $(h^* = 1.5)$: a) Dimensionless crater depth; b) Dimensionless crater diameter.

to the previous cases, in which the temperature increase influences the crater development exclusively at later stages during crater retraction and ejection. The maximum diameter is similar to all impact conditions, however it occurs for a later stage for non-isothermal conditions in comparison to $\theta = 0$. For $\theta > 0$, the study cases progress in identical patterns, and the diameter measurements are slightly higher for later stages, however less noticeable in comparison to fuels. This pattern becomes more evident for $h^* = 1.5$, where the measurements associated with non-isothermal conditions follow analogous paths and are distinct from $\theta = 0$. Opposite to fuels, the delay of the capillary wave is more pronounced between iso and non-isothermal conditions in comparison to its dependency with temperature. Nevertheless, the liquid film temperature plays a role in the crater ejection times.

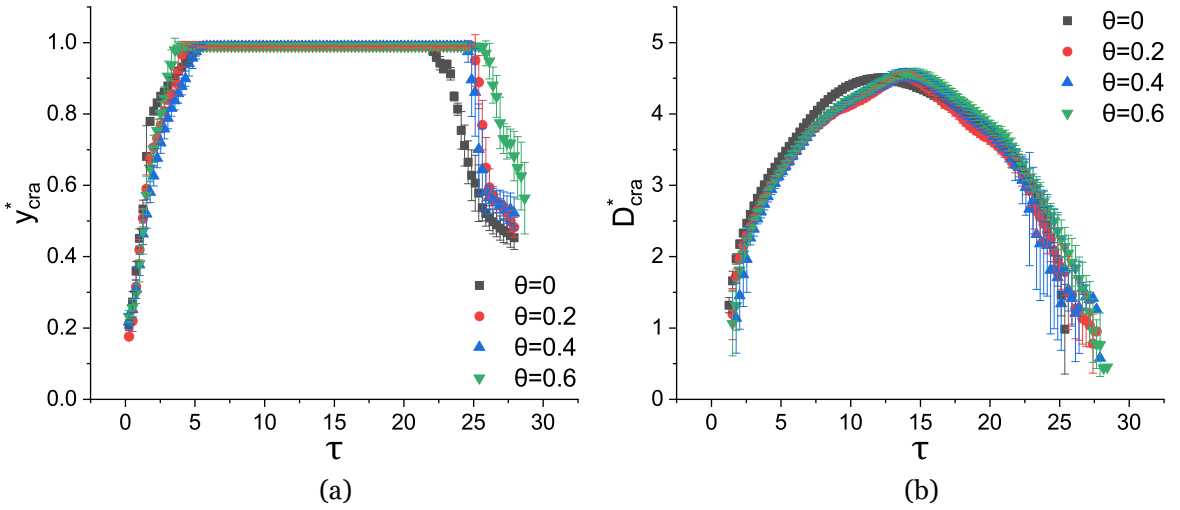

Figure 4.18: Crater measurements of a water droplet impacting a liquid film for a range of dimensionless temperatures $(0 \leq \theta \leq 0.6)$ and impact conditions $(h^* = 1.0)$: a) Dimensionless crater depth; b) Dimensionless crater diameter.

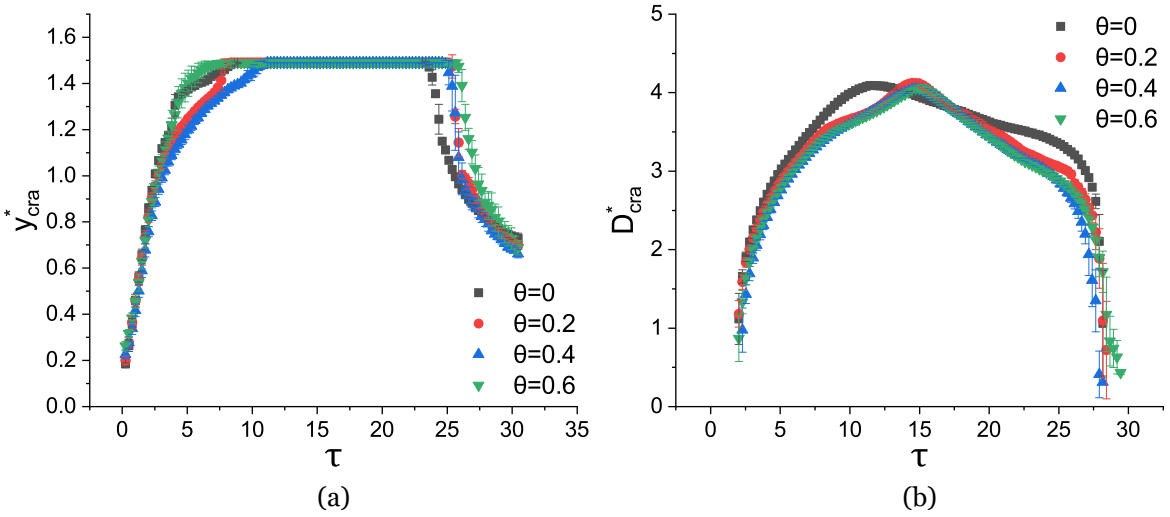

Figure 4.19: Crater measurements of a water droplet impacting a liquid film for a range of dimensionless temperatures ($0 \leq \theta \leq 0.6$) and impact conditions ($h^* = 1.5$): a) Dimensionless crater depth; b) Dimensionless crater diameter.

4.1.2.3 Theoretical Analysis

In order to support the experimental findings, a theoretical approach to the crater geometrical parameters was performed. As mentioned in the literature review, to the author knowledge, no theoretical work was developed regarding crater propagation depth in thin liquid films. For the crater diameter, several models were formulated in the scope of the research, including the propagation of a kinematic discontinuity by Roisman et al. [95], maximum crater diameter [93] and energy models based on the crater depth and diameter measurements [92]. Considering the impact conditions of the different studies, the model developed by Roisman et al. [95] was selected and compared with the obtained experimental data.

The model developed by Roisman et al. [95] estimates the crater diameter based on several dimensionless numbers, namely the Weber, Reynolds and Froude numbers, the dimensionless thickness of the liquid film, and theoretical parameters obtained based on experimental results, as presented in equation (2.9). This model was developed for similar impact conditions of the current work, in which distilled water and 1-propanol were considered, and certain theoretical parameters were studied and fitted for liquid film thicknesses ranging from $h^* = 0.5$ to $h^* = 2.0$. The fully developed model is represented by equations (2.9)-(2.14).

Figure 4.20 exhibits the experimental and theoretical results of the crater diameter measurements for the water droplet impact for two liquid film thicknesses, $h^* = 1.0$ and $h^* = 1.5$, and isothermal conditions, $\theta = 0$. Overall, the experimental results follow a similar tendency in comparison to the theoretical model. For $h^* = 1.0$, the crater propagation follows a similar pattern during both the initial expansion and retraction. The theoretical curve exhibits a behaviour analogous to a parabolic function. However, for $h^* = 1.5$, despite the experimental data being in good agreement with the theoretical model, the curve exhibits a different path. For the experimental condition, the existence of capillary waves during the expansion and

retraction stages leads to regions where these crater stages may be advanced or delayed depending on the propagation of the capillary wave. This effect becomes more pronounced for higher liquid film temperatures, as the capillary wave is delayed, and the maximum diameter is achieved for later stages of the crater expansion.

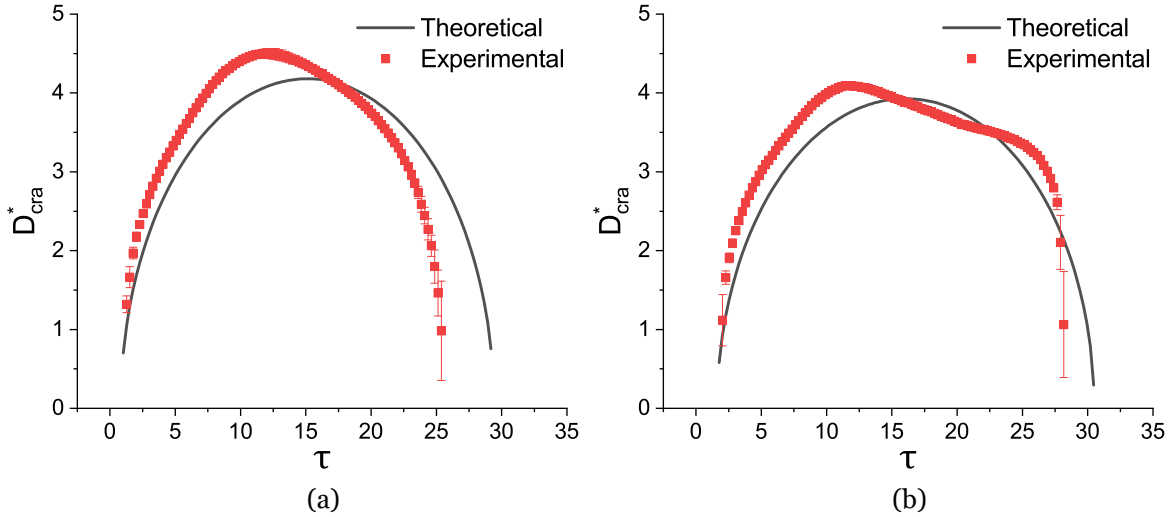

Figure 4.20: Comparison of theoretical and experimental results regarding crater diameter measurements of a water droplet impact for isothermal conditions: a) $h^* = 1.0$; b) $h^* = 1.5$.

For fuels, the theoretical model underpredicts the values obtained experimentally, as displayed by figure 4.21. Despite the distinct results, the experimental curve deviates marginally from a smooth parabolic function due to the capillary wave. Similar to the water results, for non-isothermal conditions, the delay of the capillary wave prolongs the period during which the diameter is maximum, diverging from the expected theoretical behaviour. The comparison between iso and non-isothermal conditions can be verified in figures 4.16 to 4.19 across all fluids.

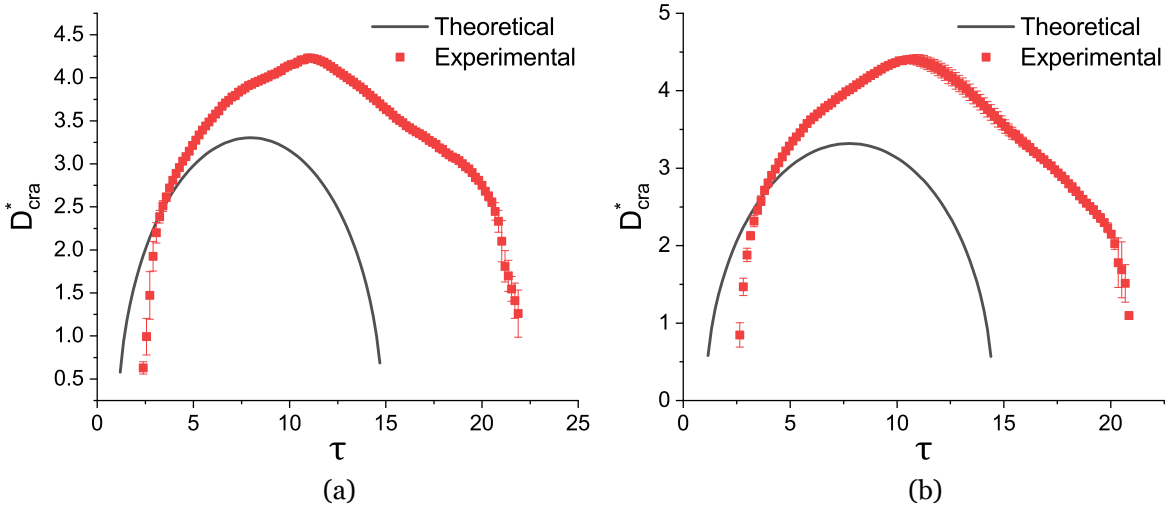

Figure 4.21: Comparison of theoretical and experimental results regarding crater diameter measurements for isothermal conditions and a dimensionless thickness of $h^* = 1.5$: a) N-heptane; b) N-decane.

In general, the experimental results related to the water droplet impact are in good agreement with the theoretical model, however the curves tend to deviate for heated liquid films.

For fuels, the model underpredicts the measured experimental results. In order to adapt the existing theory for non-isothermal conditions, a different approach would be required, such as implementing the thermophysical properties of the liquid film and the temperature differences in the estimation of the crater radius. Additionally, a wider range of impact conditions should be considered, as well as improving both optical access and crater post-processing.

4.1.3 Splashing

In order to study the spread-splash transition, the impact conditions previously defined for the central jet and crater analysis require adaptation to account for both spread and splashing regimes. Table 4.2 exhibits the experimental conditions for the analysis of the splashing phenomenon for water, n-heptane and n-decane. The splashing dynamics are evaluated by mainly varying the droplet impact velocity and dimensionless temperature of the liquid film. The considered values range from non-splash to splash conditions, therefore providing insight into the different regimes. The splashing is characterised by the formation of secondary droplets from the crown rim, whereas spreading displays a smooth crown development with no associated breakup. The qualitative and quantitative analysis are divided into splashing dynamics and overall crown evolution, and the splashing probability and consequent non-splash/splash correlation, respectively. This study has been previously detailed [229], with results further expanded in the following sections.

Table 4.2: Impact parameters of the splashing study for different fluids.

Fluid	D_d [mm]	U_d [m/s]	h^*	θ
Water	2.67	$1.88 - 2.71$	1.0	$0 - 0.75$
N-heptane	2.56	$1.23 - 2.09$	1.0	$0 - 0.81$
N-decane	2.72	$1.40 - 2.21$	1.0	$0 - 0.82$

4.1.3.1 Visualisation

Figure 4.22 shows the crown formation and possible secondary atomisation for the water droplet impact for different liquid film temperatures. For the isothermal condition, no formation of secondary droplets is visible, and the crown rim exhibits a rather smooth configuration. The evolving crown reaches its maximum height, followed by a continuous decrease until merging with the liquid film. For $\theta = 0.23$, an increase in temperature affects the crown formation. Instabilities arise on the developing crown, which are denominated as fingers or cusps. These are typically associated with secondary atomisation, as these structures tend to experience both stretching and thinning, which may lead to their breakup, resulting in the release of secondary droplets. The temperature increase is not sufficient to induce secondary atomisation, as the ligaments formed on the crown rim do not break up. For the following condition, $\theta = 0.44$, the ligaments of the crown rim reach a critical thickness, leading to the formation of secondary droplets. Additionally, the crown displays an irregular shape, which is also a result of the chaotic nature of splashing due to liquid ligament breakup. The regime transition from spreading to splashing is associated with the differences in thermophysical

properties, namely the density, viscosity, and surface tension, which decrease with temperature. The transition regime may exhibit some fluctuations, as illustrated by the subsequent temperature. For $\theta = 0.6$, several of the crown rim instabilities are attenuated, presenting similar structures to the isothermal condition. The spread/splash transition requires further studies to fully comprehend the underlying mechanisms associated with splashing under non-isothermal conditions.

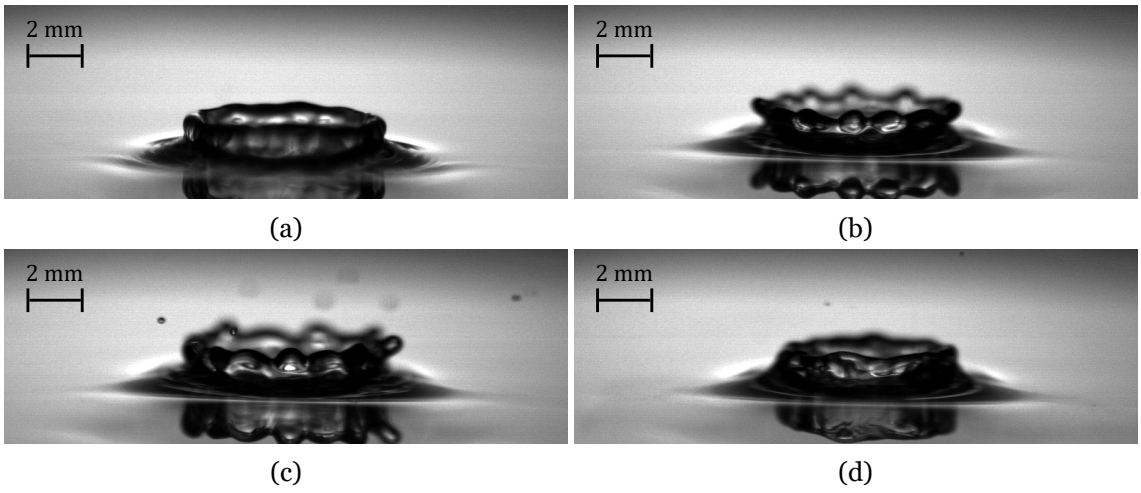

Figure 4.22: Visualisation of the impact phenomena of a water droplet onto a liquid film for different temperatures ($U_d = 2.42\ \mathrm{m/s},\ D_d = 2.67\ \mathrm{mm}$): a) $\theta = 0$, $\tau = 2.72$; b) $\theta = 0.23$, $\tau = 2.27$; c) $\theta = 0.44$, $\tau = 2.72$; d) $\theta = 0.60$, $\tau = 2.49$.

The impact of liquid film temperature can also be observed for the n-heptane droplet impact presented in figure 4.23. For ambient temperature ($\theta = 0$), the droplet impacts the surface, originating a liquid crown with several cusps in its rim, which produce secondary atomisation. Opposite to the previous case, the isothermal condition falls within the splashing regime. For $\theta = 0.19$, however, the splashing phenomenon is suppressed. The developing crown features several cusps in its rim, which do not lead to breakup, contrary to the previous condition. The number of instabilities in the crown rim is also reduced, exhibiting a more stable structure. From this point onward, for $\theta = 0.37$, the number of cusps in the crown rim increases, similar to the initial temperature increase of the water liquid film. Despite this, the liquid cusps do not break up, and no secondary atomisation is verified for this condition. Substantially increasing the liquid film temperature to $\theta = 0.81$ ultimately results in the breakup of the liquid ligaments, producing secondary droplets. The crown displays a more irregular and erratic crown rim in comparison to lower temperatures. As previously mentioned, the splashing phenomenon for water is reduced for $\theta = 0.6$. Similarly, n-heptane manifests an intermediate region in which an increase in the liquid film temperatures reduces or even suppresses splashing. Transitional regimes, which correspond to the regions neighbouring the spread/splash transition, require further research to evaluate fluctuations associated with splashing thresholds.

N-decane shows similar patterns to n-heptane, as represented by figure 4.24. For $\theta = 0$, the crown rim is relatively homogeneous in terms of shape and cusps. The secondary droplets

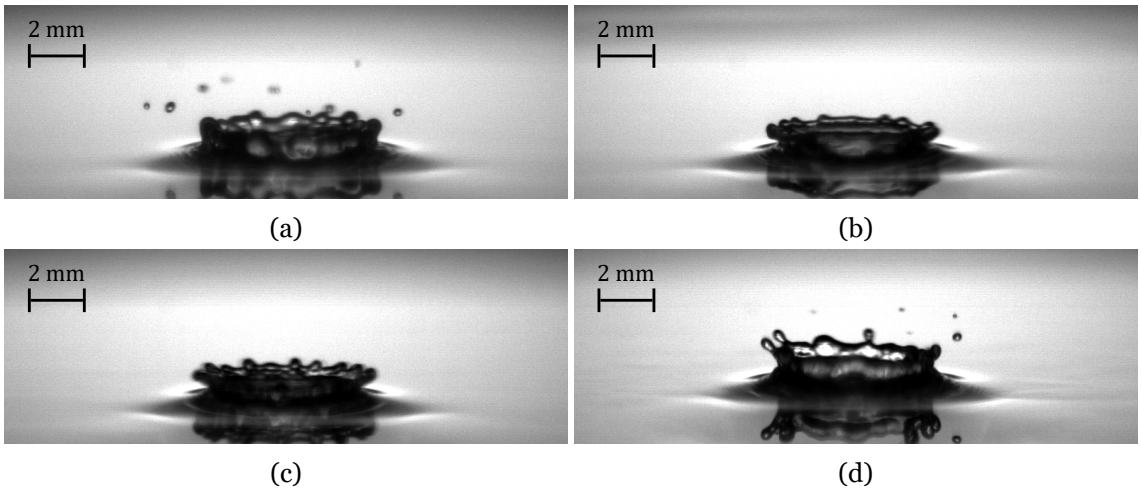

Figure 4.23: Visualisation of the impact phenomena of an n-heptane droplet onto a liquid film for different temperatures ($U_d = 1.52$ m/s, $D_d = 2.56$ mm): a) $\theta = 0$, $\tau = 1.78$; b) $\theta = 0.19$, $\tau = 1.48$; c) $\theta = 0.37$, $\tau = 1.48$; d) $\theta = 0.81$, $\tau = 1.63$.

originate from prompt splashing, which occurs at earlier stages of the impact phenomena due to their reduced dimensions. No clear distinctions are visible between isothermal and the following condition, $\theta = 0.1$. An increase in the liquid film temperature to $\theta = 0.19$ causes a sudden suppression of splashing, whereas the crown rim remains smooth throughout the crown development. The splashing phenomenon re-emerges at $\theta = 0.37$, and the secondary droplets exhibit a greater size in comparison to lower temperatures.

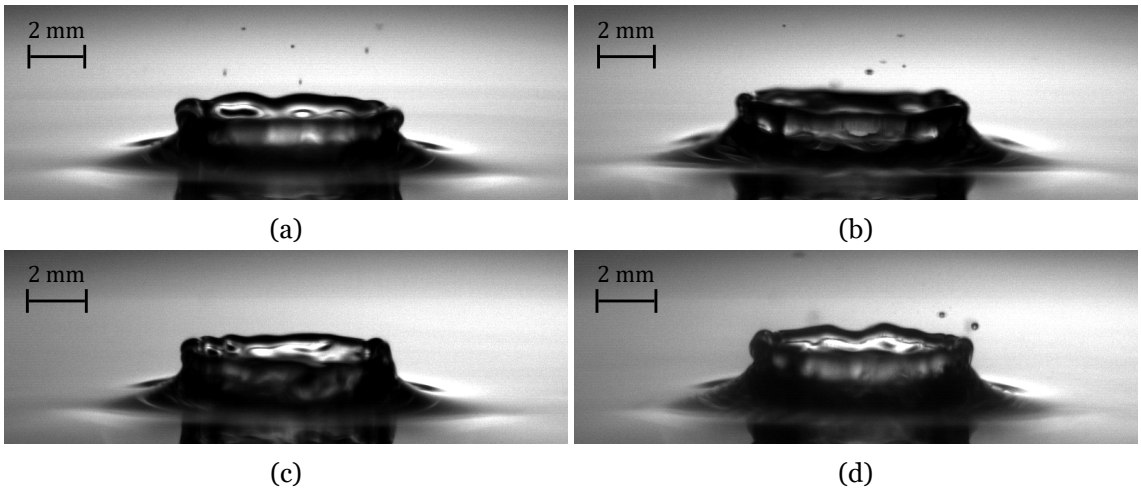

Figure 4.24: Visualisation of the impact phenomena of an n-decane droplet onto a liquid film for different temperatures ($U_d = 1.80$ m/s, $D_d = 2.72$ mm): a) $\theta = 0$, $\tau = 6.62$; b) $\theta = 0.10$, $\tau = 7.94$; c) $\theta = 0.19$, $\tau = 5.96$; d) $\theta = 0.37$, $\tau = 6.62$.

4.1.3.2 Splashing Occurrence

In order to quantify the influence of liquid film temperature on the impact phenomena, the splashing was evaluated in terms of occurrence probability for a variety of liquid film temperatures and impact velocities. Table 4.3 displays the splashing occurrence analysis for the water droplet impact. The green color represents splashing, which occurs for a probability of $p > 70\%$, the red color relates to spreading with a probability of $p < 30\%$, and the

yellow color is the transition regime ($30\% \leq p \leq 70\%$). Overall, an increase in the impact velocity causes the transition from the spreading to splashing regimes. For intermediate velocities, $2.19\ \mathrm{m/s} \leq U_d \leq 2.42\ \mathrm{m/s}$, an increase in the dimensionless temperature results in a higher chance of splashing, progressing from a splashing probability of 0% for $\theta = 0$ and $\theta = 0.11$ to $p > 90\%$ for $\theta = 0.44$. Mid-range temperatures, such as $\theta = 0.23$, exhibit transitional behaviour regarding splashing occurrence, including $p = 38.5\%$ for $U_d = 2.19\mathrm{m/s}$ and $p = 10\%$ for $U_d = 2.42\ \mathrm{m/s}$. Beyond this regime, in the outer regions ($U_d = 1.88\ \mathrm{m/s}$ and $U_d = 2.71\ \mathrm{m/s}$), there is no significant variation in the splashing occurrence. For the lower threshold, the spreading phenomenon is consisting across the various temperatures, as the temperature increase is not sufficient to induce splashing. On the opposite end, for $U_d = 2.71\ \mathrm{m/s}$, higher liquid film temperatures generate more droplets as a result of lower viscosity and surface tension values. Several discrepancies are spotted in the boundaries of the spread/splashing phenomenon, in which an increase in the impact velocity and/or dimensionless temperature may result in a decrease or suppression of splashing. This is verified in figure 4.22, as the impact condition correspondent to $\theta = 0.6$ manifests smoother crowns and a reduction in the splashing phenomenon in comparison to the previous temperatures. This condition corresponds to $U_d = 2.42\ \mathrm{m/s}$ and displays a slight decrease in the splashing occurrence percentage from $p = 100\%$ to $p = 64\%$ when increasing the liquid film dimensionless temperature from $\theta = 0.44$ to $\theta = 0.6$, respectively. Additionally, for a fixed liquid film temperature in the transitional regime, such as $\theta = 0.23$, increasing the impact velocity from $U_d = 2.29\ \mathrm{m/s}$ to $U_d = 2.42\ \mathrm{m/s}$ causes a sudden decrease in the splashing occurrence percentage from $p = 90\%$ to $p = 10\%$.

Table 4.3: Splashing occurrence percentage as a function of the impact velocity and dimensionless temperature for water: - Splashing; - Spreading; - Transition.

	Impact velocity [m/s]					
θ	1.88	2.11	2.19	2.29	2.42	2.71
0	0	0	0	0	0	100
0.11	0	0	0	0	0	100
0.23	0	0	38.5	90	10	100
0.44	0	0	90	100	100	100
0.60	0	30	100	80	64	100
0.75	10	10	100	90	80	100

Table 4.4 indicates the splashing occurrence probability for n-heptane under different impact velocities and dimensionless temperatures. For isothermal conditions, the spread/splash transition occurs between $U_d = 1.43\ \mathrm{m/s}$ and $U_d = 1.52\ \mathrm{m/s}$. The outer regions show a similar tendency to water, as the temperature increase for $U_d = 1.23\ \mathrm{m/s}$ does not induce splashing, and for $U_d = 2.09\mathrm{m/s}$, the splashing regime is maintained throughout the dimensionless temperatures. The transition regimes occur for an impact velocity range of $1.52\ \mathrm{m/s} \leq U_d \leq 1.68\ \mathrm{m/s}$. For the lower temperatures, $\theta = 0$ and $\theta = 0.1$, splashing occurrence percentages close to $p = 100\%$ are visualised. Despite the splashing dominance for isothermal and low temperature conditions, increasing the dimensionless temperature

to $\theta = 0.2$ leads to the suppression of the splashing phenomenon. For $U_d = 1.52$ m/s, the suppression regime extends from $\theta = 0.19$ to $\theta = 0.59$, shifting back to splashing for higher liquid film temperatures ($\theta = 0.81$). For the upper boundary, $U_d = 1.68$ m/s, this regime is limited to $\theta = 0.19$ and $\theta = 0.37$, as the latter shows signs of transition, with a splashing probability of $p = 38.5\%$. From this point onward, splashing is promoted for higher liquid film temperatures.

Table 4.4: Splashing occurrence percentage as a function of the impact velocity and dimensionless temperature for n-heptane: - Splashing; - Spreading; - Transition.

	Impact velocity [m/s]				
θ	1.23	1.43	1.52	1.68	2.09
0	0	0	90	100	100
0.10	0	0	80	100	100
0.19	0	10	0	0	100
0.37	0	0	0	38.5	100
0.59	0	10	10	100	100
0.81	0	80	100	100	100

Analogous to visualisation, n-decane exhibits comparable tendencies to n-heptane, as illustrated by table 4.5. For impact conditions distant from the splashing threshold ($U_d = 1.4$ m/s and $U_d = 2.21$ m/s), the observed phenomena remain unchanged across the temperature range. For $U_d = 1.65$ m/s and $U_d = 1.72$ m/s, isothermal conditions are characterised by the spreading phenomenon, corresponding to a splashing occurrence of $p = 0\%$. This value tends to increase with higher temperatures, displaying $p = 60\%$ and $p = 20\%$ for $\theta = 0.6$, and $p = 100\%$ for $\theta = 0.82$. This is in accordance with the n-heptane impact condition of $U_d = 1.43$ m/s. In terms of splashing irregularities, the transitional regimes are represented by $U_d = 1.8$ m/s and $U_d = 2.05$ m/s. Splashing is visualised for isothermal conditions ($\theta = 0$) and the subsequent temperature ($\theta = 0.1$). Further increasing the temperature to $\theta = 0.19$ suppresses and reduces splashing for $U_d = 1.8$ m/s and $U_d = 2.05$ m/s, respectively. This condition is limited to $\theta = 0.19$, as higher temperatures revert this effect. The n-decane splashing fluctuations are restricted to a specific temperature opposite to the n-heptane intermediate regime.

Table 4.5: Splashing occurrence percentage as a function of the impact velocity and dimensionless temperature for n-decane: - Splashing; - Spreading; - Transition.

	Impact velocity [m/s]					
θ	1.40	1.65	1.72	1.80	2.05	2.21
0	0	0	0	100	100	900
0.10	0	0	0	80	100	90
0.19	0	0	0	10	60	100
0.42	0	10	10	100	100	100
0.60	0	60	20	100	100	100
0.82	0	100	100	100	100	100

Overall, the liquid film temperature and thermophysical properties play a major role in the impact dynamics, as mainly demonstrated by the splashing occurrence percentages. The differences in thermophysical properties, namely lower values of viscosity and surface tension, contribute to higher Reynolds and Weber numbers, promoting the occurrence of splashing. This is in accordance with the existing splashing correlations displayed in table 2.2.

4.1.3.3 Non-Splash/Splash Threshold

In order to translate the influence of liquid film temperature on the impact phenomena and, consequently, splashing, the experimental results were compared with existing correlations in the literature. As previously mentioned, most recent correlations have been adapted to account for distinct dynamics related to splashing, such as flowing films, and prompt and crown splash distinction. For isothermal conditions, the correlation developed by Wander Wal et al. [115] shows a good fit with the obtained experimental data. This correlation utilises the splashing threshold parameter, K, as a function of the Ohnesorge and Reynolds numbers, as represented by equation (4.8):

$$K = OhRe^{1.17} = 63 \tag{4.8}$$

These dimensionless numbers are based on the droplet thermophysical properties at ambient temperature, meaning that the existing correlations do not account for temperature differences between the droplet and the liquid film. In order to properly adapt the Vander Wal et al. [115] correlation, the present work utilises the geometrical properties of the droplet, namely its diameter and impact velocity, and the thermophysical properties of the liquid film, to calculate the dimensionless parameters. This approach is based on the assumption that the liquid film volume is several orders of magnitude higher than the droplet, meaning that the impact phenomena develop at liquid film temperature. The adapted Reynolds, Weber and Ohnesorge numbers can be described by equations (4.9), (4.10) and (4.11), respectively:

$$Re_{d,f} = D_d U_d \rho_f / \mu_f \tag{4.9}$$

$$We_{d,f} = D_d U_d^2 \rho_f / \sigma_f \tag{4.10}$$

$$Oh_{d,f} = \mu_f / \sqrt{\rho_f \sigma_f D_d} \tag{4.11}$$

Therefore, the impact conditions presented by table 4.2 are coupled with thermophysical properties of the heated liquid film, which can be determined by the equations introduced in Appendix A. This results in the experimental conditions shown in table 4.6. The wide range

of conditions is obtained through the impact velocity and dimensionless temperature variations. Due to the strong dependency of surface tension and viscosity with temperature in comparison to density, the adapted Weber and Reynolds numbers increase for $\theta > 0$. The Ohnesorge number is determined by the relative magnitude between the viscous and the density and surface tension forces. Opposite to the previous numbers, the Ohnesorge number decreases with temperature, meaning that the highest value corresponds to isothermal conditions, whereas the lowest relates to $\theta \approx 0.8$.

Table 4.6: Experimental conditions for the different fluids in terms of adapted Weber, Reynolds and Ohnesorge numbers.

Fluid	$We_{d,f}$	$Re_{d,f}$	$Oh_{d,f}$
Water	$75 - 304$	$3807 - 19756$	$8.8 \times 10^{-4} - 2.3 \times 10^{-3}$
N-heptane	$110 - 502$	$4820 - 14628$	$1.5 \times 10^{-3} - 2.2 \times 10^{-3}$
N-decane	$114 - 632$	$2440 - 14269$	$1.8 \times 10^{-3} - 4.4 \times 10^{-3}$

To bring this concept into effect, the correlation developed by Wander Wal et al. [115] was adapted for non-isothermal conditions, as exhibited by equation (4.12). The adapted correlation maintains the original exponents for a more direct approach by providing adaptability for both isothermal and non-isothermal conditions.

$$K = Oh_{d,f} Re_{d,f}^{1.17} \tag{4.12}$$

Following this, the experimental data is exhibited in figure 4.25 in terms of the adapted splashing threshold parameters as a function of the dimensionless temperature. For visualisation purposes, the black color refers to spreading, whereas splashing is defined by the red color for all fluids. Overall, it is possible to identify a positive slope in the dependency of the splashing parameter on θ, as the splashing threshold increases for higher values of θ.

In spite of the dependence of the splashing parameter on the thermophysical properties of the heated liquid film, the spreading and splashing regimes suggest a linear positive pattern with the dimensionless temperature. This tendency is represented by the blue dashed line, which apparently separates both regimes and is expressed by equation 4.25:

$$K = Oh_{d,f} Re_{d,f}^{1.17} = 63\,(1 + 0.35\theta) \tag{4.13}$$

Several outliers should be mentioned regarding the proposed correlation. For the fuels, the spreading regime is displayed for $0.2 \lesssim \theta \lesssim 0.4$ despite being above the threshold. These results correspond to the region in which an increase in the liquid film temperature leads to a reduction/suppression of the splashing phenomenon, such as $U_d = 1.52\,\mathrm{m/s}$ for n-heptane and $U_d = 1.8\,\mathrm{m/s}$ for n-decane. For isothermal conditions, $\theta = 0$, the proposed splashing parameter is equal to $K = 63$, meaning that it corresponds to the original correlation proposed

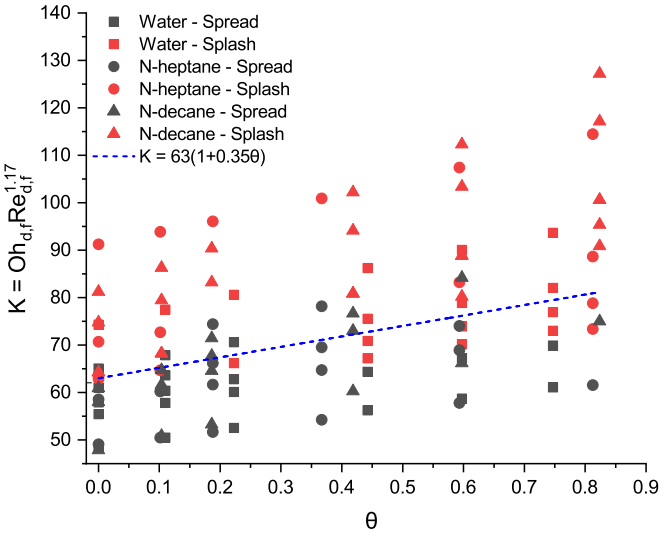

Figure 4.25: Adapted splashing threshold parameter, K, as a function of the dimensionless temperature, θ, for the various fluids.

by Wander Wal et al. [115]. An increase in the liquid film temperature increases the splashing parameter considerably, as the highest temperature considered, $\theta = 0.82$, corresponds to a threshold value of $K = 81$. Temperature conditions from this point onward were not considered for the splashing analysis, as the liquid film enters a boiling state. This regime is characterised by mass transfer mechanisms, including bubble nucleation, growth and possible detachment from the impact surface. The released vapour bubbles ascend, reaching the liquid-gas interface and bursting chaotically. This induces instabilities in the form of mechanical waves that propagate through the liquid film, causing local thickness oscillations. The splashing correlation is only applicable for static liquid films with no nucleation sites associated with boiling. The experimental results can also be displayed as a function of the adapted Ohnesorge and Reynolds numbers, as represented by figure 4.26, similar to the studies developed in the literature.

The previously proposed correlation corresponds to the grey region, which is delimited by the lower and upper boundaries that correspond to $K = 63$ for $\theta = 0$ and $K = 82$ for $\theta = 0.82$, respectively. In terms of value displacement, n-decane is positioned near the top margin due to the high viscosity and low surface tension values, equating to high Ohnesorge numbers. On the other hand, water is located close to the lower margin due to high surface tension values. N-heptane exhibits viscosity and surface tension values similar to water and n-decane, respectively, consequently being positioned between these fluids. Overall, the grey region captures the spread/splash transition rather accurately, however it presents similar challenges to those depicted in figure 4.25. For water, the spread/splash transition occurs close to the lower boundary, $K = 63$, whereas fuels require higher Reynolds and Ohnesorge values to induce splashing, which is associated with the transitional regimes previously detailed ($6000 < Re_{d,f} < 10000$ for $0.2 < \theta < 0.4$).

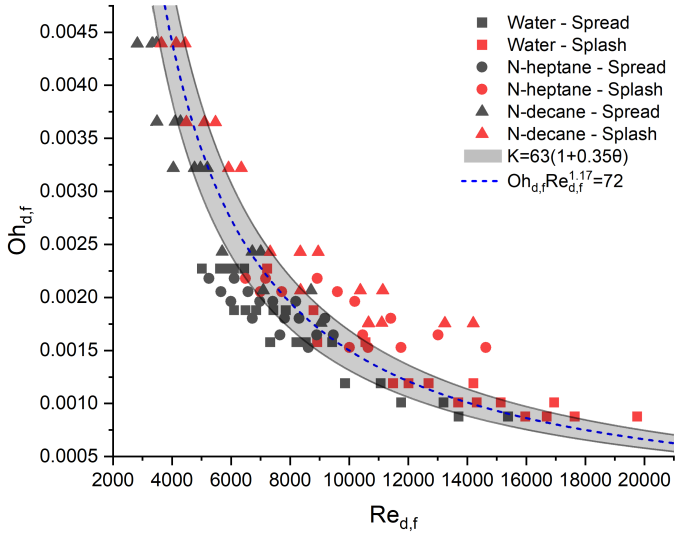

Figure 4.26: Splashing evaluation in terms of adapted Ohnesorge and Reynolds numbers for the experimental conditions.

To accommodate the experimental results regarding the different fluids and impact conditions, the grey region can be reduced to a single boundary, as revealed by the blue dashed line. This curve is a simplification of equation (4.13) and corresponds to the central line of the grey region, which is exhibited by equation 4.14:

$$K = Oh_{d,f} Re_{d,f}^{1.17} = 72 \tag{4.14}$$

In this aspect, the splashing threshold can be calculated in terms of the liquid film thermophysical properties, as well as the geometrical properties of the droplet. Refining the proposed correlations requires new studies focused on transitional regimes and temperature-related dynamics. The suppression of splashing for low temperatures under non-isothermal conditions requires a deep understanding of fluid and heat flow, specifically Marangoni stress and local evaporation.

4.1.4 Bubble Encapsulation

Similarly to the analysis of the splashing phenomenon as a function of temperature, the occurrence probability of bubble encapsulation was investigated. Table 4.7 shows the impact conditions related to the n-heptane and n-decane droplet impact onto heated liquid films. In comparison to the splashing analysis, higher impact velocities are required to induce bubble encapsulation.

The experimental conditions were defined based on the work developed by Ribeiro et al. [122]. The onset of bubble encapsulation was studied for a number of 10 droplets per impact

Table 4.7: Experimental conditions for the bubbling outcome of n-heptane and n-decane droplet impact.

Fluid	D_d [mm]	U_d [m/s]	h^*	θ
N-heptane	2.56	$1.3 - 4.9$	1.0	$0 - 0.6$
N-decane	2.72	$1.6 - 5.0$	1.0	$0 - 0.6$

condition. According to the authors, the emergence of bubble encapsulation occurs within a region denominated as a band. A lower and upper transition boundaries confine the regime, where the former refers to the transition from splashing to bubble encapsulation, and the latter to the reverse process. Amongst the existing correlations in the literature for single droplet impact onto a liquid film, the splashing threshold proposed by Vander Wal et al. [115] is in best agreement with the experimental data on both within and outer regions of the validation domain. This correlation was adapted to account for the liquid film thickness, considering it as the characteristic length in the Ohnesorge number, whereas the Reynolds number utilised the droplet diameter prior to impact. The adapted correlation is represented by equation (4.15):

$$a = \frac{\ln\left(34.5/Re\right)}{\ln\left(Oh_f\right)}, \forall\, a \in [1.022, 1.142] \tag{4.15}$$

This equation is valid for $0.4 < h^* < 1$ and for the a values mentioned. The experimental results regarding the occurrence of bubble encapsulation are illustrated in figure 4.27 for the droplet Reynolds number and the liquid film Ohnesorge number. The grey region corresponds to the bubble encapsulation regime, where the lower threshold is defined by the red curve and the upper threshold by the blue curve. The outer region of the validation domain is dominated by the splashing regime. The proposed correlation was created for bubble encapsulation probability occurrences of $p > 50\%$. It is possible to visualise that the majority of the results extend beyond the bubble encapsulation regime, as the experimental data is categorised as splashing under the lower threshold [230]. Therefore, the criterion developed by Ribeiro et al. [122] is limited to isothermal conditions and requires further adaptation when involving heated liquid films.

Due to the influence of temperature on liquid films and, consequently, on the impact phenomena, a similar approach to splashing is performed. This approach consists on adapting the dimensionless numbers with the thermophysical properties of the heated liquid film, implementing the influence of temperature directly in the dimensionless analysis. The previous correlation is then adapted by utilising the characteristic length of the droplet in the Reynolds number, and the thermophysical properties of the heated liquid film. Analogously, the Ohnesorge number maintains the liquid film thickness as its characteristic length, and the thermophysical properties are adapted for non-isothermal conditions. As a result, the previously proposed correlation by Ribeiro et al. [122] is adapted to account for non-isothermal conditions in the form of the thermophysical properties of the liquid film [230] as represented by

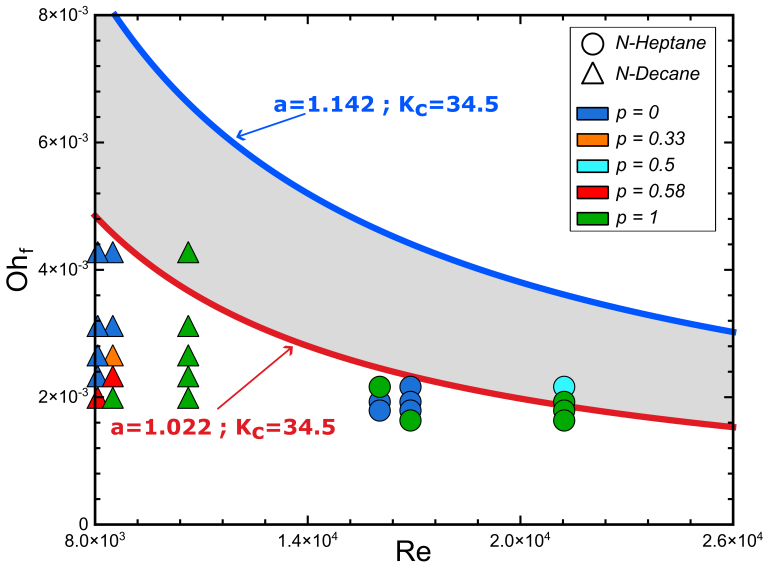

Figure 4.27: Evaluation of bubble encapsulation in terms of Ohnesorge and Reynolds numbers using the threshold proposed by Ribeiro et al. [122].

equation (4.16):

$$a = \frac{\ln\left(34.5/Re_{d,f}\right)}{\ln\left(Oh_f\right)}, \forall\, a \in [1.022, 1.142] \tag{4.16}$$

Figure 4.28 exhibits the bubble encapsulation occurrence probability of the experimental results as a function of the adapted Reynolds and Ohnesorge numbers. In comparison to the non-adapted correlation, several data points previously outside of the grey region are now positioned above the lower threshold, namely for $p > 50\%$. The experimental results corresponding to splashing ($p < 50\%$) do not fall within the validation domain.

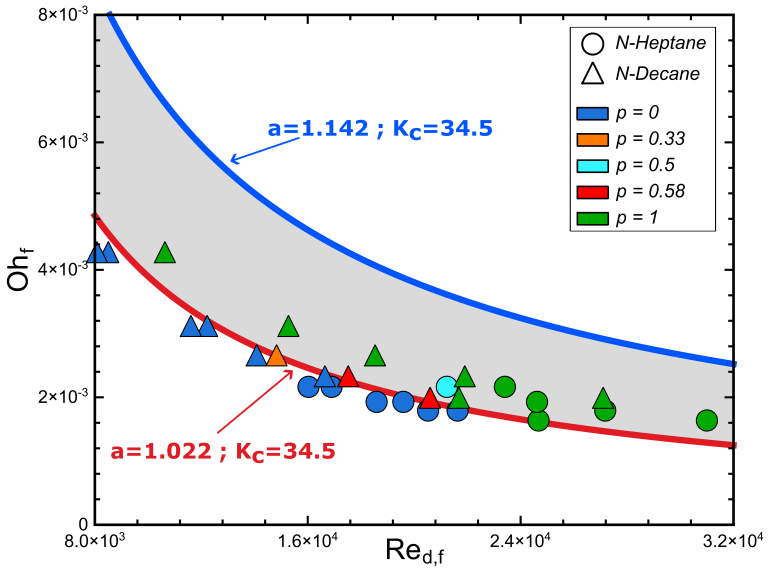

Figure 4.28: Evaluation of bubble encapsulation in terms of adapted Ohnesorge and Reynolds numbers using the adapted threshold.

Overall, the distribution of the experimental data follows the tendency of the threshold boundaries, where the splashing results are displayed below the lower threshold, and the bubble encapsulation results fall within the corresponding region. Therefore, the experimental results are in agreement with the adapted correlation by modifying the thermophysical properties in a direct approach to account for heated liquid films. Despite this, additional research should be considered, such as evaluating the upper boundary threshold as a function of the thermophysical properties, as well as a wider range of temperatures, liquid film thicknesses and impact conditions.

4.2 Subcooled Boiling Regime

In the presence of a heat flux or a high temperature environment, the fluid temperature will increase until reaching a saturation point. In terms of liquid films, considerably increasing their temperature intensifies the mass and heat transfer phenomena. This leads to the nucleation of vapour bubbles on the impact surface. If the vapour bubbles remain attached to the surface, or sporadically detach without reaching the liquid-gas interface due to condensation, the liquid film enters a subcooled boiling regime. This behaviour is typical for relatively high temperature liquid films under the boiling point. If the temperature reaches the saturation point, the vapour bubbles detach from the surface with increased frequency, reaching the liquid film and bursting, creating mechanical waves. This is characterised as the saturated boiling regime. These regimes are evaluated in terms of vapour bubble nucleation, growth and detachment. The post-processing regarding vapour bubble diameter measurements has been previously detailed.

Two different regions containing vapour bubbles were considered, which consist of the surface boundaries (adjacent to the radial walls), and the surface impact region. This is due to the distinct behaviour of the vapour bubbles, which require a separate analysis. The vapour bubbles on the surface impact region were identified and measured in terms of spatial distribution and diameter, respectively. The heating phase of the liquid film starts at $t = 0\,\mathrm{s}$, in which the temperature will slowly increase until reaching a stabilisation temperature. This temperature is defined as the liquid film temperature achieved after the heating phase. The vapour bubbles are evaluated for both the heating and the stabilisation phases across all liquid film temperatures. Each of these phases last approximately $10\ \mathrm{min}$ and $30\ \mathrm{min}$, respectively. Due to heat losses, the measured temperature of the liquid film is lower in comparison to the temperature value defined on the heating device. For water, the liquid film reaches a temperature of $T_f = 79.6^{\circ}\mathrm{C} \pm 0.6^{\circ}\mathrm{C}$ for a heating element temperature of $T_{he} = 110^{\circ}\mathrm{C}$. This condition relates to the subcooled boiling regime, where the static liquid film contains several vapour bubbles across the impact surface. A heating element temperature of $T_{he} = 150^{\circ}\mathrm{C}$ corresponds to a water liquid film temperature of $T_f = 95.7^{\circ}\mathrm{C} \pm 1.9^{\circ}\mathrm{C}$, leading to temperatures close to the saturation point. In the case of n-heptane, the liquid reaches a temperature of $T_f = 97.6^{\circ}\mathrm{C} \pm 0.5^{\circ}\mathrm{C}$ for $T_{he} = 110^{\circ}\mathrm{C}$, meaning that, for higher temperatures, the liquid film is at saturation temperature. This study has been extensively documented [231].

Figures 4.29, 4.30 and 4.31 exhibit the vapour bubble growth and distribution on the impact surface for different fluids and stages. Overall, it is possible to identify major differences between the fluids. The onset of subcooled boiling regime is represented by figure 4.29 for water. During the heating phase, vapour bubbles are spotted in the boundaries of the container, with no nucleation sites in the impact surface for $t = 150\,\mathrm{s}$. As the liquid film reaches the stabilisation temperature, for $t > 10\,\mathrm{min}$, several vapour bubbles are dispersed in the impact surface, and the void region in the boundaries of the container was filled with additional vapour bubbles. The distribution of the vapour bubbles remains relatively stable throughout the stabilisation procedure, increasing in diameter for later stages, as represented by figure 4.29c.

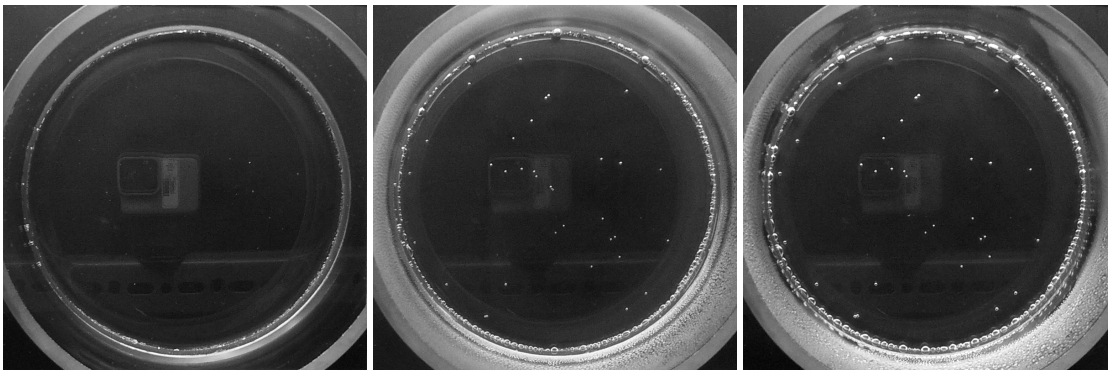

(a) (b) (c)

Figure 4.29: Top view of the vapour bubble growth and distribution on the surface impact region for water ($T_{he} = 110^{\circ}\mathrm{C}$): a) $t = 150\,\mathrm{s}$; b) $t = 765\,\mathrm{s}$; c) $t = 1620\,\mathrm{s}$.

Increasing the liquid film temperature to conditions close to the boiling point leads to the vapour bubble distribution displayed by figure 4.30. The initial liquid film behaviour is similar to the previous condition, as vapour bubbles emerge close to the radial walls. However, during the heating phase, vapour bubbles develop more rapidly, increasing in both diameter and release rate. This tendency is verified for later stages, as several bubbles detach from the impact surface, causing a decrease in the number of existing vapour bubbles. Analogous to the lower liquid film temperature, the boundaries of the container are more susceptible to bubble nucleation sites due to the surface roughness differences in comparison to the impact surface. The material of the impact surface is borosilicate glass, whereas the outer regions are composed of both borosilicate glass and acetoxy silicone due to the bonding process of these parts. Consequently, the local surface roughness increases, originating potential nucleation sites for the formation of vapour bubbles. This can also be visualised in figure 4.31 for n-heptane. The heating and stabilisation phases reveal no vapour bubbles in either regions, despite of the liquid film temperature. However, for the onset of boiling, several nucleation sites are visualised in figure 4.31b. The formed vapour bubbles detach instantaneously, which is associated with the thermophysical properties of fuels. Lower values of surface tension, which correlate to lower contact angles, suppress the adhesion of the vapour bubbles on the surface. The bubbles formed detach with reduced size in comparison to water, entering a boiling state.

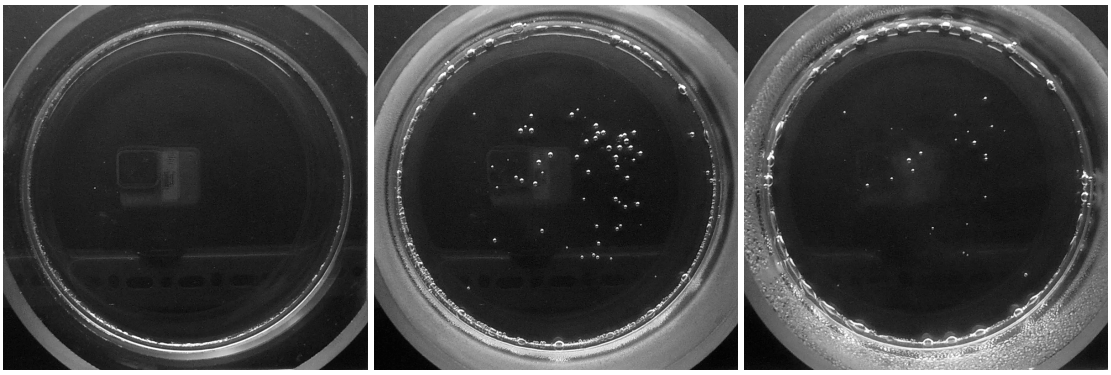

(a) (b) (c)

Figure 4.30: Top view of the vapour bubble growth and distribution on the surface impact region for water ($T_{he} = 150°\mathrm{C}$): a) $t = 15$ s; b) $t = 375$ s; c) $t = 810$ s.

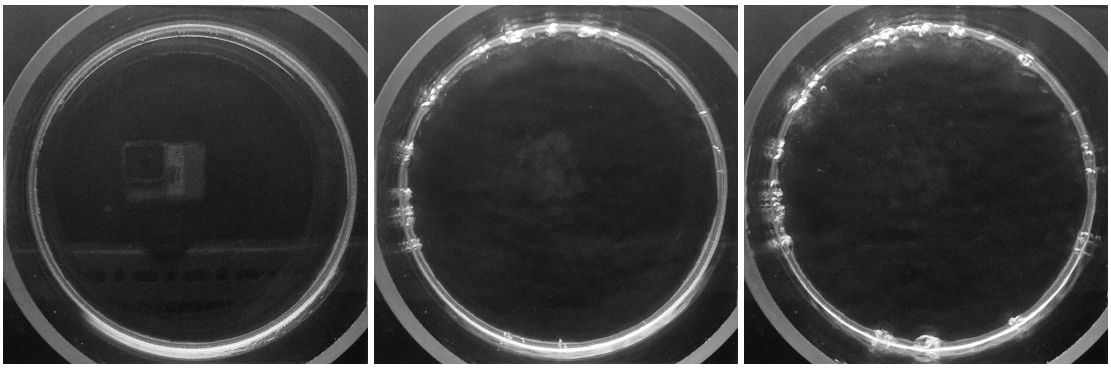

(a) (b) (c)

Figure 4.31: Top view of the vapour bubble growth and distribution on the surface impact region for n-heptane ($T_{he} = 130°\mathrm{C}$): a) $t = 15$ s; b) $t = 105$ s; c) $t = 300$ s.

Figure 4.32 shows the quantitative analysis of the number, N_b, and diameter, D_b, of vapour bubbles over extended periods of time as a function of the heating element temperature for water. The heating and stabilisation phases are divided for $t < 10$ min and $t > 10$ min, respectively. For figure 4.32a, both the number and size of vapour bubbles increase steadily during the initial heating phase, being more pronounced for higher liquid film temperatures. Increasing values of the heating element temperature also lead to higher maximum values of vapour bubbles. For $T_{he} = 90°\mathrm{C}$ and $T_{he} = 110°\mathrm{C}$, the number of bubbles reaches a maximum value of approximately $N_b \approx 33$ during the stabilisation phase. For $T_{he} = 130°\mathrm{C}$ and $T_{he} = 150°\mathrm{C}$, a gradual decrease accompanied by oscillations is verified subsequent to the initial spike. This is explained by the increasing temperatures and boiling effects, leading to liquid film instabilities and potential vapour bubble detachment. Figure 4.32b depicts the evolution of diameter at different temperatures for the heating and stabilisation stages. For lower temperatures, $T_{he} = 90°\mathrm{C}$ and $T_{he} = 110°\mathrm{C}$, as the vapour bubbles do not detach from the surface, these continuously increase in size. The initial heating stage is similar for both conditions and, from that point onward, the vapour bubble diameters for $T_{he} = 110°\mathrm{C}$ are higher in comparison to the lower temperature. For $T_{he} = 130°\mathrm{C}$ and $T_{he} = 150°\mathrm{C}$, the diameter measurements for the initial phase follow a similar tendency to the previous conditions, displaying a greater slope and attaining higher values. The vapour bubble mea-

surements during the stabilisation phase show oscillations due to the ongoing cycle of nucleation, growth and detachment of new vapour bubbles. This results in a lower mean and a higher standard deviation throughout this stage. The maximum area percentage occupied by the vapour bubbles on the surface impact region (neglecting the surface boundaries) ranges from 0.13% for $T_{he} = 90°\mathrm{C}$ to 0.42% for $T_{he} = 150°\mathrm{C}$. It is important to mention that these are achieved for different stages of the vapour bubble development. The maximum values are obtained during the heating and stabilisation phases for $T_{he} = 150°\mathrm{C}$ and $T_{he} = 90°\mathrm{C}$, respectively.

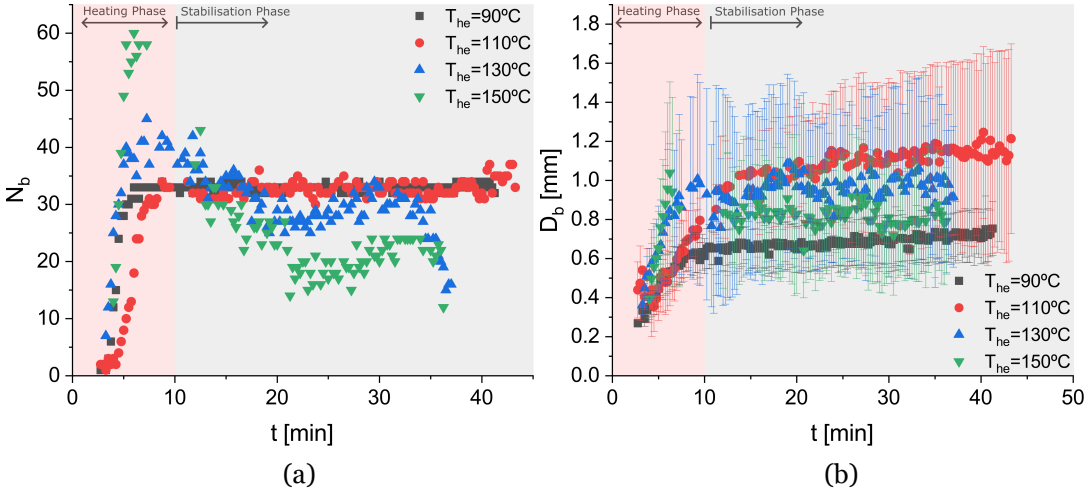

Figure 4.32: Water vapour bubble analysis as a function of the liquid temperature for both heating and stabilisation phases: a) Number of bubbles (N_b); b) Bubble diameter (D_b).

4.3 Saturated Boiling Regime

According to the qualitative results, the boiling phenomenon occurs exclusively at the boundaries of the container for the studied range, whereas the surface impact region does not exhibit any nucleation sites. In contrast to the vapour bubbles on the surface impact region, these affect the impact phenomena due to the chaotic nature of boiling, which generates mechanical waves in the liquid-gas interface and causes a shift from static to dynamic liquid films. Thus, assessing bubble formation and detachment, and their direct influence on impact outcomes, is crucial for understanding liquid films under saturated boiling regimes.

4.3.1 Vapour Bubbles

Figures 4.33 and 4.34 display the formation, growth, and detachment of vapour bubbles on the surface boundaries for water and n-heptane, respectively. For water, it is possible to visualise the deposited vapour bubbles on the surface boundaries. The size of the vapour bubbles is dependent on the liquid film temperature, as identified by figures 4.33a and 4.33b. For these experimental conditions, no boiling was verified, as the liquid film temperatures are relatively low in comparison to the saturation temperature of the fluid. The liquid film temperatures are defined as a function of the selected heating device, which has been presented in figure 3.12. For $T_{he} = 150°\mathrm{C}$, the vapour bubbles reach a critical size, detaching from the

surface due to the thinning of the ligament, and rise until contacting the liquid-gas interface, bursting and creating mechanical waves that propagate throughout the liquid film. In terms of size, the vapour bubbles for the boiling condition exhibit higher fluctuations in comparison to lower temperatures. Qualitatively, these differ due to the different life cycles of the vapour bubbles, which is a consequence of the boiling occurrence. When a vapour bubble detaches from the surface, the continuous heat flux contributes to the nucleation of new vapour bubbles, repeating the previous cycle. These events are illustrated in figure 4.35. Following the vapour bubble growth and detachment, the residual vapour adheres to the impact surface, acting as a nucleation site for the formation of the subsequent vapour bubbles.

(a) (b) (c)

Figure 4.33: Visualisation of the formation, growth and detachment of water vapour bubbles on the surface boundaries: a) $T_{he} = 110°\mathrm{C}$; b) $T_{he} = 130°\mathrm{C}$; c) $T_{he} = 150°\mathrm{C}$.

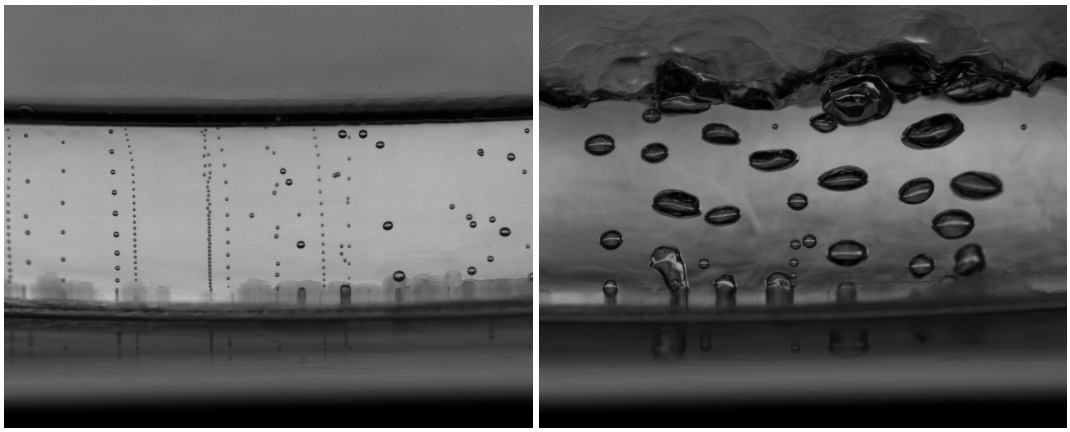

(a) (b)

Figure 4.34: Visualisation of the formation, growth and detachment of n-heptane vapour bubbles on the surface boundaries: a) $T_{he} = 110°\mathrm{C}$; b) $T_{he} = 130°\mathrm{C}$.

For n-heptane, due to lower surface tension values in comparison to water, the vapour bubbles display smaller diameters. Additionally, these do not stick to the surface, inducing higher release frequencies. Increasing the heating element temperature from $T_{he} = 110°\mathrm{C}$ to $T_{he} = 130°\mathrm{C}$ leads to an increase in the boiling phenomenon and, consequently, to larger bubbles. A heating element temperature of $T_{he} = 90°\mathrm{C}$ was also considered for the vapour analysis. However, no boiling-related phenomena were captured and, contrary to water, no vapour bubbles were deposited on the impact surface. For $T_{he} = 110°\mathrm{C}$, several streams of vapour bubbles corresponding to different nucleation sites are captured with the high-speed digital camera, ranging in terms of spacing, size, and release frequency. In comparison to water, the life cycle of n-heptane vapour bubbles is considerably faster, which can be explained by the differences in thermophysical properties. For $T_{he} = 130°\mathrm{C}$, the boiling be-

comes increasingly more chaotic with the continuous formation and detachment of vapour bubbles. These merge with surrounding bubbles and rupture when contacting the liquid-gas interface. The instabilities on the liquid film that originated from this process are evident in comparison to lower temperatures. The continuous streams observed in the previous condition transition to a disorderly state due to the intensified boiling regime. Overall, n-heptane displays smaller bubble diameters and a higher bubble release rate, whereas water bubbles are significantly larger and detach at lower rates.

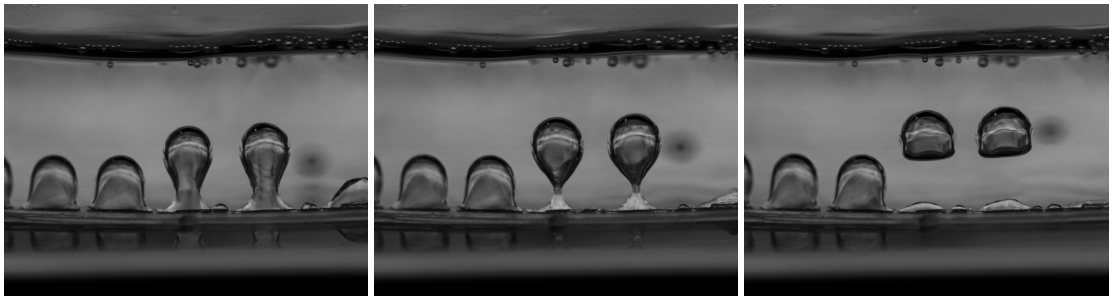

(a) (b) (c)

Figure 4.35: Visualisation of the vapour bubbles life cycle: a) Initial vapour bubble detachment; b) Ligament critical thickness; c) Ligament breakup leading to vapour bubble release.

4.3.2 Impact Outcomes

In order to correlate the influence of the different boiling regimes on the impact phenomena, figures 4.36 and 4.37 exhibit the crown formation with splashing occurrence and central jet formation with possible jet breakup for water, respectively. The impact conditions are $We = 481$, $Re = 9639$, $Oh = 0.0023$, $Fr = 501$ and $h^* = 1.0$. In comparison to the experimental conditions regarding the water central jets, an increase in the Weber and Reynolds numbers was required in order to obtain higher jets and possible secondary atomisation which was not visualised in previous cases, as exhibited by figure 4.9. Study cases include dimensionless temperatures of $\theta = 0.75$, $\theta = 0.83$ and $\theta = 0.95$ for similar impact conditions. For $\theta = 0.75$ and $\theta = 0.83$, a subcooled boiling regime was verified for the water liquid film, as vapour bubbles were distributed on the impact surface without detaching, maintaining a static liquid film. For $\theta = 0.95$, however, the liquid film enters a saturated boiling regime characterised by vapour bubble detachment and liquid film oscillations.

In terms of crown development, figure 4.36 illustrates the influence of liquid film temperature and boiling regimes on crown development and posterior secondary atomisation. The evolving crowns display resembling structures across the temperature range. The existence of several cusps in the crown rim is associated with secondary atomisation, which is also verified for the different temperatures. Qualitatively, the liquid film temperature does not exhibit a clear influence on the geometrical parameters of the crown, specifically its height, diameter and angle. Despite the transition from subcooled boiling (figures 4.36a and 4.36b) to saturated boiling regimes (figure 4.36c, which would indicate the existence of dynamic liquid films with variable thickness, the crowns are relatively similar in terms of overall development. A possible explanation could be related to the dimensionless temperature of $\theta = 0.95$

corresponding to the onset of boiling. For this condition, the oscillations induced on the liquid film are not sufficient to affect the impact phenomena. In order to properly evaluate this effect, an increase in the heat flux provided to the liquid film would result in a more violent boiling due to the increased bubble detachment rate and, consequently, the liquid film oscillations. This could provide meaningful insight into saturated boiling regimes ($\theta > 0.9$).

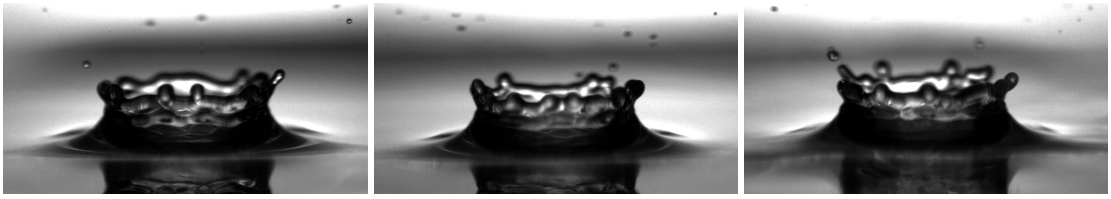

(a) (b) (c)

Figure 4.36: Visualisation of the crown formation subsequent to the water droplet impact as a function of temperature: a) $\theta = 0.75$, $\tau = 6.7$; b) $\theta = 0.83$, $\tau = 6.1$; c) $\theta = 0.95$, $\tau = 6.4$.

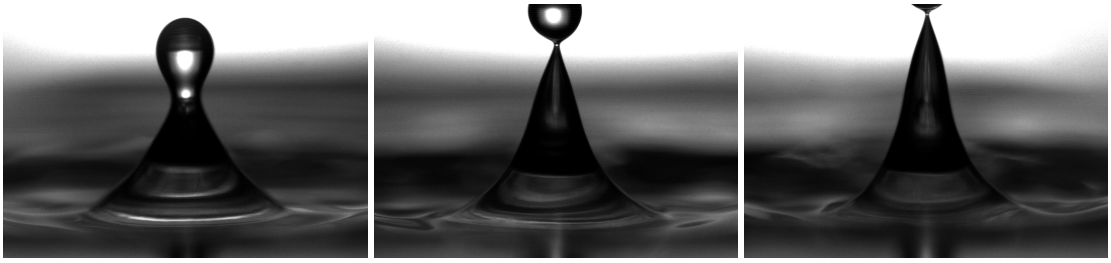

(a) (b) (c)

Figure 4.37: Visualisation of the central jet maximum height subsequent to the water droplet impact as a function of temperature: a) $\theta = 0.75$, $\tau = 86.2$; b) $\theta = 0.83$, $\tau = 84.2$; c) $\theta = 0.95$, $\tau = 81.8$.

Succeeding the crown formation and crater retraction, there is the possible formation of a central jet, with or without breakup. Figure 4.37 presents the maximum jet height for the water droplet impact under subcooled and saturated boiling regimes. Similar to the crown analysis, the central jet is evaluated in terms of height and possible jet breakup. For $\theta = 0.75$, due to the crater retraction, the central jet expands until reaching its maximum height. No breakup is visualised for this condition, and no secondary droplets originate from the central jet. Raising the liquid film temperature to $\theta = 0.83$ results in an increase in the maximum jet height. As demonstrated by figure 4.37b, the liquid ligament positioned in the upper region of the central jet reaches a critical minimum thickness, breaking and leading to the formation of a secondary droplet. For saturated boiling regimes, $\theta = 0.95$, the central jet reaches a higher maximum followed by its breakup, similar to the previous condition. Therefore, in terms of central jet height, increasing the liquid film temperature leads to higher jets and promotes the occurrence of secondary atomisation. These results are in agreement with the quantitative analysis regarding central jet height and posterior breakup for $0 < \theta < 0.6$ [227] and with available experimental data in the literature [75, 79]. Additionally, the boiling occurrence corresponding to $\theta = 0.95$ does not display a significant influence on the impact phenomena, which follows similar tendencies to the subcooled boiling regimes.

Chapter 5

Numerical Setup

Proceeding the experimental results, the current chapter describes the numerical setup adopted for simulating two-phase flows. Initially, an introduction to the open-source software Basilisk is provided. The second and third sections formulate the incompressible Navier-Stokes equations coupled to an interface tracking method. The temporal and spatial discretisation will be thoroughly detailed, including advective and viscous terms on structured grids. The subsequent section displays the computational domain regarding the flow geometry, boundary and initial conditions, and general settings. A convergence study will be provided in terms of grid size, boundaries of the domain and correspondent time step.

5.1 Introduction

The increased complexity of multiphase flows, ranging from interface tracking methods to heat and mass transfer phenomena, requires numerical solvers capable of accurately predicting heat and fluid flow. These may include Euler-Euler or Euler-Lagrange formulations, complex geometries, irregular meshing, higher-order numerical solutions, among others.

Basilisk is an open-source software designed to solve partial differential equations on adaptive Cartesian meshes, focusing on fluid mechanics. The solver ranges from Saint-Venant to Navier-Stokes and electrohydrodynamics, rendering it suitable for a variety of multiphase applications. The Basilisk solver exceeds in terms of adaptive mesh refinement (AMR), being capable of refining/coarsening particular regions of the grid based on local variables, such as volume fraction. This increases the efficiency of the computational model, which is commonly coupled with parallel processing and possible scalability. Additionally, in comparison with other available software, such as Ansys Fluent and OpenFOAM, the structured VOF method exhibits improved results with the aid of height functions [232]. Limitations of Basilisk include domain rigidity, as the solver does not allow the combination of non-cubic domains and message passing interface (MPI) parallelism with tree grids [233].

For two-phase flow environments, specifically impacting single droplets onto thin liquid films positioned over flat surfaces, a quadrilateral geometry implies simplicity in terms of domain and meshing. This also leads to less complex solution methods, as structured grids are associated with easier implementation schemes. This results in the Basilisk solver being superior in terms of both simplicity and efficiency for the current study.

5.2 Governing Equations

The general form of the Navier-Stokes governing equations was previously presented in equations (2.15), (2.16) and (2.17). However, further modifications are required to adapt these equations to the current study. The temporal term in the general mass conservation equation is neglected due to the incompressibility condition applied to the numerical model. This assumption relates to the fact that, for isothermal conditions, or for non-isothermal conditions under low temperature gradients, density changes are negligible. This means that density can be treated as constant for both liquid and gas phases throughout its motion, not changing over time or space. The source terms associated with phase change, Q, and radiation on the energy equation are not considered. Similarly, low temperature conditions do not require taking into consideration phase change processes, such as evaporation and condensation. However, numerically simulating impacting droplets under saturated boiling conditions would require the incorporation of energy source terms. Additionally, due to the current application, temperature is defined as the intensive property considered in the energy equation. Therefore, in simplified form, the mass, momentum and energy equations that define our model are given by equations (5.1), (5.2) and (5.3), respectively:

$$\nabla \cdot \mathbf{U} = 0 \tag{5.1}$$

$$\frac{\partial}{\partial t}(\rho \mathbf{U}) + \nabla \cdot (\rho \mathbf{U}\mathbf{U}) = -\nabla p + \nabla \cdot (2\mu \mathbf{D}) + \rho \mathbf{g} - \mathbf{F}_\sigma \tag{5.2}$$

$$\frac{\partial}{\partial t}(\rho T) + \nabla \cdot (\rho \mathbf{U} T) = \nabla \cdot \left(\frac{k}{C_p} \nabla T \right) \tag{5.3}$$

where $\mathbf{D}$ is the deformation tensor, as shown by equation (5.4). This is identical to the general momentum equation and was displayed in a different format for the sake of simplicity.

$$\mathbf{D} = \frac{1}{2}\left[\nabla \mathbf{U} + (\nabla \mathbf{U})^T\right] \tag{5.4}$$

Due to the existence of a two-phase flow, the physical properties of the liquid and gas phases must be defined on the numerical field and are calculated as a function of the volume fraction scalar. This is associated with the interface tracking method, which will be thoroughly detailed in the following section. An arithmetic mean is defined for the density calculation, as displayed by equation (5.5), whereas the remaining thermophysical properties, such as viscosity, thermal conductivity and heat capacity, are estimated through harmonic means. These properties are given by equations (5.6), (5.7) and (5.8), respectively:

$$\rho = \alpha\rho_l + (1-\alpha)\,\rho_g \tag{5.5}$$

$$\mu = \frac{1}{\frac{\alpha}{\mu_l} + \frac{1-\alpha}{\mu_g}} \tag{5.6}$$

$$k = \frac{1}{\frac{\alpha}{k_l} + \frac{1-\alpha}{k_g}} \tag{5.7}$$

$$C_p = \frac{1}{\frac{\alpha}{C_{p_l}} + \frac{1-\alpha}{C_{p_g}}} \tag{5.8}$$

The harmonic mean for the viscosity increases the stability of the solver for large liquid-gas ratios [234]. This is also applicable to the thermal conductivity and heat capacity.

5.3 Interface Tracking Method

In order to solve the incompressible Navier-Stokes equations applied for two-phase flows, these must be coupled to an interface tracking method to accurately predict the liquid-gas interface. The VOF method [173] is employed by solving a single set of momentum equations and tracking the volume fraction, α, throughout the domain. As displayed by equation (2.18), this parameter is a color function that ranges from 0 for the gas phase to 1 for the liquid phase. The scalar advection equation for the volume fraction is defined by equation (5.9):

$$\frac{\partial \alpha}{\partial t} + \nabla \cdot (\mathbf{U}\alpha) = 0 \tag{5.9}$$

As previously stated, the existence of an interface between phases requires special treatment in terms of interfacial balance. The surface tension is modelled as an explicit term in the momentum equation by the continuum surface force (CSF) model [183], as expressed by equation (5.10).

$$\mathbf{F}_\sigma = \sigma\kappa\delta_s\mathbf{n} \tag{5.10}$$

The interface normal vector and curvature are evaluated based on height functions [181], as the standard VOF approach [173] is typically associated with poor capabilities in numerically calculating these parameters. Figure 5.1 illustrates the interface normal vector and height functions for a PLIC representation of the interface. The interface normal vector and curvature are determined by equations (5.11) and (5.12), respectively:

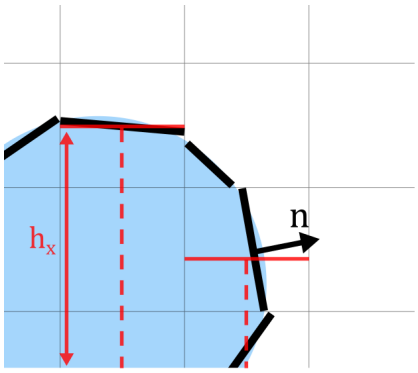

Figure 5.1: Visual representation of the PLIC method, interface normal vector and height functions.

$$\mathbf{n} = (h_x, -1) \tag{5.11}$$

$$\kappa = \frac{h_{xx}}{(1 + h_x^2)^{3/2}} \tag{5.12}$$

where h_x and h_{xx} are the first and second derivatives of the height function, respectively. Extending this method to three dimensions would require a second orientation (y-axis) to calculate partial derivatives. Due to the explicit nature of surface tension in the momentum equation, the maximum time step corresponds to the oscillation period of the smallest capillary wave, as displayed by equation (5.13):

$$\Delta t_{max} = \sqrt{\frac{\rho_m \Delta_{min}^3}{\pi \sigma}} \tag{5.13}$$

where $\rho_m = (\rho_g + \rho_l)/2$ is the averaged density between the phases and Δ_{min} is the minimum grid size. Additionally, the fluid flow is conditioned by the Courant number. This parameter indicates how much information propagates between grid cells, and is represented by equation (5.14). For explicit methods, the Courant number is typically limited to CFL < 1, meaning that information must travel to adjacent grid points in each time step. If the information moves across multiple cells, accuracy loss is expected, and the numerical model becomes unstable.

$$\text{CFL} = \frac{\Delta t U}{\Delta x} \tag{5.14}$$

Prior to the advection step of the volume fraction, the reconstruction of the liquid-gas interface is required.

5.4 Numerical Model

Following the description of the numerical setup, the temporal and spatial discretisation of the governing equations and interface tracking method is required. These equations must be converted from a continuous to a discrete form for computation of the resulting algebraic equations. The different terms of the Navier-Stokes equations are handled uniquely, requiring specific discretisation schemes.

5.4.1 Time Integration Scheme

5.4.1.1 Volume of Fluid (VOF)

In order to discretise the scalar advection equation for the volume fraction defined by equation (5.9), an operator-split advection method proposed by Weymouth and Yue [235] is employed. This method uses a cell-centre approach to estimate volume fraction from the dilatation term to ensure complete mass conservation. The operator-split methods are designed to account for conservative flux terms, zero-sum divergence terms, and no clipping or filling of cells, guaranteeing mass conservation [236]. The split version is represented by equations (5.15a) and (5.15b):

$$\frac{\alpha^{*}_{i,j} - \alpha^{n-\frac{1}{2}}_{i,j}}{\Delta t} + \frac{F^{n}_{i+\frac{1}{2},j} - F^{n}_{i-\frac{1}{2},j}}{\Delta x} = \alpha_{ch}\frac{u_{i+\frac{1}{2},j} - u_{i-\frac{1}{2},j}}{\Delta x} \tag{5.15a}$$

$$\frac{\alpha^{n+\frac{1}{2}}_{i,j} - \alpha^{*}_{i,j}}{\Delta t} + \frac{G^{n}_{i,j+\frac{1}{2}} - G^{n}_{i,j-\frac{1}{2}}}{\Delta y} = \alpha_{ch}\frac{v_{i,j+\frac{1}{2}} - v_{i,j-\frac{1}{2}}}{\Delta y} \tag{5.15b}$$

where F and G are volume fluxes across the cell faces in the x and y directions, respectively, and α_{ch} is the characteristic volume fraction, which varies between 0 and 1 similarly to the numerical approximation of the Heaviside function by Brackbill et al. [183], displayed by equation (2.25). After obtaining $\alpha^{n+\frac{1}{2}}_{i,j}$, the fluid properties, such as density and viscosity, are updated to a mid-step $n+1/2$, meaning that these are lagging by half a step compared to the velocity and pressure fields.

$$\rho^{n+1/2} = \rho_l \alpha^{n+1/2} + \rho_g \left(1 - \alpha^{n+1/2}\right) \tag{5.16}$$

$$\mu^{n+1/2} = \mu_l \alpha^{n+1/2} + \mu_g \left(1 - \alpha^{n+1/2}\right) \tag{5.17}$$

5.4.1.2 Advection Term

The nonlinear advective term is computed by a second-order unsplit upwind scheme developed by Bell, Collela and Glaz [237]. This is based on unsplit second-order Godunov schemes

initially proposed by Collela [238] and Van Leer [239]. The main procedure consists of three main steps, which include reconstruction, characteristic interpolation and flux evaluation. The reconstruction step consists of computing the linear profile within each cell, as depicted by equation (5.18).

$$u_x \approx \frac{\Delta_x u}{\Delta x} \tag{5.18}$$

An initial iteration of $\Delta_x u$ is required, as described by equation (5.19), followed by proper limiting to prevent the initial slope calculation from exceeding the global minimum and maximum velocity values. This is accomplished by reducing its magnitude through equation (5.20):

$$(\Delta_x u)^I = \frac{u_{i+1,j} - u_{i-1,j}}{2} \tag{5.19}$$

$$|\Delta_x u| \leq 2 \max\left(|u_{i+1,j} - u_{i,j}|, |u_{i,j} - u_{i-1,j}|\right) \tag{5.20}$$

The characteristic extrapolation step is employed to predict velocity values on cell edges using simple Taylor series expansion to second-order accuracy, as represented by equation (5.21):

$$U^{n+1/2,L}_{i+1/2,j} = U^n_{ij} + \frac{\Delta x}{2} U_{x,ij} + \frac{\Delta t}{2} U_{t,ij} \tag{5.21a}$$

$$U^{n+1/2,R}_{i-1/2,j} = U^n_{ij} - \frac{\Delta x}{2} U_{x,ij} + \frac{\Delta t}{2} U_{t,ij} \tag{5.21b}$$

$$U^{n+1/2,B}_{i,j+1/2} = U^n_{ij} + \frac{\Delta y}{2} U_{y,ij} + \frac{\Delta t}{2} U_{t,ij} \tag{5.21c}$$

$$U^{n+1/2,T}_{i,j-1/2} = U^n_{ij} - \frac{\Delta y}{2} U_{y,ij} + \frac{\Delta t}{2} U_{t,ij} \tag{5.21d}$$

The cell boundary velocities, $U_{x,ij}$ and $U_{y,ij}$, are evaluated using the limited slopes computed in the previous step. The time derivatives are converted to spatial derivatives through differential equations using a pressure approximation to estimate the projection variable. Additionally, the numerical evaluation of the derivatives normal to the cell edge occurs through limited slopes, whereas transverse derivatives are treated through an upwind scheme to increase stability [238].

The final step of the procedure relates to the computation of the flux differences. The constraint of incompressibility leads to divergence-free vector fields, leading to equation (5.22):

$$(\mathbf{U} \cdot \nabla)\,\mathbf{U} = \nabla \cdot (\mathbf{U} \otimes \mathbf{U}) \tag{5.22}$$

This relation does not hold at $t^{n+1/2}$ due to old pressure values being utilised for the approximation of the projection. The optimal approach to compute this term involves differentiating in a conservative manner and subtracting the terms required to convert from a differentiating to an advective form. Therefore, the term $(\mathbf{U} \cdot \nabla)\,\mathbf{U}$ can be expressed by equation (5.23):

$$\begin{aligned}\mathbf{U} \cdot \nabla \mathbf{U} = u\mathbf{U}_x + v\mathbf{U}_y \approx &\frac{u_{i+1/2,j} + u_{i-1/2,j}}{2}\frac{\mathbf{U}_{i+1/2,j} + \mathbf{U}_{i-1/2,j}}{\Delta x} + \\ &\frac{u_{i,j+1/2} + u_{i,j-1/2}}{2}\frac{\mathbf{U}_{i,j+1/2} + \mathbf{U}_{i,j-1/2}}{\Delta x}\end{aligned} \tag{5.23}$$

Supplementary information regarding this method can be found explicitly [237], including ambiguities in edge values, upwinding procedures and time-step restrictions.

5.4.1.3 Viscous Forces

The viscous term is integrated with an implicit scheme, and the diffusion equation is described by equation (5.24):

$$\rho\frac{\partial \mathbf{U}}{\partial t} = \nabla \cdot \left(\mu\left[\nabla \mathbf{U} + \nabla \mathbf{U}^T\right]\right) \tag{5.24}$$

Subsequent to temporal discretisation, equation (5.25) is obtained:

$$-\frac{\rho}{\Delta t}\mathbf{U}^{n+1} + \nabla \cdot \left(\mu\left[\nabla \mathbf{U} + \nabla \mathbf{U}^T\right]\right)^{n+1} = -\frac{\rho}{\Delta t}\mathbf{U}^{n} \tag{5.25}$$

The resulting equation is analogous to the Poisson-Helmholtz equation, which can be solved efficiently using a multigrid solver [240]. These solvers are typically known for their efficiency and scalability in solving systems of equations, namely elliptic or parabolic equations. Therefore, let us consider an overall solution to a generic linear problem:

$$\mathcal{L}\left(\mathbf{a}\right) = \nabla \cdot \left(\mu\left[\nabla \mathbf{a} + \nabla \mathbf{a}^T\right]\right) = \mathbf{b} \tag{5.26}$$

where $\mathcal{L}$ is a linear operator, and $\mathbf{a}$ and $\mathbf{b}$ are vectors. For time-dependent systems, a typical approach to solving the Poisson-Helmholtz equation is to provide an initial guess, $\tilde{\mathbf{a}} = \mathbf{a} - d\mathbf{a}$, where $d\mathbf{a}$ is an unknown correction. This term is used to compute equation (5.27):

$$\mathcal{L}\left(d\mathbf{a}\right) = \mathbf{b} - \mathcal{L}\left(\tilde{\mathbf{a}}\right) = \mathbf{res} \tag{5.27}$$

where $\mathbf{res}$ is the residual. If the residual value falls below a certain tolerance defined by the user, the iterative process is concluded. Otherwise, $\mathcal{L}(d\mathbf{a}) \simeq \mathbf{res}$ is solved, and the correction value is added to the initial guess. From this point onward, the residual is computed with the provided updated value, and this procedure repeats until reaching convergence. The error is reduced significantly by employing relaxation techniques, such as Gauss-Seidel or Jacobi. This strategy has been implemented in the standard Poisson solver [233].

5.4.1.4 Projection method

Subsequent to the discretisation of the advection, diffusion and volume fraction terms, a staggered in time general discretisation is required, leading to the mass, volume fraction and momentum equations represented by equations (5.28), (5.29) and (5.30), respectively:

$$\nabla \cdot \mathbf{U}^{n+1} = 0 \tag{5.28}$$

$$\begin{aligned}\frac{\mathbf{U}^{n+1} - \mathbf{U}^{n}}{\Delta t} + \mathbf{U}^{n+1/2} \cdot \nabla \mathbf{U}^{n+1/2} = &\frac{1}{\rho^{n+1/2}} \left(-\nabla p^{n} + \nabla \cdot \left[2\mu^{n+1/2} \left(\mathbf{D}^{n+1} + \mathbf{D}^{n} \right) \right] + \right. \\ &\left. \sigma \kappa^{n+1/2} \nabla \alpha^{n+1/2} \right)\end{aligned} \tag{5.29}$$

$$\frac{\alpha^{n+1/2} - \alpha^{n-1/2}}{\Delta t} + \nabla \cdot (\alpha^{n} \mathbf{U}^{n}) = 0 \tag{5.30}$$

In order to solve the incompressible Navier-Stokes equations, a second-order time-splitting projection method based on the method developed by Bell, Collela and Glaz [237] is employed. The projection method based on Chorin [241] consists in decoupling pressure and velocity by Helmholtz decomposition, splitting the velocity field into solenoid and irrotational components. The simplified system using a time-stepping projection method is described by equations (5.31), (5.32) and (5.33):

$$\begin{aligned}\frac{\mathbf{U}^{*} - \mathbf{U}^{n}}{\Delta t} + \mathbf{U}^{n+1/2} \cdot \nabla \mathbf{U}^{n+1/2} = &\frac{1}{\rho^{n+1/2}} \left(\nabla \cdot \left[2\mu^{n+1/2} \left(\mathbf{D}^{*} + \mathbf{D}^{n} \right) \right] + \right. \\ &\left. \sigma \kappa^{n+1/2} \nabla \alpha^{n+1/2} \right)\end{aligned} \tag{5.31}$$

$$\mathbf{U}^{n+1} = \mathbf{U}^{*} - \frac{\Delta t}{\rho^{n+1/2}} \nabla p^{n+1} \tag{5.32}$$

$$\nabla \cdot \mathbf{U}^{n+1} = 0 \tag{5.33}$$

This method is divided onto two main steps. In the first step, the pressure gradient term from the momentum equation and an intermediate velocity field, $\mathbf{U}^{*}$, is computed. This

step is typically not divergence-free, meaning that it does not satisfy the incompressibility condition. The following step adjusts the pressure field, ensuring that the final velocity field satisfies the incompressibility condition. The updated pressure can be obtained by solving a Poisson equation, as shown by equation (5.34):

$$\nabla \cdot \left(\frac{\Delta t}{\rho^{n+1/2}} \nabla p^{n+1} \right) = \nabla \cdot \mathbf{U}^{*} \tag{5.34}$$

The momentum equation can then be rearranged into a Helmholtz-Poisson equation, as depicted by equation (5.35):

$$\begin{aligned} \frac{\rho^{n+1/2}}{\Delta t}\mathbf{U}^{*} - \nabla \cdot \left(\mu^{n+1/2}\mathbf{D}^{*} \right) =& \nabla \cdot \left(\mu^{n+1/2}\mathbf{D}^{n} \right) + \sigma \kappa^{n+1/2} \nabla \alpha^{n+1/2} + \\ & \rho^{n+1/2} \left(\frac{\mathbf{U}^{n}}{\Delta t} - \mathbf{U}^{n+1/2} \cdot \nabla \mathbf{U}^{n+1/2} \right) \end{aligned} \tag{5.35}$$

where the right-hand-side values depend only on previous calculated values or at a time step of $n + 1/2$. These types of equations can be solved using a variant of the multigrid Poisson solver. Additional information on these methods has been reported in the literature [242, 243].

5.4.2 Spatial Discretisation

Once all the numerical terms have been temporally discretised, these require spatial translation from a continuous mathematical model onto a discrete approach. The numerical approximation of the advective and viscous terms requires specific methods for evaluating partial differential equations. These methods focus on reducing the exact differential equations onto approximate algebraic systems, which can be numerically solved using iterative methods. The governing equations are numerically approximated using a staggered grid approach, meaning that scalar variables, such as pressure and temperature, are stored in cell centres, whereas vector fields are stored in cell faces. This is illustrated in figure 5.2, where $u.x$ and $u.y$ are the horizontal and vertical velocities, and Δx and Δy are the horizontal and vertical grid sizes, respectively. In order to access field values, such as centered, face and vertex variables, stencils are employed. These are geometrical arrangements of nodes in the computational domain, typically adjacent to the point of interest, utilised for numerical computations. Basilisk adopts standard 3×3 stencils, which can be increased for higher-order numerical schemes. Different discretisation schemes, such as finite difference or finite element methods, will not be detailed in the present study.

A substantial amount of control volumes, neighbouring one another, creates a grid within the numerical domain. Basilisk adopts base Cartesian orthogonal grids with tree-based data structures for possible adaptive mesh refinement. Cartesian grids are relatively straightforward due to their simplicity and ease of implementation, as well as their evaluation of spatial

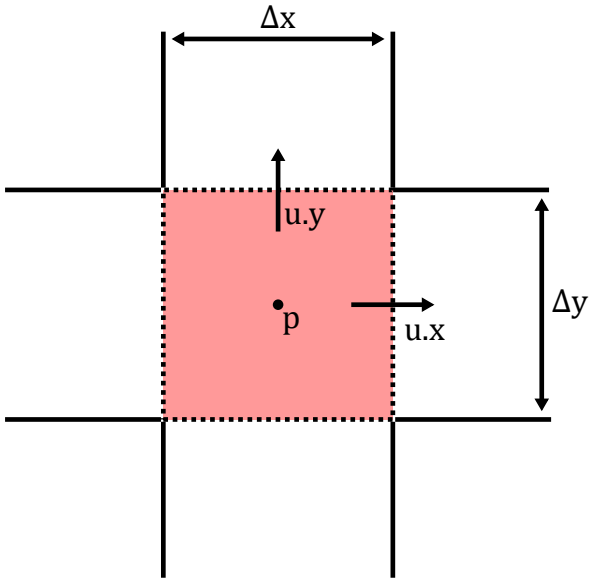

Figure 5.2: Representation of scalar and vector fields in a staggered grid.

derivatives. Quadtree is a two-dimensional tree-based data structure that enables mesh refinement and coarsening based on local scalar/vector fields, increasing the efficiency of the numerical computation. Figure 5.3 exemplifies how nodes divide, creating finer partitions in the numerical domain. Cells prior to division are denominated as parent cells, corresponding to a lower level on figure 5.3c. Increasing the grid levels leads to the deconstruction of these cells, originating four children cells with reduced size. If the process repeats, the previous children cells are defined as parent cells in the following refinement process. This occurs in the top right boundary of figure 5.3a. Additionally, ghost cells are required to allow simple Cartesian stencil operations [244] at the same level as refinement, as demonstrated by figure 5.3b.

In terms of adaptive mesh refinement, Basilisk employs an adaptive wavelet algorithm based on the estimation of numerical discretisation errors. This algorithm is embedded in the field of multi-resolution analysis [233]. Wavelets are special mathematical functions similar to Fourier analysis, which analyse data over a wide range of scales. This means that wavelet transforms process data differently in comparison to other functions. For example, Fourier transforms are characterised by the superposition of sinusoidal functions, which are non-local by nature. However, wavelet-based algorithms approximate functions contained within finite boundaries, making them suitable for approximating sharp discontinuities. Additionally, this provides a natural criterion for adaptive mesh refinement, estimating the local interpolation error between the measured value and its propagation to a coarser grid. This is applied for both local coarsening and refinement depending on the local estimation of the interpolation error [240, 244]. Figure 5.4 exemplifies the adaptive mesh refinement process for a developing crown subsequent to a single droplet impact onto a liquid film. The volume fraction and velocity fields are analysed for the coarsening/refinement of the numerical grid. As expected, the region surrounding the crown evolution is refined, and secondary droplets originating from the crown rim also require local refinement due to higher ejection veloci-

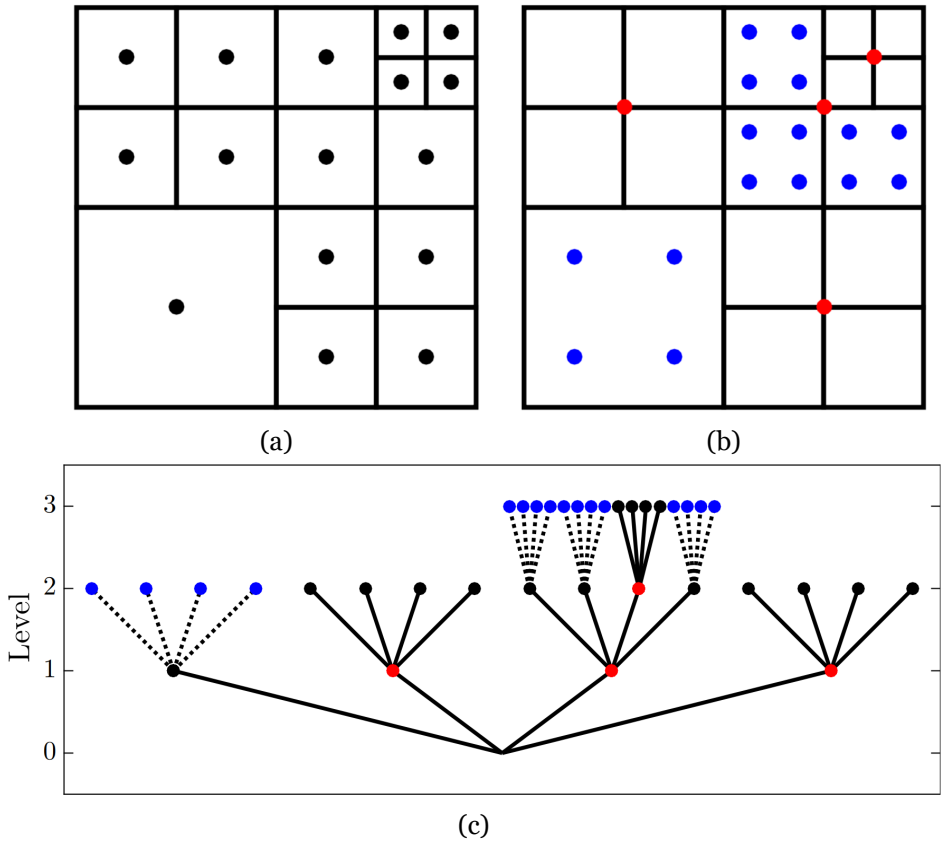

Figure 5.3: Tree-grid structure on an orthogonal Cartesian mesh: a) Spatial structure of grid cells under different levels of refinement; b) Spatial structure of ghost points defined by the red (downsampling) and blue (upsampling) circles; c) Tree representation corresponding to the various grid cells and ghost points at different levels. Adapted from Van Hooft et al. [244].

ties. Outer regions, mainly near the top boundary, display coarse grids due to the absence of a liquid-gas interface and low velocities.

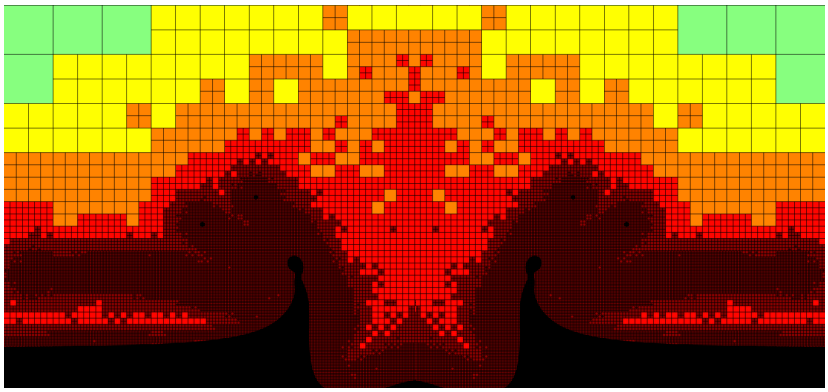

Figure 5.4: Example of adaptive mesh refinement based on the discretisation errors of velocity and volume fraction.

5.5 Computational Domain

Figure 5.5 exhibits a schematic of the physical setup. A single droplet of diameter D_d and impact velocity U_d impinges onto a liquid film of thickness h. For isothermal conditions, the

droplet and the liquid film possess identical thermophysical properties, and no vapour bubbles are positioned inside the liquid film. For non-isothermal conditions, the liquid film is heated through conduction, which corresponds to a specific temperature value on the impact surface. The vapour bubbles are artificially introduced into the liquid film to simulate subcooled and saturated boiling regimes. These can be defined by the vapour bubble spacing, x_v, vapour bubble diameter, D_v, and initial vapour bubble displacement in relation to the axis of symmetry, x_s. These bubbles are set as gas phase ($\alpha = 0$) for numerical simplification.

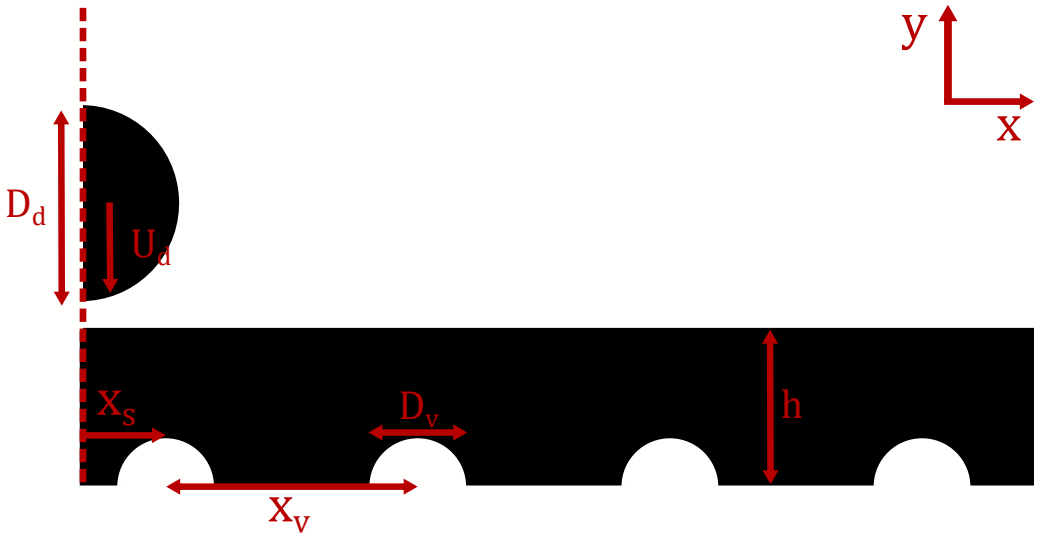

Figure 5.5: Numerical setup.

The numerical domain is defined as a quadrilateral with four boundary conditions. The left boundary is defined as the axis of symmetry and it is used as the centerline for the axisymmetric simulations. The top and right boundaries are pressure-outlets to represent the far-field. The bottom boundary is the impact surface, characterised by a no-slip condition for the velocity and a fixed wall temperature equal to the liquid film temperature. Gravity forces are enabled and act in the negative direction of the y-axis. Jet fuel and HVO are the fluids adopted for the preliminary analysis regarding isothermal conditions, whereas water and n-decane are selected for non-isothermal conditions. The thermophysical properties of the different fluids and corresponding impact conditions will be detailed in the following section, prior to the description of the numerical results. In terms of wall adhesion, the contact angle is implemented by using a VOF tracer and height functions [233]. Due to the hydrophilic nature of the fuels in contact with the borosilicate glass surface, the contact angle tends towards $0°$. For water, the contact angle was evaluated in a previous study [245] with a value of $\theta_w = 50.3°$.

As previously mentioned, an orthogonal grid with adaptive mesh refinement based on the volume fraction and velocity is adopted. The maximum grid size, which corresponds to its base size, is equal to 3 cells per diameter (cpd) of the droplet. This is the maximum value allowed for the current numerical simulations, as cell sizes above this threshold would not register the volume fraction input onto a scalar field. The grid levels, as displayed in figure 5.3, due to adaptive mesh refinement, will be evaluated in terms of grid convergence in the

following section. In terms of initial conditions, the volume fraction of the droplet and liquid film is initialised onto the field, and a velocity is imposed on the droplet to simulate the impact phenomena. A minimum of 3 grid cells between the droplet and the liquid film is required to avoid initial liquid merging prior to the numerical simulations. The instant the droplet impacts the liquid surface corresponds to $t = 0\ \mathrm{ms}$.

5.6 Convergence Studies

Sensitivity analysis, also known as independence/convergence studies, involves evaluating the numerical solution as a function of certain parameters, such as mesh resolution. These studies play a significant role in obtaining accurate and valid numerical results, ensuring that the numerical solution is independent of the analysed parameter above a certain level of refinement.

For two-phase flows, specifically impacting droplets onto thin liquid films, the domain, grid size, and time step are the parameters which require sensitivity analysis. The impact conditions for the independence study are $D_0 = 3.0\ \mathrm{mm}$, $U_0 = 3.0\ \mathrm{m/s}$ and $h^* = 0.5$. The fluid adopted for the numerical simulation is a $75\%/25\%$ jet fuel and biofuel mixture, specifically Jet A-1 and Neste Renewable Diesel (NExBTL), respectively. The physical properties of this fluid are $\rho_l = 795\,\mathrm{kg/m^3}$, $\mu_l = 1.44 \times 10^{-3}\,\mathrm{Pa.s}$ and $\sigma = 25.5 \times 10^{-3}\,\mathrm{N/m}$, and the gas phase physical properties are $\rho_g = 1.23\,\mathrm{kg/m^3}$ and $\mu_g = 1.79 \times 10^{-5}\,\mathrm{Pa.s}$. This study case was selected due to its lower liquid film thickness and higher impact velocity, leading to thinner crown walls and increased instabilities in the crown rim, respectively. The geometrical parameters of the crown, namely height and outer diameter, are measured during the initial and intermediate stages of the impact phenomena, which correspond to the crown formation and evolution, respectively. The crown geometrical parameter measurements are performed at the crown rim, as represented in figure 2.14. The validation of the axisymmetric numerical simulations is performed using available experimental data [101]. These results are presented in the following chapter.

5.6.1 Domain

For semi-infinite liquid layers such as thin liquid films (finite thickness and far field boundaries), the crown expands with no restrictions until collapsing and merging with the liquid film. However, numerically simulating semi-infinite fields would require tremendous computational power. Due to the physical nature of impacting droplets, the analysis of the domain in terms of radial and axial dimensions is required. Due to the cubic domain and quadtree restrain imposed by Basilisk, the axial and radial distances representing the numerical domain must be equal.

Figure 5.6 displays the crown interface at early stages of the impact $(t = 4\ \mathrm{ms})$ for different dimensions of the numerical domain. For $2.7D_0$, the expanding crown is restricted due to the limited domain, displaying a lower diameter. This is emphasised for later stages of the

impact, as the capillary wave formed on the liquid-gas interface due to the initial impact reaching the boundary, rebounding and influencing the impact phenomena. Additionally, the crown height and diameter may exceed the domain dimensions, limiting the crown measurements. For $5.3D_0$, the influence of the boundaries on the impact phenomena is significantly reduced as the crown diameter and height increase, and the crown wall exhibits a greater vertical orientation. No visible differences can be noticed between $5.3D_0$ and $10.7D_0$ in terms of interface evolution, meaning that an increase in the axial and radial domain does not alter the numerical results, and the solution is independent of the domain size. Therefore, the dimensions of the domain are defined as $5.3D_0$ for the numerical simulations. The maximum relative errors of the domain for crown height and outer diameter measurements are 2.7% and 0.4%, respectively.

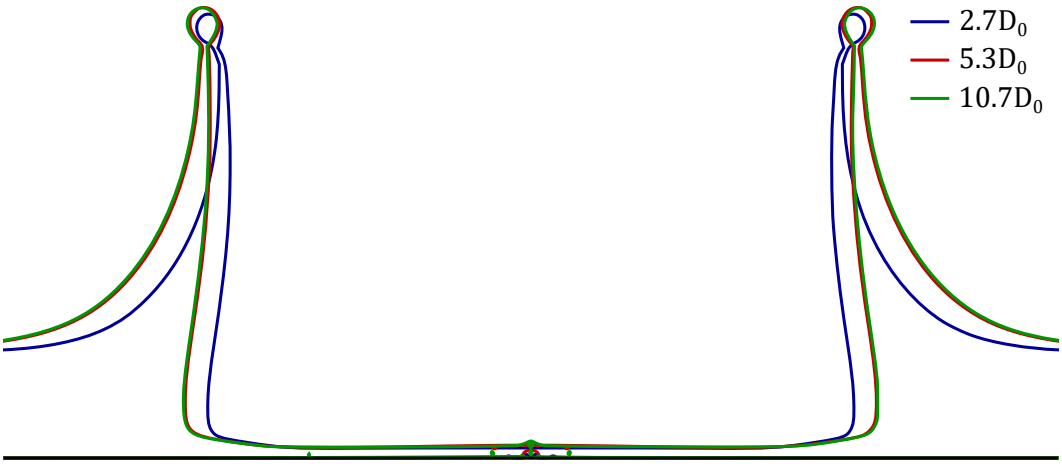

Figure 5.6: Interface evolution as a function of the axial and radial dimensions of the numerical domain.

5.6.2 Time step

For explicit methods, the time step is constrained by the Courant–Friedrich–Levy (CFL) condition and the oscillation period of the smallest capillary wave. For Basilisk, in order to ensure the stability of the VOF scheme, the CFL must be smaller than 0.5 [233, 246].

Figure 5.7 exhibits the crown interface evolution at early stages of the impact ($t = 4$ ms) as a function of the CFL number. Despite the previous condition (CFL < 0.5), CFL values ranging from CFL $= 0.1$ to CFL $= 1.0$ were evaluated for the current study. Overall, the Courant number does not display a significant impact in the interface evolution, as the crowns expand similarly through early and intermediate impact stages. No visible differences are noticed in terms of numerical instabilities associated with accuracy loss. Due to this, and according to the previous constraints, a CFL number of CFL $= 0.5$ was selected for the numerical simulations.

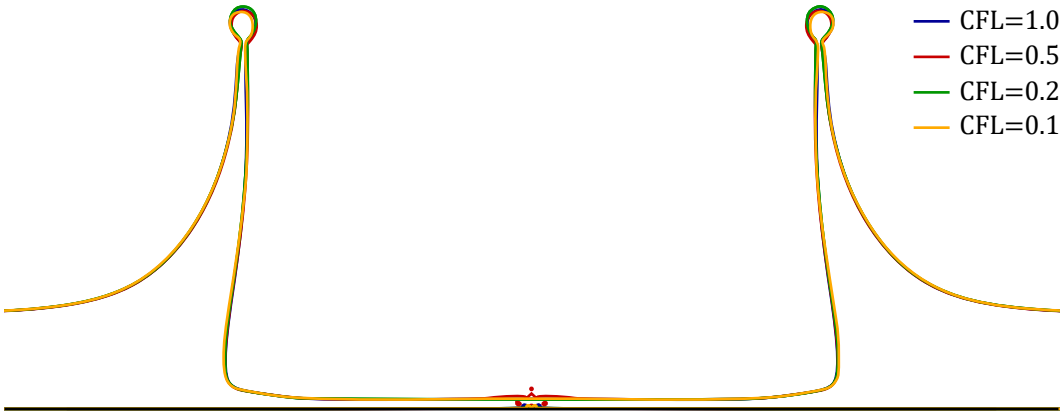

Figure 5.7: Interface evolution as a function of the CFL condition.

5.6.3 Grid

The mesh sensitivity study is a crucial step in guaranteeing accurate and reliable results of the numerical model. Initially, a base grid must be established for the computational domain. Due to the quadrilateral simplicity of the domain, a Cartesian orthogonal grid is adopted for the numerical simulations. A base size of 3 cells per diameter (cpd) is defined, which corresponds to a grid size of $\Delta x = \Delta y = 1\ \mathrm{mm}$. A coarser base grid would not register the volume fraction input onto a scalar field during initialisation, therefore requiring a minimum grid level. The refinement/coarsening occurs through adaptive mesh refinement, locally altering the grid resolution as a function of a wavelet algorithm based on the estimation of numerical discretisation errors for both velocity and volume fraction. These processes regarding spatial discretisation have been thoroughly detailed in previous sections.

Figure 5.8 illustrates the evolution of the crown interface as a function of the grid size. In comparison to the domain and time step convergence studies, the crown evolution is significantly affected by grid size, displaying clear differences in terms of both diameter and height. Overall, increasing the grid resolution leads to higher values of the crown height, and the crown angle tends to $90°$. The crown diameter is not as affected as the previous parameter. These parameters tend to stabilise for higher resolutions, such as 96 cpd and 192 cpd.

Due to the dependence of the crown diameter and height on grid size, the measurements of these parameters are also presented in subfigures 5.9a and 5.9b, respectively. Low-level grids, such as 24 cpd and 48 cpd, display irregular tendencies in comparison to higher resolutions, such as higher diameters and lower crown heights. Low grid resolutions induce crown shattering and secondary atomisation at early stages due to not accurately capturing the liquid-gas interface. The thin liquid ligaments of the crown rupture, as they are not capable of maintaining cohesion, leading to the results presented in figure 5.9. For more refined grids, as represented by 96 cpd and 192 cpd, the crown diameter and height follow similar tendencies during initial and intermediate impact stages. From this point onward, further refinement of the mesh does not significantly affect the numerical solution, whereas the com-

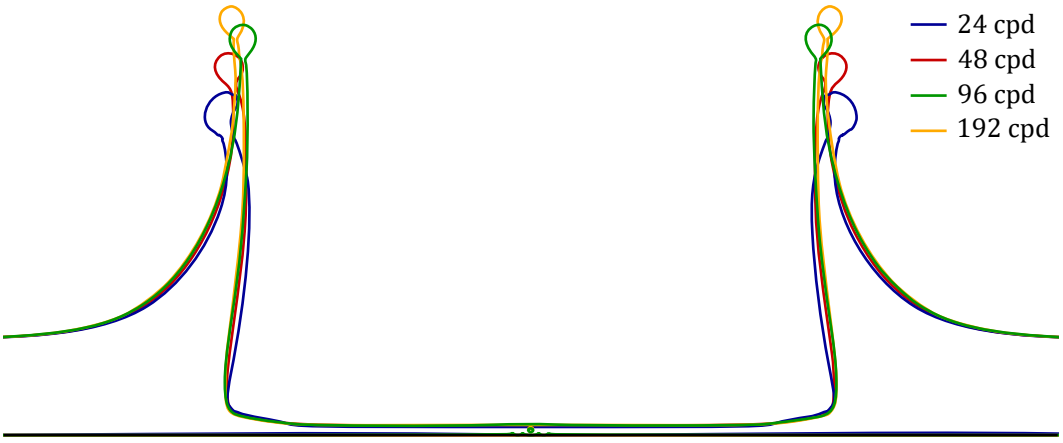

Figure 5.8: Interface evolution as a function of the grid size.

putational cost increases exponentially due to the nature of the adaptive grid. Therefore, a grid resolution of 96 cpd was adopted for the numerical simulations, corresponding to a cell size of $\Delta x = \Delta y = 31.3$ µm. The maximum relative errors of the grid size for crown height and outer diameter measurements are 4.6% and 4.5%, respectively.

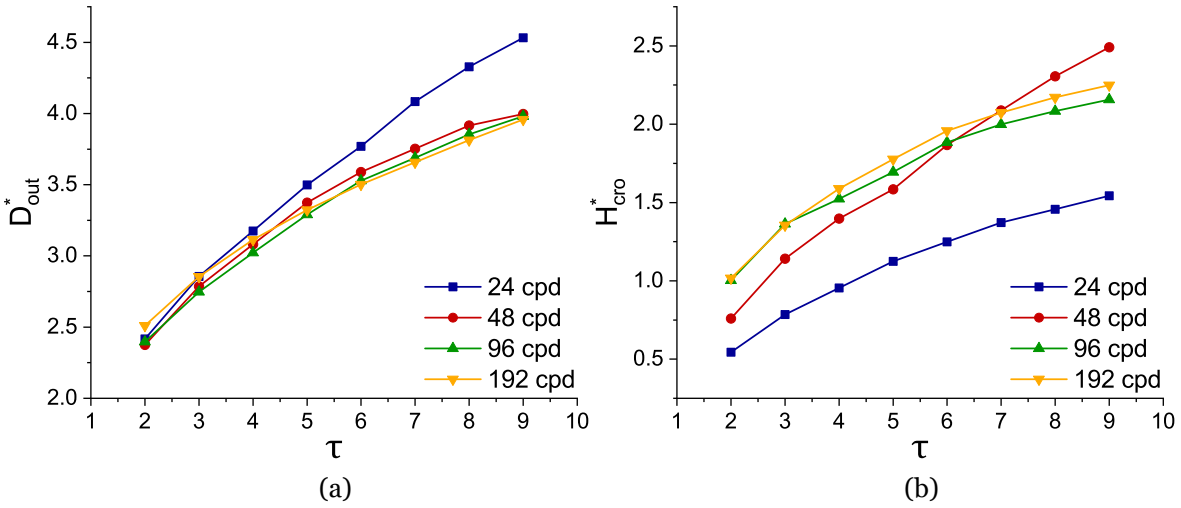

Figure 5.9: Crown measurements for single droplet impact as a function of grid size: a) Dimensionless crown outer diameter; b) Dimensionless crown height.

Chapter 6

Numerical Results

The present chapter details the numerical results of 2D axisymmetric simulations regarding single droplets impacting onto liquid films under both isothermal and non-isothermal conditions. In section 6.1, the validation of the axisymmetric numerical simulations is performed with available experimental data in the literature [99]. The following section (section 6.2), consists of the qualitative and quantitative analysis of droplet impact onto a liquid film in the presence of vapour bubbles. These will be evaluated in terms of bubble detachment, coalescence and surface breakup, and crown parameters measurements, namely height and diameter. The vapour bubble size, spacing and initial displacement are varied to study crown morphology. These studies have been detailed in previous studies [247, 248].

6.1 Isothermal Conditions

The available experimental data developed by Ribeiro et al. [99] is used to validate the numerical model. Three scenarios are explored, where $D_d = 3.0$ mm and $U_d = 3.0$ m/s, with varying liquid film thicknesses of $h^* = 0.2$, $h^* = 0.5$ and $h^* = 1.0$. These conditions provide different outcomes in regards to crown evolution and secondary atomisation, specifically liquid ligaments and associated breakup. The fluid adopted was a $75\%/25\%$ jet fuel and biofuel mixture, which corresponds to the experimental conditions. The thermophysical properties of this fluid are $\rho = 795$ kg/m^3, $\mu = 1.44 \times 10^{-3}$ Pa.s and $\sigma = 25.5$ mN/s. The crown height and outer diameter are measured as illustrated by figure 2.14.

Figure 6.1 exhibits the crown outer diameter and height measurements as a function of time for the lower liquid film thickness, $h^* = 0.2$. In terms of crown diameter, the numerical model slightly underpredicts the outer crown measurements in comparison to the experimental results. Despite this, the measurements follow an identical tendency in terms of initial expansion and maximum growth. For the crown height, the numerical results are in very good agreement with the experimental data.

This study case is represented in figure 6.2 for different impact stages. For $\tau = 2$, a smooth crown formation accompanied by secondary atomisation is visualised for both experimental and numerical results. The crown shape and curvature are similar following the droplet impact. The crown develops, both in height and diameter, and exhibits a thin liquid crown without ligament breakup. However, secondary atomisation from the crown rim is more pronounced in the experimental condition in comparison to the numerical analysis for $\tau = 5$. This is due to the 3D nature of the liquid instabilities formed at the crown rim, which are

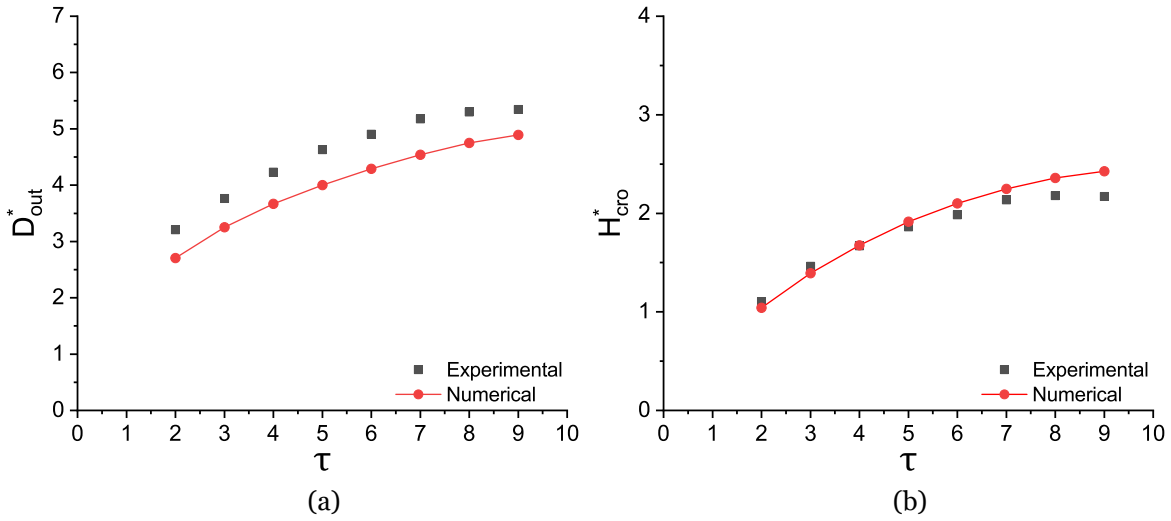

Figure 6.1: Comparison of experimental and numerical results of crown parameter measurements as a function of dimensionless time ($D_d = 3.0\,\mathrm{mm}$, $U_d = 3.0\,\mathrm{m/s}$, $h^* = 0.2$): a) Dimensionless crown outer diameter; b) Dimensionless crown height.

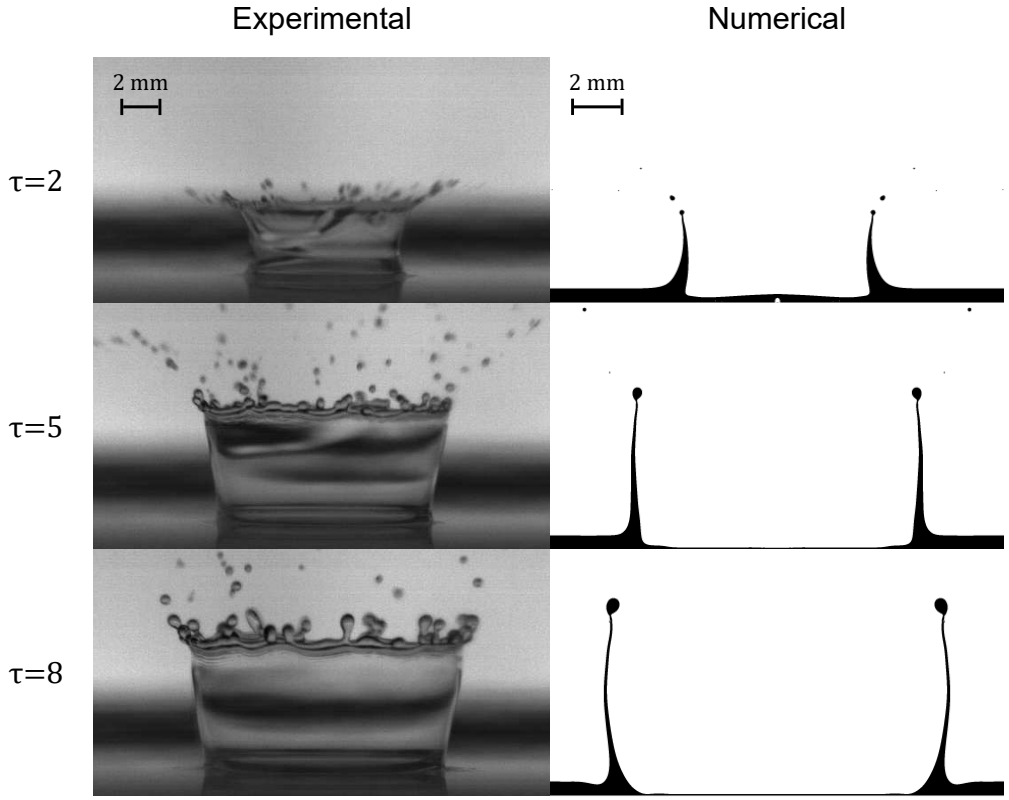

Figure 6.2: Qualitative comparison of the droplet impact phenomenon regarding the experimental and numerical results ($D_d = 3.0\,\mathrm{mm}$, $U_d = 3.0\,\mathrm{m/s}$, $h^* = 0.2$).

not accurately predicted in 2D axisymmetric simulations. For later stages, $\tau = 8$, the crowns exhibit a near vertical shape with no disintegration mechanisms, as these occur during the crown descent subsequent to reaching the maximum height.

For the intermediate liquid film thickness, $h^* = 0.5$, the crown outer diameter numerical measurements are in good agreement with the experimental tendency and display lower dis-

parities in comparison with the lower thickness study, as shown by figure 6.3. Due to the higher liquid film thickness, the evolving crown manifests fewer instabilities and a more smooth development. This is also associated with the effect of capillary waves that propagate on both the liquid film and crown, being less predominant for thicker liquid films and, consequently, thicker liquid ligaments. For the height measurements, the numerical model accurately estimates the crown evolution, displaying an identical growth rate throughout the different stages. Lastly, figure 6.4 shows the crown geometrical parameter measurements for the higher thickness condition, $h^* = 1.0$. The crown outer diameter and height measurements follow a similar tendency to the previous case. Overall, the numerical results are in better agreement for higher liquid film thicknesses, $h^* = 0.5$ and $h^* = 1.0$, in comparison to the lower thickness, $h^* = 0.2$. A thorough analysis should be considered for future studies regarding thin liquid films, crown evolution and ligament breakup in order to improve the numerical model.

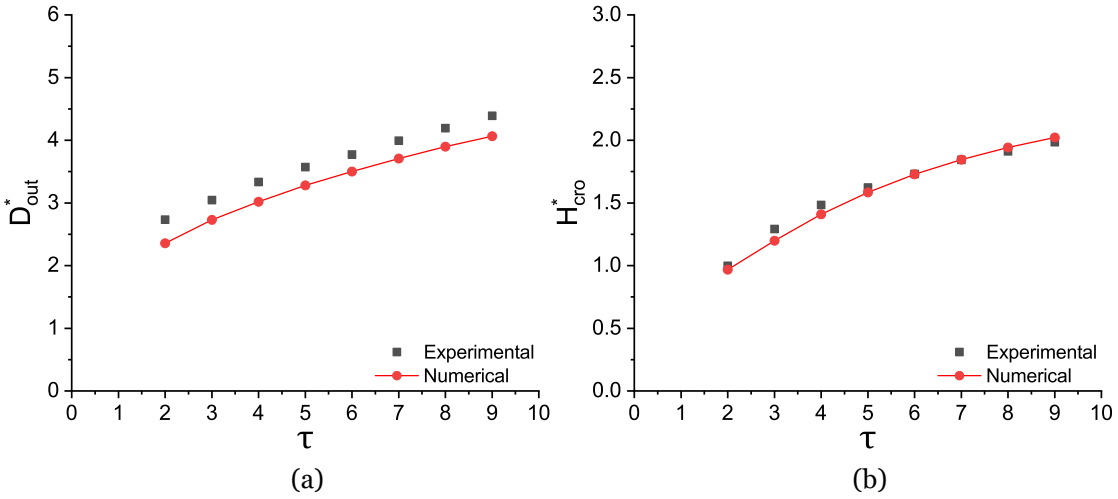

Figure 6.3: Comparison of experimental and numerical results of crown parameter measurements as a function of dimensionless time ($D_d = 3.0\,\mathrm{mm}$, $U_d = 3.0\,\mathrm{m/s}$, $h^* = 0.5$): a) Dimensionless crown outer diameter; b) Dimensionless crown height.

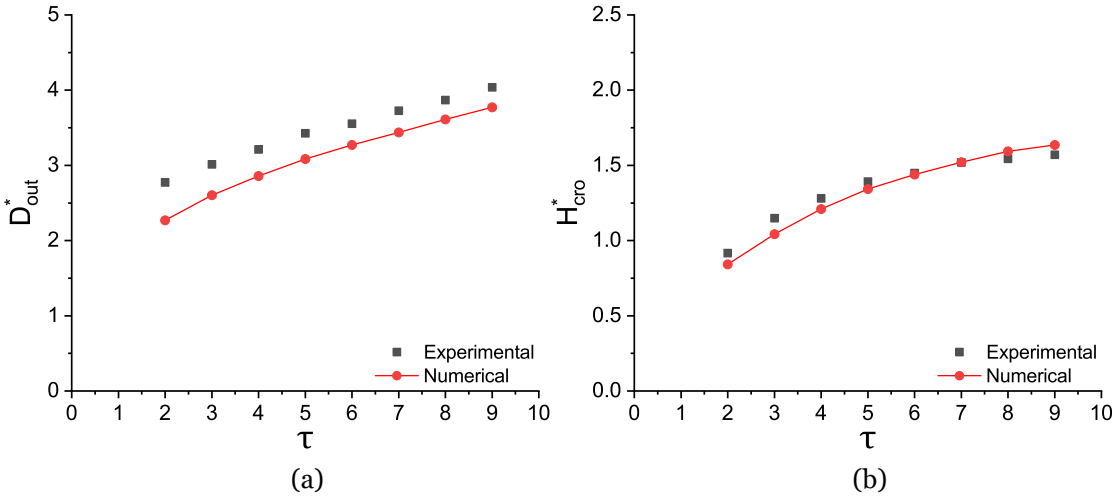

Figure 6.4: Comparison of experimental and numerical results of crown parameter measurements as a function of dimensionless time ($D_d = 3.0\,\mathrm{mm}$, $U_d = 3.0\,\mathrm{m/s}$, $h^* = 1.0$): a) Dimensionless crown outer diameter; b) Dimensionless crown height.

6.2 Subcooled Boiling Regimes - Vapour Bubbles

The experimental analysis regarding vapour bubbles was performed in terms of life cycle and distribution on the impact surface. However, nucleation sites spread across the impact surface depending on local temperature and wall roughness, among others factors. Inducing nucleation onto specific points, such as the droplet impact region, requires complex surface treatments and a fundamental understanding of both heat and transfer phenomena, as well as surface properties. In order to evaluate the influence of vapour bubbles on the impact phenomena, these were numerically implemented in the impact region. Investigating these parameters in the numerical model helps to overcome the limitations of the experimental conditions.

Table 6.1 displays the fluids adopted for the current study and associated thermophysical properties for the established liquid film temperatures. The numerical simulations are conducted under the simplifying assumption that the thermophysical properties remain constant and do not vary with temperature. The droplet and the liquid film assume the thermophysical properties of the heated liquid film. The temperatures exhibited in table 6.1 correspond to a dimensionless temperature of approximately $\theta \approx 0.4$. Phase-change processes such as evaporation/condensation and boiling are neglected for the current simulations. The impact conditions are $D_d = 3.0\,\mathrm{mm}$, $U_d = 3.0\,\mathrm{m/s}$ and $h^* = 0.5$.

Table 6.1: Thermophysical properties for water and n-decane at atmospheric pressure.

Fluid	T_f $[^\circ C]$	ρ $[kg/m^3]$	μ $[mPa.s]$	σ $[mN/m]$	k $[J/\,(m.s.K)]$	C_p $[J/\,(Kg.K)]$
Water	50	988.0	0.547	67.94	0.631	4181.0
N-decane	80	686.1	0.449	18.25	0.119	2332.5

6.2.1 Size and Spacing

Different vapour bubble sizes and spacings are considered for the numerical analysis, which consists of $D_v^* = D_v/D_d = 1/2$, $D_v^* = 1/3$, $D_v^* = 1/5$ and $D_v^* = 1/10$, and $x_v^* = x_v/D_d = 1/2$, $x_v^* = 1$ and $x_v^* = 2$, respectively. No initial bubble displacement is considered for the current analysis ($x_s^* = 0$). Figure 6.5 exhibits the crown parameter measurements for different vapour bubble sizes and a spacing of $x_v^* = 1.0$. Overall, the evolving crowns are more affected in terms of height in comparison to their diameter. For the latter, the smaller vapour bubbles, $D_v^* = 1/3$, $D_v^* = 1/5$ and $D_v^* = 1/10$, exhibit similar patterns in terms of crown formation. A decrease in the vapour bubbles size leads to an increase in the crown outer diameters. For $D_v^* = 1/2$, it is possible to visualise a sudden decrease of the crown diameter for $\tau = 8$, which relates to a vapour bubble contacting the inner crown wall at earlier stages and propagating through the liquid-gas interface. Regarding crown height, the vapour bubbles show a more pronounced effect for higher bubble diameters. For $D_v^* = 1/5$ and $D_v^* = 1/10$, the crowns expand until reaching a maximum height, followed by a gradual decrease. No erratic behaviour, such as discontinuities or irregular trajectories, is verified for these conditions. However, an increase in the vapour bubble size to $D_v^* = 1/3$ and $D_v^* = 1/2$ significantly

influences the crown height, leading to lower measured values. This case study can be visualised in figure 6.6 for intermediate impact stages, $\tau = 6.5$. For $D_v^* = 1/5$ and $D_v^* = 1/10$, the liquid crowns are relatively stable, with several vapour bubbles positioned on the impact surface. An increase in the vapour bubble diameter to $D_v^* = 1/3$ causes a reduction in the crown height, as the vapour bubbles detach and merge with the expanding crown, affecting its growth. Furthermore, increasing the gas phase in the liquid film causes the expanding liquid due to the impacting droplet to move towards empty spaces, diminishing its contribution to the crown height. For the higher bubble size, $D_v^* = 1/2$, both the inner and outer walls of the crown exhibit fluctuations as a result of vapour bubbles contacting the expanding crown, resulting in surface breakup. Consequently, its height is reduced. The dynamics of bubble detachment and surface breakup are presented in the following condition.

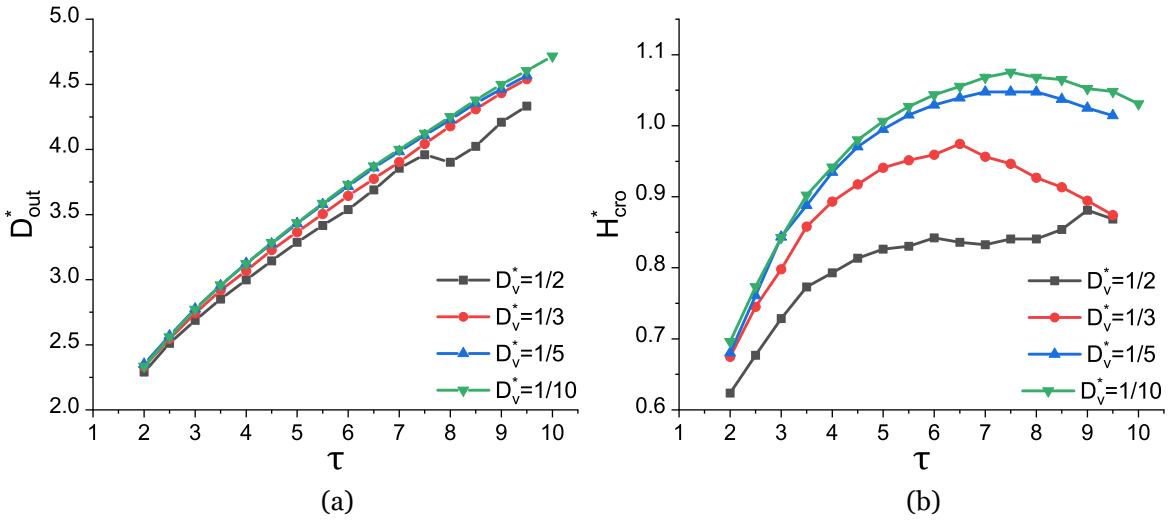

Figure 6.5: Crown measurements for water droplet impact as a function of the vapour bubble size for $x_v^* = 1.0$: a) Dimensionless crown outer diameter; b) Dimensionless crown height.

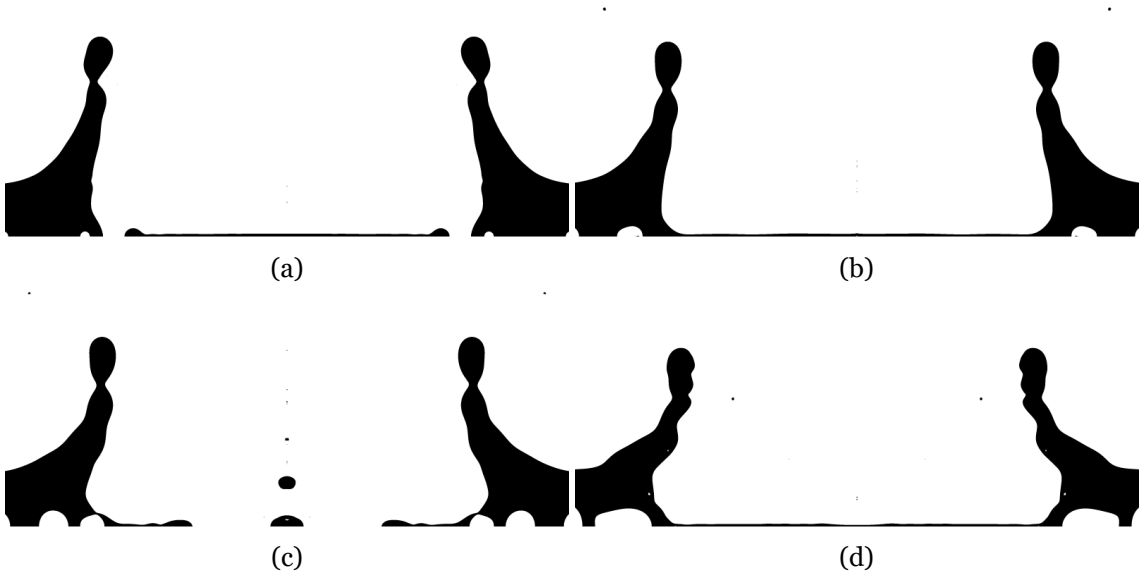

Figure 6.6: Visualisation of water droplet impact as a function of the vapour bubble size for $x_v^* = 1.0$ and $\tau = 6.5$: a) $D_v^* = 1/10$; b) $D_v^* = 1/5$; c) $D_v^* = 1/3$; d) $D_v^* = 1/2$.

Figure 6.7 shows the influence of the vapour bubble spacing for a fixed bubble diameter on the

n-decane impact phenomena. The results show a tendency where an increase in the bubble spacing causes the crown geometrical parameters to also increase. Despite that, the crown height and diameter measurements show a slight decrease from $x_v^* = 1.0$ to $x_v^* = 2.0$. This can be related to the crown rim instabilities associated with the low surface tension of n-decane at higher temperatures. Additionally, the spacing analysis is performed for a lower vapour bubble diameter, $D_v^* = 1/5$, therefore exhibiting fewer differences on the crown evolution. These factors could play a role in comprehending regime oscillations. For both fluids, the influence of vapour bubbles is lower on the crown outer diameter and higher on the crown height despite showing similar tendencies. The crown evolution can be visualised in figure 6.8 for lower spacings and increased diameters to emphasise the underlying dynamics of vapour bubbles.

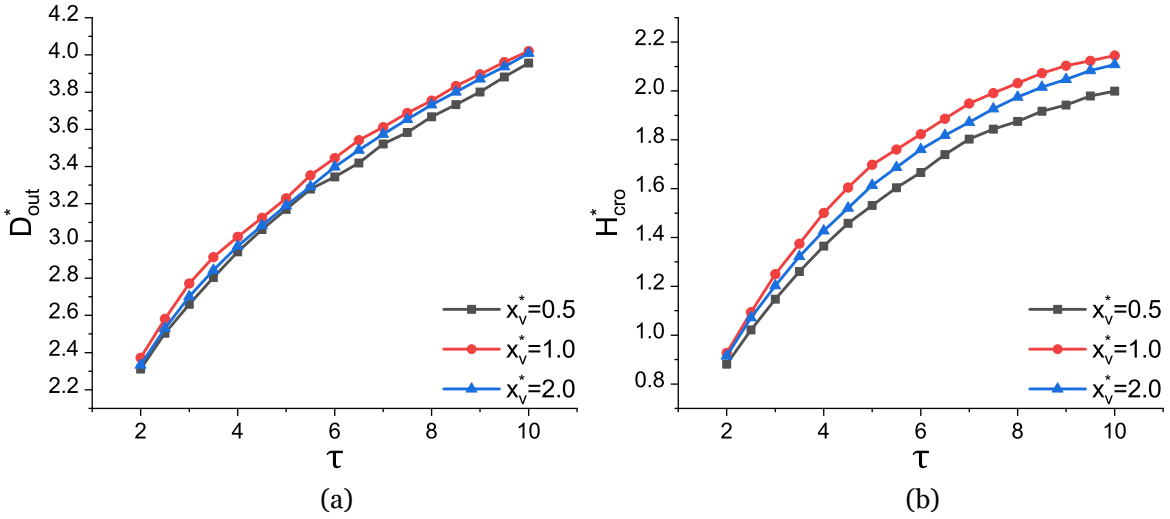

Figure 6.7: Crown measurements for n-decane droplet impact as a function of the vapour spacing for $D_v^* = 1/5$: a) Dimensionless crown outer diameter; b) Dimensionless crown height.

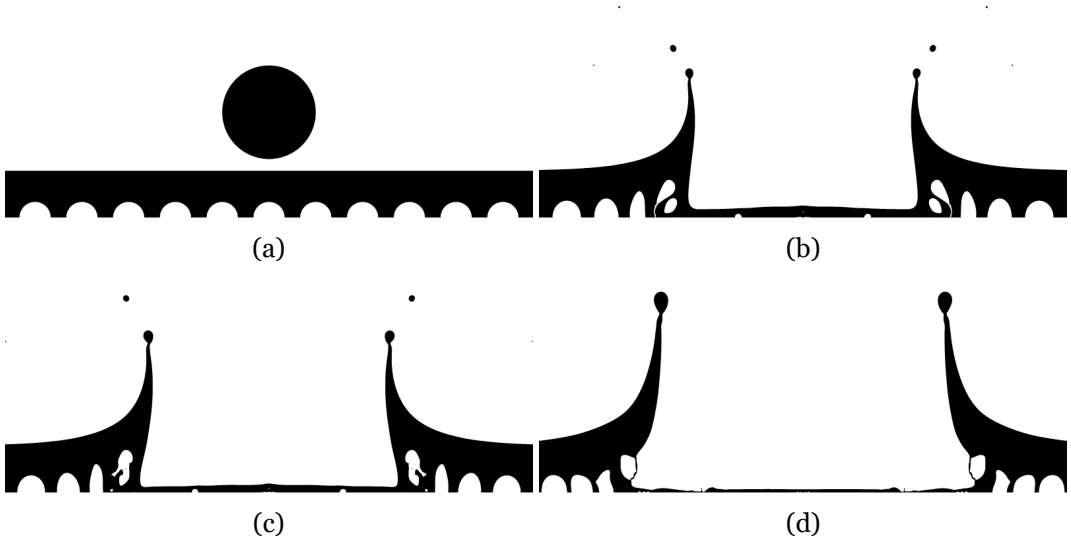

Figure 6.8: N-decane droplet impact at different time frames for $D_v^* = 1/3$ and $x_v^* = 0.5$: a) $\tau = 0$; b) $\tau = 2.5$; c) $\tau = 3$; d) $\tau = 5$.

Subsequent to the droplet impact, a crown accompanied by secondary atomisation is developed at $\tau = 2.5$. Several vapour bubbles are detached from the surface, which are located

near the crown base. Due to the expanding crown, these may merge into a single bubble of increased size, as exhibited in the following frame at $\tau = 3$. These are also subjected to contraction and stretch due to fluid motion. For $\tau = 5$, if the vapour bubbles ascend and contact the crown walls, they will shatter, creating a capillary wave that propagates through the expanding crown, possibly leading to lower height and diameter values at later stages due to crown disintegration.

In terms of fluid comparison, figure 6.9 highlights the differences in height measurements for varying bubble spacings. Due to the differences in thermophysical properties, specifically surface tension, the crown height for water is lower in comparison to n-decane. The water crown reaches a maximum height at earlier stages, ranging from $\tau = 5.5$ for lower spacings to $\tau = 7$ for higher spacings. For n-decane, the crown is still expanding, as the maximum height is reached for $\tau > 10$. Nevertheless, both fluids show similar tendencies, as increased vapour bubble spacings lead to an increase in the crown height.

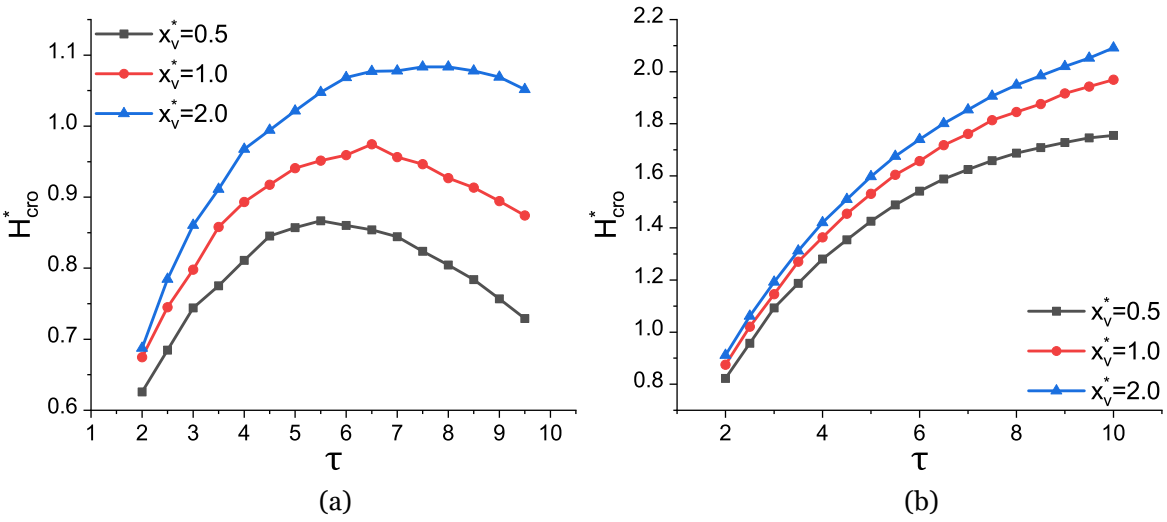

Figure 6.9: Dimensionless crown height measurements for droplet impact for $D_v^* = 1/3$: a) Water; b) N-decane.

6.2.2 Initial Displacement

To complement the vapour bubble analysis regarding size and spacing, the initial bubble displacement from the axis of symmetry is varied between $x_s^* = 0$ and $x_s^* = 2.0$. The vapour bubble size was limited to $D_v^* = 1/2$ and $D_v^* = 1/3$ for a spacing of $x_v^* = 1.0$ to reduce the number of study cases for the current analysis. The crown height and outer diameter measurements are conducted based on the initial bubble displacement, which is consistent with the prior analysis.

Figure 6.10 exhibits the crown parameter measurements as a function of the initial bubble displacement for $D_v^* = 1/2$. The outer diameter measurements exhibit consistent patterns under different bubble conditions. For earlier impact stages, $\tau < 5$, the outer diameter measurements are lower for $x_s^* \leq 1.0$ in comparison to $x_s^* > 1.0$, which is consistent with the presence of vapour bubbles in the impact region influencing the development of the crown.

For later stages, these differences are negligible with the exception of $x_s^* = 0.5$, which displays lower values. The influence of the initial bubble displacement is more noticeable for the crown height measurements. For $x_s^* \leq 1.0$, the liquid crowns reach a maximum height for $\tau \approx 5.5$, and manifest irregular patterns for later stages. For higher initial displacements, $x_s^* > 1.0$, the crowns manifest greater height values throughout the crown development, and the corresponding time for the crown to reach its maximum height occurs at later stages. Among the lower displacements, the impact condition related to $x_s^* = 0.5$ reflects the lowest values. For a more straightforward evaluation of the numerical results, figure 6.11 shows the developed crowns for later stages of the impact and different initial displacements.

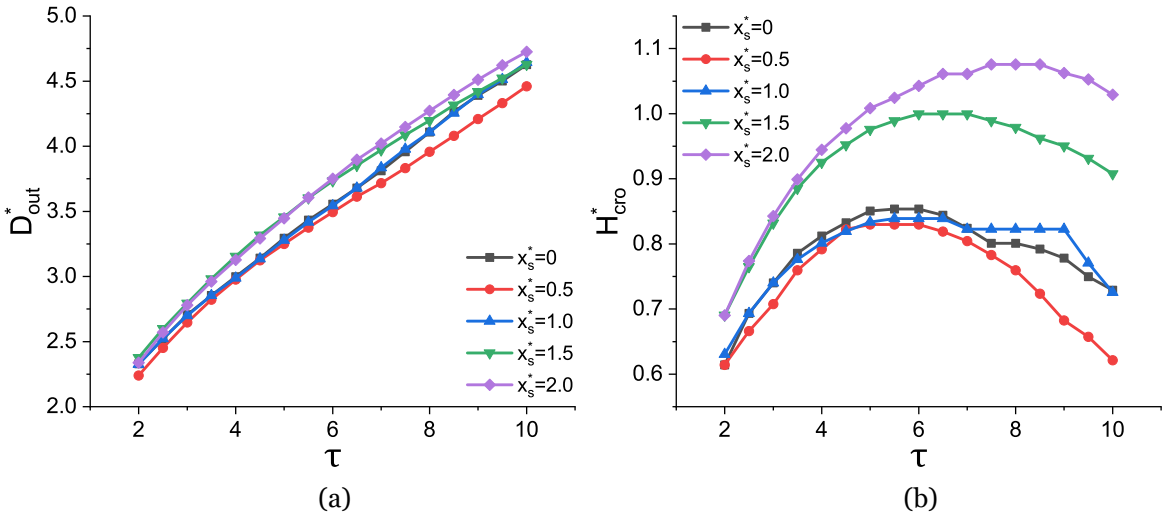

Figure 6.10: Crown measurements for water droplet impact for $D_v^* = 1/2$ and $x_v^* = 1.0$: a) Dimensionless crown outer diameter; b) Dimensionless crown height.

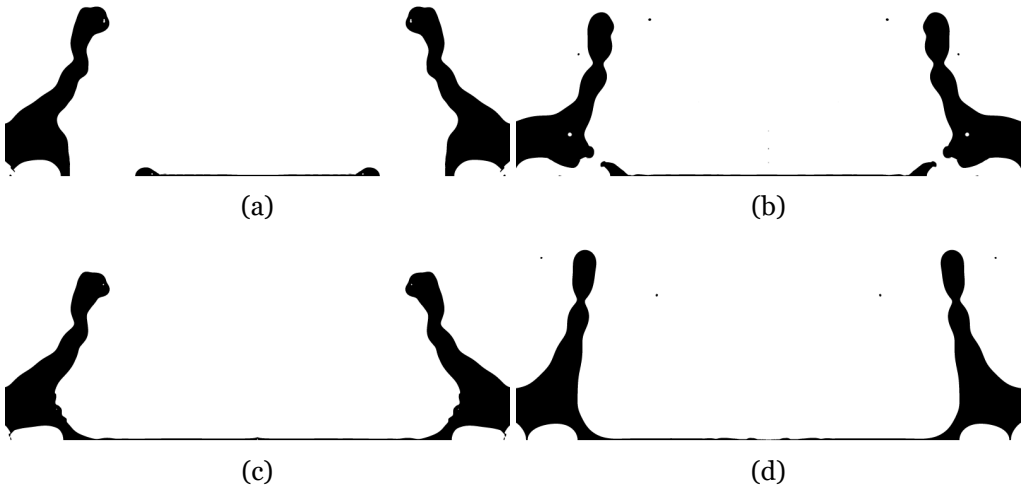

Figure 6.11: Visualisation of water droplet impact as a function of the vapour bubble initial displacement for $D_v^* = 1/2$, $x_v^* = 1.0$ and $\tau = 8$: a) $x_s^* = 0$; b) $x_s^* = 0.5$; c) $x_s^* = 1.0$; d) $x_s^* = 2.0$.

As illustrated, the existence of vapour bubbles in the proximity of the impact region for $x_s^* \leq 1.0$ leads to the bursting of these structures. The liquid-gas instabilities propagate along the crown walls, affecting its development. For outer regions, such as $x_s^* = 2.0$, the crown formation is not disturbed by the vapour bubbles, as these remain on the impact sur-

face and do not collide with the expanding crown. This condition reveals a greater degree of similarities to the standard crown formation represented by figure 6.2. For n-decane, the crowns expand more uniformly, and do not achieve a maximum height for the specified time frame ($\tau < 10$), as exhibited by figure 6.12. For this condition, the diameter measurements vary more significantly than water. Lower diameters are verified for $x_s^* \leq 1.0$, emphasising the lowest tendency for $x_s^* = 0.5$, whereas $x_s^* = 1.5$ and $x_s^* = 2.0$ display increased diameters, similar to the previous condition. Regarding crown height, the overall growth is similar to the outer diameter, as the expanding crowns respond similarly to the vapour bubble initial displacement.

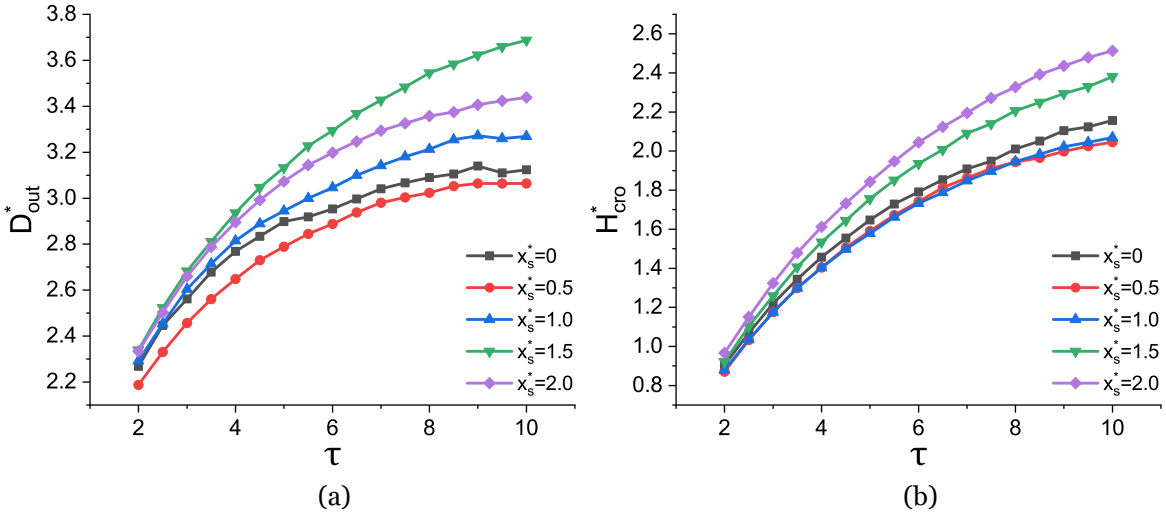

Figure 6.12: Crown measurements for n-decane droplet impact for $D_v^* = 1/2$ and $x_v^* = 1.0$: a) Dimensionless crown outer diameter; b) Dimensionless crown height.

The influence of the vapour bubble initial displacement for decreased bubble sizes is presented by figure 6.13. In comparison to $D_v^* = 1/2$, the differences regarding the crown parameters are not as pronounced. The crown diameters are unaffected by the vapour bubble initial displacement, essentially overlapping for different impact stages. Similar to figure 6.10b, the crown height measurements vary with the initial bubble displacement. The crown height tends to increase with higher values of x_s^*, reaching its lowest point for $x_s^* \leq 1.0$ and showing higher measurements for $x_s^* > 1.0$. The transition of the vapour bubble size from $D_v^* = 1/2$ to $D_v^* = 1/3$ leads to a smaller disparity between curves. In order to properly evaluate the influence of the initial bubble displacement on the impact phenomena, ranging from bubble detachment to wall collision, figure 6.14 illustrates how a single vapour bubble behaves during the impact phenomena. The displayed frames correspond to a time frame of $\tau = 3.7$ for varying initial bubble displacements. For $x_s^* = 0$, the vapour bubble is aligned with the impacting droplet for $\tau = 0$, which will be compressed during the initial droplet propagation. Due to this, the fluid moves into the region occupied by the gas phase, and vapour bubbles can be observed in the residual liquid film thickness situated between the crown walls above the impact surface. The vapour bubble positioned at $x_s^* = 0$ does not detach to the outer regions of the crown. However, for $x_s^* = 0.5$, the vapour bubble detaches and shatters with the crown wall in the vicinity of the impact surface. Due to this, the evolving

crown is not supported by fluid in its base, delaying its growth for following stages. As mentioned earlier, the bubble bursting also creates a capillary wave that spreads into the crown rim, affecting its evolution. Increasing the initial displacement to $x_s^* = 1.0$ causes the vapour bubble to contact the crown wall closer to its rim, which is further away from the impact surface. For this instant, the vapour bubble has yet to collide the crown wall, opposite to the bursted bubble in the previous condition. For a vapour bubble positioned at $x_s^* = 2.0$, the droplet impact and subsequent crown formation are not substantially affected by its presence, as the vapour bubble is pushed outwards with no detachment from the impact surface. The crown expands regularly with no associated breakup and interface instabilities.

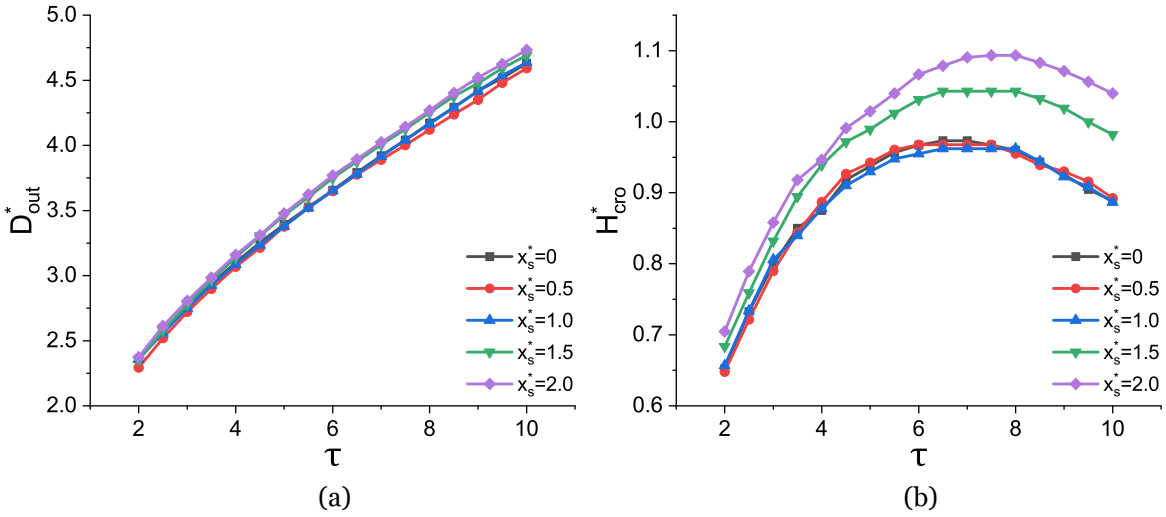

Figure 6.13: Crown measurements for water droplet impact for $D_v^* = 1/3$ and $x_v^* = 1.0$: a) Dimensionless crown outer diameter; b) Dimensionless crown height.

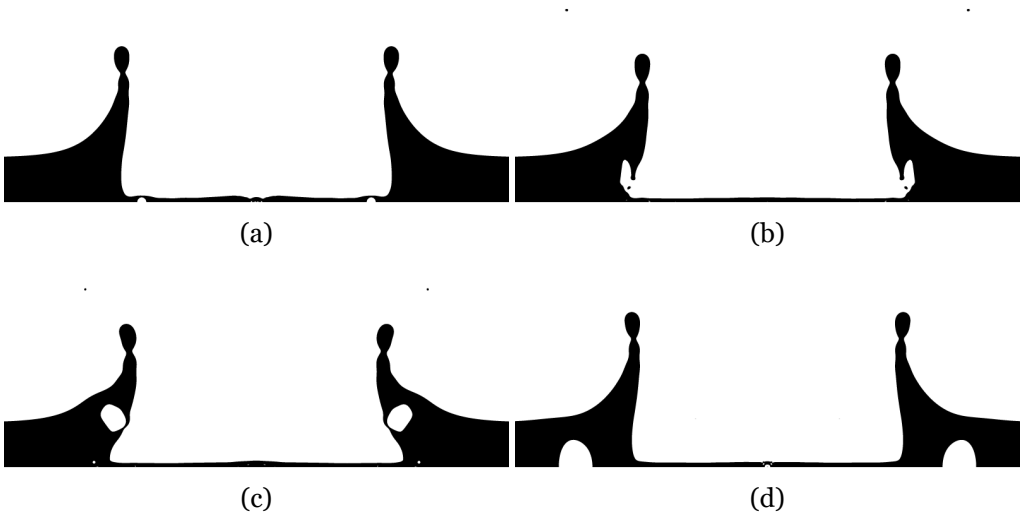

Figure 6.14: Visualisation of water droplet impact as a function of a single vapour bubble initial displacement ($D_v^* = 1/2$ and $\tau = 3.7$): a) $x_s^* = 0$; b) $x_s^* = 0.5$; c) $x_s^* = 1.0$; d) $x_s^* = 2.0$.

Therefore, the presence of vapour bubbles in the impact region decrease both the crown diameter and height, with its effect being more pronounced for the latter. This is verified by the bubble size and spacing studies, which follow the same principles in terms of bubble dynamics regarding detachment, bursting and propagation of capillary waves.

Chapter 7

Conclusions and Future Work

7.1 Conclusions

The present work focuses on the fundamental study of single droplets impacting liquid films under non-isothermal conditions. An experimental facility was designed to account for extended temperature regimes, ranging from isothermal conditions ($\theta = 0$) up to the onset of boiling near the saturation temperature of the fluids ($\theta \approx 1$). Water, n-decane and n-heptane were adopted for the experiments due to their differences in thermophysical properties and saturation temperatures. Additionally, the impact parameters, such as impact velocity and dimensionless thickness, were varied in order to evaluate their influence on the impact outcomes. These include the formation of central jets, craters, splashing and bubbling. The experimental study is complemented with theoretical work regarding kinematic discontinuity propagation and time scales. The validation of the numerical model occurs with available experimental data, followed by the influence of vapour bubbles on crown morphology.

For the central jets, qualitative and quantitative analyses are performed regarding jet evolution, and central jet height and breakup measurements, respectively. For fuels, the central jets are significantly higher and exhibit thinner appearances for higher temperatures, which is associated with the thermophysical properties of the liquid film. An increase in the liquid film temperature also induces central jet breakup. Water exhibits a distinct visual behaviour, as the central jets display thicker ligaments and reduced heights with no secondary breakup from the rising jet. This is due to higher values of surface tension in comparison to the remaining fluids. In terms of quantitative measurements, the central jet height measurements for n-heptane and n-decane show a progressive increase across the different dimensionless temperatures, ranging from $\theta = 0$ to $\theta = 0.6$. The growth and merging of the central jet is also affected by the liquid film temperature. The maximum jet height occurs at later stages of impact for higher temperatures, which leads to an elongation of the jet development. In terms of breakup, both fuels display identical trends, as higher temperatures promote jet break and increase the number of secondary droplets originating from the central jet. The influence of temperature on the fluids thermophysical properties is also a defining factor in the impact phenomena, as higher temperatures lead to lower values of surface tension and viscosity. However, the influence of temperature on the water central jet evolution differs from the remaining fluids. The maximum jet height shows a reduction from $\theta = 0$ to $\theta = 0.2$, followed by a gradual increase of the jet height with higher liquid film temperatures, analogous to fuels. Due to the unexpected reduction regarding water central jet height measurements for $\theta = 0.2$, a time scale analysis was considered for the current application. The surface ten-

sion, convective and gravitational time scales were calculated as a function of θ. For fuels, the gravitational has more influence than the surface tension time scale, regardless of the temperature range. For water, due to the high surface tension and associated temperature variation, the curve correspondent to this property diminishes over time, meaning that surface tension has a more dominant effect in comparison to fuels. Consequently, these time scales intercept at $\theta = 0.27$, leading to a region where the surface tension time scale is predominant ($\theta < 0.27$), and a region where gravitational forces exceed surface tension, $\theta > 0.27$. This shift between prevalent time scales might provide insight into the distinctions regarding jet height reduction at $\theta = 0.2$.

Similarly to central jets, the evolution stages of crater formation were investigated, ranging from the initial expansion to its retraction period. Qualitative and quantitative analyses are performed regarding crater expansion, and depth and diameter measurements, respectively. For non-isothermal conditions, temperature-related dynamics begin to emerge close to the impact surface and expanding crater. These are denominated as recirculation zones and are promoted by increasing values of θ. These regions are a consequence of the mixing of the cold droplet and heated liquid film, inducing refraction due to density differences. Higher temperatures also lead to an increase in the duration of the impact phenomena, namely the crater expansion and posterior retraction, leading to a delay in the crater ejection times. Similarly, the delay of the capillary wave also influences the crater detachment. For the crater parameter measurements, initial diameters are similar during the initial crater expansion, and the maximum diameters are identical to the various dimensionless temperatures. The liquid film temperature plays a role in the crater ejection times, as the duration for which the craters are maintained at maximum diameter and the delay of capillary waves are increased for higher temperatures, leading to the crater entering the retraction period at later stages. The theoretical model, which is based on the propagation of a kinematic discontinuity, is in good agreement with the isothermal crater measurements for the water droplet impact. For fuels, the theoretical model underpredicts the measured experimental results.

The increase in liquid film temperature affects splashing dynamics by promoting cusp formation in the crown rim. Overall, an increase in the liquid film temperature induces a transition between spreading and splashing across all fluids. However, fuels manifest an intermediate region in which an increase in the liquid film temperatures reduces or even suppresses splashing, similarly to water for $\theta = 0.6$. This is a similar phenomenon to the central jet reduction previously described. A splashing correlation was proposed based on the thermophysical properties of the liquid film and the geometrical parameters of the droplet. A similar approach was performed for the onset of bubble encapsulation, adapting the existing criterion for non-isothermal conditions.

For increased heat fluxes, the fluid will reach its saturation temperature, entering a boiling condition. The subcooled and saturated boiling regimes were evaluated in terms of vapour bubble nucleation, growth and detachment. For water, a reduced number of vapour bubbles are spotted in the impact surface. The regions close to the boundaries of the container are

filled with vapour bubbles due to the increased local surface roughness. For fuels, nucleation sites are solely spotted in the surface boundaries, as no vapour bubbles were deposited on the impact surface. N-heptane displays smaller bubble diameters and a higher bubble release rate, whereas water bubbles are significantly larger and detach at lower rates. For the onset of boiling, the oscillations induced on the liquid film are not sufficient to affect the impact phenomena. Due to the difficulty in inducing nucleation in specific regions of the impact surface, such as the impact region, the vapour bubbles were numerically implemented to examine their influence on the crown morphology. Prior to this study, the numerical model was validated with existing experimental data. Different vapour bubble sizes, spacings and initial displacements are considered for the current analysis. Increasingly vapour bubble diameters causes a reduction in the crown height, as the vapour bubbles detach and merge with the expanding crown, affecting its growth. The set of results for various bubble spacings exhibit fewer differences in the crown evolution in comparison to its size. Overall, the presence of vapour bubbles in the impact region decreases both the crown diameter and height, with its effect being more pronounced for the latter. This is verified by the initial displacement for a single bubble, as vapour bubbles positioned within the impact region may detach and shatter with the crown wall in the vicinity of the impact surface. Due to this, the evolving crown is not supported by fluid in its base, delaying its growth for following stages.

Overall, the liquid film temperature plays a crucial role in the impact dynamics, which is associated with differences in thermophysical properties. The different outcomes were analysed and quantified for a variety of impact conditions and temperature regimes. However, the height reduction for the central jets and the suppression of splashing for low temperatures under non-isothermal conditions require a deep understanding of fluid and heat flow, specifically Marangoni stress and local evaporation. Comprehending underlying mechanics associated with interfacial dynamics and heat and mass transfer mechanisms could provide insights into droplet impact applications.

7.2 Future Work

The foundation for single droplets impacting onto heated liquid films has been established, providing a basis for further research in terms of fluid dynamics, and heat and mass transfer mechanisms. Despite this, there are numerous aspects that require adaptation and improvement for future works.

For the experimental facility, it is crucial to enhance optical access regarding impact outcomes for qualitative analysis. Additionally, due to the presence of a heat flux, local evaporation occurs in the liquid-gas interface, distorting the visualisation process. These can be improved by redesigning the impact surface as a single piece, thus avoiding the use of a sealing agent for bonding and removing the constraint related to operating temperatures. The setup should also feature optical access from a bottom perspective, giving insight into distinct dynamics associated with the impact phenomena. However, this would require a complete

overhaul of the heating system, which is challenging with the current setup. The experimental procedure regarding liquid film thickness variation involves a manual process with the aid of a precision scale. The accuracy of these measurements would benefit from an automated system designed to maintain constant liquid film thickness, which could be extended for temperature fields. The latter could be complemented by infrared thermal imaging, providing detailed insights into temperature gradients along the liquid film and during the impact phenomena.

The scope of the experimental study should be broadened to incorporate more fluids with different thermophysical properties and saturation temperatures. In terms of liquid film temperature regimes, saturated boiling regimes require further studies regarding vapour bubble cycles under increased heat fluxes. Specifically, the detachment of vapour bubbles induces a characteristic vibration frequency in the liquid film, causing local film thickness fluctuations. Quantifying the liquid film oscillations and their direct effect on the impact phenomena could offer different perspectives on fluid dynamics and phase-change processes within boiling regimes.

The numerical model requires the implementation of a phase change model based on the kinetic theory of gases or energy jump conditions to account for evaporation and condensation. Similarly, this framework facilitates the formulation of a numerical model capable of simulating the nucleation, growth and detachment of vapour bubbles as a function of the interfacial mass transfer rate without relying on artificial methods. These adaptations would require the variation of the fluids thermophysical properties as a function of the local temperature to apply the model to non-isothermal regimes.

Bibliography

[1] I. E. Agency, *World Energy Statistics 2019*. International Energy Agency, 2019.

[2] D. S. Lee, D. W. Fahey, P. M. Forster, P. J. Newton, R. C. Wit, L. L. Lim, B. Owen, and R. Sausen, "Aviation and global climate change in the 21st century," *Atmospheric Environment*, vol. 43, no. 22-23, pp. 3520–3537, 2009.

[3] V. Undavalli, O. B. G. Olatunde, R. Boylu, C. Wei, J. Haeker, J. Hamilton, and B. Khandelwal, "Recent advancements in sustainable aviation fuels," *Progress in Aerospace Sciences*, vol. 136, p. 100876, 2023.

[4] A. Moreira, A. Moita, and M. Panão, "Advances and challenges in explaining fuel spray impingement: How much of single droplet impact research is useful?" *Progress in Energy and Combustion Science*, vol. 36, no. 5, pp. 554–580, 2010.

[5] G. Liang and I. Mudawar, "Review of mass and momentum interactions during drop impact on a liquid film," *International Journal of Heat and Mass Transfer*, vol. 101, pp. 577–599, 2016.

[6] İ. Dinçer and C. Zamfirescu, *Drying phenomena: theory and applications*. John Wiley & Sons, 2016.

[7] S. Honnet, K. Seshadri, U. Niemann, and N. Peters, "A surrogate fuel for kerosene," *Proceedings of the Combustion Institute*, vol. 32, no. 1, pp. 485–492, 2009.

[8] L. Zhao, T. Yang, R. I. Kaiser, T. P. Troy, M. Ahmed, D. Belisario-Lara, J. M. Ribeiro, and A. M. Mebel, "Combined experimental and computational study on the unimolecular decomposition of jp-8 jet fuel surrogates. i. n-decane (n-c10h22)," *The Journal of Physical Chemistry A*, vol. 121, no. 6, pp. 1261–1280, 2017.

[9] J. Farrell, N. Cernansky, F. Dryer, C. K. Law, D. Friend, C. Hergart, R. McDavid, A. Patel, C. J. Mueller, and H. Pitsch, "Development of an experimental database and kinetic models for surrogate diesel fuels," SAE Technical Paper, Tech. Rep., 2007.

[10] R. Lindstedt and L. Maurice, "Detailed kinetic modelling of n-heptane combustion," *Combustion Science and Technology*, vol. 107, no. 4-6, pp. 317–353, 1995.

[11] A. Behzadi, R. Issa, and H. Rusche, "Modelling of dispersed bubble and droplet flow at high phase fractions," *Chemical Engineering Science*, vol. 59, no. 4, pp. 759–770, 2004.

[12] E. E. Michaelides and Z.-G. Feng, “Fundamentals of multiphase flow,” in *Multiphase Flow Handbook*. CRC Press, 2016, pp. 1–78.

[13] P. Sobieszuk, J. Aubin, and R. Pohorecki, “Hydrodynamics and mass transfer in gas-liquid flows in microreactors,” *Chemical Engineering & Technology*, vol. 35, no. 8, pp. 1346–1358, 2012.

[14] F. Saidj, A. Hasan, H. Bouyahiaoui, A. Zeghloul, and A. Azzi, “Experimental study of the characteristics of an upward two-phase slug flow in a vertical pipe,” *Progress in Nuclear Energy*, vol. 108, pp. 428–437, 2018.

[15] S. Hosseini, O. Taylan, M. Abusurrah, T. Akilan, E. Nazemi, E. Eftekhari-Zadeh, F. Bano, and G. H. Roshani, “Application of wavelet feature extraction and artificial neural networks for improving the performance of gas–liquid two-phase flow meters used in oil and petrochemical industries,” *Polymers*, vol. 13, no. 21, p. 3647, 2021.

[16] L. C. Gómez and F. E. Milioli, “Numerical study on the influence of various physical parameters over the gas–solid two-phase flow in the 2d riser of a circulating fluidized bed,” *Powder Technology*, vol. 132, no. 2-3, pp. 216–225, 2003.

[17] H. Liu, R. Zailani, and B. M. Gibbs, “Comparisons of pulverized coal combustion in air and in mixtures of o2/co2,” *Fuel*, vol. 84, no. 7-8, pp. 833–840, 2005.

[18] J. C. Bird, S. S. Tsai, and H. A. Stone, “Inclined to splash: triggering and inhibiting a splash with tangential velocity,” *New Journal of Physics*, vol. 11, no. 6, p. 063017, 2009.

[19] G. Zhang, M. A. Quetzeri-Santiago, C. A. Stone, L. Botto, and J. R. Castrejón-Pita, “Droplet impact dynamics on textiles,” *Soft Matter*, vol. 14, no. 40, pp. 8182–8190, 2018.

[20] A. L. Yarin, “Drop impact dynamics: splashing, spreading, receding, bouncing...,” *Annual Review of Fluid Mechanics*, vol. 38, pp. 159–192, 2006.

[21] J. D. Bernardin, C. J. Stebbins, and I. Mudawar, “Mapping of impact and heat transfer regimes of water drops impinging on a polished surface,” *International Journal of Heat and Mass Transfer*, vol. 40, no. 2, pp. 247–267, 1997.

[22] A. M. Worthington, “Xxviii. on the forms assumed by drops of liquids falling vertically on a horizontal plate,” *Proceedings of the Royal Society of London*, vol. 25, no. 171-178, pp. 261–272, 1877.

[23] A. M. Worthington, “Iii. a second paper on the forms assumed by drops of liquids

falling vertically on a horizontal plate," *Proceedings of the Royal Society of London*, vol. 25, no. 171-178, pp. 498–503, 1877.

[24] A. M. Worthington, "On impact with a liquid surface," *Proceedings of the Royal Society of London*, vol. 34, no. 220-223, pp. 217–230, 1883.

[25] A. M. Worthington and R. S. Cole, "V. impact with a liquid surface, studied by the aid of instantaneous photography," *Philosophical Transactions of the Royal Society of London. Series A, Containing Papers of a Mathematical or Physical Character*, no. 189, pp. 137–148, 1897.

[26] L. Rayleigh, "Some applications of photography 1," 1891.

[27] A. M. Worthington, *A study of splashes*. Longmans, Green, and Company, 1908.

[28] H. E. Edgerton and J. R. Killian, *Flash!: Seeing the unseen by ultra high-speed photography*. CT Branford Company, 1954.

[29] G. J. Franz, "Splashes as sources of sound in liquids," *The Journal of the Acoustical Society of America*, vol. 31, no. 8, pp. 1080–1096, 1959.

[30] A. Prosperetti and H. N. Oguz, "The impact of drops on liquid surfaces and the underwater noise of rain," *Annual Review of Fluid Mechanics*, vol. 25, no. 1, pp. 577–602, 1993.

[31] M. Lesser and J. Field, "The impact of compressible liquids," *Annual Review of Fluid Mechanics*, vol. 15, pp. 97–122, 1983.

[32] O. G. Engel *et al.*, "Waterdrop collisions with solid surfaces," *Journal of Research of the National Bureau of Standards*, vol. 54, no. 5, pp. 281–298, 1955.

[33] F. Heymann, "High-speed impact between a liquid drop and a solid surface," *Journal of Applied Physics*, vol. 40, no. 13, pp. 5113–5122, 1969.

[34] L. Wachters and N. Westerling, "The heat transfer from a hot wall to impinging water drops in the spheroidal state," *Chemical Engineering Science*, vol. 21, no. 11, pp. 1047–1056, 1966.

[35] L. Wachters, L. Smulders, J. Vermeulen, and H. Kleiweg, "The heat transfer from a hot wall to impinging mist droplets in the spheroidal state," *Chemical Engineering Science*, vol. 21, no. 12, pp. 1231–1238, 1966.

[36] L. Wachters, H. Bonne, and H. Van Nouhuis, "The heat transfer from a hot horizontal plate to sessile water drops in the spherodial state," *Chemical Engineering Science*,

vol. 21, no. 10, pp. 923–936, 1966.

[37] J. G. Leidenfrost, *De aquae communis nonnullis qualitatibus tractatus*. Ovenius, 1756.

[38] S. Chandra and C. Avedisian, "On the collision of a droplet with a solid surface," *Proceedings of the Royal Society of London. Series A: Mathematical and Physical Sciences*, vol. 432, no. 1884, pp. 13–41, 1991.

[39] T. Young, "Iii. an essay on the cohesion of fluids," *Philosophical Transactions of the Royal Society of London*, no. 95, pp. 65–87, 1805.

[40] M. Pasandideh-Fard, Y. Qiao, S. Chandra, and J. Mostaghimi, "Capillary effects during droplet impact on a solid surface," *Physics of Fluids*, vol. 8, no. 3, pp. 650–659, 1996.

[41] C. D. Stow and M. G. Hadfield, "An experimental investigation of fluid flow resulting from the impact of a water drop with an unyielding dry surface," *Proceedings of the Royal Society of London. A. Mathematical and Physical Sciences*, vol. 373, no. 1755, pp. 419–441, 1981.

[42] D. Peregrine, "The fascination of fluid mechanics," *Journal of Fluid Mechanics*, vol. 106, pp. 59–80, 1981.

[43] C. Wang, "Exact solutions of the steady-state navier-stokes equations," *Annual Review of Fluid Mechanics*, vol. 23, no. 1, pp. 159–177, 1991.

[44] Z. Levin and P. V. Hobbs, "Splashing of water drops on solid and wetted surfaces: hydrodynamics and charge separation," *Philosophical Transactions of the Royal Society of London. Series A, Mathematical and Physical Sciences*, vol. 269, no. 1200, pp. 555–585, 1971.

[45] A. L. Yarin and D. A. Weiss, "Impact of drops on solid surfaces: self-similar capillary waves, and splashing as a new type of kinematic discontinuity," *Journal of Fluid Mechanics*, vol. 283, pp. 141–173, 1995.

[46] E. A. Igel and M. Kristiansen, *Rotating mirror streak and framing cameras*. SPIE Press, 1997, vol. 43.

[47] W. S. Boyle and G. E. Smith, "Charge coupled semiconductor devices," *Bell System Technical Journal*, vol. 49, no. 4, pp. 587–593, 1970.

[48] S. T. Thoroddsen, T. G. Etoh, and K. Takehara, "High-speed imaging of drops and bubbles," *Annual Review of Fluid Mechanics*, vol. 40, pp. 257–285, 2008.

[49] M. R. Panão and A. L. N. Moreira, "Flow characteristics of spray impingement in pfi injection systems," *Experiments in Fluids*, vol. 39, no. 2, pp. 364–374, 2005.

[50] W. Jia and H.-H. Qiu, "Experimental investigation of droplet dynamics and heat transfer in spray cooling," *Experimental Thermal and Fluid Science*, vol. 27, no. 7, pp. 829–838, 2003.

[51] Š. Šikalo and E. Ganić, "Phenomena of droplet–surface interactions," *Experimental Thermal and Fluid Science*, vol. 31, no. 2, pp. 97–110, 2006.

[52] D. B. van Dam and C. Le Clerc, "Experimental study of the impact of an ink-jet printed droplet on a solid substrate," *Physics of Fluids*, vol. 16, no. 9, pp. 3403–3414, 2004.

[53] C. Tropea and M. Marengo, "The impact of drops on walls and films," *Multiphase Science and Technology*, vol. 11, no. 1, 1999.

[54] Z. Han, Z. Xu, and N. Trigui, "Spray/wall interaction models for multidimensional engine simulation," *International Journal of Engine Research*, vol. 1, no. 1, pp. 127–146, 2000.

[55] G. E. Cossali, A. Coghe, and M. Marengo, "The impact of a single drop on a wetted solid surface," *Experiments in Fluids*, vol. 22, no. 6, pp. 463–472, 1997.

[56] R. L. Vander Wal, G. M. Berger, and S. D. Mozes, "Droplets splashing upon films of the same fluid of various depths," *Experiments in Fluids*, vol. 40, no. 1, pp. 33–52, 2006.

[57] A.-B. Wang and C.-C. Chen, "Splashing impact of a single drop onto very thin liquid films," *Physics of Fluids*, vol. 12, no. 9, pp. 2155–2158, 2000.

[58] C. Motzkus, F. Gensdarmes, and E. Géhin, "Parameter study of microdroplet formation by impact of millimetre-size droplets onto a liquid film," *Journal of Aerosol Science*, vol. 40, no. 8, pp. 680–692, 2009.

[59] W. M. Healy, J. Hartley, and S. Abdel-Khalik, "On the validity of the adiabatic spreading assumption in droplet impact cooling," *International Journal of Heat and Mass Transfer*, vol. 44, no. 20, pp. 3869–3881, 2001.

[60] H. Zhang, X. Zhang, X. Yi, F. He, F. Niu, and P. Hao, "Effect of wettability on droplet impact: Spreading and splashing," *Experimental Thermal and Fluid Science*, vol. 124, p. 110369, 2021.

[61] G. Coppola, G. Rocco, and L. de Luca, "Insights on the impact of a plane drop on a thin liquid film," *Physics of Fluids*, vol. 23, no. 2, p. 022105, 2011.

[62] D. F. S. Ribeiro, "Experimental study of a single droplet impinging upon liquid films: Jet fuel and biofuel mixtures," Master's thesis, Universidade da Beira interior, 2018.

[63] B. Ray, G. Biswas, and A. Sharma, "Generation of secondary droplets in coalescence of a drop at a liquid–liquid interface," *Journal of Fluid Mechanics*, vol. 655, pp. 72–104, 2010.

[64] F. Blanchette and T. P. Bigioni, "Dynamics of drop coalescence at fluid interfaces," *Journal of Fluid Mechanics*, vol. 620, pp. 333–352, 2009.

[65] H. Aryafar and H. Kavehpour, "Drop coalescence through planar surfaces," *Physics of Fluids*, vol. 18, no. 7, p. 072105, 2006.

[66] H. P. Kavehpour, "Coalescence of drops," *Annual Review of Fluid Mechanics*, vol. 47, pp. 245–268, 2015.

[67] R. Kumar, Lokesh, and A. K. Das, "Fluidics of an immiscible drop impact onto a hot oil film," *Physics of Fluids*, vol. 34, no. 1, p. 012108, 2022.

[68] J. S. Eow, M. Ghadiri, A. O. Sharif, and T. J. Williams, "Electrostatic enhancement of coalescence of water droplets in oil: a review of the current understanding," *Chemical Engineering Journal*, vol. 84, no. 3, pp. 173–192, 2001.

[69] G. Liang, Y. Yang, Y. Guo, N. Zhen, and S. Shen, "Rebound and spreading during a drop impact on wetted cylinders," *Experimental Thermal and Fluid Science*, vol. 52, pp. 97–103, 2014.

[70] B. Ding, H. Wang, X. Zhu, R. Chen, and Q. Liao, "Water droplet impact on superhydrophobic surfaces with various inclinations and supercooling degrees," *International Journal of Heat and Mass Transfer*, vol. 138, pp. 844–851, 2019.

[71] R. Rioboo, C. Tropea, and M. Marengo, "Outcomes from a drop impact on solid surfaces," *Atomization and Sprays*, vol. 11, no. 2, 2001.

[72] B. Chen, B. Wang, F. Mao, R. Tian, and C. Lu, "Analysis of liquid droplet impacting on liquid film by clsvof," *Annals of Nuclear Energy*, vol. 143, p. 107468, 2020.

[73] J. Eggers and E. Villermaux, "Physics of liquid jets," *Reports on Progress in Physics*, vol. 71, no. 3, p. 036601, 2008.

[74] S. J. Kim, S. Kim, and S. Jung, "Extremes of the pinch-off location and time in a liquid column by an accelerating solid sphere," *Physical Review Fluids*, vol. 3, no. 8, p. 084001, 2018.

[75] E. Castillo-Orozco, A. Davanlou, P. K. Choudhury, and R. Kumar, "Droplet impact on deep liquid pools: Rayleigh jet to formation of secondary droplets," *Physical Review E*, vol. 92, no. 5, p. 053022, 2015.

[76] S. Chandrasekhar, *Hydrodynamic and hydromagnetic stability*. Courier Corporation, 2013.

[77] S. L. Manzello and J. C. Yang, "An experimental study of high weber number impact of methoxy-nonafluorobutane c4f9och3 (hfe-7100) and n-heptane droplets on a heated solid surface," *International Journal of Heat and Mass Transfer*, vol. 45, no. 19, pp. 3961–3971, 2002.

[78] H. Ma, C. Liu, X. Li, H. Huang, and J. Dong, "Deformation characteristics and energy conversion during droplet impact on a water surface," *Physics of Fluids*, vol. 31, no. 6, p. 062108, 2019.

[79] G.-J. Michon, C. Josserand, and T. Séon, "Jet dynamics post drop impact on a deep pool," *Physical Review Fluids*, vol. 2, no. 2, p. 023601, 2017.

[80] E. Ghabache, A. Antkowiak, C. Josserand, and T. Séon, "On the physics of fizziness: How bubble bursting controls droplets ejection," *Physics of Fluids*, vol. 26, no. 12, p. 121701, 2014.

[81] I. V. Roisman and C. Tropea, "Impact of a drop onto a wetted wall: description of crown formation and propagation," *Journal of Fluid Mechanics*, vol. 472, pp. 373–397, 2002.

[82] A. Geppert, A. Terzis, G. Lamanna, M. Marengo, and B. Weigand, "A benchmark study for the crown-type splashing dynamics of one-and two-component droplet wall–film interactions," *Experiments in Fluids*, vol. 58, pp. 1–27, 2017.

[83] X. Gao and R. Li, "Impact of a single drop on a flowing liquid film," *Physical Review E*, vol. 92, no. 5, p. 053005, 2015.

[84] G. Liang, Y. Guo, and S. Shen, "Gas properties on crown behavior and drop coalescence," *Numerical Heat Transfer, Part B: Fundamentals*, vol. 65, no. 6, pp. 537–553, 2014.

[85] L. Lu, Y. Pei, J. Qin, Z. Peng, and K. Zhong, "Analysis of the breaking process and the components of the crown structure after a single droplet hits thin liquid film," *Applied Thermal Engineering*, vol. 219, p. 119514, 2023.

[86] G. Cossali, M. Marengo, A. Coghe, and S. Zhdanov, "The role of time in single drop

splash on thin film," *Experiments in Fluids*, vol. 36, pp. 888–900, 2004.

[87] G. Liang, Y. Guo, S. Shen, and Y. Yang, "Crown behavior and bubble entrainment during a drop impact on a liquid film," *Theoretical and Computational Fluid Dynamics*, vol. 28, no. 2, pp. 159–170, 2014.

[88] S. Mukherjee and J. Abraham, "Crown behavior in drop impact on wet walls," *Physics of Fluids*, vol. 19, no. 5, p. 052103, 2007.

[89] M. Xu, C. Wang, and S. Lu, "Experimental study of a droplet impacting on a burning fuel liquid surface," *Experimental Thermal and Fluid Science*, vol. 74, pp. 347–353, 2016.

[90] E. Berberović, N. P. van Hinsberg, S. Jakirlić, I. V. Roisman, and C. Tropea, "Drop impact onto a liquid layer of finite thickness: Dynamics of the cavity evolution," *Physical Review E*, vol. 79, no. 3, p. 036306, 2009.

[91] A. Bisighini, G. E. Cossali, C. Tropea, and I. V. Roisman, "Crater evolution after the impact of a drop onto a semi-infinite liquid target," *Physical Review E*, vol. 82, no. 3, p. 036319, 2010.

[92] W. Xu, D. Yuan, H. Sun, T. Guo, F. Zhao, H. Ma, and C. Liu, "Evolution of cavity size and energy conversion due to droplet impact on a water surface," *Chinese Journal of Chemical Engineering*, vol. 62, pp. 261–269, 2023.

[93] W. Macklin and G. Metaxas, "Splashing of drops on liquid layers," *Journal of Applied Physics*, vol. 47, no. 9, pp. 3963–3970, 1976.

[94] G. K. Batchelor, *An introduction to fluid dynamics*. Cambridge university press, 2000.

[95] I. V. Roisman, N. P. van Hinsberg, and C. Tropea, "Propagation of a kinematic instability in a liquid layer: capillary and gravity effects," *Physical Review E—Statistical, Nonlinear, and Soft Matter Physics*, vol. 77, no. 4, p. 046305, 2008.

[96] A. I. Fedorchenko and A.-B. Wang, "On some common features of drop impact on liquid surfaces," *Physics of Fluids*, vol. 16, no. 5, pp. 1349–1365, 2004.

[97] N. E. Ersoy and M. Eslamian, "Phenomenological study and comparison of droplet impact dynamics on a dry surface, thin liquid film, liquid film and shallow pool," *Experimental Thermal and Fluid Science*, vol. 112, p. 109977, 2020.

[98] Y. Wu, Q. Wang, and C. Zhao, "Three-dimensional droplet splashing dynamics mea-

surement with a stereoscopic shadowgraph system," *International Journal of Heat and Fluid Flow*, vol. 83, p. 108576, 2020.

[99] D. F. Ribeiro, M. R. Panão, J. M. Barata, and A. R. Silva, "Insights on bubble encapsulation after drop impact on thin liquid films," *International Journal of Multiphase Flow*, vol. 164, p. 104450, 2023.

[100] Z. Che and O. K. Matar, "Impact of droplets on liquid films in the presence of surfactant," *Langmuir*, vol. 33, no. 43, pp. 12 140–12 148, 2017.

[101] D. F. Ribeiro, A. R. Silva, and M. R. Panão, "Insights into single droplet impact models upon liquid films using alternative fuels for aero-engines," *Applied Sciences*, vol. 10, no. 19, p. 6698, 2020.

[102] D. A. Burzynski and S. E. Bansmer, "Droplet splashing on thin moving films at high weber numbers," *International Journal of Multiphase Flow*, vol. 101, pp. 202–211, 2018.

[103] J. A. F. Plateau, *Statique expérimentale et théorique des liquides soumis aux seules forces moléculaires*. Gauthier-Villars, 1873, vol. 2.

[104] L. Rayleigh *et al.*, "On the capillary phenomena of jets," *Proceedings of the Royal Society of London*, vol. 29, no. 196-199, pp. 71–97, 1879.

[105] J. W. S. B. Rayleigh, *Scientific Papers: 1881-1887*. University Press, 1900, vol. 2.

[106] G. I. Taylor, "The instability of liquid surfaces when accelerated in a direction perpendicular to their planes. i," *Proceedings of the Royal Society of London. Series A. Mathematical and Physical Sciences*, vol. 201, no. 1065, pp. 192–196, 1950.

[107] O. Breslouer, "Rayleigh-plateau instability: falling jet," *Project Report*, 2010.

[108] G. Agbaglah, C. Josserand, and S. Zaleski, "Longitudinal instability of a liquid rim," *Physics of Fluids*, vol. 25, no. 2, 2013.

[109] L. Lu, Y. Pei, J. Qin, Z. Peng, Y. Wang, and Q. Zhu, "Impingement behaviour of single ethanol droplet on a liquid film of glycerol solution," *Fuel*, vol. 276, p. 117820, 2020.

[110] R. L. Vander Wal, G. M. Berger, and S. D. Mozes, "The combined influence of a rough surface and thin fluid film upon the splashing threshold and splash dynamics of a droplet impacting onto them," *Experiments in Fluids*, vol. 40, no. 1, pp. 23–32, 2006.

[111] C. Motzkus, E. Géhin, and F. Gensdarmes, "Study of airborne particles produced by normal impact of millimetric droplets onto a liquid film," *Experiments in Fluids*,

vol. 45, no. 5, pp. 797–812, 2008.

[112] C. Mundo, M. Sommerfeld, and C. Tropea, "Droplet-wall collisions: experimental studies of the deformation and breakup process," *International Journal of Multiphase Flow*, vol. 21, no. 2, pp. 151–173, 1995.

[113] R. Rioboo, C. Bauthier, J. Conti, M. Voue, and J. De Coninck, "Experimental investigation of splash and crown formation during single drop impact on wetted surfaces," *Experiments in Fluids*, vol. 35, no. 6, pp. 648–652, 2003.

[114] T. Okawa, T. Shiraishi, and T. Mori, "Production of secondary drops during the single water drop impact onto a plane water surface," *Experiments in Fluids*, vol. 41, pp. 965–974, 2006.

[115] R. L. V. Wal, G. M. Berger, and S. D. Mozes, "The splash/non-splash boundary upon a dry surface and thin fluid film," *Experiments in Fluids*, vol. 40, no. 1, pp. 53–59, 2006.

[116] Q. Huang and H. Zhang, "A study of different fluid droplets impacting on a liquid film," *Petroleum Science*, vol. 5, pp. 62–66, 2008.

[117] T. Okawa, K. Kubo, K. Kawai, and S. Kitabayashi, "Experiments on splashing thresholds during single-drop impact onto a quiescent liquid film," *Experimental Thermal and Fluid Science*, vol. 121, p. 110279, 2021.

[118] J. Zhu, C. Tu, T. Lu, Y. Luo, K. Zhang, and X. Chen, "Behavior of a water droplet impacting a thin water film," *Experiments in Fluids*, vol. 62, pp. 1–13, 2021.

[119] O. G. Engel, "Crater depth in fluid impacts," *Journal of Applied Physics*, vol. 37, no. 4, pp. 1798–1808, 1966.

[120] K.-L. Pan, K.-R. Cheng, P.-C. Chou, and C.-H. Wang, "Collision dynamics of high-speed droplets upon layers of variable thickness," *Experiments in Fluids*, vol. 45, pp. 435–446, 2008.

[121] K.-L. Pan and C.-Y. Hung, "Droplet impact upon a wet surface with varied fluid and surface properties," *Journal of Colloid and Interface Science*, vol. 352, no. 1, pp. 186–193, 2010.

[122] D. Ribeiro, A. Silva, and M. Panão, "Criterion for bubble encapsulation on drop impact onto a liquid film," *Physics of Fluids*, vol. 35, no. 3, p. 033305, 2023.

[123] M. Rein, "Phenomena of liquid drop impact on solid and liquid surfaces," *Fluid Dynamics Research*, vol. 12, no. 2, p. 61, 1993.

[124] Y. Ko and S. Chung, "An experiment on the breakup of impinging droplets on a hot surface," *Experiments in Fluids*, vol. 21, no. 2, pp. 118–123, 1996.

[125] A.-M. Cazabat and G. Guena, "Evaporation of macroscopic sessile droplets," *Soft Matter*, vol. 6, no. 12, pp. 2591–2612, 2010.

[126] K. Gleason, H. Voota, and S. A. Putnam, "Steady-state droplet evaporation: Contact angle influence on the evaporation efficiency," *International Journal of Heat and Mass Transfer*, vol. 101, pp. 418–426, 2016.

[127] G. Liang, X. Mu, Y. Guo, S. Shen, S. Quan, and J. Zhang, "Contact vaporization of an impacting drop on heated surfaces," *Experimental Thermal and Fluid Science*, vol. 74, pp. 73–80, 2016.

[128] J. Shen, C. Graber, J. Liburdy, D. Pence, and V. Narayanan, "Simultaneous droplet impingement dynamics and heat transfer on nano-structured surfaces," *Experimental Thermal and Fluid Science*, vol. 34, no. 4, pp. 496–503, 2010.

[129] K. Sefiane, L. Tadrist, and M. Douglas, "Experimental study of evaporating water–ethanol mixture sessile drop: influence of concentration," *International Journal of Heat and Mass Transfer*, vol. 46, no. 23, pp. 4527–4534, 2003.

[130] M. diMarzo and D. D. Evans, "Evaporation of a water droplet deposited on a hot high thermal conductivity surface," *Journal of Heat Transfer (Transcations of the ASME (American Society of Mechanical Engineers), Series C);(USA)*, vol. 111, no. 1, 1989.

[131] J. Rymkiewicz and Z. Zapalowicz, "Analysis of the evaporation process for water droplet on flat heated surface," *International Communications in Heat and Mass Transfer*, vol. 20, no. 5, pp. 687–697, 1993.

[132] N. Z. Mehdizadeh and S. Chandra, "Boiling during high-velocity impact of water droplets on a hot stainless steel surface," *Proceedings of the Royal Society A: Mathematical, Physical and Engineering Sciences*, vol. 462, no. 2074, pp. 3115–3131, 2006.

[133] N. Zuber, "Nucleate boiling. the region of isolated bubbles and the similarity with natural convection," *International Journal of Heat and Mass Transfer*, vol. 6, no. 1, pp. 53–78, 1963.

[134] G. Cossali, M. Marengo, and M. Santini, "Secondary atomisation produced by single drop vertical impacts onto heated surfaces," *Experimental Thermal and Fluid Science*, vol. 29, no. 8, pp. 937–946, 2005.

[135] A. Moita and A. Moreira, "Drop impacts onto cold and heated rigid surfaces: Morpho-

logical comparisons, disintegration limits and secondary atomization," *International Journal of Heat and Fluid Flow*, vol. 28, no. 4, pp. 735–752, 2007.

[136] H. Chaves, A. M. Kubitzek, and F. Obermeier, "Dynamic processes occurring during the spreading of thin liquid films produced by drop impact on hot walls," *International Journal of Heat and Fluid Flow*, vol. 20, no. 5, pp. 470–476, 1999.

[137] Y. Xu, L. Tian, C. Zhu, and N. Zhao, "Numerical investigation of droplet impact on heated surfaces with pillars," *Physics of Fluids*, vol. 34, no. 2, 2022.

[138] J. G. Leidenfrost, "On the fixation of water in diverse fire," *International Journal of Heat and Mass Transfer*, vol. 9, no. 11, pp. 1153–1166, 1966.

[139] J. Bernardin and I. Mudawar, "The leidenfrost point: experimental study and assessment of existing models," *ASME Journal of Heat and Mass Transfer*, 1999.

[140] C. Cai, I. Mudawar, H. Liu, and C. Si, "Theoretical leidenfrost point (lfp) model for sessile droplet," *International Journal of Heat and Mass Transfer*, vol. 146, p. 118802, 2020.

[141] G. F. Hewitt, G. Shires, and I. Polezhaev, "International encyclopedia of heat & mass transfer," 1997.

[142] V. Talari, P. Behar, Y. Lu, E. Haryadi, and D. Liu, "Leidenfrost drops on micro/nanostructured surfaces," *Frontiers in Energy*, vol. 12, pp. 22–42, 2018.

[143] S. Y. Misyura, "The effect of weber number, droplet sizes and wall roughness on crisis of droplet boiling," *Experimental Thermal and Fluid Science*, vol. 84, pp. 190–198, 2017.

[144] Y. Qiao and S. Chandra, "Experiments on adding a surfactant to water drops boiling on a hot surface," *Proceedings of the Royal Society of London. Series A: Mathematical, Physical and Engineering Sciences*, vol. 453, no. 1959, pp. 673–689, 1997.

[145] L. Maquet, M. Brandenbourger, B. Sobac, A.-L. Biance, P. Colinet, and S. Dorbolo, "Leidenfrost drops: Effect of gravity," *Europhysics Letters*, vol. 110, no. 2, p. 24001, 2015.

[146] F. Celestini and G. Kirstetter, "Effect of an electric field on a leidenfrost droplet," *Soft Matter*, vol. 8, no. 22, pp. 5992–5995, 2012.

[147] B. Gottfried, C. Lee, and K. Bell, "The leidenfrost phenomenon: film boiling of liquid droplets on a flat plate," *International Journal of Heat and Mass Transfer*, vol. 9,

no. 11, pp. 1167–1188, 1966.

[148] B. Richter, K. Dullenkopf, and H.-J. Bauer, "Investigation of secondary droplet characteristics produced by an isooctane drop chain impact onto a heated piston surface," *Experiments in Fluids*, vol. 39, pp. 351–363, 2005.

[149] G. Castanet, T. Liénart, and F. Lemoine, "Dynamics and temperature of droplets impacting onto a heated wall," *International Journal of Heat and Mass Transfer*, vol. 52, no. 3-4, pp. 670–679, 2009.

[150] M. Zhang, J. Zhu, Z. Tao, and L. Qiu, "A quantitative phase diagram of droplet impingement boiling," *International Journal of Heat and Mass Transfer*, vol. 177, p. 121535, 2021.

[151] Q. Ma, X. Wu, and T. Li, "Droplet impact on superheated surfaces with different wettabilities," *International Journal of Heat and Mass Transfer*, vol. 141, pp. 1181–1186, 2019.

[152] D. Kwon, D. Kang, and E. Yeom, "Impact and boiling characteristics of an impinging ethanol drop on a heated al alloy surface," *International Journal of Heat and Mass Transfer*, vol. 169, p. 120927, 2021.

[153] S. Jowkar and M. Morad, "Water drop impact on a semi-cylindrical convex hot surface for a diameter ratio of unity," *Experimental Thermal and Fluid Science*, vol. 106, pp. 68–77, 2019.

[154] P. Dhar, S. R. Mishra, A. Gairola, and D. Samanta, "Delayed leidenfrost phenomenon during impact of elastic fluid droplets," *Proceedings of the Royal Society A*, vol. 476, no. 2243, p. 20200556, 2020.

[155] L. Guo, Y. Chen, N. Cai, W. Sun, Y. Yan, H. Wang, and Y. Gao, "Dynamic behaviors of fuel droplets impacting on the wall surfaces with different wettability and temperatures," *Applied Thermal Engineering*, vol. 212, p. 118536, 2022.

[156] G. Liang and I. Mudawar, "Review of drop impact on heated walls," *International Journal of Heat and Mass Transfer*, vol. 106, pp. 103–126, 2017.

[157] S. Akhtar, G. G. Nasr, and A. J. Yule, "Characteristics of water droplet impaction behavior on a polished steel heated surface: Part i," *Atomization and Sprays*, vol. 17, no. 8, 2007.

[158] G. E. Soriano, T. Zhang, and J. L. Alvarado, "Study of the effects of single and multiple periodic droplet impingements on liquid film heat transfer," *International Journal of*

Heat and Mass Transfer, vol. 77, pp. 449–463, 2014.

[159] M. Xu, C. Li, C. Wu, X. Chen, and S. Lu, "Regimes during single water droplet impacting on hot ethanol surface," *International Journal of Heat and Mass Transfer*, vol. 116, pp. 817–824, 2018.

[160] H. Wu, C. Liu, L. Tang, C. Cen, S.-L. Lin, C.-E. Huang *et al.*, "Inhibition of the wall-attached fuel combustion and the formation of aerosol particle," *Aerosol and Air Quality Research*, vol. 21, no. 10, p. 210138, 2021.

[161] X. Fan, C. Wang, F. Guo, B. Chen, and M. Li, "Water droplet impact on high-temperature peanut oil surface: The effects of droplet diameter and oil temperature," *International Journal of Thermal Sciences*, vol. 159, p. 106601, 2021.

[162] H. Wu, C. Liu, C. Cen, C.-E. Huang, S.-L. Lin *et al.*, "Study on dynamic characteristics of single droplet impingement on heated liquid film," *Aerosol and Air Quality Research*, vol. 23, no. 2, p. 220366, 2023.

[163] D. Qiu, V. Dhir, D. Chao, M. Hasan, E. Neumann, G. Yee, and A. Birchenough, "Single-bubble dynamics during pool boiling under low gravity conditions," *Journal of Thermophysics and Heat Transfer*, vol. 16, no. 3, pp. 336–345, 2002.

[164] J. P. McHale and S. V. Garimella, "Bubble nucleation characteristics in pool boiling of a wetting liquid on smooth and rough surfaces," *International Journal of Multiphase Flow*, vol. 36, no. 4, pp. 249–260, 2010.

[165] S. Gong, W. Ma, and H. Gu, "An experimental investigation on bubble dynamics and boiling crisis in liquid films," *International Journal of Heat and Mass Transfer*, vol. 79, pp. 694–703, 2014.

[166] Y. Li, K. Zhang, M.-C. Lu, and C. Duan, "Single bubble dynamics on superheated superhydrophobic surfaces," *International Journal of Heat and Mass Transfer*, vol. 99, pp. 521–531, 2016.

[167] E. Y. Gatapova and K. B. Gatapova, "Bubble dynamics in thin liquid films and breakup at drop impact," *Soft Matter*, vol. 16, no. 46, pp. 10 397–10 404, 2020.

[168] A. Faghri and Y. Zhang, *Modeling Multiphase Flow and Heat Transfer*. Cham: Springer International Publishing, 2020, pp. 95–188.

[169] S. Popinet, "Numerical models of surface tension," *Annual Review of Fluid Mechanics*, vol. 50, pp. 49–75, 2018.

[170] M. F. Trujillo, "Reexamining the one-fluid formulation for two-phase flows," *International Journal of Multiphase Flow*, vol. 141, p. 103672, 2021.

[171] F. H. Harlow and J. E. Welch, "Numerical calculation of time-dependent viscous incompressible flow of fluid with free surface," *The Physics of Fluids*, vol. 8, no. 12, pp. 2182–2189, 1965.

[172] F. H. Harlow and J. P. Shannon, "The splash of a liquid drop," *Journal of Applied Physics*, vol. 38, no. 10, pp. 3855–3866, 1967.

[173] C. W. Hirt and B. D. Nichols, "Volume of fluid (vof) method for the dynamics of free boundaries," *Journal of Computational Physics*, vol. 39, no. 1, pp. 201–225, 1981.

[174] W. F. Noh and P. Woodward, "Slic (simple line interface calculation)," in *Proceedings of the fifth international conference on numerical methods in fluid dynamics June 28–July 2, 1976 Twente University, Enschede*. Springer, 2005, pp. 330–340.

[175] D. L. Youngs, "Time-dependent multi-material flow with large fluid distortion," *Numerical Methods for Fluid Dynamics*, 1982.

[176] O. Ubbink and R. Issa, "A method for capturing sharp fluid interfaces on arbitrary meshes," *Journal of Computational Physics*, vol. 153, no. 1, pp. 26–50, 1999.

[177] D. K. Walters and N. M. Wolgemuth, "A new interface-capturing discretization scheme for numerical solution of the volume fraction equation in two-phase flows," *International Journal for Numerical Methods in Fluids*, vol. 60, no. 8, pp. 893–918, 2009.

[178] S. Osher and J. A. Sethian, "Fronts propagating with curvature-dependent speed: algorithms based on hamilton-jacobi formulations," *Journal of Computational Physics*, vol. 79, no. 1, pp. 12–49, 1988.

[179] M. Sussman and E. G. Puckett, "A coupled level set and volume-of-fluid method for computing 3d and axisymmetric incompressible two-phase flows," *Journal of Computational Physics*, vol. 162, no. 2, pp. 301–337, 2000.

[180] G. Tryggvason, B. Bunner, A. Esmaeeli, D. Juric, N. Al-Rawahi, W. Tauber, J. Han, S. Nas, and Y.-J. Jan, "A front-tracking method for the computations of multiphase flow," *Journal of Computational Physics*, vol. 169, no. 2, pp. 708–759, 2001.

[181] S. J. Cummins, M. M. Francois, and D. B. Kothe, "Estimating curvature from volume fractions," *Computers & Structures*, vol. 83, no. 6-7, pp. 425–434, 2005.

[182] S. Popinet and S. Zaleski, "A front-tracking algorithm for accurate representation of

surface tension," *International Journal for Numerical Methods in Fluids*, vol. 30, no. 6, pp. 775–793, 1999.

[183] J. U. Brackbill, D. B. Kothe, and C. Zemach, "A continuum method for modeling surface tension," *Journal of Computational Physics*, vol. 100, no. 2, pp. 335–354, 1992.

[184] C. S. Peskin, "Flow patterns around heart valves: a numerical method," *Journal of Computational Physics*, vol. 10, no. 2, pp. 252–271, 1972.

[185] S. O. Unverdi and G. Tryggvason, "A front-tracking method for viscous, incompressible, multi-fluid flows," *Journal of Computational Physics*, vol. 100, no. 1, pp. 25–37, 1992.

[186] R. P. Fedkiw, T. Aslam, B. Merriman, and S. Osher, "A non-oscillatory eulerian approach to interfaces in multimaterial flows (the ghost fluid method)," *Journal of Computational Physics*, vol. 152, no. 2, pp. 457–492, 1999.

[187] F. Gibou, L. Chen, D. Nguyen, and S. Banerjee, "A level set based sharp interface method for the multiphase incompressible navier–stokes equations with phase change," *Journal of Computational Physics*, vol. 222, no. 2, pp. 536–555, 2007.

[188] B. A. Nichita and J. R. Thome, "A level set method and a heat transfer model implemented into fluent for modeling of microscale two phase flows," in *AVT-178 Specialists' Meeting on System Level Thermal Management for Enhanced Platform Efficiency*, no. CONF, 2010.

[189] H. Ganapathy, A. Shooshtari, K. Choo, S. Dessiatoun, M. Alshehhi, and M. Ohadi, "Volume of fluid-based numerical modeling of condensation heat transfer and fluid flow characteristics in microchannels," *International Journal of Heat and Mass Transfer*, vol. 65, pp. 62–72, 2013.

[190] D.-L. Sun, J.-L. Xu, and L. Wang, "Development of a vapor–liquid phase change model for volume-of-fluid method in fluent," *International Communications in Heat and Mass Transfer*, vol. 39, no. 8, pp. 1101–1106, 2012.

[191] C. R. Kharangate and I. Mudawar, "Review of computational studies on boiling and condensation," *International Journal of Heat and Mass Transfer*, vol. 108, pp. 1164–1196, 2017.

[192] R. W. Schrage, *A theoretical study of interphase mass transfer*. Columbia University Press, 1953.

[193] H. Hertz, "Ueber die verdunstung der flüssigkeiten, insbesondere des quecksilbers, im

luftleeren raume," *Annalen der Physik*, vol. 253, no. 10, pp. 177–193, 1882.

[194] M. Knudsen, "The kinetic theory of gases: some modern aspects," *(No Title)*, 1950.

[195] Z. Liang, T. Biben, and P. Keblinski, "Molecular simulation of steady-state evaporation and condensation: Validity of the schrage relationships," *International Journal of Heat and Mass Transfer*, vol. 114, pp. 105–114, 2017.

[196] G. Vaartstra, Z. Lu, J. H. Lienhard, and E. N. Wang, "Revisiting the schrage equation for kinetically limited evaporation and condensation," *Journal of Heat Transfer*, vol. 144, no. 8, p. 080802, 2022.

[197] H. Wang, S. V. Garimella, and J. Y. Murthy, "Characteristics of an evaporating thin film in a microchannel," *International Journal of Heat and Mass Transfer*, vol. 50, no. 19-20, pp. 3933–3942, 2007.

[198] M. Kassemi and O. Kartuzova, "Effect of interfacial turbulence and accommodation coefficient on cfd predictions of pressurization and pressure control in cryogenic storage tank," *Cryogenics*, vol. 74, pp. 138–153, 2016.

[199] J. Voigtländer, F. Stratmann, D. Niedermeier, H. Wex, and A. Kiselev, "Mass accommodation coefficient of water: A combined computational fluid dynamics and experimental data analysis," *Journal of Geophysical Research: Atmospheres*, vol. 112, no. D20, 2007.

[200] W. H. Lee, "Pressure iteration scheme for two-phase flow modeling," *IN" MULTIPHASE TRANSPORT: FUNDAMENTALS, REACTOR SAFETY, APPLICATIONS"*., pp. 407–432, 1980.

[201] H. Wu, X. Peng, P. Ye, and Y. E. Gong, "Simulation of refrigerant flow boiling in serpentine tubes," *International Journal of Heat and Mass Transfer*, vol. 50, no. 5-6, pp. 1186–1195, 2007.

[202] E. Da Riva, D. Del Col, S. V. Garimella, and A. Cavallini, "The importance of turbulence during condensation in a horizontal circular minichannel," *International Journal of Heat and Mass Transfer*, vol. 55, no. 13-14, pp. 3470–3481, 2012.

[203] Z. Tong, H. Wu, X. Li, and Z. Han, "Cfd simulation on the operation characteristics of co2 two-phase thermosyphon loop," *Applied Thermal Engineering*, vol. 224, p. 120103, 2023.

[204] M. Rieber and A. Frohn, "A numerical study on the mechanism of splashing," *International Journal of Heat and Fluid Flow*, vol. 20, no. 5, pp. 455–461, 1999.

[205] L. Rayleigh, "On the instability of jets," *Proceedings of the London mathematical society*, vol. 1, no. 1, pp. 4–13, 1878.

[206] G. Liang, T. Zhang, L. Chen, Y. Chen, and S. Shen, "Single-phase heat transfer of multi-droplet impact on liquid film," *International Journal of Heat and Mass Transfer*, vol. 132, pp. 288–292, 2019.

[207] G. Liang, T. Zhang, Y. Chen, L. Chen, and S. Shen, "Two-phase heat transfer of multi-droplet impact on liquid film," *International Journal of Heat and Mass Transfer*, vol. 139, pp. 832–847, 2019.

[208] Y.-B. Wang, X.-D. Wang, T.-H. Wang, and W.-M. Yan, "Asymmetric heat transfer characteristics of a double droplet impact on a moving liquid film," *International Journal of Heat and Mass Transfer*, vol. 126, pp. 649–659, 2018.

[209] S. Hardt and F. Wondra, "Evaporation model for interfacial flows based on a continuum-field representation of the source terms," *Journal of Computational Physics*, vol. 227, no. 11, pp. 5871–5895, 2008.

[210] R. Ranjan, J. Y. Murthy, and S. V. Garimella, "A microscale model for thin-film evaporation in capillary wick structures," *International Journal of Heat and Mass Transfer*, vol. 54, no. 1-3, pp. 169–179, 2011.

[211] Y. Qiu, H. Lee, and C. R. Kharangate, "Computational investigation of annular flow condensation in microgravity with two-phase inlet conditions," *International Communications in Heat and Mass Transfer*, vol. 118, p. 104877, 2020.

[212] S. C. De Schepper, G. J. Heynderickx, and G. B. Marin, "Modeling the evaporation of a hydrocarbon feedstock in the convection section of a steam cracker," *Computers & Chemical Engineering*, vol. 33, no. 1, pp. 122–132, 2009.

[213] G. Son and V. K. Dhir, "Numerical simulation of film boiling near critical pressures with a level set method," *ASME Journal of Heat and Mass Transfer*, 1998.

[214] S. Chen, Z. Yang, Y. Duan, Y. Chen, and D. Wu, "Simulation of condensation flow in a rectangular microchannel," *Chemical Engineering and Processing: Process Intensification*, vol. 76, pp. 60–69, 2014.

[215] Y. Yap, H. Li, J. Lou, L. Pan, and Z. Shang, "Numerical modeling of three-phase flow with phase change using the level-set method," *International Journal of Heat and Mass Transfer*, vol. 115, pp. 730–740, 2017.

[216] A. Sielaff, J. Dietl, S. Herbert, and P. Stephan, "The influence of system pressure on

bubble coalescence in nucleate boiling," *Heat Transfer Engineering*, vol. 35, no. 5, pp. 420–429, 2014.

[217] P. Pournaderi and A. Pishevar, "A numerical investigation of droplet impact on a heated wall in the film boiling regime," *Heat and Mass Transfer*, vol. 48, pp. 1525–1538, 2012.

[218] A. Alizadehdakhel, M. Rahimi, and A. A. Alsairafi, "Cfd modeling of flow and heat transfer in a thermosyphon," *International Communications in Heat and Mass Transfer*, vol. 37, no. 3, pp. 312–318, 2010.

[219] Y. Sato and B. Ničeno, "A sharp-interface phase change model for a mass-conservative interface tracking method," *Journal of Computational Physics*, vol. 249, pp. 127–161, 2013.

[220] A. B. Aljedaani, C. Wang, A. Jetly, and S. T. Thoroddsen, "Experiments on the breakup of drop-impact crowns by marangoni holes," *Journal of Fluid Mechanics*, vol. 844, pp. 162–186, 2018.

[221] S. L. Manzello and J. C. Yang, "An experimental study of a water droplet impinging on a liquid surface," *Experiments in Fluids*, vol. 32, no. 5, pp. 580–589, 2002.

[222] B. R. Mitchell, J. C. Klewicki, Y. P. Korkolis, and B. L. Kinsey, "The transient force profile of low-speed droplet impact: measurements and model," *Journal of Fluid Mechanics*, vol. 867, pp. 300–322, 2019.

[223] I. Ferrão, D. Vasconcelos, D. Ribeiro, A. Silva, and J. Barata, "A study of droplet deformation: The effect of crossflow velocity on jet fuel and biofuel droplets impinging onto a dry smooth surface," *Fuel*, vol. 279, p. 118321, 2020.

[224] N. Otsu, "A threshold selection method from gray-level histograms," *IEEE Transactions on Systems, Man, and Cybernetics*, vol. 9, no. 1, pp. 62–66, 1979.

[225] R. O. Duda and P. E. Hart, "Use of the hough transformation to detect lines and curves in pictures," *Communications of the ACM*, vol. 15, no. 1, pp. 11–15, 1972.

[226] N. P. Van Hinsberg, M. Budakli, S. Göhler, E. Berberović, I. V. Roisman, T. Gambaryan-Roisman, C. Tropea, and P. Stephan, "Dynamics of the cavity and the surface film for impingements of single drops on liquid films of various thicknesses," *Journal of Colloid and Interface Science*, vol. 350, no. 1, pp. 336–343, 2010.

[227] D. A. Vasconcelos, A. R. Silva, and J. M. Barata, "The impact of temperature on heated liquid films: Crater and jetting impact dynamics," *Experimental Thermal and Fluid*

Science, vol. 147, p. 110944, 2023.

[228] M. Rein, *Drop-surface interactions*. Springer, 2014, vol. 456.

[229] D. A. Vasconcelos, A. R. Silva, and J. M. Barata, "Splashing morphology and crown dynamics of single droplets impinging heated liquid films."

[230] A. Mendes, "The influence of temperature in regime transition boundaries for single droplet impact upon heated liquid films," Master's thesis, University of Beira Interior, 2023.

[231] D. Vasconcelos, A. Silva, and J. Barata, "Influence of bubble growth and liquid film instabilities on droplet impact phenomena under saturated boiling regimes," *Atomization and Sprays*, vol. 34, no. 4, 2024.

[232] A. Lippert, T. Tolle, A. Dörr, and T. Maric, "A benchmark for surface-tension-driven incompressible two-phase flows," *arXiv preprint arXiv:2212.02904*, 2022.

[233] S. Popinet. (2013) Basilisk flow solver. [Online]. Available: http://www.basilisk.fr

[234] B. D. Fudge, R. Cimpeanu, and A. A. Castrejón-Pita, "Dipping into a new pool: The interface dynamics of drops impacting onto a different liquid," *Physical Review E*, vol. 104, no. 6, p. 065102, 2021.

[235] G. D. Weymouth and D. K.-P. Yue, "Conservative volume-of-fluid method for free-surface simulations on cartesian-grids," *Journal of Computational Physics*, vol. 229, no. 8, pp. 2853–2865, 2010.

[236] G. D. Weymouth, D. G. Dommermuth, K. Hendrickson, and D. K.-P. Yue, "Advancements in cartesian-grid methods for computational ship hydrodynamics," in *26th Symposium on Naval Hydrodynamics*, 2006.

[237] J. B. Bell, P. Colella, and H. M. Glaz, "A second-order projection method for the incompressible navier-stokes equations," *Journal of Computational Physics*, vol. 85, no. 2, pp. 257–283, 1989.

[238] P. Colella, "A multidimensional second order godunov scheme for conservation laws," *Journal of Computational Physics*, vol. 87, pp. 171–200, 1990.

[239] B. Vanleer, "Multidimensional explicit difference schemes for hyperbolic conservation laws," Delft University of Technology, Tech. Rep., 1983.

[240] S. Popinet, "A quadtree-adaptive multigrid solver for the serre–green–naghdi equations," *Journal of Computational Physics*, vol. 302, pp. 336–358, 2015.

[241] A. J. Chorin, "On the convergence of discrete approximations to the navier-stokes equations," *Mathematics of Computation*, vol. 23, no. 106, pp. 341–353, 1969.

[242] S. Popinet, "An accurate adaptive solver for surface-tension-driven interfacial flows," *Journal of Computational Physics*, vol. 228, no. 16, pp. 5838–5866, 2009.

[243] L. Guo, "Numerical investigation of taylor bubble and development of phase change model," Ph.D. dissertation, Université de Lyon, 2020.

[244] J. A. Van Hooft, S. Popinet, C. C. Van Heerwaarden, S. J. Van der Linden, S. R. De Roode, and B. J. Van de Wiel, "Towards adaptive grids for atmospheric boundary-layer simulations," *Boundary-Layer Meteorology*, vol. 167, pp. 421–443, 2018.

[245] D. d. A. V. Rodrigues, "Numerical analysis of a single droplet impinging upon liquid films using the vof method," Master's thesis, Universidade da Beira Interior (Portugal), 2018.

[246] J.-M. López-Herrera, S. Popinet, and A.-A. Castrejón-Pita, "An adaptive solver for viscoelastic incompressible two-phase problems applied to the study of the splashing of weakly viscoelastic droplets," *Journal of Non-Newtonian Fluid Mechanics*, vol. 264, pp. 144–158, 2019.

[247] D. Vasconcelos, A. Silva, and J. Barata, "Comparison of commercial and open-source cfd solvers on surface tension dominated flows," in *International Conference on Liquid Atomization and Spray Systems (ICLASS)*, vol. 1, no. 1, 2021.

[248] D. Vasconcelos, A. Silva, and J. M. Barata, "Influence of vapour bubbles size and spacing on droplet impact outcomes under subcooled boiling regimes," in *ILASS–Europe 2022, 31st Conference on Liquid Atomization and Spray Systems*. ILASS-Europe, Institute for Liquid Atomization and Spray Systems.

Appendix A

Fluids Thermophysical Properties

A.1 Water

Table A.1: Thermophysical properties of pure water at atmospheric pressure [6].

T [K]	ρ $[\mathrm{kg\,m^{-3}}]$	μ $[\mathrm{kg\,m^{-1}\,s^{-1}}]$	σ $[\mathrm{N\,m^{-1}}]$	C_p $[\mathrm{J\,kg^{-1}\,K^{-1}}]$	k $[\mathrm{J\,s^{-1}\,m^{-1}\,K^{-1}}]$
278.2	1000	0.001519	0.07494	4200	0.5576
283.2	999.7	0.001307	0.07422	4188	0.5674
288.2	999.1	0.001138	0.07348	4184	0.5769
293.2	998.2	0.001002	0.07273	4183	0.5861
298.2	997.1	0.0008905	0.07197	4183	0.5948
303.2	995.7	0.0007977	0.07119	4183	0.603
308.2	994.0	0.0007196	0.0704	4183	0.6107
313.2	992.2	0.0006533	0.06959	4182	0.6178
318.2	990.2	0.0005963	0.06877	4182	0.6244
323.2	988.0	0.0005471	0.06794	4181	0.6305
328.2	985.7	0.0005042	0.0671	4182	0.636
333.2	983.2	0.0004666	0.06624	4183	0.641
338.2	980.6	0.0004334	0.06536	4184	0.6455
343.2	997.8	0.000404	0.06448	4187	0.6495
348.2	974.9	0.0003779	0.06358	4190	0.653
353.2	971.8	0.0003545	0.06267	4194	0.6562
358.2	968.6	0.0003335	0.06175	4199	0.6589
363.2	965.3	0.0003145	0.06081	4204	0.6613
368.2	961.9	0.0002974	0.05987	4210	0.06623
373.2	0.5896	0.00001227	0.05891	2042	0.02506

A.2 N-heptane

Density: $\rho = 0.23237 \times 0.26020^{-(1-T(K)/540.26)^{0.2791}} \left[\mathrm{g\,cm^{-3}}\right]$

Viscosity: $log_{10}(\mu) = -5.7782 + 8.0587 \times 10^2/T(K) + 1.3355 \times 10^{-2}T(K) - -1.4794 \times 10^{-5}T^2(K) \left[\mathrm{mPa\,s}\right]$

Surface tension: $\sigma = 53.64\,(1 - T(K)/540.26)^{1.2431} \left[\mathrm{mN\,m^{-1}}\right]$

Thermal conductivity: $log_{10}(k) = -1.8482 + 1.1843\,(1 - T(K)/536.40)^{2/7} \left[\mathrm{W\,m^{-1}\,K^{-1}}\right]$

Specific heat capacity: $C_p = \left(101.121 + 9.7739 \times 10^{-1} T(K) - 3.0712 \times 10^{-3} T^2(K) + \right.$
$\left. + 4.1844 \times 10^{-6} T^3(K)\right) / 100.2019 \left[\mathrm{J\,kg^{-1}\,K^{-1}}\right]$

A.3 N-decane

Density: $\rho = 0.23276 \times 0.25240^{-(1-T(K)/618.45)^{0.28570}} \left[\mathrm{g\,cm^{-3}}\right]$

Viscosity: $log_{10}(\mu) = -6.0716 + 1.0177 \times 10^3 / T(K) + 1.2247 \times 10^{-2} T(K) -$
$-1.1892 \times 10^{-5} T^2(K)$ [mPa s]

Surface tension: $\sigma = 55.777 \left(1 - T(K)/618.45\right)^{1.3198} \left[\mathrm{mN\,m^{-1}}\right]$

Thermal conductivity: $log_{10}(k) = -1.7768 + 1.0839 \left(1 - T(K)/618.45\right)^{2/7} \left[\mathrm{W\,m^{-1}\,K^{-1}}\right]$

Specific heat capacity: $C_p = \left(79.741 + 1.6926 T(K) - 4.5287 \times 10^{-3} T^2(K) + \right.$
$\left. + 4.9769 \times 10^{-6} T^3(K)\right) / 142.264 \left[\mathrm{J\,kg^{-1}\,K^{-1}}\right]$

Appendix B

Aluminium Block

B.1 Design

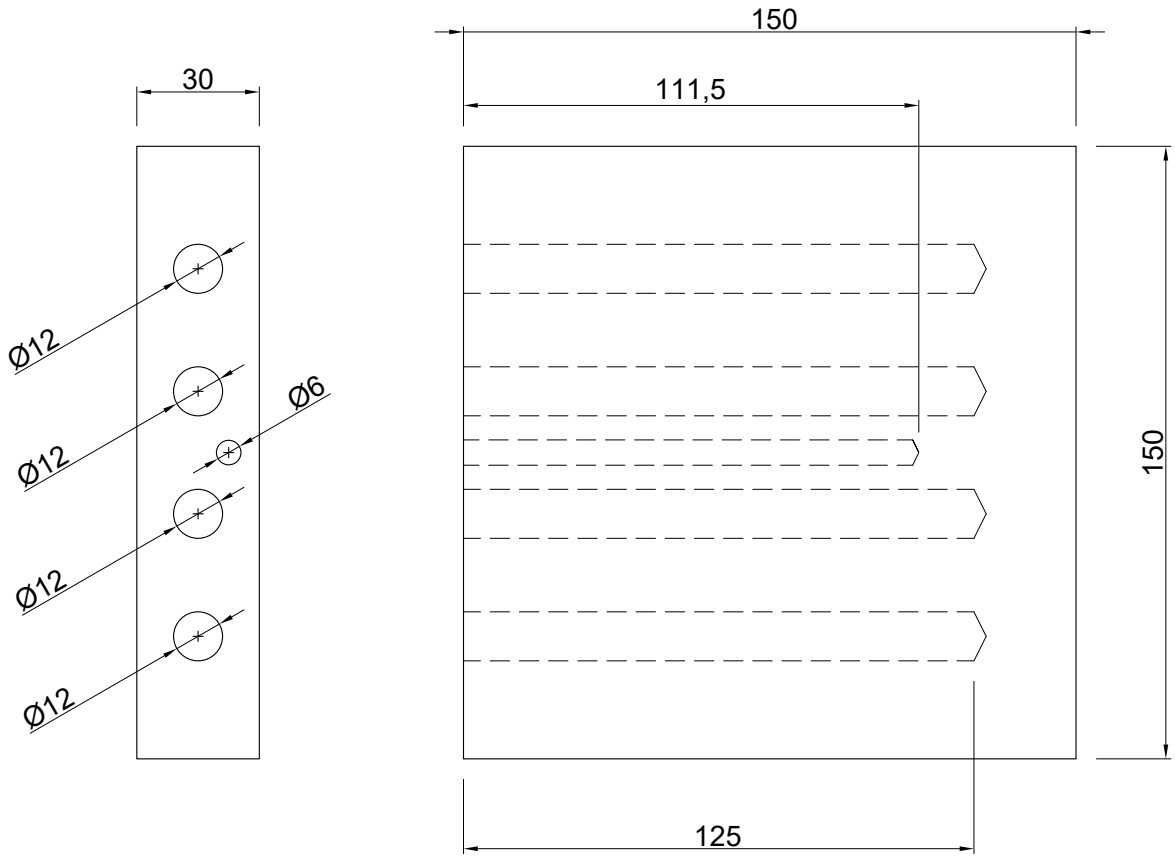

Figure B.1: Side and top views of the aluminium block, including embedded cartridge heaters, a thermocouple, and respective dimensions [mm].

B.2 Datasheet

Table B.1: Aluminium 5083 datasheet.

Chemical Element	**% Present**
Manganese (Mn)	$0.40 - 1.00$
Iron (Fe)	$0.0 - 0.40$
Copper (Cu)	$0.0 - 0.10$
Magnesium (Mg)	$4.00 - 4.90$
Silicon (Si)	$0.0 - 0.40$
Zinc (Zn)	$0.0 - 0.10$
Chromium (Cr)	$0.05 - 0.25$
Titanium (Ti)	$0.05 - 0.25$
Other (Each)	$0.0 - 0.05$
Others (Total)	$0.0 - 0.15$
Aluminium (Al)	Balance

Physical Property	**Value**
Density	$2650\ \mathrm{kg\,m^{-3}}$
Melting Point	$570^{\circ}\mathrm{C}$
Thermal Expansion	$25 \times 10^{-6}\ \mathrm{K^{-1}}$
Modulus of Elasticity	$72\ \mathrm{GPa}$
Thermal Conductivity	$121\ \mathrm{W\,m^{-1}\,K^{-1}}$
Electrical Resistivity	$0.05810 \times 10^{-6}\ \Omega\,\mathrm{m}$

Mechanical Property	**Value**
Proof Stress	$115\ \mathrm{Min\ MPa}$
Tensile Strength	$270 - 345\ \mathrm{MPa}$
Hardness Brinell	$75\ \mathrm{HB}$

Appendix C

Thermocouples

Table C.1: Specification of the mini-sheathing thermocouples acquired from Therma Thermofühler GmbH, Germany.

Component	**Description**
Sheathed thermocouple pairing	Type K
Limiting deviation	Cl. 1 as per DIN EN $60584 - 1: 2014 - 07$
Sheathing material	Inconel600
Sheathing material	hot junction insulated
Probe diameter	0.5 mm
Element length	50 mm
Element length	5.0×40 mm
Conductor	Fibreglass with VA braid
Conductor	Strand, 2×0.22 mm
Wire Length	2500 mm
Connection	Mini-Plug, green